Department of Chemistry
Imperial College London

Development of Fluorescence Lifetime Measurement Techniques for Use in Microfluidic Channels

Margarita Antonia Stapountzis

December 2012

A thesis submitted in partial fulfilment of the requirement for the degree of Doctor of Philosophy

ABSTRACT

Fluorescence lifetime measurements are a powerful tool in biomedical research and advances in detection technology make them ideally suited for the study of biomolecular interactions. Time-resolved techniques, compared to more conventional methods, provide improved precision and contrast in the monitoring of complex biological processes. Fluorescence lifetimes are extracted by using time-correlated single-photon counting, which offers single photon sensitivity, high temporal resolution and excellent signal to noise ratio. Furthermore, combining this technique with microfluidics offers unprecedented advantages. For example, in analytical applications, apart from the high sensitivity required, the study of analytes often demands low sample consumption and short mixing times to allow for the monitoring of quick reactions. These parameters can nicely be achieved with the use of microfluidics. Hydrodynamic focusing within 3-inlet 1-outlet continuous flow microfluidic devices can be used as a molecular confinement mechanism to improve the detection efficiency as well as a means to enhance mixing within microchannels for the study of fast reaction kinetics.

In this work, a powerful combination of confocal microscopy and microfluidics was used to perform fluorescence lifetime measurements on freely diffusing and freely flowing molecules. For this purpose, a home-built scanning confocal system was developed to ensure sufficient reduction in background levels, enabling the detection of fluorescence signal that arises from single molecules. Fluorescence lifetime imaging along with a maximum likelihood estimator adapted from single molecule studies was performed to visualise hydrodynamic focusing and characterise mixing within microfluidic devices. Time-resolved methods were also employed to detect single molecules freely flowing within microchannels. A novel fluorescence lifetime approach was developed to perform Förster resonance energy transfer measurements on freely diffusing molecules and subsequently applied for the study of streptavidin-biotin binding and protein conformational changes upon unfolding.

ACKNOWLEDGEMENTS

I would like to take this opportunity to thank my supervisor Dr. Joshua Edel for his continuous inspiration and guidance. I am grateful for his patience and invaluable support. I would also like to thank the members of the Dr. Edel group for providing the necessary lab training. I gratefully acknowledge funding from the Engineering and Physical Sciences Research Council (EPSRC). Finally, I would like to thank my dear friend Billy for his continuous and unconditional support and my family for their enduring help and encouragement throughout this research.

DECLARATION OF ORIGINALITY

I certify that all work presented in this thesis is my own unless otherwise stated in the text. Material provided by other researchers has been properly acknowledged and referenced.

Margarita Antonia Stapountzis

COPYRIGHT DECLARATION

TABLE OF CONTENTS

LIST OF FIGURES

LIST OF TABLES

LIST OF SYMBOLS AND ABBREVIATIONS

Symbols

α	side-to-central inlet flow rate ratio
α_D	amplitude of donor component in multi-exponential decay
α_{DA}	amplitude of donor-acceptor component in multi-exponential decay
α_l	factor expressing acceptor leakage into the donor channel
α_S	amplitude of setup component in multi-exponential decay
β_l	factor expressing donor leakage into the acceptor channel
CR	biotin/streptavidin concentration ratio
d	diffusion distance
D	molecular diffusion coefficient
d_1, d_2	channel dimension parameters
ΔG_u	free energy of protein unfolding reaction
ΔG_u^{H2O}	free energy of protein unfolding reaction at zero SDS concentration
ε	channel aspect ratio
ε_{abs}	absolute error
ε_A	extinction coefficient of the acceptor
ε_D	extinction coefficient of the donor
E_{FRET}	efficiency of resonance energy transfer
ε_{rel}	relative error
f	volumetric flow rate – subscripts c, f, o, s denote central inlet, focused stream, outlet and side inlet respectively
F_c	correction performed on the experimentally determined folded protein fraction
F_f	fraction of proteins in a sample that are folded
f_{obj}	objective focal length
f_{tot}	total flow rate
$f_{tot,n}$	normalised total flow rate
F_u	fraction of proteins in a sample that are unfolded
γ	parameter related to donor and acceptor quantum yields and channel detection efficiencies
h	channel height
η	solvent viscosity
η_A, η_D	detection efficiencies of the acceptor and the donor channels
I	electrical current
I	fluorescence intensity
I_0	fluorescence intensity at time zero

I_A	fluorescence intensity of the acceptor in the absence of the donor
I_{AD}	fluorescence intensity of the acceptor in the presence of the donor
I_D	fluorescence intensity of the donor in the absence of the acceptor
I_{DA}	fluorescence intensity of the donor in the presence of the acceptor
I_H	fluorescence intensity of hybridised DNA
$J(\lambda)$	spectral overlap between the donor an acceptor at wavelength λ
k	Boltzmann constant
K_a	association constant
k_{FRET}	resonance energy transfer rate constant
k_r	radiative rate constant
k_{nr}	non-radiative rate constant
k_{obs}	observed unfolding rate constant
k_q	biomolecular quenching rate coefficient
κ^2	relative orientation in space factor between the transition dipoles of a donor and an acceptor
ℓ	channel length
λ	wavelength
M_{obj}	objective magnification
M_{syst}	system magnification
M_{tot}	total magnification factor
MLE	maximum likelihood estimator
μ	solvent dynamic viscosity
n	refractive index
n_A	average number of acceptors interacting with one donor
NA	numerical aperture
P	pressure
p_1, p_2, p_3, p_4	fitting parameters
Q	quantum yield
Q_A	quantum yield of the acceptor
Q_D	quantum yield of the donor
r	hydrodynamic radius
R	fluidic resistance
R_0	characteristic Förster distance
R_{airy}	airy disk radius
R_{beam}	laser beam radius
R_{DA}	distance between donor and acceptor molecules
R_e	Reynolds number

R_g	gas constant
ρ	solvent density
σ	standard deviation
t	time
T	temperature
t_{mix}	mixing time
τ	fluorescence lifetime
τ_0	lifetime in the absence of the quencher
τ_D	fluorescence lifetime of the donor in the absence of the acceptor
τ_{DA}	fluorescence lifetime of the donor in the presence of the acceptor
τ_S	fluorescence lifetime of the setup component
v	average flow velocity – subscripts c, f, o, s denote central inlet, focused stream, outlet and side inlet respectively
V	electrical potential
V	confocal probe volume
w	channel width – subscripts c, f, o, s denote central inlet, focused stream, outlet and side inlet respectively
w_{beam}	diffraction limited beam waist radius
χ_R^2	reduced chi-square
χ_{SDS}	dimensionless SDS mole fraction
Z'	half the probe depth

Abbreviations

2-D, 3-D	2-dimensional, 3-dimensional
A168C	bacteriorhodopsin cysteine mutation at alanine 168
AcrOr	acridin orange hydrochloride hydrate
AF488	AlexaFluor488
AF647	AlexaFluor647
AOC	AOTF controller
AOD	AOTF device
AOTF	acousto-optic tuneable filter
APD	avalanche photodiode
bO	bacterioopsin
bp	base pairs
BPF	band pass filter
bR	bacteriorhodopsin

C	collimator
CCD	charge-coupled device
CHAPS	3-[(3-cholamidopropyl)dimethylammonio]-1-propanesulfonate
D102C	bacteriorhodopsin cysteine mutation at position 102
DDM	*n*-dodecyl-b-D-maltoside
DL549	DyLight549
DL633	DyLight633
DM	dichroic mirror
DMPC	1,2-dimyristoyl-*sn*-glycero-3-phosphocholine
DNA488B	single stranded DNA sample labelled with AlexaFluor488 and biotin
DNA647	single stranded DNA sample labelled with AlexaFluor647
DNA647B	hybridised DNA sample labelled with AlexaFluor647 and biotin
dsDNA	double-stranded DNA
F	filter
FC	fibre coupler
FCS	fluorescence correlation spectroscopy
FITC	fluorescein 5-isothiocyanate
FLIM	Fluorescence lifetime imaging
FM	flip-mount mirror
FRET	Förster resonance energy transfer
FRET04	DNA labelled with DyLight549 and DyLight633 at 4 base pairs separation
FRET09	DNA labelled with DyLight549 and DyLight633 at 9 base pairs separation
FRET14	DNA labelled with DyLight549 and DyLight633 at 14 base pairs separation
Fsc	fluorescein
FV300	Fluoview 300
HybrDNA	hybridised DNA sample labelled with AlexaFluor488 and AlexaFluor647
IRF	instrument response function
L	lens
LPF	long pass filter
M	mirror
NaP	sodium phosphate buffer
NHS esters	N-hydroxysuccinimide esters
OBJ	objective
OD	neutral density filter
OF	optical fibre
Pdf	probability density function
PDL(D)	pulsed diode laser (driver)

PDMS	poly(dimethylsiloxane)
RF	radio frequency
PH	pinhole
PMMA	poly(methylmethacrylate)
PMT	photomultiplier tube
PZT	piezoelectric transducer
Rd110	rhodamine 110 chloride
S_0	ground electronic state
S_1	first excited state
SDS	sodium dodecylsulfate
SM	scanning mirror
SMD	single molecule detection
S/N	signal-to-noise ratio
SS	supercontinuum source
ssDNA	single-stranded DNA
Str48	AlexaFluor488 streptavidin conjugate
T_1	triplet state
TCSPC	time-correlated single-photon counting
TIRFM	total internal reflection fluorescence microscopy
Tris-HCl	tris(hydroxymethyl) aminomethane hydrochloride
TTTR	time-tagged time-resolved
ZMWs	zero mode waveguides

CHAPTER 1
INTRODUCTION

1.1. Fluorescence microscopy: principles and considerations

1.1.1. Basic principles

Fluorescence is a phenomenon whereby photon emission occurs by a molecule (or fluorophore) following absorption of one or more photons from the ground to the excited state. This process can be simply demonstrated by plotting a modified Jablonski diagram [1] as it is shown in figure 1.1.

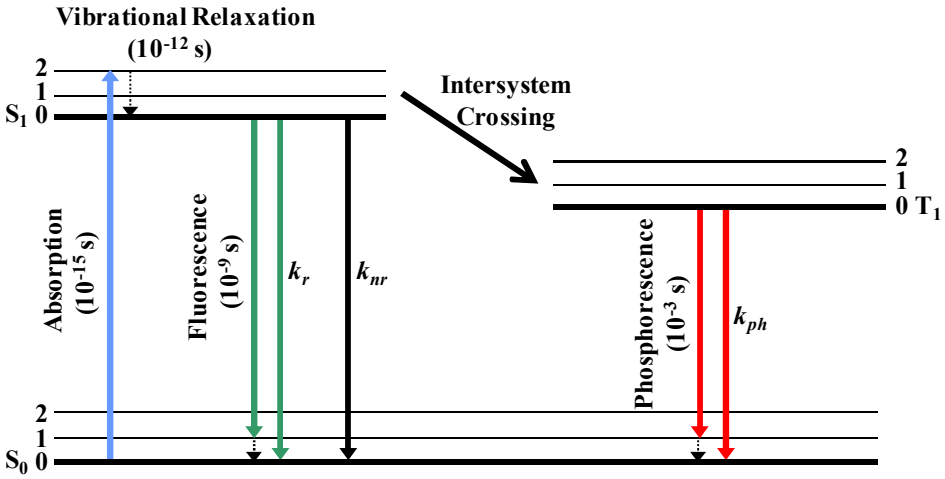

Figure 1.1. Simplified Jablonski diagram. S_0 denotes the ground electronic state, S_1 the first excited state and T_1 the triplet state. Fluorophore excitation is followed by rapid relaxation to the lowest vibrational level in S_1 and return to S_0 either via fluorescence emission (k_r) or non-radiatively (k_{nr}). Intersystem crossing (to T_1) followed by phosphorescence emission (k_{ph}) may also occur.

Briefly, the fluorophore is excited from the ground state S_0 to a vibrational level of the excited state S_1. This is followed by rapid relaxation to the lowest vibrational level in S_1 (vibrational relaxation) and occurs on a 10^{-12} s timescale. The return to the ground state S_0 follows with either photon emission (fluorescence) at a rate k_r or non-radiatively at a rate k_{nr}. k_{nr} is defined to include all possible non-radiative decay processes. For most fluorophores the excitation - emission cycle can be repeated thousands of times before the molecule becomes photobleached resulting in the termination of fluorescence [1]. Following vibrational relaxation, excited molecules can also pass to a triplet state T_1, via intersystem crossing, and can subsequently return to the ground state through phosphorescence. Transition from the T_1

to S_0 state is spin-forbidden therefore phosphorescence is much slower than fluorescence (on the order of milliseconds to seconds). T_1 state is lower in energy than S_1 causing phosphorescence wavelengths to be generally longer compared to fluorescence (red-shifted).

The fluorescence emission spectrum typically represents only the S_1 to S_0 transition. During the excitation-emission cycle, energy loss occurs due to vibrational relaxation, solvent effects, excited-state reactions, complex formation, or energy transfer. As a result, fluorescence occurs at longer wavelengths than that of the absorption spectra. The difference between the peak maxima, defined as the Stokes shift, is a property with great importance in fluorescence spectroscopy as it allows for optical filters to be used to separate emitted signal from excitation light.

The ratio of the number of fluorescence photons emitted to the number of excitation photons absorbed is defined as the quantum yield Q and is expressed via equation 1.1 [1]:

$$Q = \frac{k_r}{k_r + k_{nr}} \tag{1.1}$$

Assuming single exponential decay, the usual expression for fluorescence intensity is [1]:

$$I(t) = I_0 \exp\left(\frac{-t}{\tau}\right) \qquad \text{with} \qquad \tau = \frac{1}{(k_r + k_{nr})} = \frac{Q}{k_r} \tag{1.2}$$

where $I(t)$ is the fluorescence intensity at time t after excitation, I_0 is the intensity at time zero, and τ is the fluorescence lifetime. The fluorescence lifetime is given by the inverse of the sum of all rates depopulating the excited state (equation 1.2). τ expresses the average time the molecule remains in the excited state before returning to the ground state and can take on values from a few picoseconds to tens of nanoseconds [2]. Although the fluorescence lifetime is characteristic of each fluorophore, it can also depend on excitation and emission wavelength [3] and on local environmental conditions of the molecule such as pH, ion concentration, or viscosity [4]. The fluorescence lifetime has also been found to be influenced by the proximity to a dielectric or metallic surface [5-7] or by the interaction of the excited state of the molecule with the solvent [8].

The fluorescence emission is a random process, therefore the lifetime is solely a statistical average and few molecules will emit photons exactly at time $t = \tau$. For a single exponential

decay, at $t = \tau$ the intensity drops to $(1/e)\times I_0$. This effectively states that 63% of photons decay before $t = \tau$ and 37% thereafter. For fluorophores that display decays that are more complex than a single exponential or for a mixture of multiple fluorophores, equation 1.2 can be modified and written as [1]:

$$I(t) = \sum_{i=1}^{n} a_i \exp\left(\frac{-t}{\tau_i}\right) \tag{1.3}$$

where τ_i are the decay times, α_i the respective amplitudes and n is the number of lifetime components. The average lifetime is then given by [1]:

$$\bar{\tau} = \sum_{i=1}^{n} f_i \tau_i \qquad \text{with} \qquad f_i = \frac{\alpha_i \tau_i}{\sum_{j=1}^{n} \alpha_j \tau_j} \tag{1.4}$$

1.1.2. Fluorescence measurements: the fluorescence lifetime approach

Analysis of the fluorescence properties, intensity, wavelength and lifetime, can provide information about molecular species, states and environments. Unlike transmitted-light microscopy which mainly distinguishes individual structures based on their shape or optical density, in fluorescence microscopy the excitation light is rejected, leaving visible only the sources of emission. Objects that are smaller than the diffraction limit can be detected with high sensitivity and contrast [9]. Fluorescence measurement and imaging techniques have made continuous progress over the past twenty years. Although numerous fields including material science, solid state physics and crystal spectroscopy have emerged using fluorescence microscopy, most applications are related to biology and medicine [10]. External fluorophores with high quantum yield can be used as tags to label specific molecules of interest without perturbing their functions. Furthermore, a number of biological molecules and other bio-polymers possess intrinsic fluorescence. The autofluorescence can be used for the label-free identification of these biomolecules [10, 11].

Conventionally, fluorescence intensity measurements yield information about the location or distribution of fluorophores and their local environment. Discrimination amongst fluorescent species is achieved according to differences in intensity and shape or peak position of their spectra. Improvements on this technique for overlapping spectra involve the operation at multiple excitation/emission wavelengths [12, 13]. The fluorescence intensity often depends

on the fluorophore concentration, on attenuation by re-absorption, scattering or quenching, on detection efficiency and illumination intensity and uniformity. Therefore, an alternative, more robust approach, involves measuring the fluorescence lifetime as opposed to the intensity. Fluorescence lifetimes are determined by the radiative and non-radiative decay rates (equation 1.2) and are typically not affected by fluorophore concentration, photobleaching and excitation intensity. Hence, they can be used to locate and distinguish between fluorophore species with similar or overlapping spectra (via k_r), overcoming the artefacts arising from intensity measurements. Fluorescence lifetime measurements can also be employed to probe the local environment of a fluorophore via k_{nr}. Numerous applications of time-resolved fluorescence spectroscopy have been reported including studies on protein and membrane dynamics, immunoassays and nucleic acid technology [14].

A time-domain approach for performing fluorescence lifetime measurements involves exciting the sample with a laser pulse with duration much shorter than that of the fluorophore lifetime and measuring the fluorescence decay over time. Lifetimes are extracted by either time gating or via time-correlated single-photon counting (TCSPC). In time gating, the fluorescence intensity is measured at different time delays after the excitation pulse and the fluorescence lifetime is determined by fitting these data to an exponential curve [15]. In applications using TCSPC, single photon counting detectors (photomultiplier tubes or avalanche photodiodes) are employed to detect single photon arrival events. The relative times between excitation pulse and photon arrival time are recorded and subsequently used to form a histogram. The experimental conditions are optimized so that less than one photon is detected per excitation pulse [16]. Main advantages of TCSPC include single photon sensitivity, high temporal resolution (picoseconds) and excellent signal to noise ratio [17].

Imaging a structure of interest using fluorescence lifetimes entails determining the fluorescence decay time for each pixel in a field of view and producing a respective two-dimensional map of the lifetimes. Fluorescence lifetime imaging (FLIM) has been successfully used for a large variety of biological and biomedical applications such as imaging of living tissues and cells [10, 11, 17-21]. An example of fluorescence intensity and lifetime maps of a patient's skin is given in figure 1.2, whereby a tumour, visualised via FLIM, exhibits a lifetime significantly longer (18 ns) than that of the surrounding healthy tissue (≈10 ns). Although fluorescence intensity can also be used for localising the lesion, it presents a strong variability from patient to patient, rendering the lesion classification problematic [10]. Protein conformational changes [22] as well as protein-protein interactions [16, 23, 24] within living cells and tissues have also been investigated using FLIM.

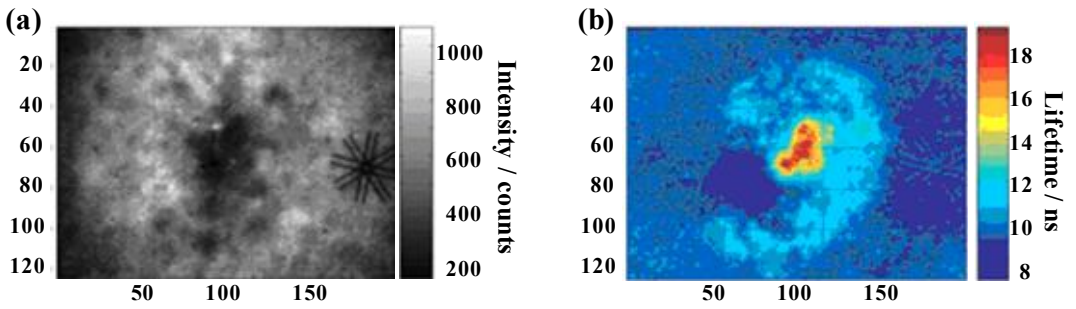

Figure 1.2. Maps of (a) the fluorescence intensity and (b) the fluorescence lifetime of the skin of a patient affected by a basal cell carcinoma. The tumour is characterised by lower fluorescence intensity and significantly longer lifetime than the surrounding tissue. The intensity however strongly varies from patient to patient, while the fluorescence lifetime is more reliable for the classification of the lesion. Adapted with permission from [10], copyright 2002, IOP Publishing Ltd.

In addition, fluorescence lifetime measurements have been employed in conjunction with microfluidics to study molecular interactions such as DNA–dye [25, 26] and DNA-enzyme [27] binding reactions within microchannels. The mixing dynamics under turbulent [28] or laminar flow [29, 30] and within microdroplet systems [31, 32] have been characterised using FLIM. Spectrally resolved FLIM [33, 34] and multi-parameter fluorescence detection, combining fluorescence intensity, spectrum, lifetime and polarization measurements, have also been proposed [35].

1.1.3. Fluorescence measurements: considerations

A primary goal in fluorescence microscopy and imaging is to efficiently distinguish between the fluorescence signal and the light arising from the billions of solvent molecules within the detection volume. Therefore, the key challenge in fluorescence measurements is to carefully optimize the signal-to-noise levels [4]. If the signal-to-noise ratio *S/N* is large, almost all the detected photons represent information originating from the molecule of interest.

S/N depends strongly on the signal rate and the duration of the measurement, hence, it can be improved by either increasing the collection efficiency of the optical setup or by extending the integration time. Increasing the excitation power can also result in improved *S/N*, as long as the limit for irreversible degradation (photobleaching) of the fluorescence molecule, usually in the order of 10^6 photons per second, is not reached [36]. It is obvious that the choice of the appropriate fluorophore is of great importance. Properties such as high extinction coefficient and high quantum yield are particularly useful in maximising the emitted signal. In addition, the fluorophore should stay photoactive over a long period of time under intense illumination before photobleaching and, for biomedical applications, it is important to ensure that binding to the molecule of interest as a marker does not cause quenching of the fluorescence.

The *S/N* can also be improved by reducing the levels of noise interfering with the original signal. Sources contributing to the noise are the detector dark count rate and background counts, typically arising due to Raman and Rayleigh scattering of the solvent molecules, fluorescence of the substrate or the detection optics and impurities in the buffers [4]. Raman and Rayleigh scattered light can be rejected with the use of appropriate optical filters, while background signal as a whole can be minimized by reducing the excitation and detection volume, so that as few solvent molecules as possible are contributing to the collected signal. Methods for efficient reduction of the excitation and detection volume involve special optical arrangements combined with miniaturized structures for sample confinement.

The most commonly employed optical configuration for achieving high *S/N* is confocal microscopy. In a confocal excitation/detection system, the excitation source is typically a laser. Lasers are near monochromatic light sources, therefore, an appropriate wavelength can be chosen to precisely match the absorption maximum of the fluorophore, yielding high signal count rate. The excitation, and thus the detection volume, is effectively minimized by tightly focusing the laser beam with a high numerical aperture objective (figure 1.3).

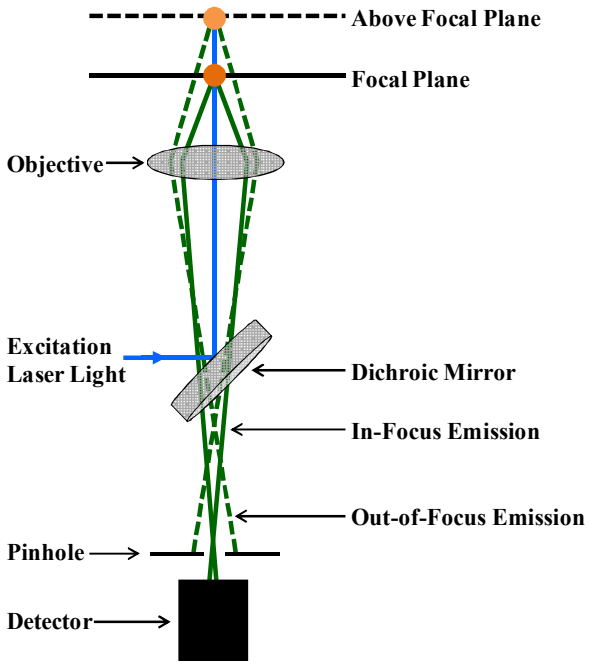

Figure 1.3. Simplified diagram illustrating the principle of confocal microscopy. The excitation laser light is tightly focused with a high numerical aperture objective and a pinhole is used to reject out-of-focus emission light, improving the signal-to-noise ratio.

Further reduction of the detection volume is achieved by introducing a small aperture (pinhole), typically 20-150 μm, in the detection path [37]. The pinhole allows only for light

from the focal plane to pass through, while signal originating from the out-of-focus volume is rejected (figure 1.3). In this way, a confocal optical arrangement restricts the detection volume resulting in reduced background signal and improved *S/N*. The effectiveness of this technique depends on the microscope objective, the pinhole size and the lens used to focus the light onto the pinhole.

Since the confocal approach was first introduced in 1957 [38], it has been extensively applied in a variety of biological research applications [39]. As only a small volume inside the sample is observed at a time, typically in the order of a few femtolitres [40], in order to obtain images, scanning of the sample is performed by moving either the specimen or the laser beam [37, 41-43].

1.2. Microfluidics

1.2.1. The need for miniaturized fluidic devices

As opposed to experiments involving molecule immobilisation on a surface, performing measurements on freely diffusing molecules overcomes issues associated with additional complexity and molecule perturbing due to the tethering procedure. However, for large and therefore slowly diffusing molecules, measurements in flowing systems are a particularly interesting alternative. In these systems, the identification of flowing molecules greatly reduces the time required for data acquisition and large populations can be analysed. Unlike diffusion limited measurements, in flowing studies each molecule is detected only once, thus accuracy is statistically guaranteed. In addition, kinetic information can be obtained through measurements taken at different positions along a microchannel as in flowing systems position corresponds to time.

Important advantages arise from the miniaturization of the fluidic structures used for sample observation and delivery. Miniaturised devices, with typical dimensions between 1-300 μm, offer sample compartments with volumes in the range of microlitres to femtolitres. This way, the quantity of reagents used is minimized [44]. Besides the reduction in sample consumption, transport times are reduced and diffusion–controlled reactions are accelerated as diffusion scales quadratically with time [45]. Heat transfer is also facilitated due to the large surface-to-volume ratio. Different functional units for reaction, detection and separation can be integrated into one device comprising all features of a complete lab. Due to the micro- and nano-scale

dimensions, many automated systems can be constructed on a single chip and run in parallel [46, 47].

Since the first introduction in 1992 [48], the field of microfluidics has shown remarkable growth [49]. Numerous applications have been demonstrated in chemistry [50] and biology [46, 51-55], as well as in physical sciences [44, 49]. Importantly, increasing interest has arisen in merging microfluidics with single molecule detection techniques [47, 56, 57].

1.2.2. Microfluidic devices: fabrication and designs

Thorough descriptions of fabrication methods, chip designs, experimental details and applications of microfluidics are provided in a series of related review papers [46, 47, 49-57].

The materials used for microfluidic device fabrication should ideally be mechanically rigid, optically transparent with low or no autofluorescence. It is also important to have stable flow for long time periods without any interference to the sample under investigation. The most popular materials used are poly(dimethylsiloxane) (PDMS), poly(methylmethacrylate) (PMMA), silicon, glass and quartz [49, 58]. The versatility of PDMS makes fabrication quick, straightforward and inexpensive. Therefore, it is the most commonly used material in microfluidics [59]. PDMS is appropriate for protein-related applications as it does not interfere with the sample [60] and is also gas-permeable [61], which is important for cellular studies. It bonds both reversibly and irreversibly to glass, enabling easy channel sealing [62]. Despite not being fully compatible with organic solvents, which are absorbed by the PDMS leading to swelling [63], it is extensively used in biomedical studies, as the majority of these employ aqueous solutions. Although devices can be thoroughly cleaned after use, PDMS is elastomeric, which may lead to shrinking or sagging over time [62]. Therefore, for long-term use, other materials, such as glass and quartz, are more suitable. These materials have lower autofluorescence, are mechanically rigid, resistant to organic solvents and denaturants. Recently, a cost effective alternative to microchip fabrication has been developed; carefully cut pieces of Parafilm, acrylic or double-sided tape, have been sandwiched between a glass slide and cover slip to act as a fluidic channel [57].

Regardless of the material used, the channels are almost always patterned using standard photolithographic techniques [64]. For glass, either dry or wet etching is used with the latter being preferred because of the absolute transparency of the resultant channels. For PDMS, channels are often cast from a suitable mould made from a photo-curable epoxy [59].

The channel design is closely related to the application. In continuous flow microfluidic devices, the flow inside the channels is almost always laminar and a parabolic velocity profile is observed, with faster fluid velocities occurring at the centre of the channel and slower near the walls [45]. Depending on application, single stream flow cells may be adequate or multi-stream configurations with two or more entry channels converging into a common one can be used. Simple single-stream designs offer a perfect platform for high throughput screening assays as well as for single molecule or single cell detection and analysis [52, 54, 65, 66]. Branching outlets may be introduced to enable molecular separation [67, 68] and sorting [69, 70]. In multi-stream flow cells, mixing between the resulting streams occurs only from diffusion and the distance a molecule diffuses scales quadratically with time [45]. Parallel laminar flow streams can be employed to create concentration or temperature gradients and to enable the quantitative investigation of phenomena involving molecular gradients [71, 72]. In addition, devices with crossing inlets may be used as ultrafast mixers when studying interactions between different reactants and species [69, 73-77]. More details on such applications are provided in following chapters.

In a slightly different experimental configuration, microfluidics can be used as a platform for interrogating single molecules tethered on the channel surface. Interactions between the immobilised molecules and a variety of species contained in the surrounding flow stream can be then monitored over time [78, 79]. Single molecule techniques combined with microfluidics are discussed in more detail in chapter 5. An alternative approach to continuous flow experiments involves the use of microfluidics for generating nanolitre or picolitre liquid volumes (droplets), which serve as containers for reaction kinetics studies, particle formation or single cell/molecule screening and analysis [52, 80].

Further details on applications related to the work presented herein are given the introduction of the respective chapters.

1.3. Project aim

Fluorescence measurements have been extensively used in biological and biomedical research due to their ability to provide high resolution and sensitivity, combined with minimal interference with the sample under investigation. More specifically, fluorescence lifetime methods exhibit significant advantages over fluorescence intensity-based techniques in terms of precision and contrast. At the same time, the increasing demand for high sensitivity, low sample consumption and short mixing and reaction times in the monitoring of complex

biological processes render microfluidics particularly attractive for the study of biomolecular interactions. Specially configured optical detection arrangements, coupled with time-resolved analysis methods and microfluidic platforms can be perfectly suitable for a variety of analytical applications.

In this thesis, a novel optical detection and analysis technique was developed which, in conjunction with microfluidics, allows for the study of freely diffusing and freely flowing molecules with high precision and sensitivity. Initially, a custom-built optical detection system was constructed, consisting of a laser scanning confocal microscope and avalanche photodiode detectors, in order to achieve high sensitivity measurements with improved signal-to-noise ratio (chapter 2). Due to its advantages over fluorescence intensity measurements, fluorescence lifetime via TCSPC was the detection and analysis method of choice. A maximum likelihood estimator approach, adapted from single molecule studies, was used to extract fluorescence lifetimes and visualise hydrodynamic focusing within microfluidic devices (chapter 3), as well as to produce two dimensional fluorescence lifetime maps of mixing within microchannels (chapter 4). The detection sensitivity of the developed system was demonstrated by performing measurements on freely flowing DNA molecules at the single molecule level (chapter 5). Furthermore, hydrodynamic focusing was employed as a sample confinement mechanism to improve the molecular detection efficiency. Finally, a fluorescence lifetime analytical method was developed to perform Förster resonance energy transfer measurements on freely diffusing molecules (chapter 6). The new analytical and optical technology was subsequently employed to monitor the dynamics of the well-known streptavidin-biotin binding model as well as to investigate protein conformational changes upon unfolding (chapter 7).

1.4. References

1. Lakowicz, J.R., *Principles of fluorescence spectroscopy, 3rd edition.* Springer Science and Business Media, New York, 2006.
2. Boens, N., W. Qin, N. Basaric, J. Hofkens, M. Ameloot, J. Pouget, J.-P. Lefevre, B. Valeur, E. Gratton, M. vandeVen, N.D. Silva, Jr., Y. Engelborghs, K. Willaert, A. Sillen, G. Rumbles, D. Phillips, A.J.W.G. Visser, A. van Hoek, J.R. Lakowicz, H. Malak, I. Gryczynski, A.G. Szabo, D.T. Krajcarski, N. Tamai, and A. Miura, *Fluorescence lifetime standards for time and frequency domain fluorescence spectroscopy.* Analytical Chemistry, 2007. **79**(5): p. 2137-2149.
3. Macklin, J.J., J.K. Trautman, T.D. Harris and L.E. Brus, *Imaging and time-resolved spectroscopy of single molecules at an interface.* Science, 1996. **272**(5259): p. 255-258.
4. Michalet, X. and S. Weiss, *Single-molecule spectroscopy and microscopy.* Comptes Rendus Physique, 2002. **3**(5): p. 619-644.
5. Ambrose, W.P., P.M. Goodwin, J.C. Martin and R.A. Keller, *Alterations of single-molecule fluorescence lifetimes in near-field optical microscopy.* Science, 1994. **265**(5170): p. 364-367.
6. Xie, X.S. and R.C. Dunn, *Probing single-molecule dynamics.* Science, 1994. **265**(5170): p. 361-364.
7. Gersen, H., M.F. Garcia-Parajo, L. Novotny, J.A. Veerman, L. Kuipers and N.F. van Hulst, *Influencing the angular emission of a single molecule.* Physical Review Letters, 2000. **85**(25): p. 5312-5315.
8. Magde, D., G.E. Rojas and P.G. Seybold, *Solvent dependence of the fluorescence lifetimes of xanthene dyes.* Photochemistry and Photobiology, 1999. **70**(5): p. 737-744.
9. Michalet, X., A.N. Kapanidis, T. Laurence, F. Pinaud, S. Doose, M. Pflughoefft and S. Weiss, *The power and prospects of fluorescence microscopies and spectroscopies.* Annual Review of Biophysics and Biomolecular Structure, 2003. **32**: p. 161-182.
10. Cubeddu, R., D. Comelli, C. D'Andrea, P. Taroni and G. Valentini, *Time-resolved fluorescence imaging in biology and medicine.* Journal of Physics D-Applied Physics, 2002. **35**(9): p. R61-R76.
11. Siegel, J., D.S. Elson, S.E.D. Webb, K.C.B. Lee, A. Vlanclas, G.L. Gambaruto, S. Leveque-Fort, M.J. Lever, P.J. Tadrous, G.W.H. Stamp, A.L. Wallace, A. Sandison, T.F. Watson, F. Alvarez, and P.M.W. French, *Studying biological tissue with fluorescence lifetime imaging: microscopy, endoscopy, and complex decay profiles.* Applied Optics, 2003. **42**(16): p. 2995-3004.
12. Anderssonengels, S., J. Johansson and S. Svanberg, *Medical diagnostic system based on simultaneous multispectral fluorescence imaging.* Applied Optics, 1994. **33**(34): p. 8022-8029.
13. Dickinson, M.E., G. Bearman, S. Tille, R. Lansford and S.E. Fraser, *Multi-spectral imaging and linear unmixing add a whole new dimension to laser scanning fluorescence microscopy.* Biotechniques, 2001. **31**(6): p. 1272-1278.

14. Holzwarth, A.R., *Time-resolved fluorescence spectroscopy.* Biochemical Spectroscopy, 1995. **246**: p. 334-362.

15. Cole, M.J., J. Siegel, S.E.D. Webb, R. Jones, K. Dowling, M.J. Dayel, D. Parsons-Karavassilis, P.M.W. French, M.J. Lever, L.O.D. Sucharov, M.A.A. Neil, R. Juskaitis, and T. Wilson, *Time-domain whole-field fluorescence lifetime imaging with optical sectioning.* Journal of Microscopy-Oxford, 2001. **203**: p. 246-257.

16. Becker, W., A. Bergmann, M.A. Hink, K. Konig, K. Benndorf and C. Biskup, *Fluorescence lifetime imaging by time-correlated single-photon counting.* Microscopy Research and Technique, 2004. **63**(1): p. 58-66.

17. Suhling, K., P.M.W. French and D. Phillips, *Time-resolved fluorescence microscopy.* Photochemical & Photobiological Sciences, 2005. **4**(1): p. 13-22.

18. Tadrous, P.J., *Methods for imaging the structure and function of living tissues and cells: 2. Fluorescence lifetime imaging.* Journal of Pathology, 2000. **191**(3): p. 229-234.

19. Elson, D., S. Webb, J. Siegel, K. Suhling, D. Davis, J. Lever, D. Phillips, A. Wallace and P. French, *Biomedical applications of fluorescence lifetime imaging.* Optics & Photonics News, 2002. **13**(11): p. 26-57.

20. Elson, D., J. Requejo-Isidro, I. Munro, F. Reavell, J. Siegel, K. Suhling, P. Tadrous, R. Benninger, P. Lanigan, J. McGinty, C. Talbot, B. Treanor, S. Webb, A. Sandison, A. Wallace, D. Davis, J. Lever, M. Neil, D. Phillips, G. Stamp, and P. French, *Time-domain fluorescence lifetime imaging applied to biological tissue.* Photochemical & Photobiological Sciences, 2004. **3**(8): p. 795-801.

21. Wallrabe, H. and A. Periasamy, *Imaging protein molecules using FRET and FLIM microscopy.* Current Opinion in Biotechnology, 2005. **16**(1): p. 19-27.

22. Caron, N.S., L.N. Munsie, J.W. Keillor and R. Truant, *Using FLIM-FRET to Measure Conformational Changes of Transglutaminase Type 2 in Live Cells.* Plos One, 2012. **7**(8).

23. Elangovan, M., R.N. Day and A. Periasamy, *Nanosecond fluorescence resonance energy transfer-fluorescence lifetime imaging microscopy to localize the protein interactions in a single living cell.* Journal of Microscopy-Oxford, 2002. **205**: p. 3-14.

24. Chen, Y., J.D. Mills and A. Periasamy, *Protein localization in living cells and tissues using FRET and FLIM.* Differentiation, 2003. **71**(9-10): p. 528-541.

25. Benninger, R.K.P., O. Hofmann, J. McGinty, J. Requejo-Isidro, I. Munro, M.A.A. Neil, A.J. deMello and P.M.W. French, *Time-resolved fluorescence imaging of solvent interactions in microfluidic devices.* Optics Express, 2005. **13**(16): p. 6275-6285.

26. Benninger, R.K.P., O. Hofmann, B. Onfelt, I. Munro, C. Dunsby, D.M. Davis, M.A.A. Neil, P.M.W. French and A.J. de Mello, *Fluorescence-lifetime imaging of DNA-dye interactions within continuous-flow microfluidic systems.* Angewandte Chemie-International Edition, 2007. **46**(13): p. 2228-2231.

27. Robinson, T., H.B. Manning, C. Dunsby, M.A.A. Neil, G.S. Baldwin, A.J. de Mello and P.M.W. French, *Investigating fast enzyme-DNA kinetics using multidimensional*

fluorescence imaging and microfluidics, in *Microfluidics, Biomems, and Medical Microsystems Viii*. 2010.

28. Redford, G.I., Z.K. Majumdar, J.D.B. Sutin and R.M. Clegg, *Properties of microfluidic turbulent mixing revealed by fluorescence lifetime imaging.* Journal of Chemical Physics, 2005. **123**(22).

29. Magennis, S.W., E.M. Graham and A.C. Jones, *Quantitative spatial mapping of mixing in microfluidic systems.* Angewandte Chemie-International Edition, 2005. **44**(40): p. 6512-6516.

30. Robinson, T., P. Valluri, H.B. Manning, D.M. Owen, I. Munro, C.B. Talbot, C. Dunsby, J.F. Eccleston, G.S. Baldwin, M.A.A. Neil, A.J. de Mello, and P.M.W. French, *Three-dimensional molecular mapping in a microfluidic mixing device using fluorescence lifetime imaging.* Optics Letters, 2008. **33**(16): p. 1887-1889.

31. Srisa-Art, M., A.J. deMello and J.B. Edel, *Fluorescence lifetime imaging of mixing dynamics in continuous-flow microdroplet reactors.* Physical Review Letters, 2008. **101**(1).

32. Solvas, X.C.i., M. Srisa-Art, A.J. demello and J.B. Edel, *Mapping of Fluidic Mixing in Microdroplets with 1 mu s Time Resolution Using Fluorescence Lifetime Imaging.* Analytical Chemistry, 2010. **82**(9): p. 3950-3956.

33. Chorvat, D., Jr. and A. Chorvatova, *Multi-wavelength fluorescence lifetime spectroscopy: a new approach to the study of endogenous fluorescence in living cells and tissues.* Laser Physics Letters, 2009. **6**(3): p. 175-193.

34. Hanley, Q.S., *Spectrally resolved fluorescent lifetime imaging.* Journal of the Royal Society Interface, 2009. **6**: p. S83-S92.

35. Widengren, J., V. Kudryavtsev, M. Antonik, S. Berger, M. Gerken and C.A.M. Seidel, *Single-molecule detection and identification of multiple species by multiparameter fluorescence detection.* Analytical Chemistry, 2006. **78**(6): p. 2039-2050.

36. Widengren, J., *Mechanisms of photobleaching investigated by fluorescence correlation spectroscopy.* . Bioimaging, 1996. **4**: p. 149-157.

37. Webb, R.H., *Confocal optical microscopy.* Reports on Progress in Physics, 1996. **59**(3): p. 427-471.

38. Minsky, M., *Memoir of inventing the confocal scanning microscope.* Scanning, 1988. **10**(4): p. 128-138.

39. Pawley, J.B., *Handbook of biological confocal microscopy, 3rd edition.* Springer Science and Business Media, New York, 2006.

40. Hill, E.K. and A.J. de Mello, *Single-molecule detection using confocal fluorescence detection: Assessment of optical probe volumes.* Analyst, 2000. **125**(6): p. 1033-1036.

41. Segers-Nolten, G.M.J., C. Wyman, N. Wijgers, W. Vermeulen, A.T.M. Lenferink, J.H.J. Hoeijmakers, J. Greve and C. Otto, *Scanning confocal fluorescence microscopy for single molecule analysis of nucleotide excision repair complexes.* Nucleic Acids Research, 2002. **30**(21): p. 4720-4727.

42. Sabanayagam, C.R., J.S. Eid and A. Meller, *High-throughput scanning confocal microscope for single molecule analysis.* Applied Physics Letters, 2004. **84**(7): p. 1216-1218.

43. Zheng, H., L.S. Goldner and S.H. Leuba, *Homebuilt single-molecule scanning confocal fluorescence microscope studies of single DNA/protein interactions.* Methods, 2007. **41**(3): p. 342-352.

44. Squires, T.M. and S.R. Quake, *Microfluidics: Fluid physics at the nanoliter scale.* Reviews of Modern Physics, 2005. **77**(3): p. 977-1026.

45. Brody, J.P., P. Yager, R.E. Goldstein and R.H. Austin, *Biotechnology at low Reynolds numbers.* Biophysical Journal, 1996. **71**(6): p. 3430-3441.

46. Sia, S.K. and G.M. Whitesides, *Microfluidic devices fabricated in poly(dimethylsiloxane) for biological studies.* Electrophoresis, 2003. **24**(21): p. 3563-3576.

47. Dittrich, P.S. and A. Manz, *Single-molecule fluorescence detection in microfluidic channels - the Holy Grail in mu TAS?* Analytical and Bioanalytical Chemistry, 2005. **382**(8): p. 1771-1782.

48. Manz, A., D.J. Harrison, E.M.J. Verpoorte, J.C. Fettinger, A. Paulus, H. Ludi and H.M. Widmer, *Planar chips technology for miniaturization and integration of separation techniques into monitoring systems - Capillary electrophoresis on a chip.* Journal of Chromatography, 1992. **593**(1-2): p. 253-258.

49. Whitesides, G.M., *The origins and the future of microfluidics.* Nature, 2006. **442**(7101): p. 368-373.

50. deMello, A.J., *Control and detection of chemical reactions in microfluidic systems.* Nature, 2006. **442**(7101): p. 394-402.

51. Tegenfeldt, J.O., C. Prinz, H. Cao, R.L. Huang, R.H. Austin, S.Y. Chou, E.C. Cox and J.C. Sturm, *Micro- and nanofluidics for DNA analysis.* Analytical and Bioanalytical Chemistry, 2004. **378**(7): p. 1678-1692.

52. Dittrich, P.S. and A. Manz, *Lab-on-a-chip: microfluidics in drug discovery.* Nature Reviews Drug Discovery, 2006. **5**(3): p. 210-218.

53. Dittrich, P.S., K. Tachikawa and A. Manz, *Micro total analysis systems. Latest advancements and trends.* Analytical Chemistry, 2006. **78**(12): p. 3887-3907.

54. Weibel, D.B. and G.M. Whitesides, *Applications of microfluidics in chemical biology.* Current Opinion in Chemical Biology, 2006. **10**(6): p. 584-591.

55. Hong, J., J.B. Edel and A.J. deMello, *Micro- and nanofluidic systems for high-throughput biological screening.* Drug Discovery Today, 2009. **14**(3-4): p. 134-146.

56. Craighead, H., *Future lab-on-a-chip technologies for interrogating individual molecules.* Nature, 2006. **442**(7101): p. 387-393.

57. Brewer, L.R. and P.R. Bianco, *Laminar flow cells for single-molecule studies of DNA-protein interactions.* Nature Methods, 2008. **5**(6): p. 517-525.

58. Qi, S.Z., X.Z. Liu, S. Ford, J. Barrows, G. Thomas, K. Kelly, A. McCandless, K. Lian, J. Goettert and S.A. Soper, *Microfluidic devices fabricated in poly(methyl*

methacrylate) using hot-embossing with integrated sampling capillary and fiber optics for fluorescence detection. Lab on a Chip, 2002. **2**(2): p. 88-95.

59. McDonald, J.C. and G.M. Whitesides, *Poly(dimethylsiloxane) as a material for fabricating microfluidic devices.* Accounts of Chemical Research, 2002. **35**(7): p. 491-499.

60. Delamarche, E., A. Bernard, H. Schmid, B. Michel and H. Biebuyck, *Patterned delivery of immunoglobulins to surfaces using microfluidic networks.* Science, 1997. **276**(5313): p. 779-781.

61. Merkel, T.C., V.I. Bondar, K. Nagai, B.D. Freeman and I. Pinnau, *Gas sorption, diffusion, and permeation in poly(dimethylsiloxane).* Journal of Polymer Science Part B-Polymer Physics, 2000. **38**(3): p. 415-434.

62. Ng, J.M.K., I. Gitlin, A.D. Stroock and G.M. Whitesides, *Components for integrated poly(dimethylsiloxane) microfluidic systems.* Electrophoresis, 2002. **23**(20): p. 3461-3473.

63. Yoo, J.S., S.J. Kim and J.S. Choi, *Swelling equilibria of mixed solvent/poly(dimethylsiloxane) systems.* Journal of Chemical and Engineering Data, 1999. **44**(1): p. 16-22.

64. Weibel, D.B., W.R. DiLuzio and G.M. Whitesides, *Microfabrication meets microbiology.* Nature Reviews Microbiology, 2007. **5**(3): p. 209-218.

65. Sundberg, S.A., *High-throughput and ultra-high-throughput screening: solution- and cell-based approaches.* Current Opinion in Biotechnology, 2000. **11**(1): p. 47-53.

66. Cai, L., N. Friedman and X.S. Xie, *Stochastic protein expression in individual cells at the single molecule level.* Nature, 2006. **440**(7082): p. 358-362.

67. Fister, J.C., S.C. Jacobson, L.M. Davis and J.M. Ramsey, *Counting single chromophore molecules for ultrasensitive analysis and separations on microchip devices.* Analytical Chemistry, 1998. **70**(3): p. 431-437.

68. Haab, B.B. and R.A. Mathies, *Single-molecule detection of DNA separations in microfabricated capillary electrophoresis chips employing focused molecular streams.* Analytical Chemistry, 1999. **71**(22): p. 5137-5145.

69. Dittrich, P. and P. Schwille, *Single molecule reactions and sorting in microfluidic channels.* Biophysical Journal, 2003. **84**(2): p. 473A-474A.

70. Wang, M.M., E. Tu, D.E. Raymond, J.M. Yang, H.C. Zhang, N. Hagen, B. Dees, E.M. Mercer, A.H. Forster, I. Kariv, P.J. Marchand, and W.F. Butler, *Microfluidic sorting of mammalian cells by optical force switching.* Nature Biotechnology, 2005. **23**(1): p. 83-87.

71. Jeon, N.L., H. Baskaran, S.K.W. Dertinger, G.M. Whitesides, L. Van de Water and M. Toner, *Neutrophil chemotaxis in linear and complex gradients of interleukin-8 formed in a microfabricated device.* Nature Biotechnology, 2002. **20**(8): p. 826-830.

72. Mao, H.B., M.A. Holden, M. You and P.S. Cremer, *Reusable platforms for high-throughput on-chip temperature gradient assays.* Analytical Chemistry, 2002. **74**(19): p. 5071-5075.

73. Wabuyele, M.B., S.M. Ford, W. Stryjewski, J. Barrow and S.A. Soper, *Single molecule detection of double-stranded DNA in poly(methylmethacrylate) and polycarbonate microfluidic devices.* Electrophoresis, 2001. **22**(18): p. 3939-3948.

74. Lipman, E.A., B. Schuler, O. Bakajin and W.A. Eaton, *Single-molecule measurement of protein folding kinetics.* Science, 2003. **301**(5637): p. 1233-1235.

75. Dittrich, P.S., B. Muller and P. Schwille, *Studying reaction kinetics by simultaneous FRET and cross-correlation analysis in a miniaturized continuous flow reactor.* Physical Chemistry Chemical Physics, 2004. **6**(18): p. 4416-4420.

76. Dittrich, P.S., S.P. Schafer and P. Schwille, *Characterization of the photoconversion on reaction of the fluorescent protein kaede on the single-molecule level.* Biophysical Journal, 2005. **89**(5): p. 3446-3455.

77. Hamadani, K.M. and S. Weiss, *Nonequilibrium single molecule protein folding in a coaxial mixer.* Biophysical Journal, 2008. **95**(1): p. 352-365.

78. Amitani, I., R.J. Baskin and S.C. Kowalczykowski, *Visualization of Rad54, a chromatin remodeling protein, translocating on single DNA molecules.* Molecular Cell, 2006. **23**(1): p. 143-148.

79. Galletto, R., I. Amitani, R.J. Baskin and S.C. Kowalczykowski, *Direct observation of individual RecA filaments assembling on single DNA molecules.* Nature, 2006. **443**(7113): p. 875-878.

80. Huebner, A., S. Sharma, M. Srisa-Art, F. Hollfelder, J.B. Edel and A.J. deMello, *Microdroplets: A sea of applications?* Lab on a Chip, 2008. **8**(8): p. 1244-1254.

CHAPTER 2
EXPERIMENTAL METHODS

2.1. Optical setup components

The optical setup used for all experiments consisted of an inverted scanning laser confocal microscope (IX71, Olympus) with an integrated custom-built detection path. The customized path provided increased sensitivity, as required for demanding applications such as measurements at the single molecule level. The core advantage of using a confocal microscope was the improvement in the signal-to-noise ratio at the imaging plane. A schematic representation of the configuration used herein is shown in figure 2.1. Briefly, a laser excitation source was used with a wavelength which was carefully chosen to match the fluorophore absorption maximum. The laser light was directed through a dichroic mirror into the back aperture of a high numerical aperture objective and finally onto the sample under investigation. The resulting fluorescence was collected by the same objective and returned through the same dichroic mirror. A high quality long pass filter was used to further separate excitation from emission light and the latter was focused by a lens onto a confocal pinhole. The confocal pinhole rejected signal originating from out-of-focus planes of the specimen achieving point detection. Fluorescence was subsequently directed via emission filters and lenses onto two avalanche photodiodes (APDs) operating in single photon counting mode. Upon photon arrival, the TCSPC electronics (TimeHarp 200, PicoQuant GmbH) were activated and the time delay between laser pulse and photon arrivals were collected in data files. The scanning laser configuration (Fluoview 300, v.6, Olympus) allowed for data to be collected from up to four dimensions (x-y-z-direction and time). Appropriate algorithms were applied in order to extract fluorescence lifetimes, match data points to pixels, and subsequently construct two-dimensional lifetime maps. Details on each component of the setup are given in the following sections.

2.1.1. Excitation Source

Confocal arrangements commonly employ lasers for sample excitation. Lasers are sources of intense, nearly single-frequency light, with high spatial coherence and collimation. Thus, the beam can be tightly focused to a very small spot with high brightness, which is favourable for the resolution. The high degree of monochromaticity enables fine matching to the dye excitation maximum and simplifies the design of filters and dichroic mirrors used in the excitation and detection paths [1-5].

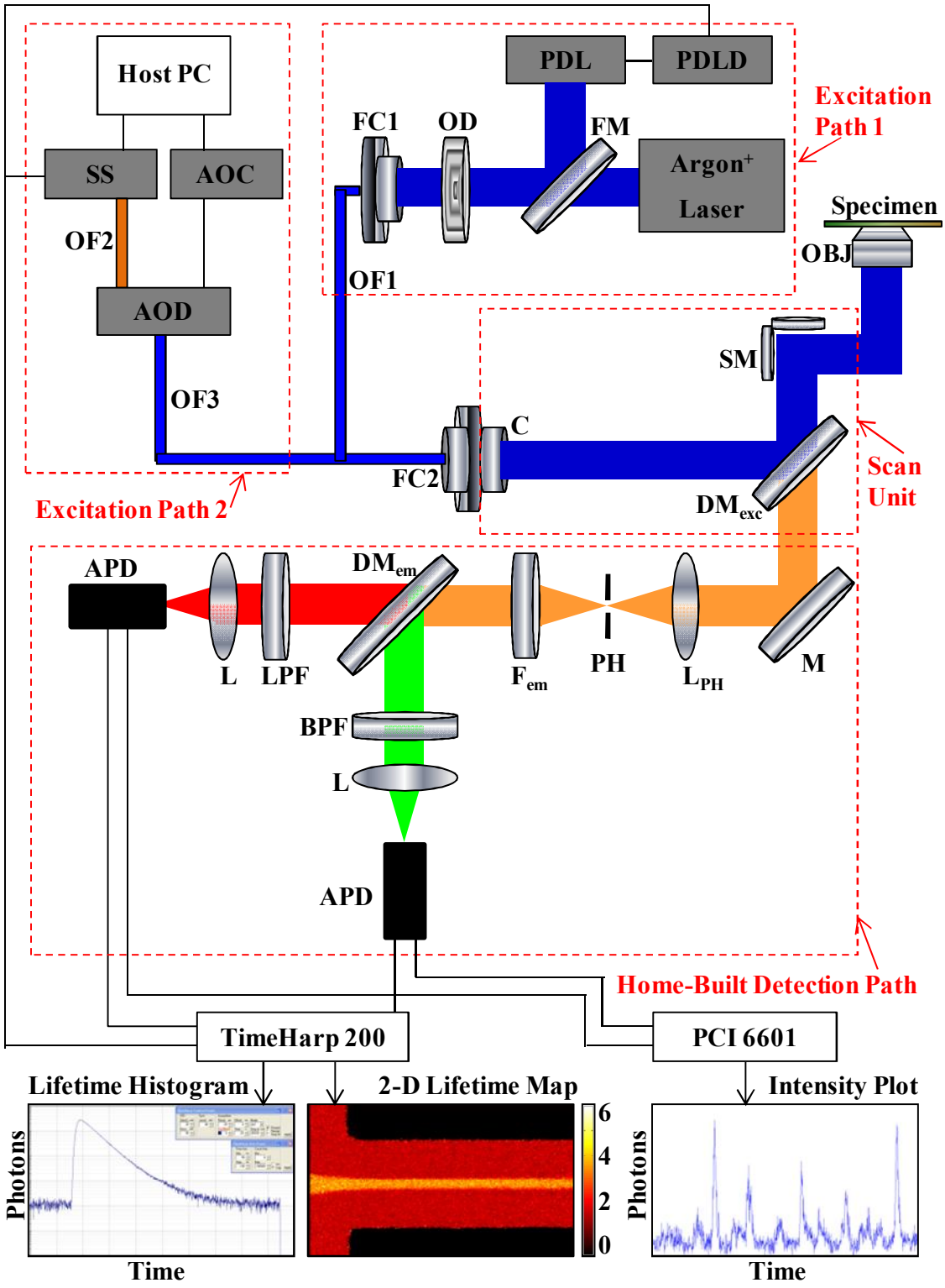

Figure 2.1. Schematic representation of the optical setup consisting of four main parts, excitation paths 1 and 2, the scanning unit and the home-built detection path. PDL(D): pulsed diode laser (driver), FM: flip-mount mirror, OD: neutral density filter, FC: fibre coupler, OF: optical fibre, SS: supercontinuum source, AOC: AOTF controller, AOD: AOTF device, C: collimator, DM: dichroic mirror, SM: scanning mirror, OBJ: objective, M: mirror, L: lens, PH: pinhole, F: filter, LPF: long pass filter, BPF: band pass filter, APD: avalanche photodiode detector). The colourbar for the 2-D image represents fluorescence lifetimes in ns. For details about the way lifetime histograms, 2-D lifetime maps and intensity plots were produced see section 2.3.

Depending on application, lasers can operate in either continuous wave mode, where the output is constant over time, or in pulsed mode, where the laser output takes the form of periodic pulses. Time-resolved measurements require pulsed lasers operating at high repetition rates. The duration of the pulse should be short compared to the fluorescence lifetime of the dye to allow high time resolution [3].

The optical setup used herein included four laser sources arranged in two optical paths. Excitation path 1 included a wavelength-tuneable argon ion laser and two pulsed diode lasers, while path 2 consisted of a supercontinuum source with an acousto-optic tuneable filter system. Experiments presented in chapters 3 and 5 were performed using excitation path 1, whilst chapters 4, 6 and 7 employed path 2. Each path is described in detail below.

2.1.1.1. Excitation path 1

A detailed schematic representation of excitation path 1 is given in figure 2.1 (top right) and a photo of the same path can be seen below (figure 2.2).

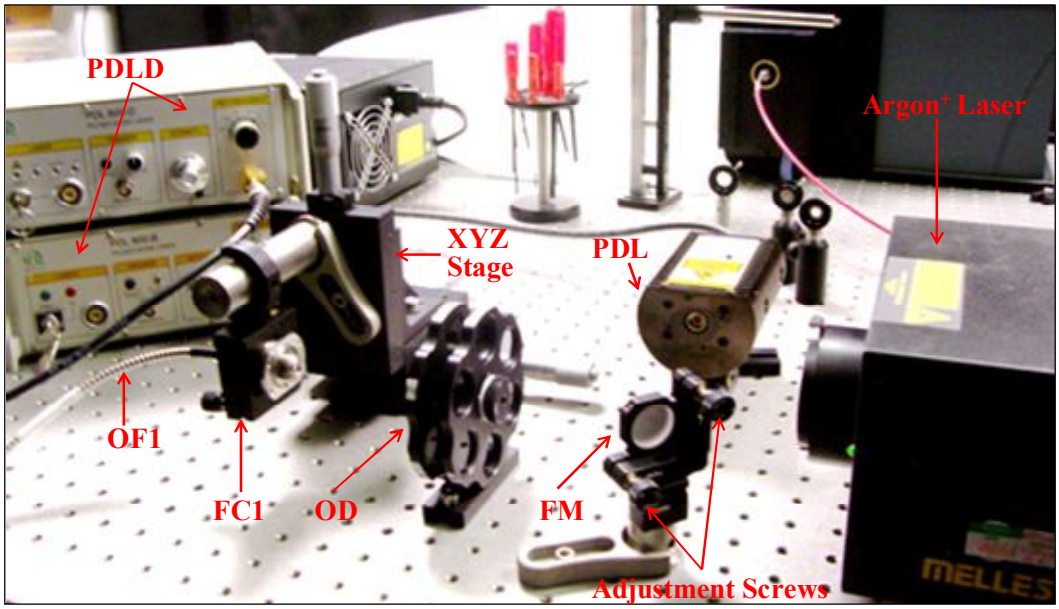

Figure 2.2. Excitation path 1. PDL(D): pulsed diode laser (drivers), FM: flip-mount mirror, OD: neutral density filter, FC: fibre coupler, OF: optical fibre.

Argon ion laser

The argon ion laser (Melles Griot) was a continuous wave, air-cooled laser with emission lines ranging from 454 nm to 514 nm and a maximum power of 82.5 mW at 488 nm, which was the main wavelength of interest for the dyes used herein. This laser was predominantly used for the pinhole and detectors alignment due to its high output power resulting in visible to the naked eye fluorescence spot.

Pulsed diode lasers

The pulsed diode lasers (PicoQuant GmbH) were used for fluorescence lifetime measurements and imaging. Initially, the model LDH-P-C-470 operating at 466 nm combined with a PDL800-B driver also from PicoQuant was installed. This driver allowed user-selectable repetition frequencies of 40, 20, 10, 5 and 2.5 MHz derived from the internal crystal controlled oscillator that generated a low jitter base frequency of 40 MHz. The laser power was also adjustable via the driver unit. A maximum power of 1.35 mW at 40 MHz and a pulse width of 73 ps was obtained. For better matching of the excitation line to fluorophore absorption maximum, a second pulsed diode laser (LDH-D-C-485) was integrated into the setup combined with a PDL800-D driver for operation at higher wavelengths. This laser was operated in both a picosecond pulsed mode at 480 nm or in continuous wave mode at 486.1 nm. In pulsed mode, the internal oscillator offered two selectable base frequencies, 80 MHz and 1 MHz and each base frequency could be further reduced by divisions of 1, 2, 4, 8, 16 or 32. The derived repetition frequencies therefore ranged from 80 MHz to 31.25 kHz. The maximum power achieved for continuous wave operation was 11.3 mW and the power after coupling in the optic fibre was approximately 3.1 mW. In pulsed mode, for a repetition frequency of 40 MHz, the maximum output was 2.6 mW resulting in a post-coupling power of approximately 180 µW. With each laser pulse, a synchronization signal (<-800 mV into 50 Ohms (NIM), 6 ns) was provided at the SYNC output of the driver for triggering of the TCSPC electronics. The SYNC signal was fed to the TimeHarp 200 board via a pulse converter (LTT 100, Picoquant), which shortened and attenuated the SYNC pulse so that it was well matched to the TimeHarp SYNC input.

Beam Attenuation and Coupling

The argon ion laser and either one of the LDH-P-C-470 or the LDH-D-C-485 pulsed diode lasers remained aligned to the scanning unit at all times. Switching between them was achieved by use of a flip mirror mount (FM90, Thorlabs). A kinematic mount with a mirror (KM100, Thorlabs) was positioned on the flip mount at a 45º angle with respect to the pulsed laser (figures 2.1 and 2.2). Beam height and alignment were controlled with the x, y adjustment screws. In order to keep photon count rates at levels appropriate for safe detector operation and prevent fluorophore photobleaching, the laser beam was attenuated using a twelve station dual filter wheel (attenuation from 0-4 OD per wheel, FW2AND, Thorlabs) positioned after the mirror. Thus, the laser power for both beams could be easily attenuated over a dynamic range of 1 to 10^8 via appropriate combination of the dual wheel filters.

The excitation light was directed into the input of the scanning unit through a 50 µm single mode optical fibre with a working wavelength range of 450 – 640 nm (LINOS). The fibre was

protected with a stainless steel jacket. Coupling between the laser beam and the fibre was achieved with an appropriate ultra stable fibre port collimator (PAF-X-18-A, Thorlabs) mounted on an XYZ translation stage (PT3, Thorlabs). The collimator utilized an AR-coated aspheric lens, which could be aligned linearly on the x, y, and z-axes and angularly for tip and tilt. Rotation of the bulkhead provided alignment with a total of six degrees of freedom. The collected light was brought into the scanning unit via an Olympus FC fibre coupler.

2.1.1.2. Excitation path 2

A high power supercontinuum source combined with an acousto-optic tuneable filter (AOTF) was integrated to the optical setup to enable the excitation of a variety of fluorescent dyes with different absorption maxima. In brief, a supercontinuum was formed via converting laser light to light with broad spectral bandwidth through a series of non-linear processes. The AOTF controller was then used to separate specific wavelengths from the supercontinuum and direct them into the scanning unit via an optical fibre. This way, the system operated like a widely tuneable laser source. A detailed schematic representation of excitation path 2 and a photo of the same path are given in figure 2.1 (top left) and figure 2.3 respectively.

Supercontinuum source

The model SC-450-4-PP from Fianium was used as a high power supercontinuum source with an additional pulse-picked system, which enabled selection of repetition rates from 1-20 MHz. The unit communicated to the host computer through a USB interface for output power and repetition frequency adjustment. Similarly to the pulsed diode lasers described in section 2.1.1.1, SC-450-4-PP also had an SMA SYNC output for connection to the TimeHarp 200 board via a pulse converter (PicoQuant).

In brief, the SC-450-4-PP supercontinuum source consists of the master source, an acousto-optic pulse-picker, a power amplifier and the supercontinuum generator. The master source is a low power mode locked fibre laser, which operates at a repetition rate of 20 MHz providing transform limited pulses of approximately 6 ps. The pulse-picker is a high speed acousto-optic modulator, which applies a division function on the master source pulse repetition rate and provides the selected by user pulse frequency. The drive current to the pump module within the fibre amplifier, and thus its output power, is also controlled by user via the USB interface. Finally, the amplifier is followed by a highly nonlinear fibre in which the supercontinuum is generated by the interaction between high intensity picosecond pulses and greatly nonlinear medium.

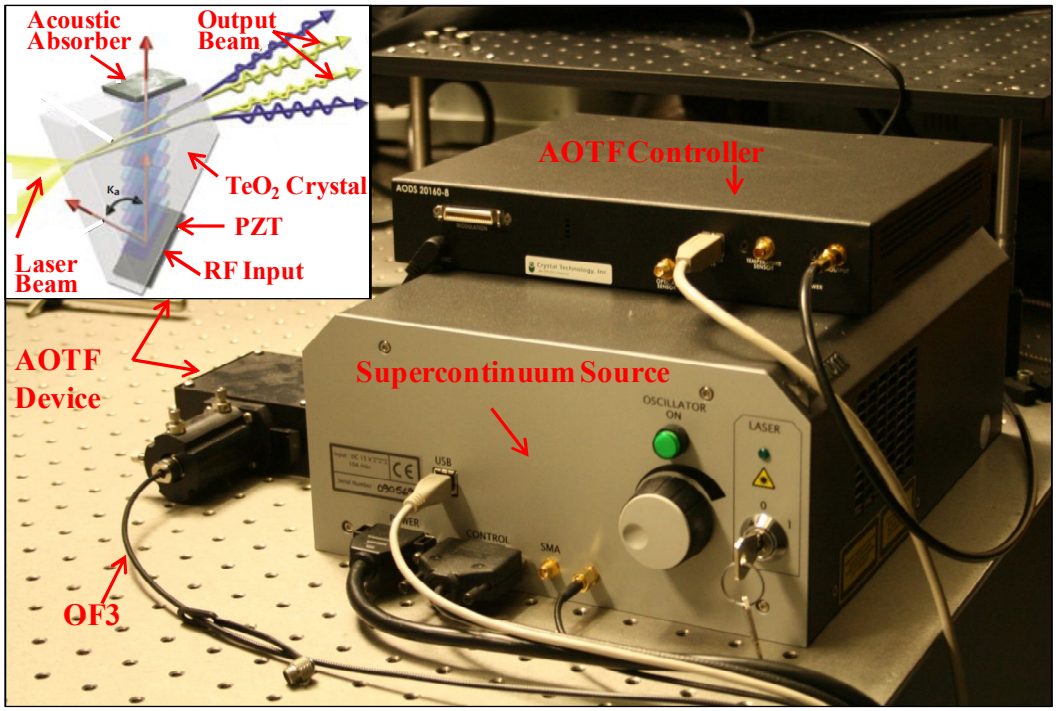

Figure 2.3. Excitation path 2. The main parts of the AOTF device are shown in the inset. OF: optical fibre, RF: radio frequency, PZT: piezoelectric transducer.

The output power and the spectral bandwidth of the supercontinuum were determined by adjusting the output of the fibre amplifier and, when viewed on a surface with the eye, the beam output changed from red to orange, yellow and eventually white as the amplifier power was increased to maximum. At full power and at the fundamental repetition rate of 20 MHz the laser delivered approximately 4.17 W of optical power over the entire optical bandwidth between 403-2000 nm. Under these conditions the generated beam diameter was approximately 3.3 mm.

AOTF system

The AOTF system (AODS 20160-8, Crystal Technology, LLC) was used to select the desired for sample excitation wavelength lines from the output of the supercontinuum.

The main components of an AOTF system are a tellurium dioxide (TeO_2) crystal with a bonded piezoelectric transducer and the AOTF driver which controls the filter output. As the supercontinuum beam is directed through the crystal, an oscillating radio frequency (RF) signal provided by the AOTF controller is applied to the piezoelectric transducer. In response to the RF signal the transducer generates acoustic waves, which propagate into the crystal and periodically modulate its refractive index (figure 2.3, inset). As a result, a transmission refraction grating is created for the incoming light, which enables only a very narrow band of wavelengths to pass, while the remainder is eliminated. By varying the frequency and intensity

of the RF signal, the wavelength and intensity of the diffracted light respectively can be adjusted.

The AOTF driver used herein contained a microcontroller for communication with the host computer via USB port and allowed for selection of up to 8 simultaneous wavelengths between 429-687 nm to be combined at the system output resulting in a maximum power of approximately 12 mW. It also contained a series of integrated sensors for monitoring of optical power, RF power and temperature to ensure optimum device performance.

Integration and control software

Both the supercontinuum source and the AOTF system communicated to the host computer via USB ports and were managed by user through the AODS 20160 controller program. As the software allowed for complete control on the supercontinuum and AOTF system output, there was no need for attenuation filters. Therefore, the AOTF output was directly fed into the scanning unit via a polarisation maintaining, 2 m long optical fibre installed by manufacturer.

In the software interface shown in figure 2.4, the bottom right window was used to adjust the frequency (A) and power (B) of the supercontinuum. In all experiments performed using excitation path 2, the selected repetition frequency was 20 MHz and the supercontinuum source output was set at maximum power, resulting in a back reflection of about 32%.

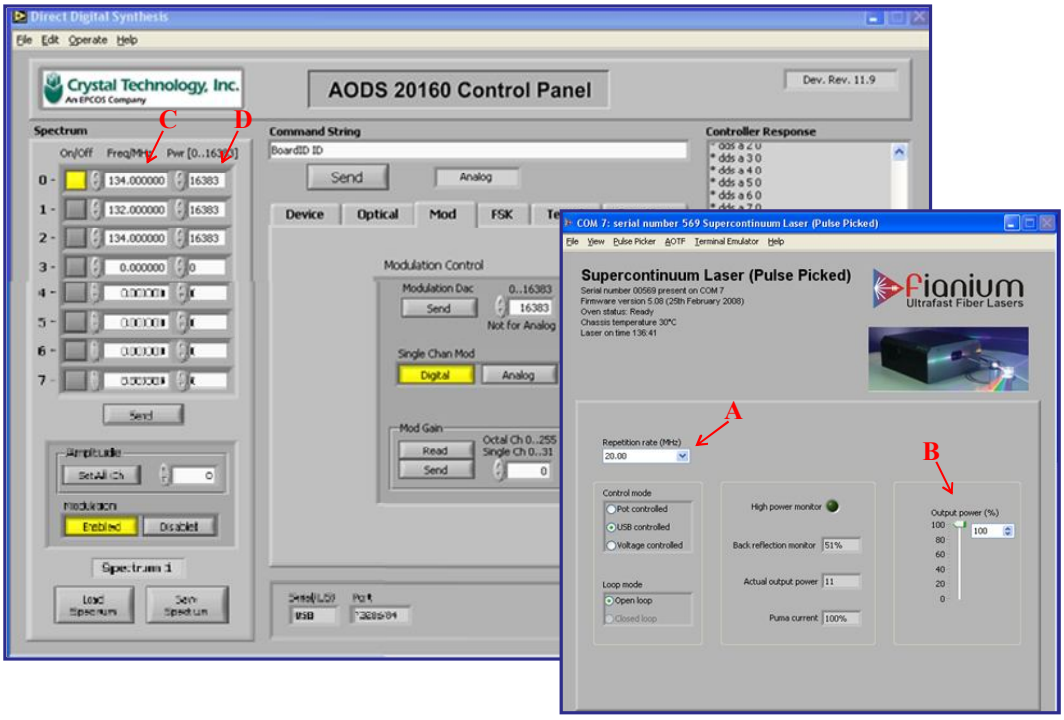

Figure 2.4. The AODS 20160 program user interface. The supercontinuum pulse frequency and power were adjusted via A and B respectively while the wavelength and power selection for the final AOTF output were set using C and D respectively.

In the main AODS window (figure 2.4, centre) up to 8 channels could be activated simultaneously at frequencies varying from 20-159.9 MHz (C) and power level varying from 0-16383 on arbitrary scale (D). The relationship between selected frequency f and corresponding laser line wavelength λ was expressed by equation 2.1 (provided by Fianium).

$$f = -2.018x10^{-6}\lambda^3 + 4.122x10^{-3}\lambda^2 - 2.972\lambda + 8.349x10^2 \quad (2.1)$$

The wavelengths used for the experiments herein were ~488 nm (chapters 4, 6 and 7) and ~543 nm (chapter 6), corresponding to frequencies of 132 MHz and 113 MHz respectively.

2.1.2. Scanning Unit and Software (Fluoview 300)

The main components of the Fluoview 300 scanning unit are illustrated in figures 2.1 (middle) and 2.5. The incoming laser light was directed through a beam collimator and then onto the scanning mechanism by either a 470 nm or a 488 nm dichroic mirror (FV3 DM470-2, FV3 DM488-2, Olympus) depending on the laser wavelength used. A dichroic mirror allowing excitation at both 488 nm and 543 nm lines (AH/FV1000/DM/11, Olympus) could also be manually inserted to replace the 470 nm dichroic when the excitation was at 543 nm (chapter 6). The dichroic mirror used for the majority of the experiments was the FV3 DM488-2.

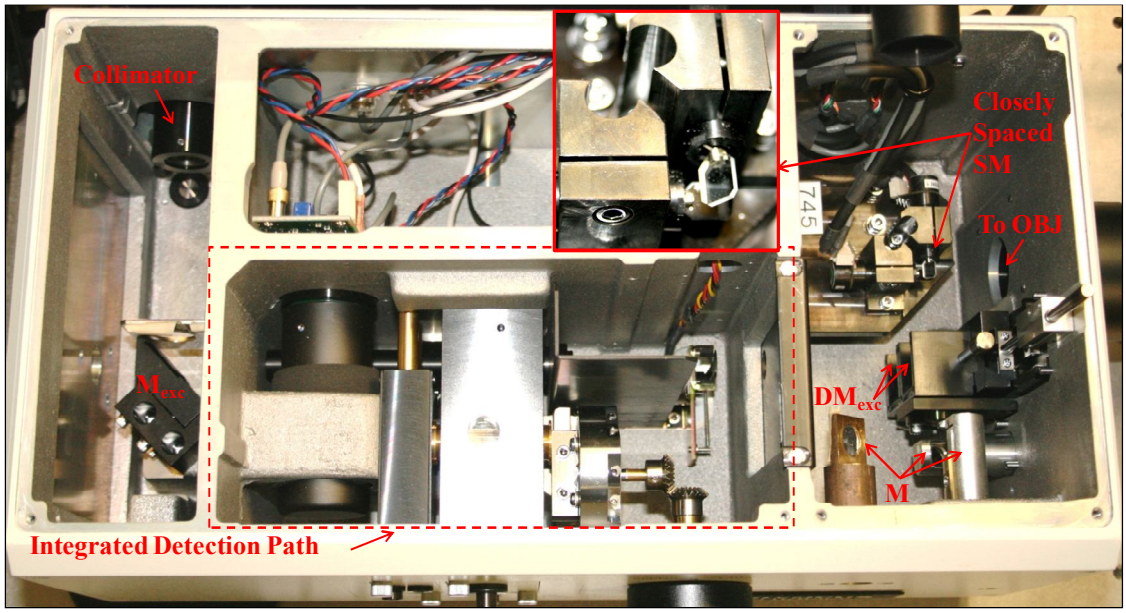

Figure 2.5. Fluoview 300 scanning unit. Inset: close-up of the scanning mirrors. M: mirror, DM: dichroic mirror, SM: scanning mirror, OBJ: objective. The integrated in the scanning unit detection path was not used. The three mirrors seen at the bottom right directed the fluorescence signal vertically upwards outside of the scanning unit and into a home-built detection path.

The scanning mechanism utilized two galvanometer-driven high-speed oscillating mirrors, one performing a fast horizontal scan along the x-axis (line scan) and the other one performing a slower vertical scan along the y-axis (frame scan). The latter offset the scanning line to sequential positions from top to bottom of the frame producing a rectilinear raster scan. The scanning speed of the mirrors was negligible compared to the speed of light, therefore the emitted fluorescence was returned along the same path through the dichroic mirror. Variations in the signal intensity corresponded to variations in the emission at different points in the specimen. The integrated in the scanning unit detection path consisted of a pinhole turret, filter selection and photomultiplier tube (PMT) detectors. This was replaced by a custom built detection system discussed in section 2.1.4.

A variety of pixel resolutions and image sizes from 256×256 to 2048×2048 could be obtained. However, for the majority of the experiments, the scanning mode consisted of bi-directional scanning yielding 512×512 pixels per scan (1.12 sec/scan). In this mode the scan time per pixel was 4.27 μs and each pixel represented an area of ~0.46×0.46 μm^2. Point excitation mode was also used for single-point non-imaging measurements. The software interface can be seen in figure 2.6.

2.1.3. Objective

In confocal microscopy the same objective is used for both sample illumination and light collection and is therefore one of the most important components of the optical system. High numerical aperture (*NA*) water immersion apochromatic objectives are generally preferred in order to maximise the collection efficiency and to obtain a high degree of correction for chromatic and spherical aberration [2]. The *NA* of the objective is expressed by the formula:

$$NA = n \times \sin\theta \tag{2.2}$$

where n is the refractive index of the medium through which the rays travel and θ is the angle between an emitted ray and the optical axis (figure 2.7a). In the case of the medium being air (n=1), the *NA* cannot be numerically larger than 1. Thus, an immersion fluid with higher n is needed to realize the maximum *NA* of the objective. Figure 2.7a illustrates how an oil immersion objective can improve the collection efficiency ($\theta_{air}<\theta_{oil}$) when the specimen is immediately adjacent to the cover glass, as the refractive indices of medium and glass are closely matched ($n_{oil}\approx n_{glass}$=1.515).

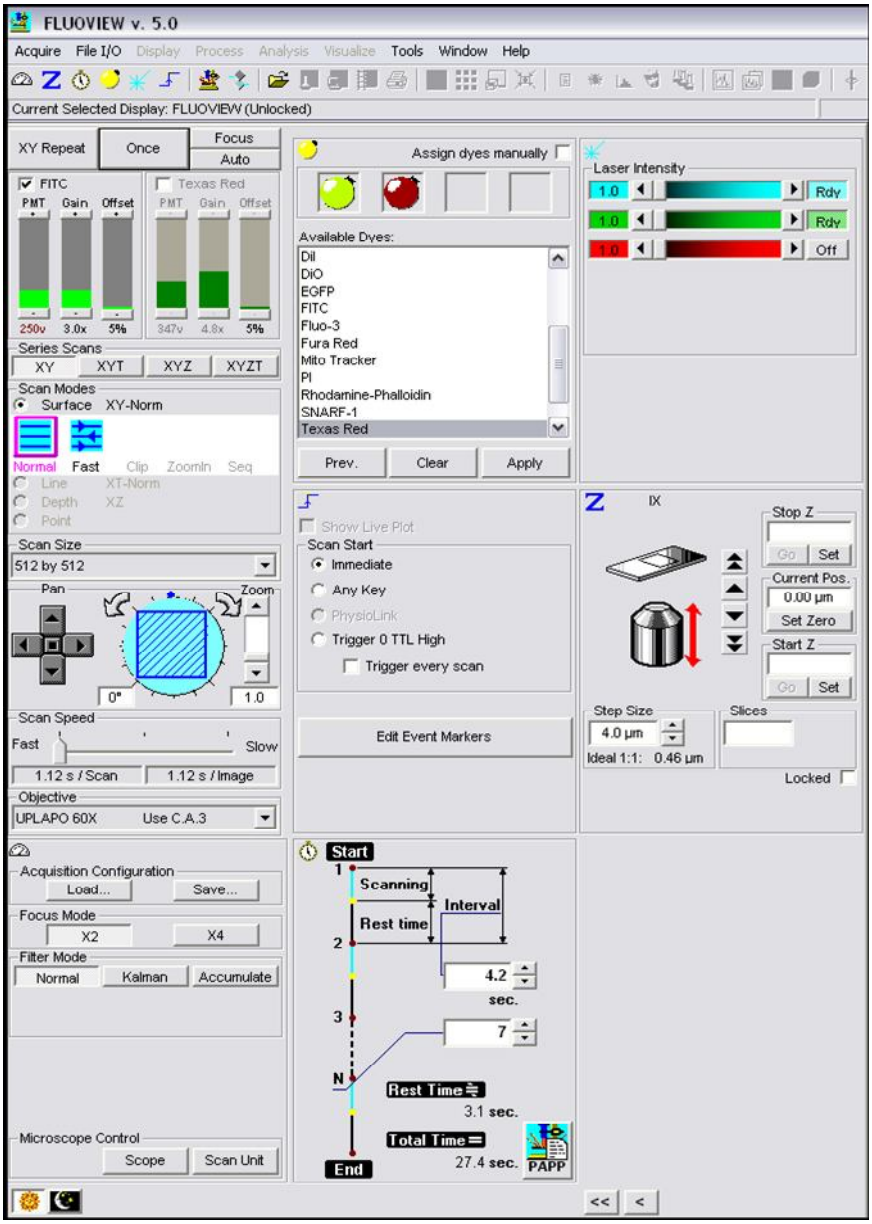

Figure 2.6. Fluoview 300 scanning software user interface, providing a variety of scanning modes.

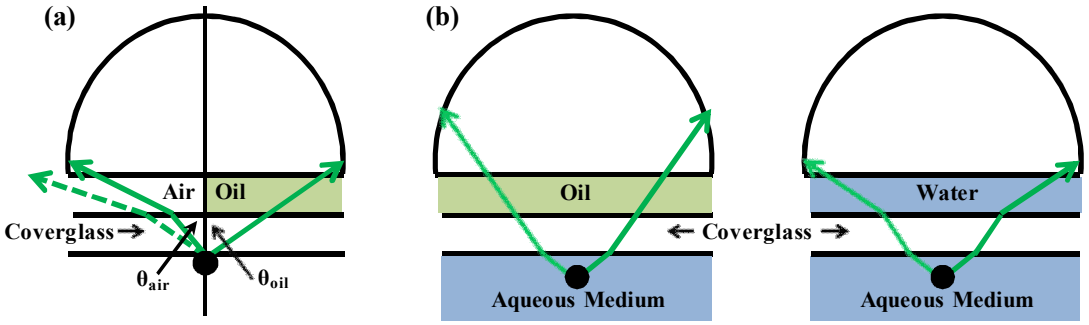

Figure 2.7. (a) When the specimen is immediately adjacent to the cover glass, an oil objective improves the collection efficiency as opposed to an air objective $\theta_{oil}>\theta_{air}$ by matching the cover glass refractive index: $n_{air}=1<n_{oil}\approx n_{glass}=1.515$ (b) When focusing deep into an aqueous solution, the artefacts due to refractive indices mismatch can be eliminated by replacing the oil with water: $n_{water}=1.33<n_{oil}\approx n_{glass}=1.515$.

However, when an oil immersion lens is focused deep into an aqueous specimen, the mismatch of the refractive indices in the optical path (water-glass-oil) leads to reduced image intensity and resolution due to spherical aberration [6] (figure 2.7b, left). This aberration increases proportionally with imaging depth and the artefacts become significant for distances greater than 15 µm. Therefore, substitution of the immersion oil with the lower-index water (n_{water}=1.33) can be advantageous by significantly reducing this spherical aberration and related artefacts (figure 2.7b, right).

As the samples used in this work were all aqueous and focusing in depth below 15 µm was needed for imaging inside microfluidic structures, a water immersion super apochromat objective with *NA* 1.2 (UPLSAPO 60x/1.2 NA, water immersion, Olympus) was chosen. This objective had field number 26.5 mm, working distance 0.28 mm and correction collars allowing for use of cover slip with thickness between 0.13 and 0.21 mm.

In confocal microscopy, the objective focuses the laser beam into the sample resulting in a probe volume typically in the order of subfemtolitres [7]. Assuming a perfectly Gaussian profile for the focused beam, the diffraction limited beam waist radius w_{beam} for a given objective focal length f_{obj} depends directly on the laser beam radius R_{beam} and is calculated by equation 2.3 [7]:

$$w_{beam} = \frac{\lambda f_{obj}}{n\pi R_{beam}} \tag{2.3}$$

where λ is the laser wavelength. Large beam diameters correspond to a sharper and narrower focus (figure 2.8a). The corresponding confocal probe volume V is defined by equation 2.4 [8]:

$$V = 2\pi\left(\frac{\lambda f_{obj}}{n\pi R_{beam}}\right)^2 Z' + \frac{2\lambda^2}{3\pi}\left(\frac{n\pi R_{beam}}{\lambda f_{obj}}\right)^2 Z'^3 = \frac{2\lambda^2 f_{obj}^2}{\pi n^2 R_{beam}^2} Z' + \frac{2\pi n^2 R_{beam}^2}{3 f_{obj}^2} Z'^3 \tag{2.4}$$

where $2Z'$ defines the probe depth, which is approximated to be 1 µm [5, 7, 8]. The first term of this expression corresponds to a cylindrical volume with radius defined by the waist of the beam, while the second term describes the extra curved volume arising from the Gaussian beam profile (figure 2.8b).

It is clear from equation 2.4 and figure 2.8b that for narrow beam widths or shallow probe depths, the probe volume can be approximated with the central cylindrical volume, while for larger diameters, the curved contribution becomes significant. It should also be noted that the

detection probe volume has a strong non-uniform intensity distribution and thereby the measured fluorescence intensities have a strong dependence on the location of the molecule within the beam [8].

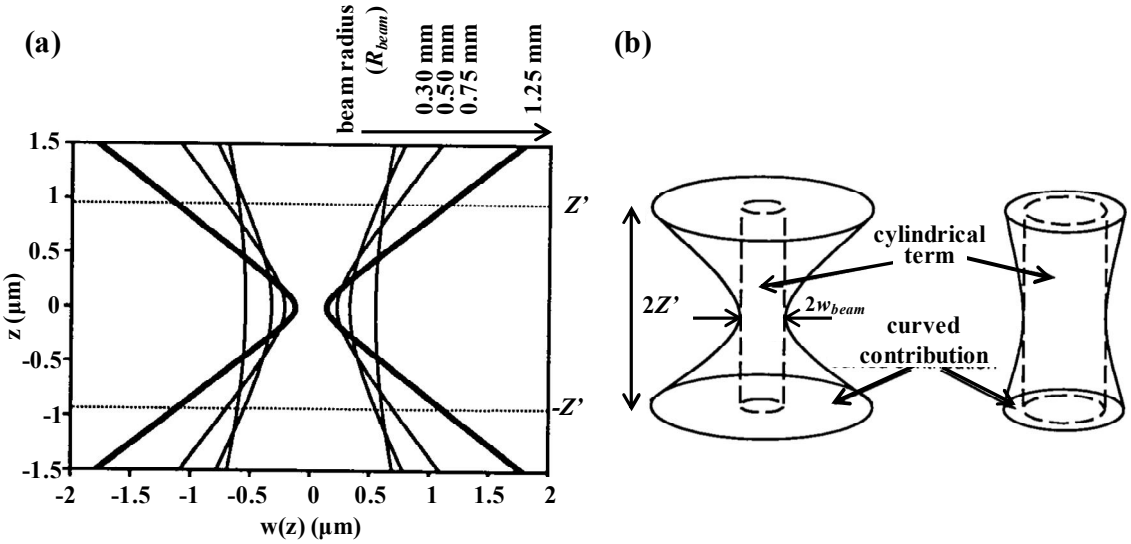

Figure 2.8. (a) $1/e^2$ Gaussian intensity contours for different beam radii, λ=488 nm, f_{obj}=1.6 mm, n=1.52 (b) Cylindrical and curved components of the Gaussian probe volume. For narrow beams the curved contribution is negligible and the probe volume can be approximated with the cylindrical component. $2Z'$ is the probe depth. Reproduced from [8] by permission of The Royal Society of Chemistry, 2000.

For the objective (60x) used in this work, the 180 mm standard focal tube length resulted in a focal length of 3 mm. When this was used in combination with the supercontinuum source (collimated beam diameter ~2 mm), it produced a focused beam with a waist radius of approximately 0.35 µm (equation 2.3), which defined a probe volume of approximately 0.44 fl (equation 2.4).

2.1.4. Detection path

Fluorescence emitted by the sample was collected by the same objective and transmitted through the dichroic mirror. Instead of using the pinholes, filters and PMTs included in the scanning unit, a home-built detection path was developed to enable single photon counting. The main parts of the detection path are show schematically in figure 2.1 (bottom) and a photo of the detection path is presented in figure 2.9.

A mirror (Thorlabs) was placed inside the scanning unit at 45º with respect to the fluorescence signal in order to direct the fluorescence vertically upwards (figure 2.5). A 1" hole was drilled in the top plate of the scanning unit to allow the fluorescence signal to exit the box. The fluorescence light was then directed on a second mirror (ME1-P01, Thorlabs) mounted in a cage system. The angle of the mirror with respect to the fluorescence signal was 45º and was

precisely adjusted by x-y screws included in the mounting system (figure 2.9). Subsequently, the fluorescent signal was focused by a plano-convex lens (LA1805-A, Thorlabs) onto a 100 µm pinhole (P100S, Thorlabs).

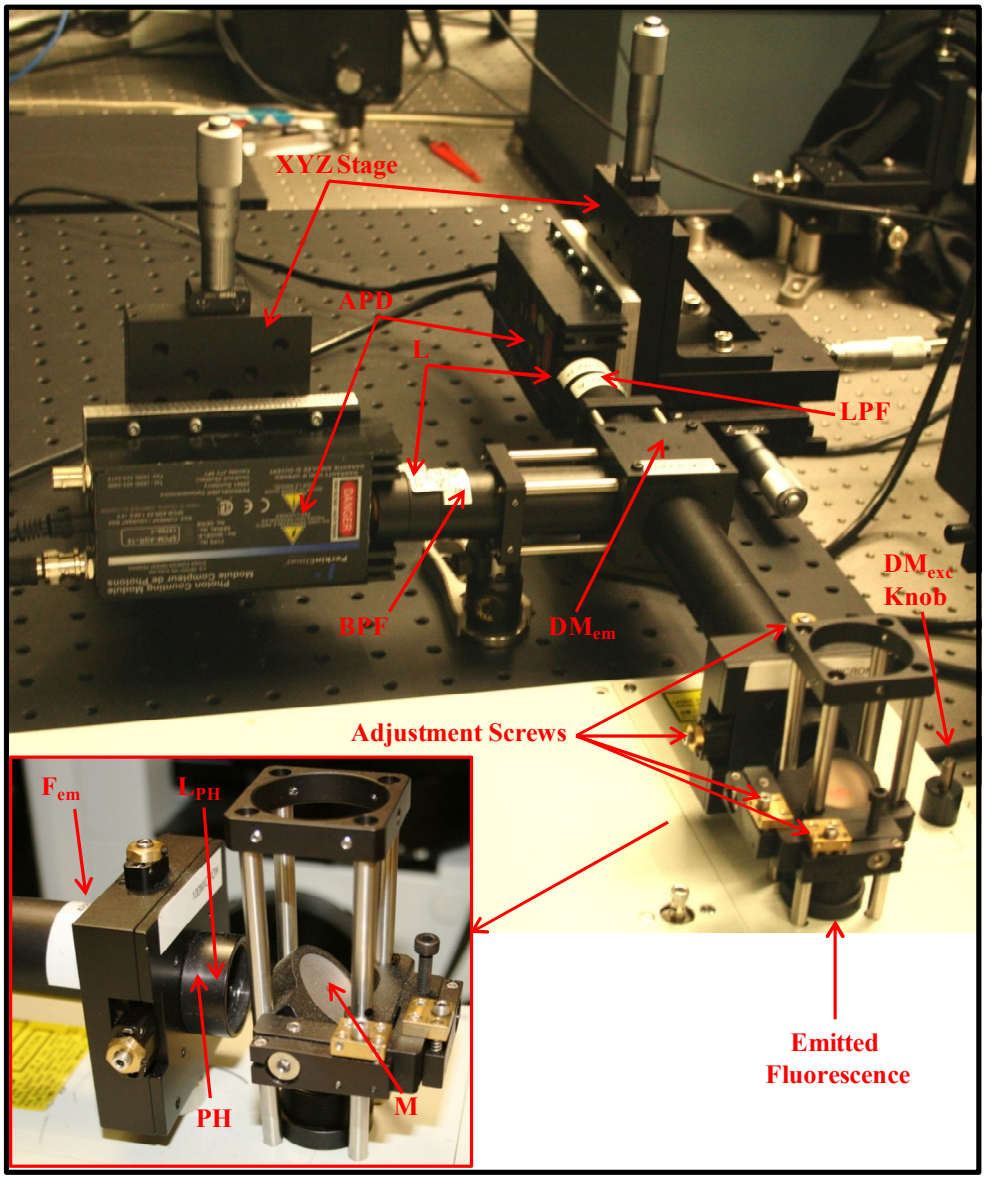

Figure 2.9. The home-built detection path. M: mirror, L: lens, PH: pinhole, F: filter, DM: dichroic mirror, LPF: long pass filter, BPF: band pass filter, APD: avalanche photodiode detector.

2.1.4.1. Pinhole

Unlike the scanning pattern of the excitation light, the fluorescence emission remained in a steady position at the pinhole aperture. Its intensity though fluctuated over time, as the illumination spot traversed the specimen.

The choice of the pinhole diameter is of high importance for the optical setup performance and its optimum value depends on the excitation wavelength, the objective *NA* and the total magnification factor of the arrangement. If the size of the pinhole is too small, there might be

significant loss of photons originating from the focal plane, while a pinhole that is too large can lead to poor lateral and axial resolution and low *S/N*.

The pinhole size can be expressed with respect to the produced airy disk diameter (airy units). For a circular pinhole the peak of *S/N* occurs at about 0.52 airy units (figure 2.10) [5], the fluorescence signal level however is reduced. Therefore, for both detection efficiency reasons and to facilitate alignment it is common to use a pinhole with diameter matched to 1 airy unit, which allows ~84% of emission signal to go through [4, 5]. The airy disk radius is given by:

$$R_{airy} = \frac{0.61 \times \lambda}{NA} \tag{2.5}$$

The physical size of the pinhole is the effective diameter calculated via equation 2.5 multiplied by the total magnification factor M_{tot} between the pinhole and the focal plane. This includes the objective magnification M_{obj} and the system magnification M_{syst}.

For the objective used herein (NA=1.2) and excitation at 488 nm, the 1 airy unit corresponded to a diameter of approximately 496 nm (equation 2.5). For the current optical arrangement with M_{obj}=60 and M_{syst}=3.426 (provided by Olympus engineers), the resulting optimal physical pinhole diameter was approximately 100 μm (accurate calculation yields 102 μm).

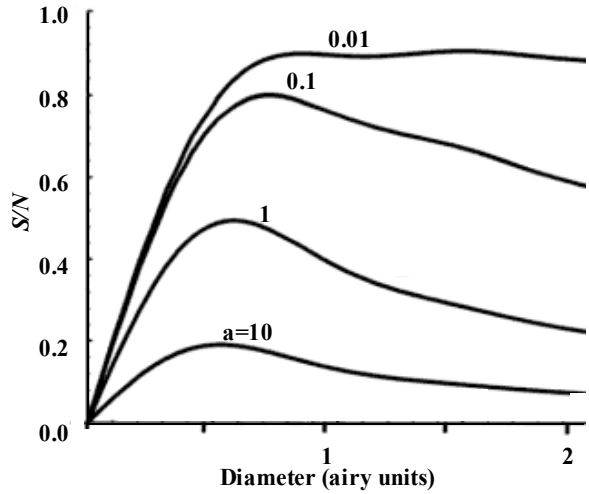

Figure 2.10. Variation in *S/N* with pinhole size for different strengths of background noise (a is small for stronger signal). Adapted from [5] with kind permission of Springer Science and Business Media, 2006.

2.1.4.2. Emission filter set

Following the confocal pinhole, the transmitted fluorescent signal was filtered by a 488 nm long pass filter (LP02-488RU-25, RazorEdge ®, Semrock, Laser 2000) and led through a 15

cm lens tube (1 inch diameter, Thorlabs) onto a 630 nm dichroic mirror (Z630RDC, Chroma Technology), which was mounted in a cube (C4W, Thorlabs) at 45º with respect to the signal propagation axis (figures 2.1 and 2.9). The dichroic mirror separated the fluorescence into two spectrum regions with wavelengths <630 nm (green detection channel) and >630 nm (red detection channel). Each channel was further filtered and focused via a plano-convex lens (LA1805-A, Thorlabs) onto a detector. A band pass filter transmitting wavelengths between 500-580 nm (HQ540/80, blocks 470 nm and 488 nm, AR coat, Chroma Technology) was chosen for the green channel and a 640 nm long pass filter (HQ640LP, Chroma Technology) was used for filtering the signal arriving to the red channel detector. A band pass filter transmitting wavelengths between 565-605 nm (ET585/40, AR coat, Chroma Technology) was also available to replace the green channel HQ540/80 filter in experiments whereby the emission maxima of the fluorescent dyes used fell in the 565-605 nm region (chapter 6). Filter transmission spectra are shown in figure 2.11.

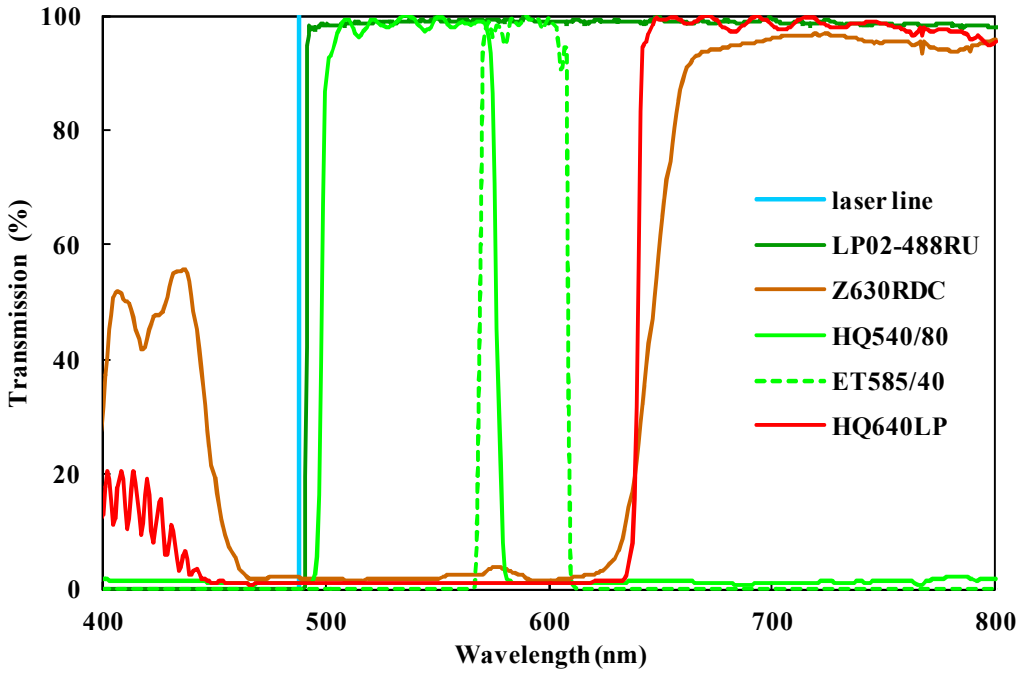

Figure 2.11. Transmission spectra of emission filters. Fluorescence emission was filtered by LP02-488RU-25 and separated in green and red regions via Z630RDC. The two channels were further filtered by HQ540/80 (or ET585/40) and HQ640LP respectively. The laser excitation line is shown in light blue.

2.1.4.3. Detectors

In order to achieve single photon sensitivity the detectors should have high quantum efficiency, short time response and low dark count to minimise the noise level [3, 5]. Instead of the integrated in the scanning unit PMTs, the detectors used for all measurements were APDs operating in the single photon counting mode.

The operation principle of an APD is based on the conversion of the power of incident photons into electrical energy through a charge avalanche. The basic structural elements of an APD are an absorption region, where the energy of incident photons is transformed into free electron-hole pairs (charge carriers), and a multiplication region, where these are accelerated under the application of high bias potential and further multiplied via the process of impact ionization. The newly created charge carriers may create new ones and thus an avalanche of electrons and holes is moving through the detector and can then be measured by external electronic equipment. At voltages above the breakdown voltage, a single photon is sufficient to generate an avalanche pulse in the order of 10^8 charge carriers allowing for single photon detection and counting [9].

Compared to the traditionally used PMTs, APDs display excellent linearity and higher quantum efficiency over a broad band of wavelengths ranging from 400-1100 nm [10, 11]. APD quantum efficiency can be a factor of 2 to 4 greater than that of a PMT for a given wavelength [11]. The peak of the quantum efficiency is 80% at around 600 nm under low gain conditions and can be as high as 95% at high gain [12]. APDs also provide fast single photon timing with reasonably low dark noise and gains over 10000 at room temperature [13, 14], the best *S/N* however occurs at gains between 200-1000 [15]. Due to their attractive characteristics APDs are gaining interest over PMTs in next generation experiments with applications in medical imaging, astronomy, high-energy physics etc. [16].

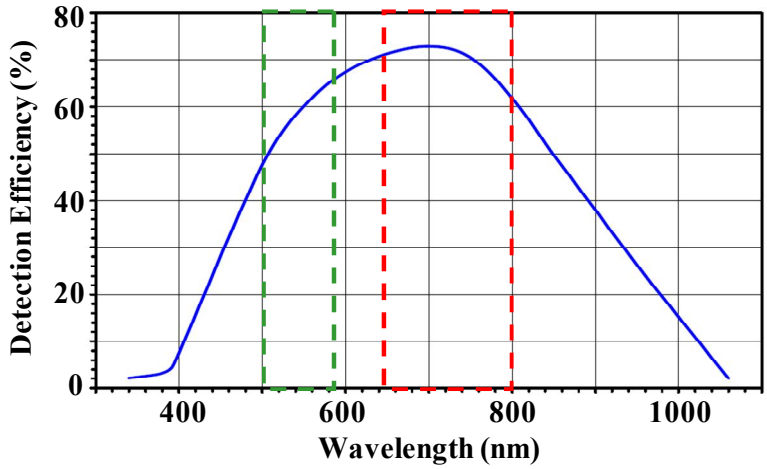

Figure 2.12. Detection efficiency of the SPCM-AQRH-13 used herein (provided by PerkinElmer Optoelectronics). For the monitored region (dashed lines: green APD 500-580 nm, red APD 640-800 nm) the efficiency is above 50%.

The detectors used herein were the SPCM-AQRH-13 from PerkinElmer Optoelectronics. The electronic output of the detectors consisted of a 5 V, 15 ns TTL pulse for each photon arrival with a dead time of 32 ns. The detectors output was connected to a NI card as well as to the

START input of a TimeHarp 200 card via a router (PRT 400, Picoquant), which allowed simultaneous measuring from up to four detectors. In this work, two detectors were used for collecting fluorescence within the green and red spectra, corresponding to regions 500-580 nm and >640 nm respectively. The dark count rate of the APDs was typically between 185 and 220 Hz. Figure 2.12 shows the detection efficiency of the APD detectors along with the wavelengths that were used for imaging.

2.1.4.4. Detection path assembly (alignment and detection efficiency)

In confocal arrangements it is crucial to ensure that all components are correctly positioned in the optical path. In order to achieve high detection efficiency and *S/N*, special care was taken during the pinhole and detectors alignment. For this purpose, fluorescein 5-isothiocyanate (FITC) from Sigma-Aldrich at high concentration (1 mM) was excited using the 488 nm line of the Melles Griot laser at maximum power (see section 2.1.1.1). Under these conditions the resulting fluorescence spot was visible to the naked eye (in absolute dark). Keeping the APDs off, the ME1-P01 mirror and the pinhole position were precisely adjusted using the provided x-y screws (figure 2.9) until maximum brightness of the fluorescence spot past the pinhole was achieved [17]. Subsequently, the laser beam was attenuated and the APDs were turned on. The emission dichroic mirror and the x-y position of the APDs were adjusted using the XYZ translation stage (figure 2.9) until maximum photon counts were obtained. Along the signal propagation axis the distance between each APD and the respective lens equalled the focal length of the lens (25.4 mm). Fine adjustment of this distance was also performed using the XYZ translation stage (z-axis).

After the alignment of the optical components was optimised, the relative detection efficiency of the APDs was verified via excitation of FITC and acridin orange hydrochloride hydrate (Sigma-Aldrich), both at 1 mM concentration. The emission spectra of the two dyes were obtained using a fluorometer (excitation at 488 nm) and the fraction of each spectrum falling into the green and red detection channels (500-580 nm and 640-800 nm respectively) was extracted via integration (figure 2.13). The red-to-green signal ratio for FITC and acridin orange were 0.01829 and 0.52614 respectively. Subsequently, emission photon counts were acquired for the two dyes using the confocal setup with the home-built detection path. The respective red-to-green signal ratios were 0.01813 and 0.52178 yielding a relative APD detection efficiency of:

$$\frac{DetEff_{APD,red}}{DetEff_{APD,green}} \approx 0.9913 \tag{2.6}$$

The extracted value (0.9913) was very close to 1, confirming the excellent performance of the custom built detection path and rendering the setup appropriate for studies which focus on the relative green and red fluorescence intensities, such as experiments described in chapter 6.

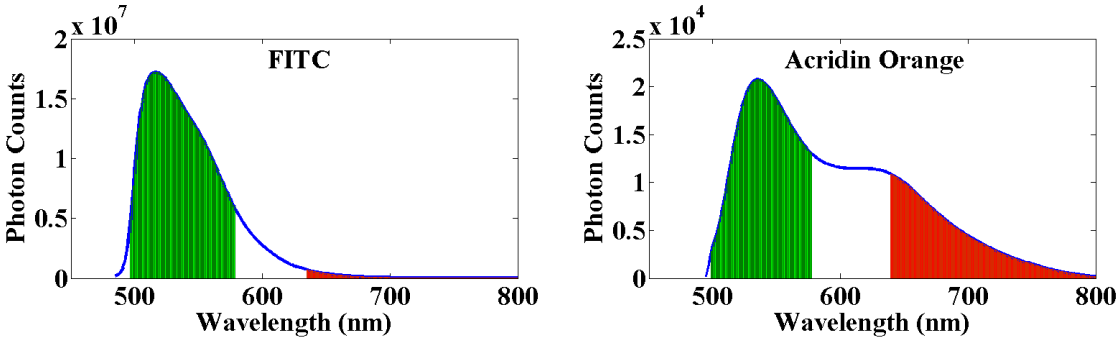

Figure 2.13. Emission spectra of FITC and acridin orange measured with a fluorometer and integration over the green and red detection regions (500-580 nm and 640-800 nm respectively).

2.1.5. Additional equipment

Additionally, the microscope was equipped with a 100 W halogen lamp and a mercury lamp, which were used for fluorescence monitoring and sample alignment. A 114 mm x 76 mm travel microscope stage with a minimum step size of 10 nm (H117 Stage, Prior Scientific) was used and software from Prior Scientific was available for precise control of the stage position. A charge-coupled device (CCD) camera (Drangonfly Express™, Point Grey Research) was used as an extra imaging tool as well as for the alignment of the pinhole (Figure 2.14).

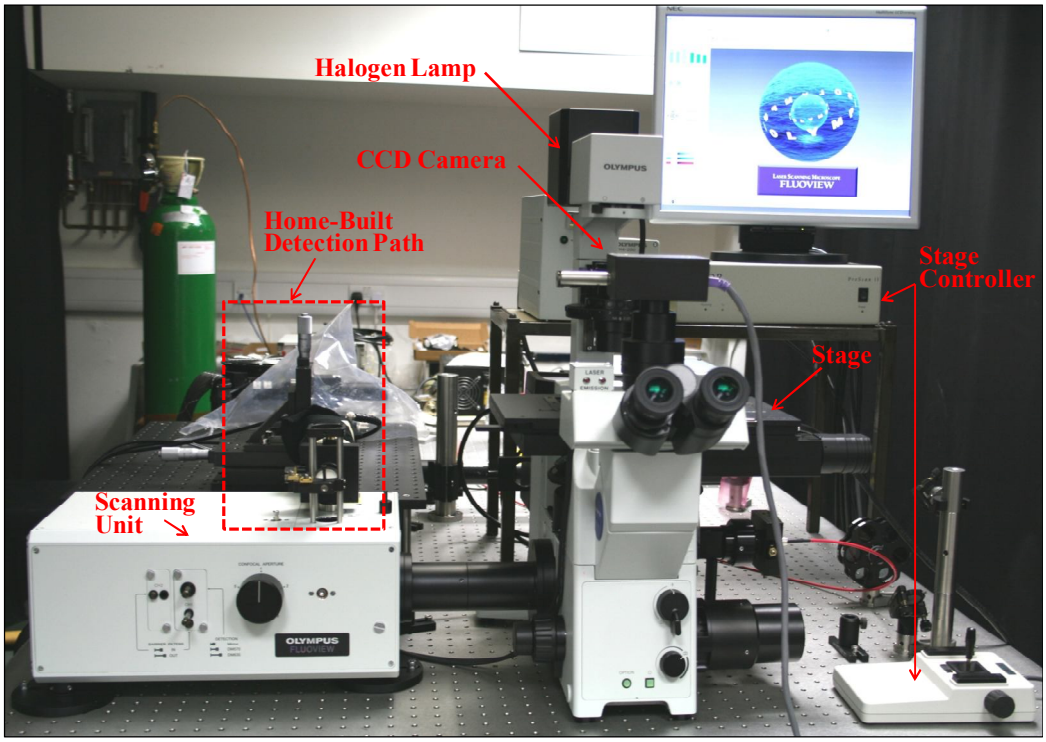

Figure 2.14. Photo of the scanning confocal setup.

2.2. Data acquisition

2.2.1. Fluorescence intensity (LabVIEW 8.5)

To determine the fluorescence photon count rate, the output of the detectors was fed to a multifunctional PCI 6601 card (National Instruments) through a BNC 2121 connector block (National Instruments). The card was configured for operation in counter mode using software written by members of the Edel research group. The TTL pulses provided by the APD were counted within user defined intervals (typically 50 µs) and then re-binned and plotted with a time resolution of 1-5 ms. The data recorded consisted of the photon count rate for each detector (.GN and .RD files for green and red detection channels respectively) and the autocorrelation function of the signal detected. This software was useful for real time monitoring of the detector output as well as for recording of single point measurements, such as that shown in figure 2.15. This was also used for detector and pinhole alignment.

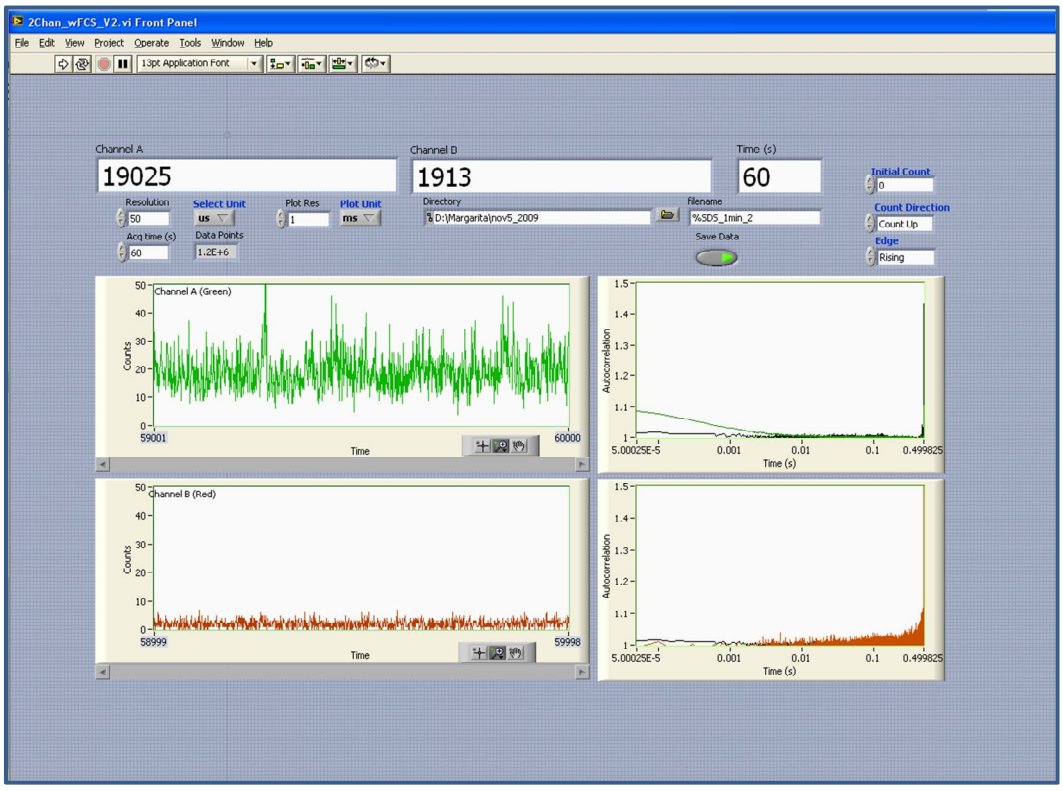

Figure 2.15. LabVIEW user interface. The photon burst scans for AlexaFluor488 streptavidin conjugate in the green and red detection channels are represented by the respective colours. Acquisition resolution is 50 µs and plotting resolution is 1 ms. Photon counts refresh every 0.5 s.

2.2.2. Fluorescence lifetime (TimeHarp 200)

The TimeHarp 200 PCI board and software (TimeHarp 200, v. 6.0, PicoQuant) were used for TCSPC fluorescence lifetime acquisition with a time resolution of 29 ps. The main principle of

TCSPC is illustrated in figure 2.16a. The electrical signal obtained from the detector was fed to the TimeHarp board START input via a router and the electric SYNC signal provided by the laser driver was fed to the board via a SYNC pulse adapter. The relative times between the laser excitation pulse (SYNC input) and the corresponding fluorescence photon arrivals (START input), termed start-stop-times, were collected in a block of memory. The memory cell held the photon counts for one corresponding time bin (time channel). When sufficient counts were collected, the start-stop-times obtained from multiple cycles were used to form a histogram representing the fluorescence decay. In practice, the times measured were not those between laser pulse and corresponding photon event, but those between photon arrival and the next laser pulse (figure 2.16a). This kept the TCSPC electronics conversion rates only as high as the actual photon rates generated by the fluorescent sample. Subsequently, the times used for the histogram were easily obtained via the excitation period.

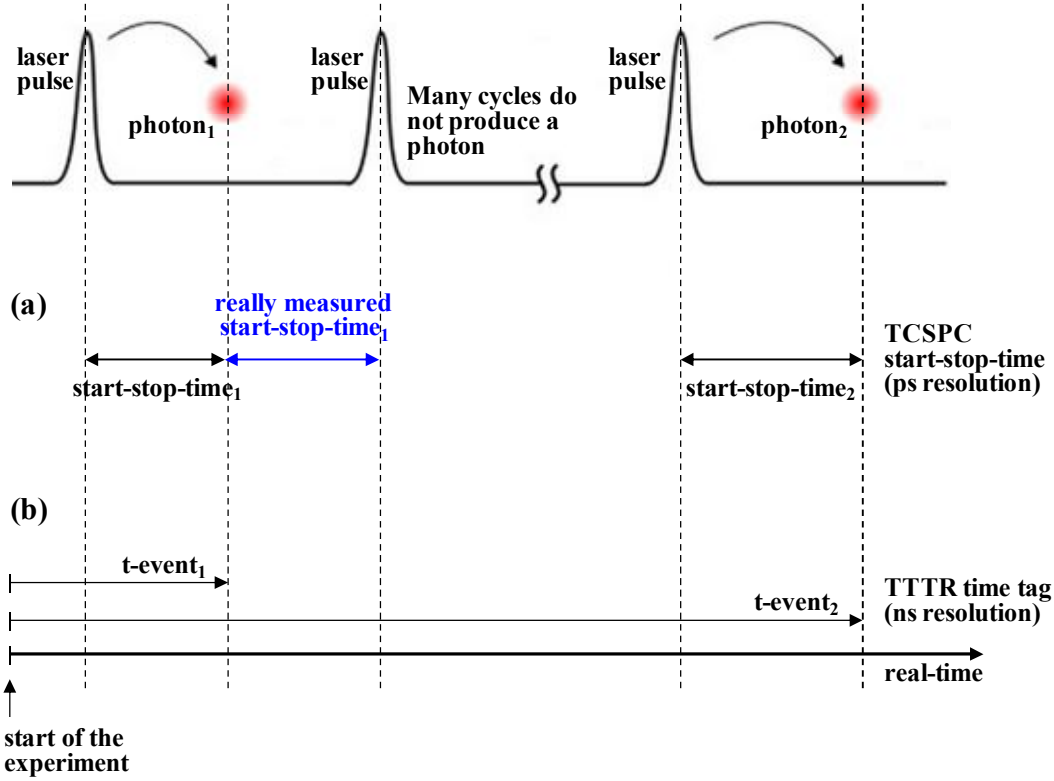

Figure 2.16. (a) The main principle of TCSPC. The time between laser pulse and fluorescence photon arrival (start-stop-time) is obtained with picosecond resolution. The start-stop-times are then used to form a histogram representing the fluorescence decay. In practice, the time between photon arrival and the next pulse is measured (shown in blue) and the start-stop-time is then extracted via the excitation period. (b) In TTTR acquisition mode an additional timing is obtained for each photon event with respect to the start of the experiment.

Due to detector dead time and dead time in the acquisition board, if the number of photons occurring in one excitation cycle was more than 1, the system would only register the first photon and miss the following ones. This would lead to an over-representation of early

photons in the histogram (pileup). It was therefore crucial to keep the probability of cycles with more than one photon as low as possible by adjusting the laser power and repetition frequency so that the average count rate at the detector was at most 1-5% of the excitation rate.

For fluorescence lifetime imaging the time-tagged time-resolved (TTTR or T3R) mode of the TimeHarp 200 was used, which recorded individual count events directly to hard disk without histogram formation. In TTTR mode, the start-stop timing of each photon event was recorded together with a time-tag from an independent digital clock running at 100 ns per tick (figure 2.16b). The resulting record for each event consisted of 12 bits for the start-stop-timing denoting the channel number that the given event fell into and 16 bits for the time-tag. A total of 6.5536 ms of data could be recorded. After this time, the counter rolled over and was marked in the data stream by the insertion of an overflow flag. Operation in this mode was fast enough to accept records at a rate of up to $3x10^6$ counts per second. In order to determine the spatial origin of the photon events when scanning with the FV300, the TimeHarp 200 board also provided inputs for synchronization of the signal derived from the scan controller. These external markers were treated almost as if they were regular TTTR photon records with a special valid flag, which distinguished between the true photon and marker records. The .TTTR files were binary, consisting of a header with the basic setup information followed by a sequence of 32 bit TTTR records, one for each event (16 bits for the time-tag, 12 bits for the start-stop timing, 2 routing bits and some flags, table 2.1). The way these files were used to construct fluorescent lifetime maps will be discussed in section 2.3.3. The TimeHarp 200 user interface used for histogramming of photon events is shown in figure 2.17.

Table 2.1. Time-tagged mode file format.

No of bits	Function	Description
16	Time-tag	Timing with respect to the independent digital clock running at 100 ns per tick
12	Start-stop timing	Relative time between the photon arrival and the laser excitation pulse with picosecond resolution
2	Routing	Denoting the acquisition channel when using more than one detector these (up to 4)
	Flag	Depending on the value of these bits the record might describe a real photon event, a system overflow or the arrival of an external trigger pulse (ex. from scan controller)

2.3. Data analysis

2.3.1. Fluorescence intensity plots

The acquired LabVIEW files (see section 2.2.1) were processed using a custom-written Matlab algorithm (provided by Dr. J.B. Edel) to produce photon counts versus time plots representing

the fluorescence intensity. The resampling time was typically 1 ms. In bulk measurements, the average fluorescence intensity over the acquisition period (0.5-3 min) in the green and red detection channels was extracted by averaging the recorded photon counts per time bin.

2.3.2. Fluorescence lifetime decays

A custom-written Matlab program referred to as *Jlife* (developed by Dr. J.B. Edel) was used to analyse the fluorescence lifetime histograms produced by TimeHarp 200. The program interface is shown in figure 2.18.

Experimentally measured fluorescence lifetimes are described by Poissonian and multinomial statistics, therefore, for a high number of photon counts, this converges to Gaussian statistics. Under high photon count conditions, the fluorescence lifetime is typically extracted by a least squares fitting approach [18].

Lifetime data was loaded in a .TXT file format and the fluorescence decay was plotted together with the instrument response function (IRF). This is the convolution of all system components IRFs (laser source, detectors, TCSPC electronics) and is typically obtained by recording the decay of a fluorescent dye with lifetime in the order of picoseconds. The dye used herein was rose bengal, yielding an IRF of approximately 650 ps. The program deconvolved the IRF and performed exponential fitting of the decay with 1-5 components according to user's selection. Most fluorophores displayed either mono- or double-exponential decays, while for a mixture of fluorophores or complex decay processes a triple-exponential fit was preferred. The average lifetime for multi-exponential decays was determined via equation 1.4. In some cases however, further analysis or an alternative interpretation of the multi-exponential decay was required, as it will be discussed in chapter 6.

The goodness of the fit was evaluated based on extracted statistics. Typically, a good fit is achieved when the reduced chi-square (χ_R^2) equals 1, with lower values (<0.75) representing data sets too small for a meaningful fit and high values (>1.5) indicating significant deviation from the exponential fitting model. As a rule of the thumb, fits that yield χ_R^2 values between 0.8-1.3 are considered satisfactory and acceptable, given some prior understanding of the system under investigation [3, 19]. The residual values were also plotted for visual inspection, with a good fit yielding residuals randomly distributed and centred around zero.

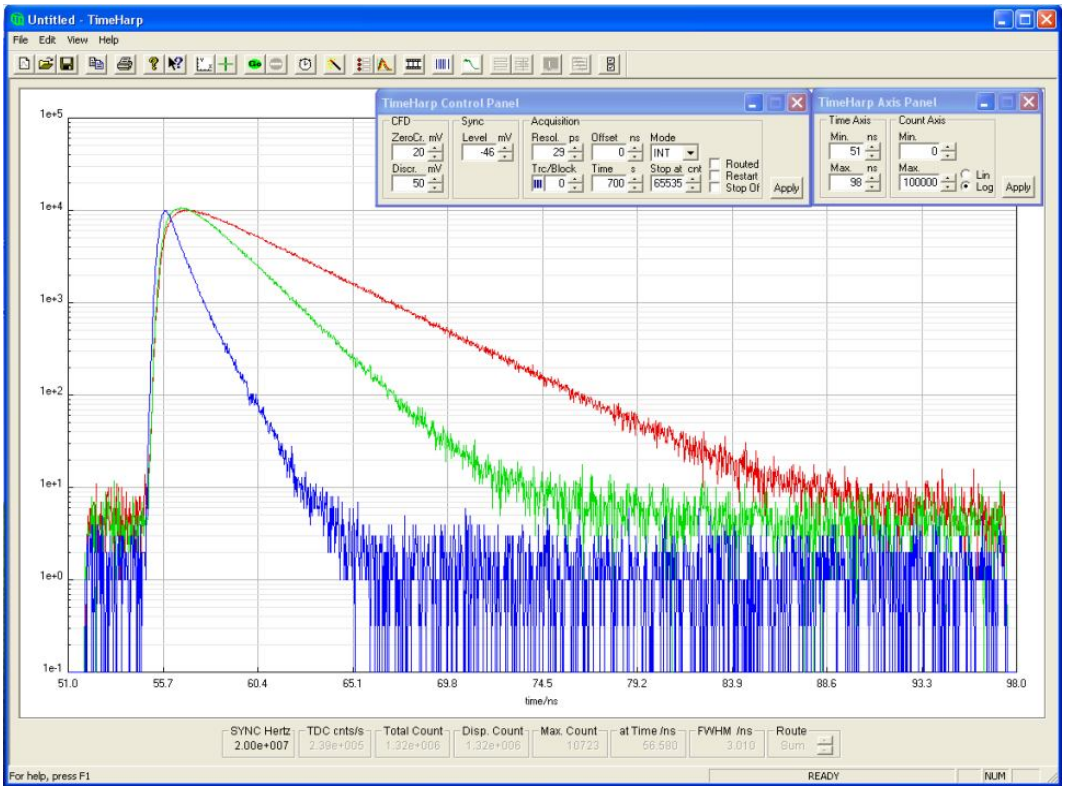

Figure 2.17. TimeHarp 200 user interface, histogram mode. Fluorescence lifetime decays of rhodamine 110 chloride (red curve, lifetime ~3.8 ns) and acridin orange (green curve, lifetime ~1.8 ns). The instrument response is shown in blue (rose bengal, lifetime ~650 ps).

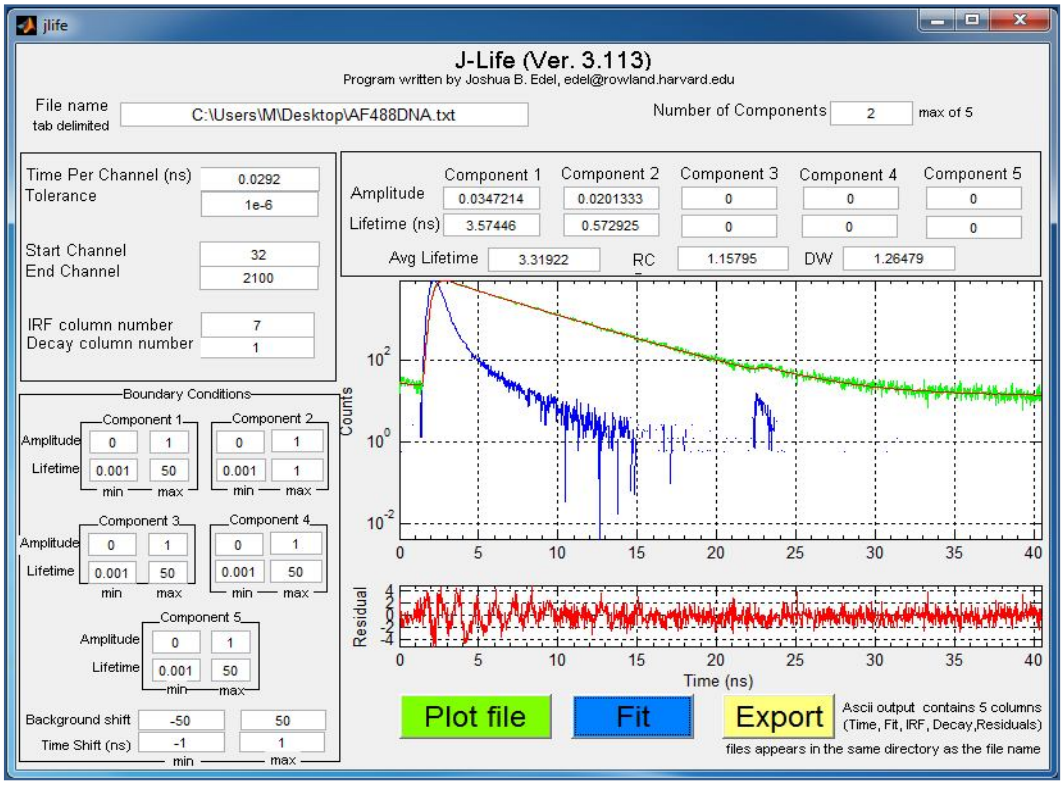

Figure 2.18. *Jlife* program user interface. The fluorescence decay of AlexaFluor488 attached to a DNA oligo (green curve) was fitted using two lifetime components (red curve) resulting in a χ_R^2 value of ~1.16. The IRF is represented by the blue curve. Residuals are plotted below the graph.

2.3.3. Two-dimensional fluorescence lifetime maps

A Matlab algorithm provided by Dr. J.B. Edel was used to process the binary .TTTR files acquired with the TimeHarp 200 to construct two-dimensional fluorescence lifetime maps. Once the photon events corresponding to each pixel of the produced image were determined (taking into account table 2.1), the fluorescence lifetime for the total photons for a given pixel was extracted from the start-stop times recorded for these events.

In the x-y scanning TTTR acquisition mode the number of photons per pixel was generally low. As it was previously mentioned (section 2.2.2), in order to avoid an over-representation of early photons as well as detector saturation, the average count rate at the detector should be at most 1-5% of the excitation rate (20 MHz). In practice, the laser power was adjusted so that the average count rate would not exceed ~3×10^5 counts per second. For the 512×512 pixels scanning that was used for the majority of the experiments (~1 sec per scan), the above count rate corresponded to a maximum of 1.2 photons per pixel per scan (or per second). For the acquisition times used herein (typically 0.5-3 min) the average number of photons detected per pixel was between 35 photons per pixel (for 30 sec acquisition time) and 220 photons per pixel (for 3 min acquisition time), given that the maximum count rate of 3×10^5 counts per second was achieved.

When less than 2000 photon events are available for calculating fluorescence lifetimes, the least squares approach is not appropriate, as the error originating from assuming a Gaussian distribution becomes significant. When determining lifetimes using between 10 and 2000 photons, which was the case for the majority of the scanned pixels, a powerful alternative to the least squares method is the use of a maximum likelihood estimator (MLE) [20-22]. The MLE approach determines the occurrence probability of a specific lifetime and is given by [23]:

$$\gamma_j = \sum_1^k n_i \log\left(\frac{n_i}{N p_i(j)}\right) \tag{2.7}$$

where, n_i is the number of photon counts in the channel i, k is the number of channels or bins for each fluorescence decay, $p_i(j)$ is the probability that a group of photons will fall in channel i if the molecules have a lifetime j and $N = \sum_1^k n_i$ is the total number of counts for a given decay. The MLE equation used herein was developed by Edel et al. to determine fluorescence lifetimes from as little as 10 photons and is given by [24]:

$$\frac{N}{1-e^{-\omega/\tau}}-\frac{Nk}{e^{k\omega/\tau}-1}=\sum_{i=1}^{k} in_i\left(\frac{i-\sum_{j=1}^{i} jr_j e^{j\omega/\tau}}{\sum_{j=1}^{i} r_j e^{j\omega/\tau}}\right) \quad (2.8)$$

where τ is the fluorescence lifetime. The IRF corresponds to r_j for each bin j, recorded with a time resolution ω. The fluorescence lifetime was determined by solving for the local minimum. As little as 10 photons were used herein to accurately extract the fluorescence lifetime for each pixel and produce two-dimensional fluorescence lifetime maps. Similarly, the number of photon events recorded per pixel were used to produce two-dimensional fluorescence intensity maps. Examples of fluorescence intensity and lifetime maps are shown in figure 2.19.

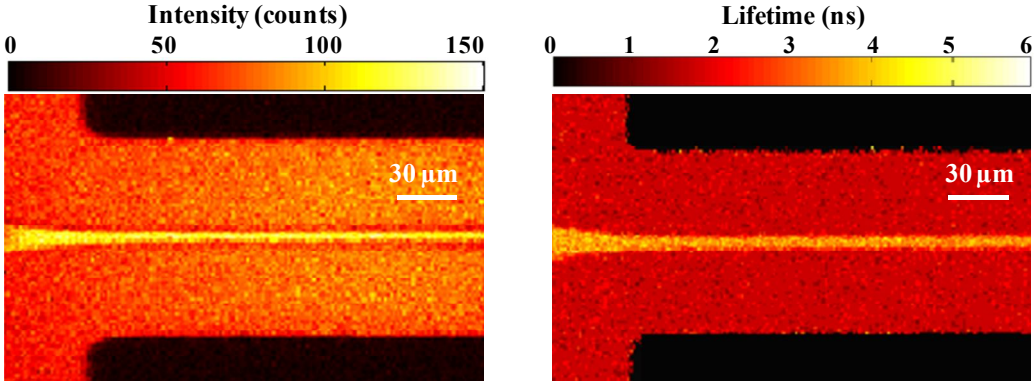

Figure 2.19. Two-dimensional fluorescence intensity (left) and fluorescence lifetime (right) maps produced via .TTTR analysis and a minimum threshold of 10 photons for the MLE routine. The images visualise hydrodynamic focusing within a microfluidic channel.

2.3.4. Measurements at the single molecule level

When single molecule measurements were performed by employing single point as opposed to laser scanning excitation mode, the TimeHarp 200 TTTR acquisition mode was used to simultaneously provide fluorescence intensity and lifetime information. In single point excitation mode, the .TTTR files did not contain external markers from synchronisation with FV300 as there was no scanning involved. Therefore, a similar data analysis to the one described above (section 2.3.3) yielded photon events per time bin instead of photon events per pixel and resulted in photon counts plots versus time instead of two-dimensional intensity maps.

In single molecule experiments, the extracted photon counts plots consisted of a baseline, representing background noise, and fluorescence intensity peaks (photon bursts),

corresponding to single molecules traversing the detection probe volume (figure 2.20a). Depending on the background signal, a threshold was applied to distinguish between noise and intensity peaks. The Matlab algorithm automatically calculated this threshold which, based on Poisson statistics, equalled three standard deviations from the mean background photon count [25]. In cases where the sample was prepared in a more complex buffer, such as a lipid containing buffer for membrane proteins, an additional threshold was set after performing independent measurements on the buffer alone. Fluorescent signal exceeding the threshold value was identified as a photon burst (figure 2.20b) and characteristics, such as burst height, width and area, were used to extract useful information.

More specifically, the burst height is defined as the maximum photon count value of the burst, while the photon area expresses the total number of photons composing one intensity peak. This was extracted via analysis of the photon counts around the burst maximum until the threshold was reached. The same analysis yielded the boundaries of an intensity peak, which determine the burst width (in ms). Burst height, width and area histograms may be used to gain insight into the characteristics of the molecule under investigation.

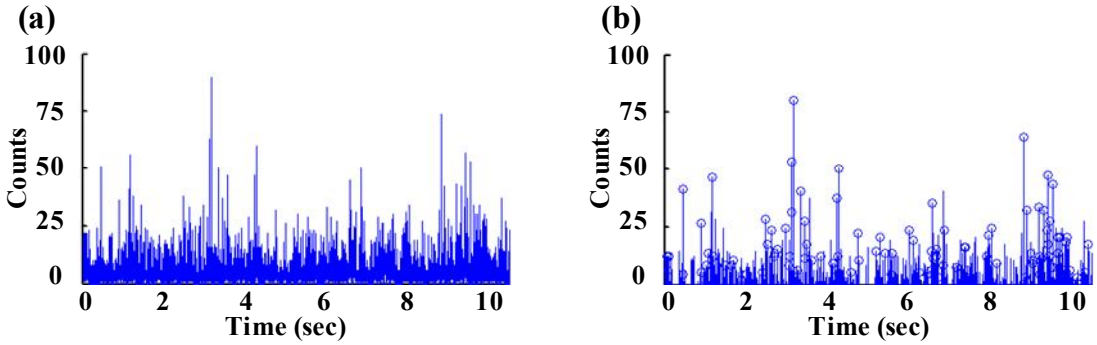

Figure 2.20. Single molecule burst scan for 100 pM AlexaFluor488 streptavidin conjugate using point excitation mode (a) photon counts plot (b) peak locating algorithm. Resampling time was 1 ms.

Fluorescence lifetime analysis was performed in an identical manner to that described in section 2.3.3, with the difference that instead of extracting lifetime values per pixel the program determined the lifetime for each photon burst. The calculated fluorescence lifetimes, which essentially represented individual molecule lifetimes, generally followed a normal distribution as it was illustrated by the resulting histograms.

2.4. Microfluidics

2.4.1. Channel designs

The microfluidic devices fabricated had a similar geometry to the one suggested by Hertzog et al. [26]. The design consisted of a 3-inlet junction allowing for fast mixing via hydrodynamic focusing (figure 2.21a). The channels were fabricated with dimensions typically varying from 8-200 µm. In addition to the simple 3-inlet 1-outlet device, a variety of designs were also fabricated according to application, some of these shown in figure 2.21b, c and d. Basic 1-inlet 1-outlet devices were also used for simple experiments. The chip designs were prepared in AutoCAD and dark field photomasks (polyester film) were produced by either JDPhoto or Micro Lithography Services Ltd.

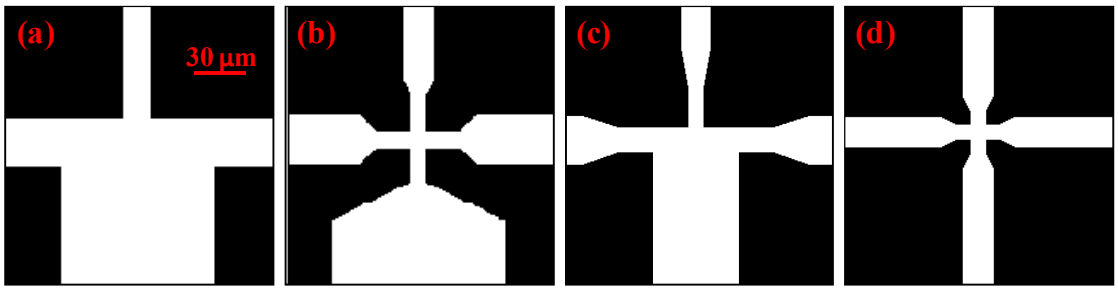

Figure 2.21. The fabricated microfluidic chip designs. (a) Simple 3-inlet 1-outlet device [26] (b), (c), (d) Optimized designs with nozzles [27].

2.4.2. Device fabrication

The microfluidic channels were fabricated in PDMS and sealed with a glass cover slip using standard photolithographic techniques. These materials were chosen based on the available options discussed in section 1.2.2. The steps describing the fabrication process are shown in figure 2.22.

2.4.2.1. PDMS master fabrication

The PDMS masters were prepared on 4-inch silicon wafers (IDB Technologies Ltd). The wafer substrates were pre-treated in piranha solution (H_2O_2:H_2SO_4 ratio 1:3, the peroxide was added to the acid) overnight, rinsed with deionised water and baked on a hot plate at 200° C for 5 minutes for surface dehydration. It should be noted that when handling piranha solution special protection equipment was required including an acid-protective apron on top of the lab coat, a full-face shield and heavy-duty rubber gloves. In general, piranha solution should be handled with extra care as it is very energetic and potentially explosive.

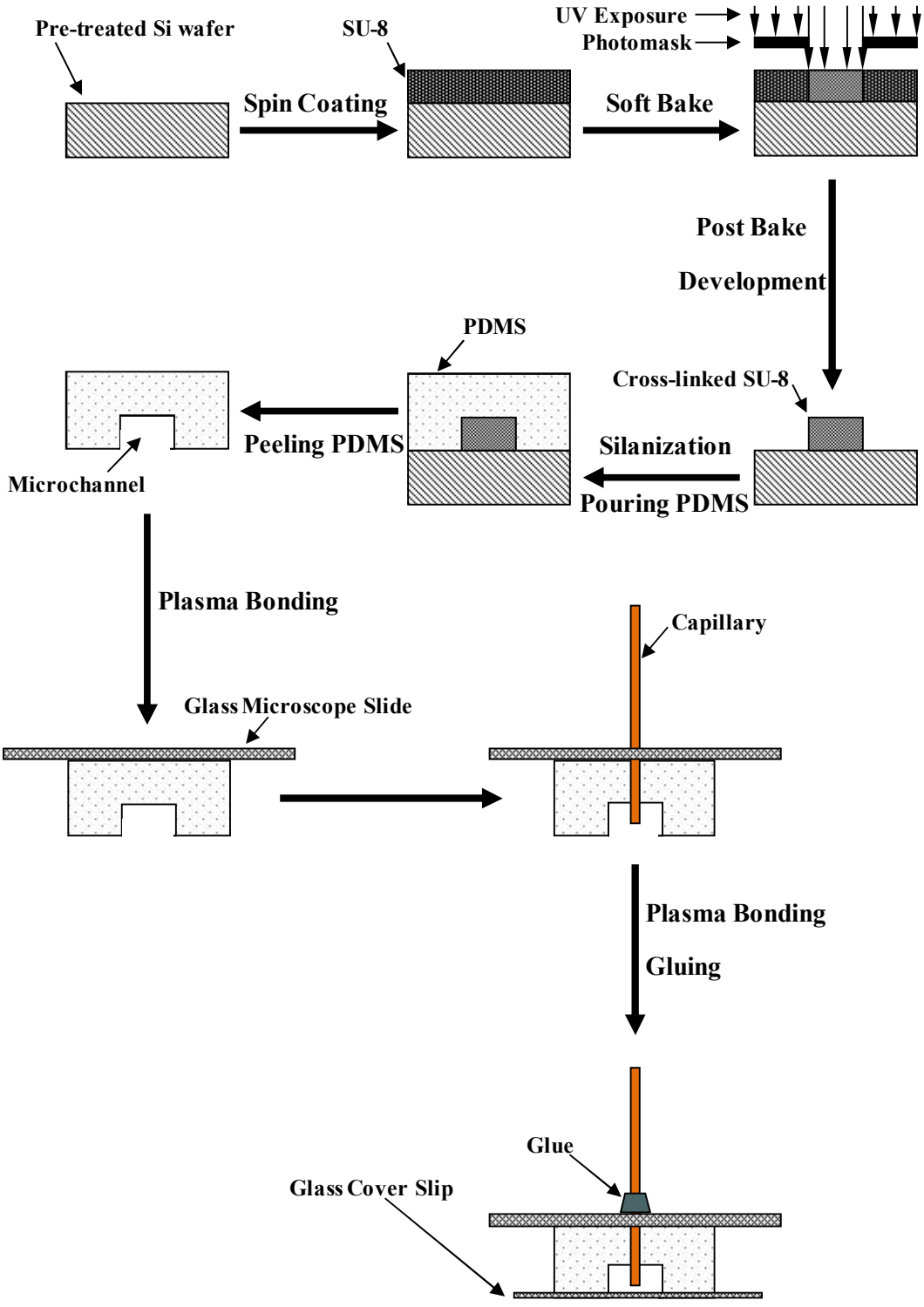

Figure 2.22. PDMS master and microfluidic chip fabrication steps.

SU-8 spin-coating

Epoxy based negative photoresist SU-8 (Michrochem, Chestech Ltd) was spin-coated (Siemens) onto the substrate. The thickness of the SU-8 coated layer, and therefore the produced channel depth, depended on the SU-8 viscosity and the spinning speed during the spin-coating procedure. SU-8 50 was chosen for channel dimensions above 20 μm, while for narrower channels SU-8 10 was used to provide the required film thickness (table 2.2). The spin conditions varied depending on the desired SU-8 coating thickness according to the manufacturer formulations. Typical coating conditions used consisted of a 500 rpm spread cycle followed by acceleration at a rate of 300 rpm/s to the final speed of either 2000 rpm or 1400 rpm depending on the desired photoresist thickness (table 2.2). The final speed was kept constant for 30 s. Following spin-coating, the substrate was soft-baked through a two step process to evaporate the solvent and densify the film.

Table 2.2. Master fabrication: SU-8 spin-coating

Product	Viscosity (cSt)	Thickness (μm)	Final Spin Speed (rpm)	Pre-bake @65°C (min)	Soft-bake @95°C (min)
SU-8 50	12250	50	2000	6	20
SU-8 10	1050	20	1400	1.5	6

UV exposure

The photomask was placed on top of the substrate with the photoresist side facing towards the SU-8 coating for UV light exposure (Light Support Ltd). During UV irradiation, a series of photochemical processes was initiated in the exposed areas (channel features) of the SU-8 film, which altered its physical and chemical properties [28]. For features above 20 μm, the exposure time was typically 20 s and decreased for smaller dimensions. A post-exposure bake was performed in two steps (table 2.3) to selectively cross-link the exposed portions of the film, rendering them stable and durable during the following development process.

Development

Development was performed by immersing the wafer into an SU-8 developer (Microposit EC Solvent), which removed the non-cross-linked SU-8 leaving only the channel designs on the wafer (non-dissolved SU-8). The wafer was then rinsed with isopropanol and dried with nitrogen gas. If during the rinsing process there was still unexposed SU-8 left on the wafer, this appeared as white and the master was re-immersed into the developer for further SU-8 removal. Finally, an optional silanization step with perfluoroctyltrichlorosilane was performed to facilitate PDMS peeling from the produced master in a later step.

Table 2.3. Master fabrication: UV light exposure and development (PEB: post-exposure bake)

Product	Thickness (μm)	Exposure (sec)	PEB1 @65°C (min)	PEB2 @95°C (min)	Development (min)
SU-8 50	50	20	1	5	6
SU-8 10	20	18	1	1.5	4

2.4.2.2. Chip fabrication

PDMS replica

PDMS silicon elastomer and curing agent (SYLGARD 184 Silicone Elastomer Kit, Dow Corning) were mixed at a 10:1 weight ratio. Following degassing for approximately 60 minutes, the mixture was poured onto the master SU-8 template to form a 5 mm PDMS layer. The substrate was then baked at 65°C for at least 5 hours. The PDMS was finally peeled off the wafer and cut into individual chips (usually 4×4=16 chips per wafer), while the master was cleaned with hexane and methanol and stored for future use.

Device assembly

Access holes were drilled (Xenox, Farnell) in 1×2 inch microscope slides (1 mm thickness, VWR International) at positions corresponding to the design inlets, using 0.25 mm diameter tungsten carbide dental drill bits (Diama International). Drilling was done under water to ensure rapid cooling of the surrounding location to minimize glass fractures. The glasses were cleaned in piranha solution for 30 minutes and sonicated in 0.5 M NaOH. Finally, the samples were immersed and sonicated in ethanol and water for 5 minutes each and dried using nitrogen gas.

Each microscope slide was subsequently plasma-bonded at the top side of an individual PDMS chip (Plasma Cleaner, Harrick Plasma). The bonding duration was 20 s for each chip. Special care was taken for precisely aligning the glass holes with the channel inlets. 3-5 cm long fused silica capillaries (375 μm o.d., 150 μm i.d., Composite Metal Services) were then pushed inside the access holes and through the PDMS. The resulting devices were cleaned using ethanol and water as before and thoroughly dried. 24×24 mm, 160 μm thick glass cover slips (thickness No 1, VWR International) were plasma-bonded (20 s) at the bottom to seal the channels. Finally, the capillaries were glued on the top glass slide using a two-part epoxy (Araldite 2014, RS Components) to increase stability. The devices were then baked at 65°C overnight and the exact dimensions of the resulting channels were confirmed by observation with a Leica microscope. Examples of complete devices are shown in figure 2.23.

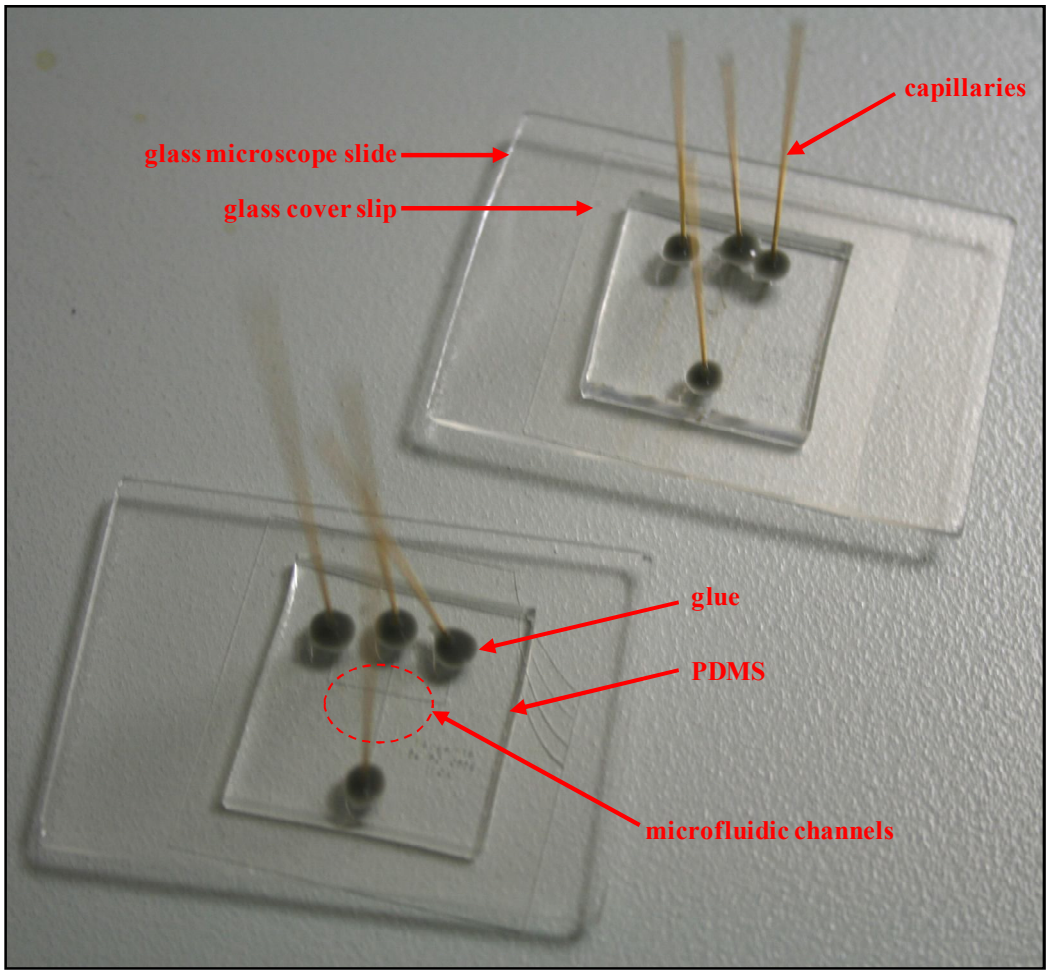

Figure 2.23. Complete microfluidic devices.

2.4.3. Microfluidic devices in experiments

1 ml Hamilton gas tight syringes (Sigma Aldrich) with Teflon PEP tubing (0.356 mm i.d., 1.55 mm o.d., Anachem, Upchruch Scientific) were used for the delivery of solutions into the channels through the inlet capillaries. The tubing was attached via PEEK fingertights and unions (1/16 inch, 10/32 threads, VWR International). The device was mounted on the microscope stage above the objective and the flow rates were controlled by precision syringe pumps (PHD 2000, Harvard Apparatus). For the majority of the experiments, the flow rates varied between 0.005-10 μl/min. At the end of each experiment, syringes and tubing were cleaned with acidic solutions, while the chips were thoroughly cleaned with water. Although the PDMS chips are considered as reusable, is was noticed that after 3-4 full-day experiments the fluorescence dye absorption into the PDMS could significantly interfere with the measurements, hence, the device should be replaced with a fresh one.

2.5. References

1. Corle, T.R. and G.S. Kino, *Confocal scanning optical microscopy and related imaging systems.* Academic Press, San Diego, London, 1996.
2. Sheppard, C., *Confocal laser scanning microscopy* BIOS Scientific, Oxford, 1997.
3. Lakowicz, J.R., *Principles of fluorescence spectroscopy, 3rd edition.* Springer Science and Business Media, New York, 2006.
4. Muller, M., *Introduction to confocal fluorescence microscopy, 2nd edition.* SPIE Press, Bellingham, Wash., 2006.
5. Pawley, J.B., *Handbook of biological confocal microscopy, 3rd edition.* Springer Science and Business Media, New York, 2006.
6. Shotton, D.M., *Electronic light microscopy: Present capabilities and future prospects.* Histochemistry and Cell Biology, 1995. **104**(2): p. 97-137.
7. Nie, S.M., D.T. Chiu and R.N. Zare, *Real-time detection of single-molecules in solution by confocal fluorescence microscopy.* Analytical Chemistry, 1995. **67**(17): p. 2849-2857.
8. Hill, E.K. and A.J. de Mello, *Single-molecule detection using confocal fluorescence detection: Assessment of optical probe volumes.* Analyst, 2000. **125**(6): p. 1033-1036.
9. Vasile, S., P. Gothoskar, R. Farrell and D. Sdrulla, *Photon detection with high gain avalanche photodiode arrays.* Ieee Transactions on Nuclear Science, 1998. **45**(3): p. 720-723.
10. de Haas, J.T.M., P. Dorenbos and C.W.E. van Eijk, *Measuring the absolute light yield of scintillators.* Nuclear Instruments & Methods in Physics Research Section a-Accelerators Spectrometers Detectors and Associated Equipment, 2005. **537**(1-2): p. 97-100.
11. McClish, M., R. Farrell, K. Vanderpuye and K.S. Shah, *A reexamination of deep diffused silicon avalanche photodiode gain and quantum efficiency.* IEEE Transactions on Nuclear Science, 2006. **53**(5): p. 3049-3054.
12. Lawrence, W.G., G. Varadi, G. Entine, E. Podniesinski and P.K. Wallace, *Enhanced red and near infrared detection in flow cytometry using avalanche photodiodes.* Cytometry Part A, 2008. **73A**(8): p. 767-776.
13. Li, L.Q. and L.M. Davis, *Single-photon avalanche diode for single-molecule detection.* Review of Scientific Instruments, 1993. **64**(6): p. 1524-1529.
14. Farrell, R., K. Vanderpuye, L. Cirignano, M.R. Squillante and G. Entine, *Radiation detection performance of very high-gain avalanche photodiodes.* Nuclear Instruments & Methods in Physics Research Section a-Accelerators Spectrometers Detectors and Associated Equipment, 1994. **353**(1-3): p. 176-179.
15. Farrell, R., R. Redus, J.S. Gordon and P. Gothoskar, *High gain APD array for photon detection*, in *Photodetectors and Power Meters Ii*. 1995. p. 266-273.
16. McClish, M., R. Farrell, R. Myers, F. Olschner, G. Entine and K.S. Shah, *Recent advances of planar silicon APD technology.* Nuclear Instruments & Methods in

Physics Research Section a-Accelerators Spectrometers Detectors and Associated Equipment, 2006. **567**(1): p. 36-40.

17. Kimura, S. and T. Wilson, *Effect of axial pinhole displacement in confocal microscopes.* Applied Optics, 1993. **32**(13): p. 2257-2261.

18. van der Meer, M.J., H. Zhang and M. Glasbeek, *Femtosecond fluorescence upconversion studies of barrierless bond twisting of auramine in solution.* Journal of Chemical Physics, 2000. **112**(6): p. 2878-2887.

19. Eaton, D.F., *Recommended methods for fluorescence decay analysis.* Pure and Applied Chemistry, 1990. **62**(8): p. 1631-1648.

20. Kollner, M., A. Fischer, J. ArdenJacob, K.H. Drexhage, R. Muller, S. Seeger and J. Wolfrum, *Fluorescence pattern recognition for ultrasensitive molecule identification: Comparison of experimental data and theoretical approximations.* Chemical Physics Letters, 1996. **250**(3-4): p. 355-360.

21. Maus, M., M. Cotlet, J. Hofkens, T. Gensch, F.C. De Schryver, J. Schaffer and C.A.M. Seidel, *An experimental comparison of the maximum likelihood estimation and nonlinear least squares fluorescence lifetime analysis of single molecules.* Analytical Chemistry, 2001. **73**(9): p. 2078-2086.

22. Srisa-Art, M., A.J. deMello and J.B. Edel, *Fluorescence lifetime imaging of mixing dynamics in continuous-flow microdroplet reactors.* Physical Review Letters, 2008. **101**(1).

23. Kollner, M. and J. Wolfrum, *How many photons are necessary for fluorescence lifetime measurements.* Chemical Physics Letters, 1992. **200**(1-2): p. 199-204.

24. Edel, J.B., J.S. Eid and A. Meller, *Accurate single molecule FRET efficiency determination for surface immobilized DNA using maximum likelihood calculated lifetimes.* Journal of Physical Chemistry B, 2007. **111**(11): p. 2986-2990.

25. Edel, J.B., E.K. Hill and A.J. de Mello, *Velocity measurement of particulate flow in microfluidic channels using single point confocal fluorescence detection.* Analyst, 2001. **126**(11): p. 1953-1957.

26. Hertzog, D.E., B. Ivorra, B. Mohammadi, O. Bakajin and J.G. Santiago, *Optimization of a microfluidic mixer for studying protein folding kinetics.* Analytical Chemistry, 2006. **78**(13): p. 4299-4306.

27. Yao, S. and O. Bakajin, *Improvements in mixing time and mixing uniformity in devices designed for studies of protein folding kinetics.* Analytical Chemistry, 2007. **79**(15): p. 5753-5759.

28. del Campo, A. and C. Greiner, *SU-8: a photoresist for high-aspect-ratio and 3D submicron lithography.* Journal of Micromechanics and Microengineering, 2007. **17**(6): p. R81-R95.

CHAPTER 3
HYDRODYNAMIC FOCUSING WITHIN MICROFLUIDIC CHANNELS

3.1. Introduction

In order to achieve single molecule detection or to minimise the sample consumption, the concentrations used in a variety of microfluidics applications are typically in the nM and pM range. Under such dilute conditions, it is vital to ensure that the majority of the sample molecules traverse the probe volume and are subsequently detected. To ensure that the latter occurs, several techniques including hydrodynamic and electrodynamic focusing (for charged particles or molecules) have been proposed [1-4]. The benefit of confining the sample under investigation within a narrow focused stream can be simply illustrated as shown in figure 3.1.

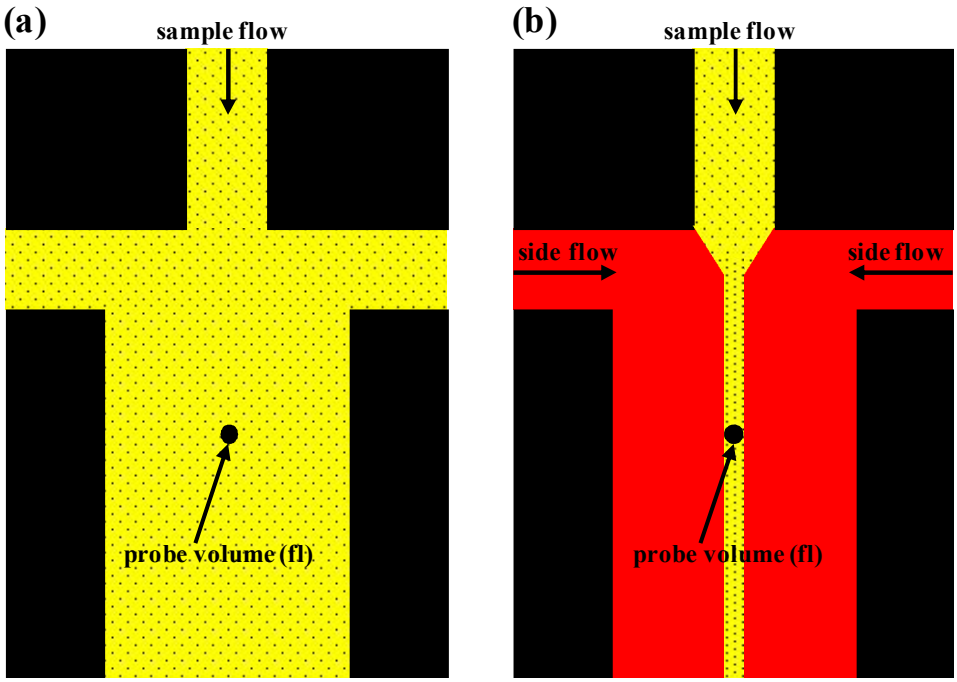

Figure 3.1. (a) No focusing is employed and the majority of the sample molecules are not detected. (b) By employing hydrodynamic focusing the sample is confined to a narrow stream with dimensions comparable to the probe volume width. This way, the majority of the sample molecules are forced through the detection volume and the detection efficiency is improved.

Typical probe volume dimensions are no larger than 1 µm in width [5]. Assuming a sample flowing within a channel which is tens of micrometres in width, it is clear that the majority of

the sample travels the length of the channel without being detected (figure 3.1a). In contrast, when focusing is employed, the sample is confined to a narrow stream with similar width to that of the probe volume [6] (figure 3.1b). This confinement results in higher molecule detection efficiency [7]. Considering the limitations of standard photolithographic techniques and the technical complications of fabricating channels with dimensions below 10 μm, employing focusing as opposed to further downsizing the microfluidic device is highly advantageous.

In a typical experiment employing hydrodynamic focusing, the sample is introduced in the central inlet of a 3-inlet 1-outlet microfluidic device [8]. The side inlet flows normally consist of a solvent or control solution and are used for 'squeezing' the central flow into a narrow stream. By varying the side inlet flow rate the dimensions of the focused stream can be controlled and adjusted so that they are comparable to the dimensions of the detection volume. This results in a larger portion of the sample under investigation flowing through the detection volume, resulting in improved detection efficiency.

Hydrodynamic focusing has been widely used in a variety of bioanalytical applications to ensure that the majority of the molecules contained in the sample are screened, hence the molecular detection efficiency is increased [9, 10]. The combination of hydrodynamic and electrodynamic focusing has been reported to yield a signal-to-noise ratio enhancement of a factor of 2, with corresponding improvements in both mass and concentration detection limits and a 3-fold increase in detection efficiency [2]. The addition of a suitable polymer with high molecular weight to the sheath stream has been proposed as means to reduce diffusional defocusing of the central stream due to the formation of a slowly diffusing complex between a small analyte molecule and the polymer [11]. Hydrodynamic focusing has been extensively used in flow cytometry in order to perform high throughput DNA fragment detection and sizing, with low sample consumption and high detection efficiency [12-16]. An improvement in the detection rate from 40-60 fragments per second to thousands of fragments per second was achieved by increasing the analyte flow rate and simultaneously monitoring multiple detection volumes within the focused stream using a CCD camera [17]. A variety of miniaturized flow cytometers employing either two- or three-dimensional hydrodynamic focusing can be fabricated using micromachining techniques [18] and used for numerous applications, including enumeration, size differentiation and sorting of particles, particle agglomerates and cells [3, 19, 20].

Prior to employing hydrodynamic focusing in experiments with sensitive and usually valuable biological samples, it is important to characterize the focusing behaviour of the microfluidic

devices. In the experiments outlined below, either a fluorescent dye and buffer or two fluorescence dyes with significantly different fluorescence lifetimes were introduced into the central and side inlets respectively. FLIM was used to image the outlet channel and monitor the width of the resultant focused stream whilst varying the inlet flow rates. FLIM was preferred to fluorescence intensity imaging, as it overcomes the artefacts arising from intensity measurements, such as edge effects and brightness variations occurring at solution interfaces (more detail in section 3.3.3).

3.2. Experimental description and methodology

3.2.1. Chemicals

Fluorescein (Fsc), rhodamine 110 chloride (Rd110) and acridin orange hydrochloride hydrate (AcrOr) were purchased from Sigma-Aldrich. All samples were prepared in phosphate buffer pH 7.0 (Fluka) with the use of de-ionized water (18 MΩ). The solutions were filtered with 0.2 μm syringe filters (Pall Corporation, UK) before being delivered into the channels to ensure sample homogeneity and to avoid device blockage. The fluorescence lifetimes of Fsc, Rd110 and AcrOr are approximately 4 ns, 4 ns and 2 ns respectively (provided by the supplier), the accurate lifetime values, however, were experimentally determined using the current optical arrangement and analysis method.

3.2.2. Chip design

The microfluidic chip design used for the majority of the hydrodynamic focusing experiments is shown in figure 3.2a. This was a simple 3-inlet 1-outlet device, where the central-to-side inlet width ratio was 1:1.6 and the central inlet-to-outlet width ratio was 1:6 [21]. Three sizes of this device, I, II and III, were tested. The channel widths in devices II and III were approximately 1.5 and 2 times, respectively, the corresponding widths in device I. More specifically, the central inlet width in design I was 11 μm, the side inlet width was 17.5 μm and the outlet width was 65.5 μm. For devices II and III these dimensions were 15.5 μm, 25 μm, 93 μm and 22 μm, 35 μm, 131.5 μm respectively. All the channels were 50 μm deep.

Measurements were also performed using the chip shown in figure 3.2b. In this design, all inlets and outlet had the same width of 14.5 μm and the channel depth was approximately 15 μm. In addition, nozzles were introduced at the channel junction in order to further decrease the focused stream width [21, 22]. The nozzle width was approximately 8.5 μm. Detailed dimensions of all designs can be found in appendix A (figure A.1 and figure A.2).

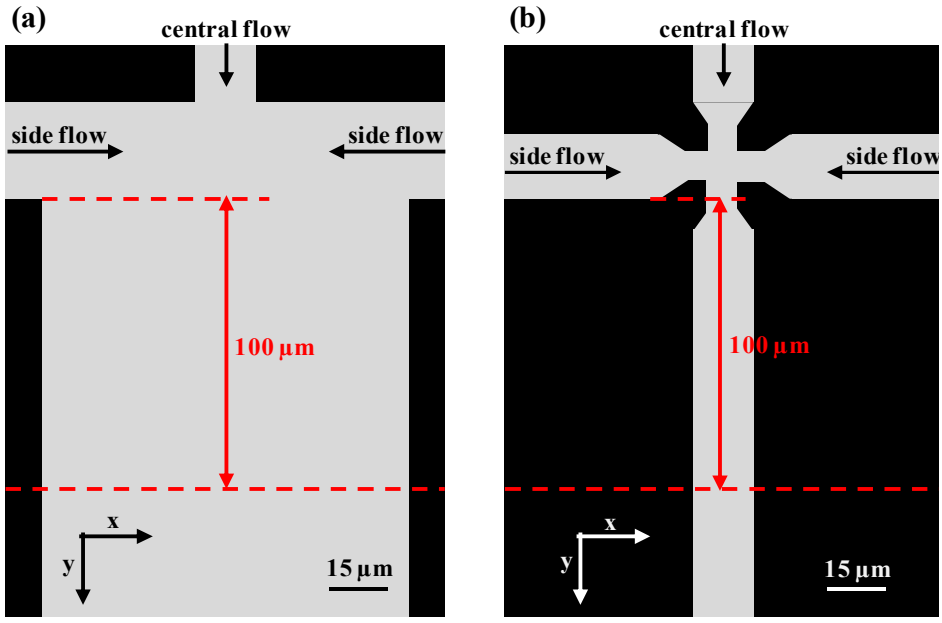

Figure 3.2. The junction area of the chip designs used for the hydrodynamic focusing experiments. The focusing width was measured at 100 µm in the direction of the flow from the side inlet-outlet intersection (y-plane indicated by the lower red dashed line).

3.2.3. Experimental procedure

Two separate syringe pumps were used to deliver the samples into the channels to allow for the analyte and sheath flow rates to be varied individually. The same pump was used for both side inlets to ensure identical flow rates and, thus, focusing symmetry. At first, measurements were performed under constant side-to-central inlet flow rate ratio, while varying the central and side inlet flow rates. The majority of the measurements were then performed under constant central inlet flow rate for different side-to-central inlet flow rate ratios. As found by trial and error, the range of flow rates used was between 0.05-10 µl/min depending on the chip design.

Fluorescent dye excitation was achieved using excitation path 1 along with the LDH-P-C-470 pulsed diode laser (see section 2.1.1.1). Fsc, Rd110 and AcrOr exhibit absorption maxima at 490 nm, 497 nm and 502 nm respectively, therefore the excitation line resulted in approximately 50% photon absorption (figure 3.3). In order to obtain sufficient photon emission for accurate results, the dye concentrations used were in the order of µM.

During the hydrodynamic focusing experiments, the laser spot was positioned approximately at the intersection of the inlet channels and 512×512 pixel x-y scans were performed. Using the 60x objective, this corresponded to an imaged area of 235×235 μm^2. Photon arrival data acquired with the TimeHarp 200 TTTR mode were processed as described in section 2.3.3 to provide fluorescence lifetime maps. The minimum number of photons per pixel for the MLE

routine was set to 10. Rose bengal in phosphate buffer pH 7.0 was used for determining the IRF. The focusing width was measured at 100 µm in the direction of the flow from the lower wall of the side inlet channel (figure 3.2).

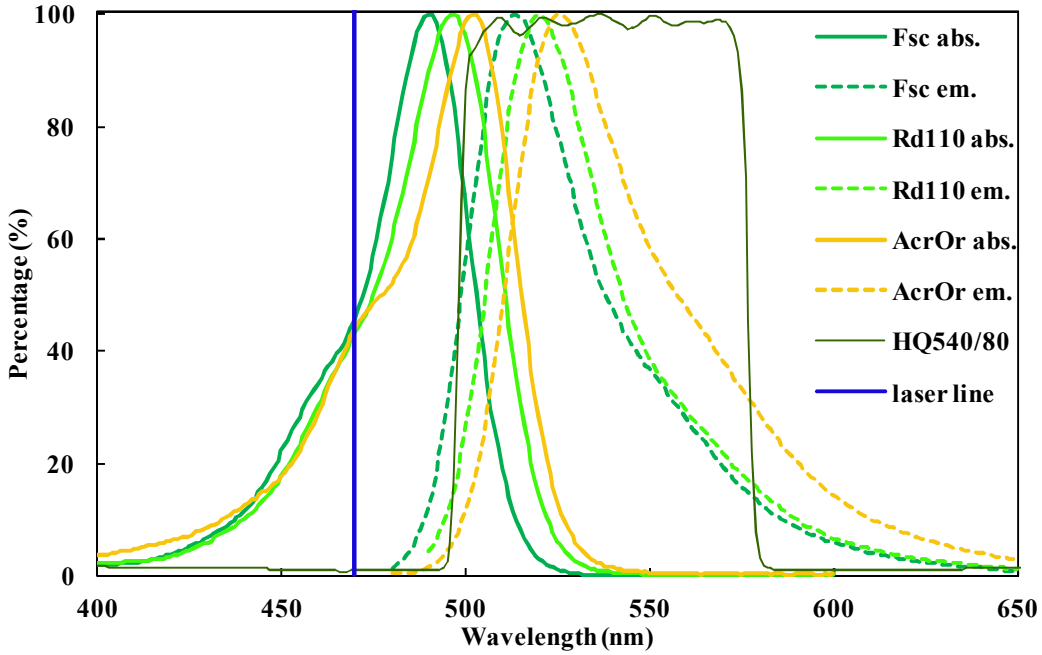

Figure 3.3. Fsc, Rd110 and AcrOr absorption (solid lines) and emission (dashed lines) spectra. The y-axis represents normalised absorption/emission. The 466 nm laser excitation line is shown in blue and the transmission spectrum of the HQ540/80 emission filter is shown in dark green.

3.2.4. Dye selection

Initial experiments were performed by pumping 100 µM Fsc into the central inlet, while the side flow consisted of plain phosphate buffer pH 7.0. In these experiments, only the focused stream could be visualized as the buffer yielded no fluorescence (figure 3.4a). Thus, it was not possible to discriminate with certainty between buffer regions and regions with insufficient photons for the MLE analysis (10 photons), as in both cases the pixels appeared the same (dark). In addition, although the chip was firmly mounted on the microscope stage, changing the solution flow rate often led to slight displacement of the device from its original position. In order to increase contrast and to achieve higher accuracy in terms of the exact location where the focusing width was measured (100 µm from the side inlet-outlet intersection), it was important to enable visualization of both analyte and sheath flows. By using fluorescent samples with significantly different lifetimes in the central and side inlets, focused stream boundaries and channel edges could be clearly determined on each image individually.

For this purpose, the buffer in the side inlets was replaced by 200 µM AcrOr (lifetime ~2 ns), this dye combination however was not successful. Hydrodynamic focusing could not be

observed and quantified, as the interface between the two dyes appeared non-fluorescent (figure 3.4b). Furthermore, significant blockage of the outlet channel occurred and gradually progressed towards the junction, entirely obstructing the flow. This was possibly due to quenching effects or other interactions between the dyes causing a decrease in fluorescence or non-fluorescent side products.

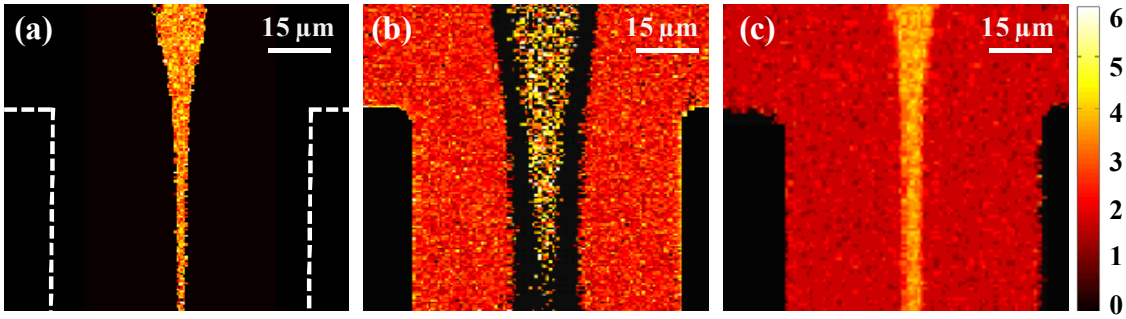

Figure 3.4. Fluorescence lifetime images of hydrodynamic focusing acquired for central and side inlet flows consisting of (a) Fsc and buffer (b) Fsc and AcrOr (c) Rd110 and AcrOr. Estimated channel walls in (a) are defined by the white dashed line. The colourbar represents fluorescence lifetimes in ns.

Therefore, Fsc was replaced by 10 µM Rd110, which possesses a similar lifetime (~4 ns) and was proved to be compatible with AcrOr (figure 3.4c). Accurate fluorescence lifetime values for these dyes were determined by processing TimeHarp200 data using *Jlife* (see section 2.3.2). The extracted lifetimes were 3.8 ns (χ_R^2=0.95) and 1.8 ns (χ_R^2=1.1) for Rd110 and AcrOr respectively (figure 3.5).

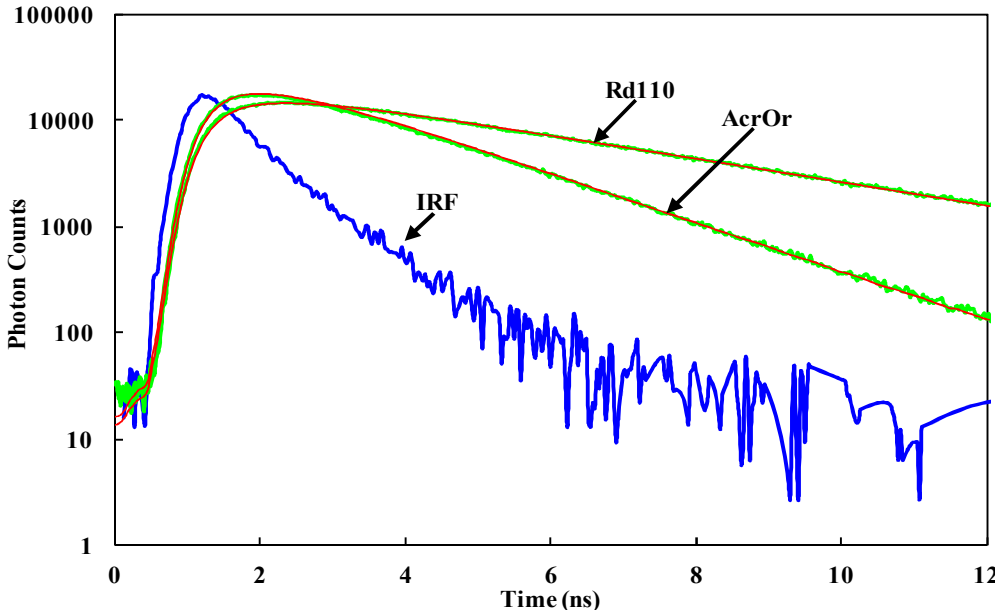

Figure 3.5. Measured fluorescence decay (green) and mono-exponential fit (red) for Rd110 and AcrOr. The two dyes exhibit clearly distinct fluorescence lifetimes of 3.8 ns and 1.8 ns respectively. The IRF (rose bengal) is shown in blue.

3.2.5. Flow profile within microchannels

At all times it was important for the flow within the microchannels to remain laminar. This was needed to ensure stable flow and to avoid turbulent mixing. For channel dimensions on the order of tens of micrometres and flow velocities on the order of millimetres per second the Reynolds number for aqueous samples is given by:

$$R_e = \frac{\rho v d_1}{\mu} \approx 10^{-2} \tag{3.1}$$

where ρ and μ are the density and viscosity of water respectively, v is the average flow velocity and d_1 is the characteristic channel dimension, related to the channel cross section area and the total wetted perimeter. As transition to turbulent flows occurs at Reynolds numbers above 2300, it is clear from equation 3.1 that the Reynolds numbers on the order of 10^{-2} obtained herein resulted in laminar flow within the microchannels.

In the case of pressure-driven flow within a rectangular microchannel, a velocity gradient is established between the centre and the walls of the channel due to friction forces. As a result, a parabolic velocity profile is formed across the outlet channel width described by the Poisseuille equation [6, 23-26]. The liquid flows faster in the centre of the channel, at an average velocity which depends on the aspect ratio $\varepsilon=h/w_o$, where h and w_o are the outlet height and width respectively (figure 3.6) [6, 26].

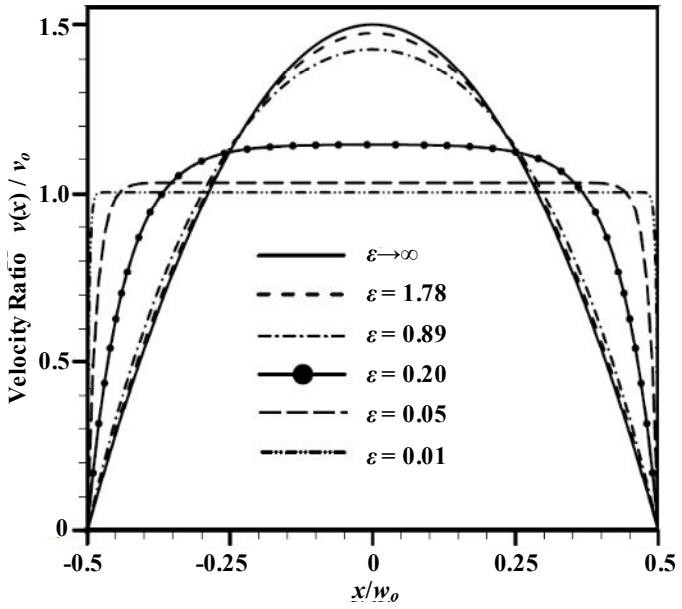

Figure 3.6. Flow velocity profile across the outlet channel width for rectangular microchannels with different aspect ratios $\varepsilon=h/w_o$ (h and w_o are the outlet channel height and width respectively). The x-axis represents the ratio of the position x along the outlet channel width to the outlet channel width w_o. The velocity ratio (y-axis) is the ratio of the flow velocity at position x across the outlet width to the average outlet velocity v_o. Adapted with permission from [26], copyright 2006, IOP Publishing Ltd.

For the devices used herein, the aspect ratio ε was 0.76, 0.54, 0.38 and 1.03 for designs I, II, III and the design with the nozzles respectively. Hence, the expected velocity at the centre of the focused stream was between approximately 1.2 and 1.5 times the total outlet flow velocity.

3.2.6. Focused stream width theoretical analysis

According to the principle of mass conservation for the simple chip design shown in figure 3.7, the total amount of liquid flowing through the outlet channel is equal to the total amount of fluid supplied at the central and side inlet channels. Moreover, the amount of sample introduced into the central inlet equals the amount of fluid constituting the focused stream.

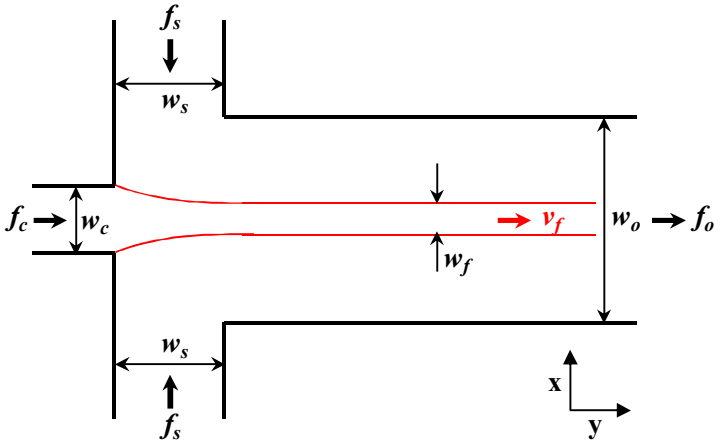

Figure 3.7. Schematic representation of symmetric hydrodynamic focusing within a simple microfluidic device. *v*, *w* and *f* correspond to average flow velocity, channel width and volumetric flow rate respectively. Subscripts *c*, *s*, *o* and *f* denote central inlet, side inlet, outlet and focused stream respectively. Reproduced with permission from [26], copyright 2006, IOP Publishing Ltd.

The above can be expressed in mathematical terms via equation 3.2 (mass conservation).

$$v_o \times w_o \times h = f_c + 2f_s \qquad \text{and} \qquad f_c = v_f \times w_f \times h \tag{3.2}$$

where *v*, *w* and *f* represent average flow velocities, channel widths and flow rates respectively and the subscripts *c*, *s*, *o* and *f* denote central inlet, side inlet, outlet and focused stream respectively. The channel height *h* is the same for all inlets and outlet. By solving equation 3.2 the width of the focused stream w_f is given by:

$$w_f = \frac{v_o}{v_f} \times \frac{f_c}{f_c + 2f_s} \times w_o = \frac{w_o}{\frac{v_f}{v_o} \times \left(1 + 2\frac{f_s}{f_c}\right)} = \frac{w_o}{\gamma \times (1 + 2\alpha)} \tag{3.3}$$

where γ is the ratio v_f/v_o, which depends on aspect ratio ε ($\varepsilon = h/w_o$) and can be extracted by velocity profile measurements similar to those shown in figure 3.6 [26], and α is the side-to-

central inlet flow rate ratio f_s/f_c. According to equation 3.3, the focusing width can be adjusted by varying either the channel dimensions or the flow rate ratio α for a specified chip design and size.

3.2.7. Focused stream width determination

In order to quantify the hydrodynamic focusing within the microfluidic devices, the width of the focused stream was measured down the outlet channel at a distance of 100 μm from the intersection of the side inlet channels and the outlet. A custom-written Matlab algorithm was developed for this purpose.

In the experiments whereby the central and side inlet flows consisted of Fsc and buffer respectively, only the Fsc stream could be imaged. Therefore, an image of the chip filled with Fsc was acquired in order to determine the side inlet-outlet intersection and to extract the exact channel dimensions (figure 3.8a). The Matlab algorithm firstly plotted the fluorescence lifetimes along the y-axis (direction of the flow) at pixel position x=5 (figure 3.8b). The position on the y-axis where lifetime turned to zero was defined as the side inlet-outlet intersection point (figure 3.8b, green line). The fluorescence lifetimes along the x direction (across the outlet channel width) at y=100 μm from the intersection were subsequently plotted (figure 3.8c). A lifetime threshold of 1 ns was applied to determine the outlet channel walls (figure 3.8c, green line) and the channel width was extracted in number of pixels as well as in micrometres according to the pixel dimension (1 pixel≈0.46×0.46 μm^2). The focused stream width at the y position determined above was then calculated in a similar way for various flow rate conditions (figure 3.9).

Figures 3.8 and 3.9 reveal that during the experiment it was likely that the device was displaced from its initial position. More specifically, the chip shown in figure 3.9a appeared to be moved towards the positive y-direction and slightly shifted to the right compared to the initial position shown in figure 3.8a. As a result, the y-position of the side inlet-outlet intersection was changed. The focusing width was determined at 100 μm in the direction of the flow from this intersection, therefore the w_f measurement point was also changed. Although it was observed that the focused stream reached its final width at y-positions significantly lower than the one described above, it was surely preferable to be able to accurately define the channel boundaries and junction location for each image individually. Replacing Fsc and buffer with Rd110 and AcrOr respectively overcame the artefact, as it allowed for simultaneous visualisation of the central and side inlet flows. This way, the position of the junction could be determined for each condition independently.

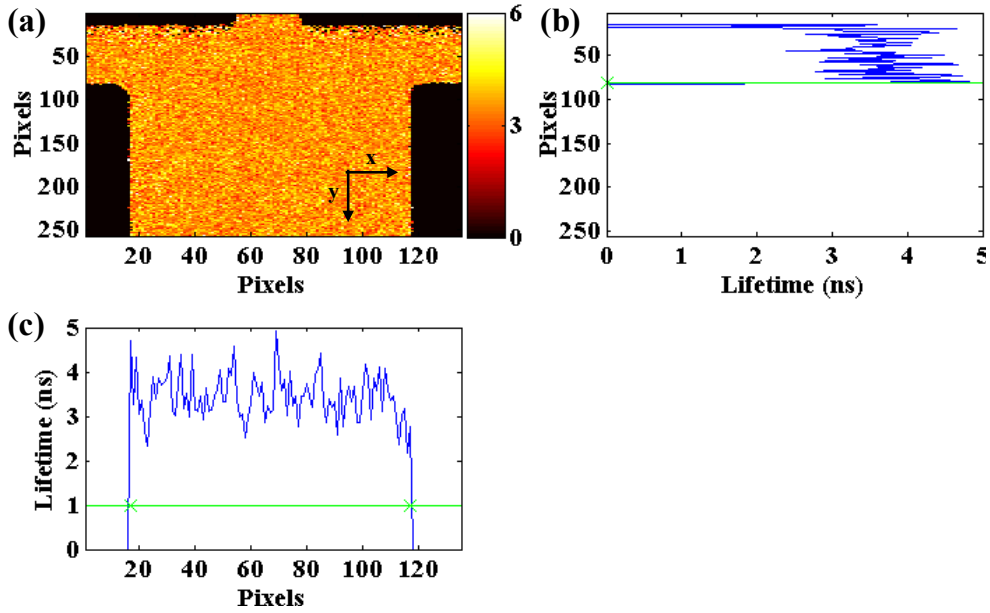

Figure 3.8. Junction position and outlet channel width determination when Fsc and buffer were used for the central and side inlet flows respectively (a) fluorescence lifetime 2-D map, the colourbar represents fluorescence lifetimes in ns (b) the fluorescence lifetime along the y-axis was plotted at pixel position x=5 and the channel intersection was determined (green line) (c) the fluorescence lifetime along the x-axis was plotted at 100 μm from the junction and a lifetime threshold of 1 ns was applied to determine the outlet channel walls (green line).

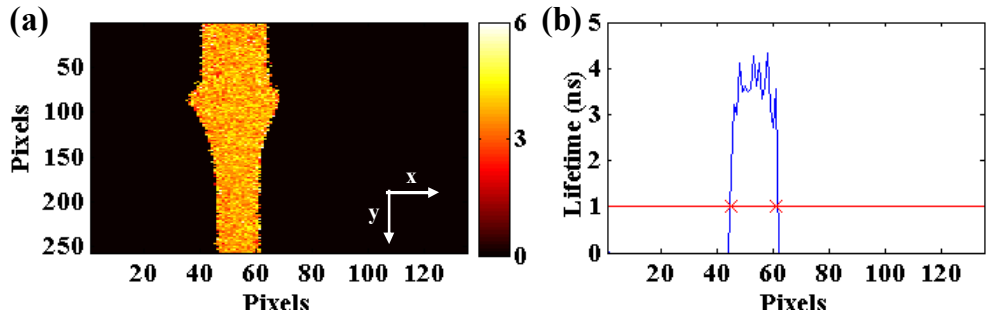

Figure 3.9. Focusing width determination for α=3 when Fsc and buffer were used for the central and side inlet flows respectively (a) fluorescence lifetime 2-D map, the colourbar represents fluorescence lifetimes in ns (b) the fluorescence lifetime along the x-axis (across the outlet width) was plotted at 100 μm from the junction and a lifetime threshold of 1 ns was applied to distinguish between the focused stream and buffer (red line).

In experiments whereby the Rd110-AcrOr combination was used, the Matlab code was adjusted in order to process each image individually (figure 3.10). Following side inlet wall determination in a similar way to that described for Fsc and buffer (figure 3.10b), a threshold was applied to distinguish between the central (Rd110) and side (AcrOr) sample flows (figure 3.10c, red line). The threshold was chosen to be 3 ns and was set based on bulk lifetime measurements (section 3.2.4). The number of pixels with fluorescence lifetime above the threshold was finally converted to micrometres representing the focusing width. The outlet channel walls were defined by applying a lifetime threshold of 1 ns (figure 3.10c, green line).

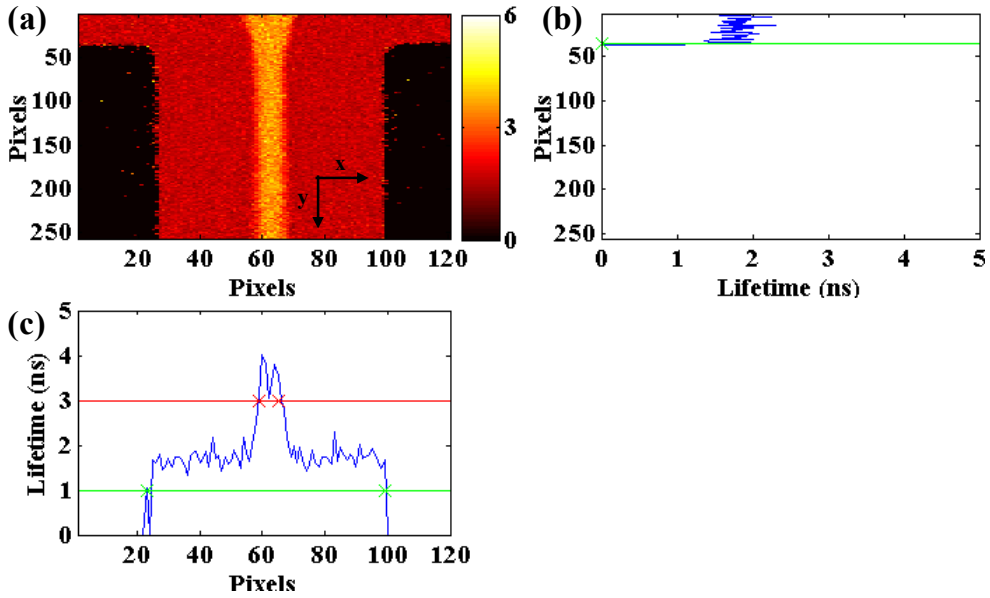

Figure 3.10. Focusing width determination for α=3 when Rd110 and AcrOr are used for the central and side inlet flows respectively (a) fluorescence lifetime 2-D map, the colourbar represents fluorescence lifetimes in ns (b) the fluorescence lifetime along the y-axis was plotted at pixel position x=5 and the channel intersection was determined (green line) (c) the fluorescence lifetime along the x-axis was plotted at 100 µm from the junction and a lifetime threshold of 1 ns was applied to determine the outlet channel walls (green line); the focused stream width was determined by applying a lifetime threshold of 3 ns to distinguish between Rd110 and AcrOr (red line).

3.3. Results and Discussion

3.3.1. Focused stream width

3.3.1.1. Focusing width measurements under constant flow rate ratio α

The width of the focused stream does not depend on the applied flow rates but rather on the ratio α of the side inlet flow rate to the central inlet flow rate [8]. This can be easily concluded by equation 3.3. For a device with specific channel dimensions (γ and w_o constant), the only factor controlling the focused stream width w_f is ratio α. The independence of the focusing width on the absolute central and side inlet flow rates is illustrated in figure 3.11 whereby very similar images were acquired for different values of f_s and f_c but the same ratio α.

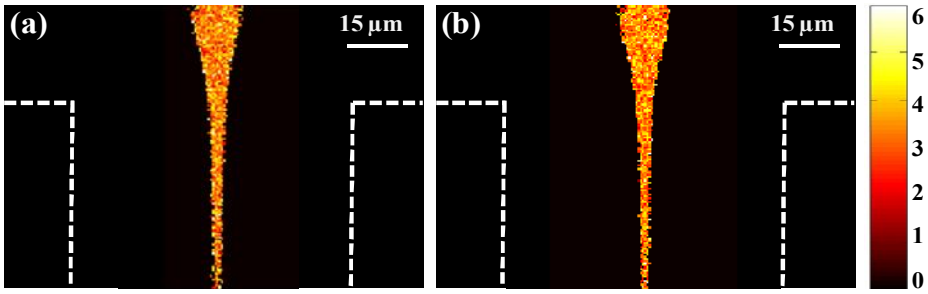

Figure 3.11. Very similar fluorescence lifetime images acquired for (a) f_s = 4.5 µl/min, f_c = 0.5 µl/min (b) f_s =9 µl/min, f_c = 1 µl/min. In both cases α=9. The colourbar represents fluorescence lifetimes in ns.

More specifically, measurements were performed using chip design I under constant α of 1, 2, 4 and 8. Figure 3.12 shows the extracted focusing width and percentage of focusing (focusing ratio w_f/w_o) versus central inlet flow rate together with a linear fit (χ_R^2 between 0.975-0.999). As expected, the width of the focused stream remained approximately the same for constant α with only a couple of micrometres deviation (max ±2 μm, ±3%). A small decreasing trend was observed as the total flow rate f_o ($f_o=f_c+2f_s$) increased, which could potentially become negligible by incorporating more data.

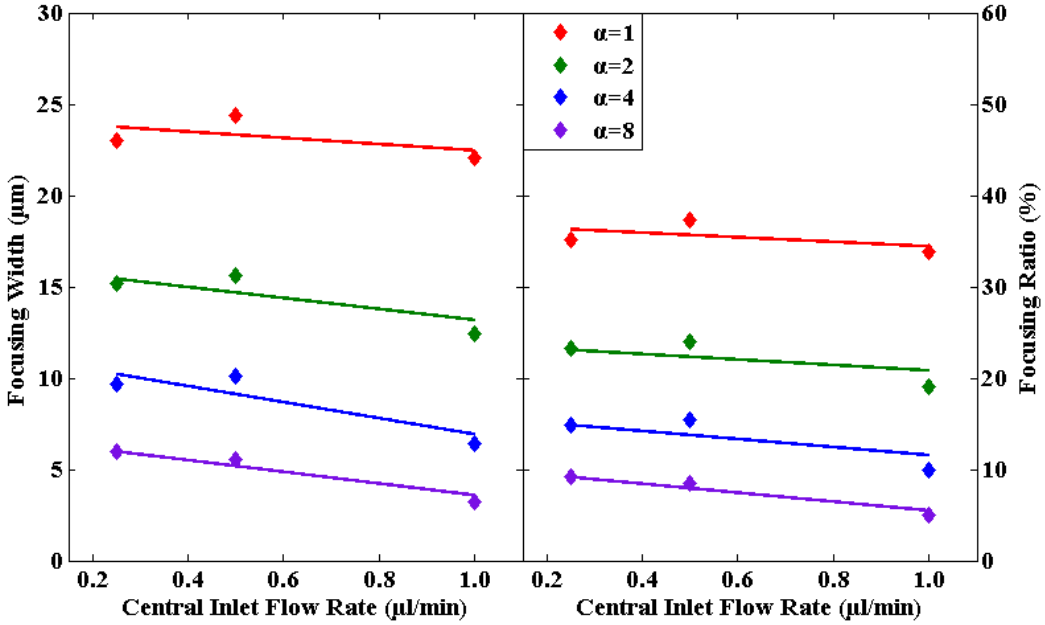

Figure 3.12. Focusing width w_f and focusing ratio w_f/w_o (%) versus central inlet flow rate for constant α=1, 2, 4, 8 in chip design I. w_f and w_f/w_o remained approximately the same for constant α.

3.3.1.2. Focusing width measurements versus flow rate ratio α

According to equation 3.3, the width of the focused stream for a given device depends only on the side-to-central inlet flow rate ratio α, with increasing values of α yielding narrower focusing. Based on equation 3.3, focusing width data versus ratio α can be fitted using an equation of the general form:

$$w_f = \frac{p_1}{p_2 + p_3 \times \alpha} + p_4 \tag{3.4}$$

where parameters p_1, p_2, p_3 and p_4 can be appropriately estimated and adjusted according to the channel geometry.

Chip designs I, II and III

In order to quantify the relationship between the focused stream width and ratio α, the hydrodynamic focusing within devices I, II and III was imaged for a variety of α values. For this purpose, the flow rate of the central inlet was kept constant while the side inlet flow rates were varied to achieve a wide range of ratios α. The choice of the flow rates to be used was based on a series of test measurements depending on the microfluidic device geometry. For design I, measurements were obtained under constant central inlet flow rate of 0.25, 0.5 and 1 µl/min, for design II under constant flow rate of 0.5 µl/min and for design III under constant central inlet flow rate of either 0.5 or 1 µl/min. The side inlet flow rate was adjusted according to the desired value of α and the design used. f_s varied between 0.05-10 µl/min.

In pressure-driven flows within microchannels α can take values between a minimum α_{min} and a maximum α_{max} which depend solely on the channel geometry [8]. For flow rates yielding an α value below α_{min} the sample delivered in the central inlet begins to enter the side channels resulting in a loss of focus. The reverse occurs for values of α above α_{max}. The α_{min} and α_{max} limiting values can be theoretically estimated by using a simple circuit model to describe hydrodynamic focusing (figure 3.13) [8].

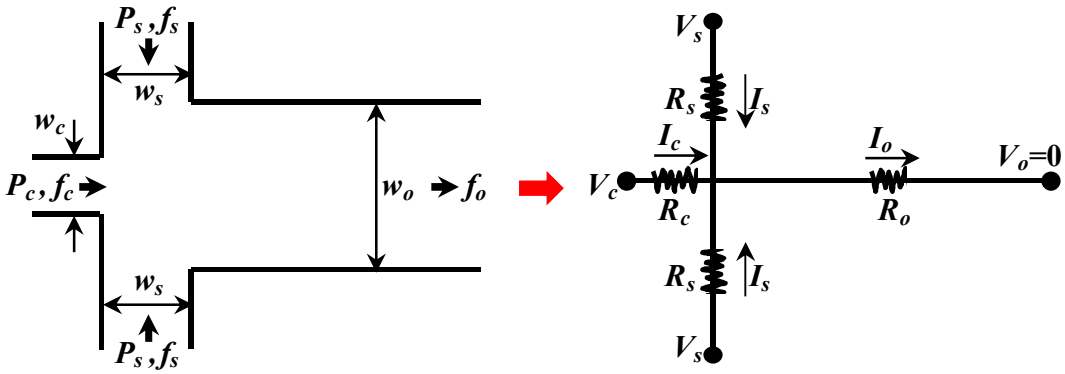

Figure 3.13. Microfluidic device and corresponding circuit. *P*: pressure, *f*: volumetric flow rate, *w*: channel width, *R*: resistance, *V*: potential, *I*: current. Indexes *c*, *s*, and *o* correspond to central inlet, side inlet and outlet respectively. The relationship between *P* and *f* is a hydrodynamic analogue to Ohm's law and the fluidic resistance for each channel can be calculated from the channel geometry.

Provided that the flow is laminar and the channel width is negligible compared to the channel length, the fluidic flow can be mapped to a network of resistors, whereby pressure (*P*) and volumetric flow rate (*f*) correspond to electric potential (*V*) and current (*I*) respectively. The relationship between flux and pressure is a hydrodynamic analogue to Ohm's law and the fluidic resistance *R* for each channel can be calculated by [27, 28]:

$$R = \frac{d_2 \mu \ell}{wh} \quad \text{with} \quad d_2 = 12 \times [1 - \frac{192h}{\pi^5 w} \tanh\left(\frac{\pi w}{2h}\right)]^{-1} \tag{3.5}$$

where w, h and ℓ are the channel width, height and length respectively. α_{min} and α_{max} limits can be extracted by solving the circuit for I_s=0 and I_c=0 respectively. The theoretically estimated α_{min} and α_{max} values for the devices used herein were 0.04 and 17.9, 0.06 and 13.4, 0.08 and 10.0 for designs I, II, III respectively. The upper α limits were in very good agreement with the experimentally observed values (~18, 12, 10 for designs I, II, III respectively), while the lowest α used was 0.1 due to flow stability issues occurring for α<0.1.

Examples of fluorescence lifetime images showing hydrodynamic focusing within microfluidic design II for α=0.1-12 are shown in figure 3.14. Linear flow velocities of the focused stream were calculated taking into account the outlet channel total volumetric flow rate and dimensions as well as the parabolic velocity profile. For the chip design II shown in figure 3.14, the focused stream over total outlet flow velocity ratio was estimated to be approximately 1.35, therefore the calculated focused stream linear flow velocities varied between 2.9-60.5 μm/ms for α=0.1-12 respectively. For these velocities, the time lapse between the intersection of the channels and the focusing width measurement point (100 μm distance) reduced from approximately 34.4 ms to 1.7 ms (for α=0.1 to α=12), while the total outlet imaged area (~225 μm) corresponded to ~77.5-3.7 ms, for α=0.1-12 respectively. Obviously, these values were different for chip designs I and III as well as for varying the central inlet flow rate.

Under the flow rate conditions mentioned above, the width of the focused stream was extracted as described in section 3.2.7. The dependence of the focusing width on ratio α for channel designs I, II and III is presented in figure 3.15. Data were fitted using the general form described by equation 3.4. Parameters p_1-p_4 were estimated according to the outlet channel dimensions and careful adjustment of their upper and lower limits yielded χ_R^2 values between 0.975-0.999 for all fits.

For all chip designs, a strong dependence of the focusing width with respect to ratio α was observed for values up to α≈3. A slight increase in α within this region resulted in a significant narrowing of the focused stream. The largest decrease in w_f was observed for design III. The same trend continued up to a value of α≈6, while increasing α beyond 6 did not have a significant effect on the width of the focused stream.

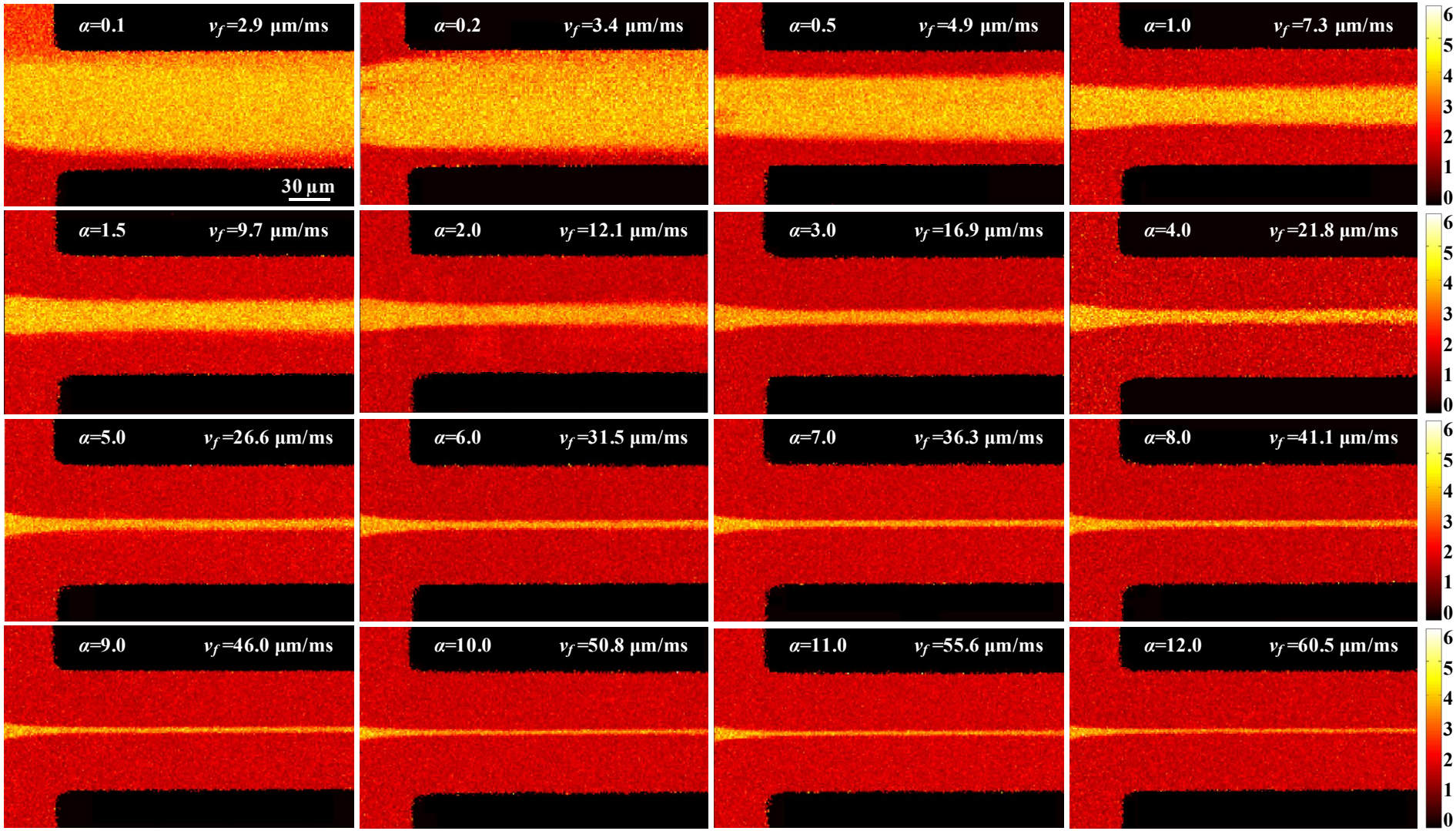

Figure 3.14. Fluorescence lifetime maps showing hydrodynamic focusing within microchannels (chip design II). The central and side inlet flows consisted of Rd110 and AcrOr respectively. Flow rate ratio α varied from 0.1-12 (constant f_c = 0.5 µl/min, f_s varied from 0.05-6 µl/min). The linear flow velocity at the centre of the focused stream increased from 2.9 µm/ms to 60.5 µm/ms for α increasing from 0.1 to 12. The colourbar represents fluorescence lifetimes in ns.

As previously shown (figure 3.12), the central inlet flow rate did not affect the focusing width in a particular or significant way when α remained the same. This is clearly demonstrated in figure 3.15 where solid, dotted and dashed lines for the same design nearly overlap.

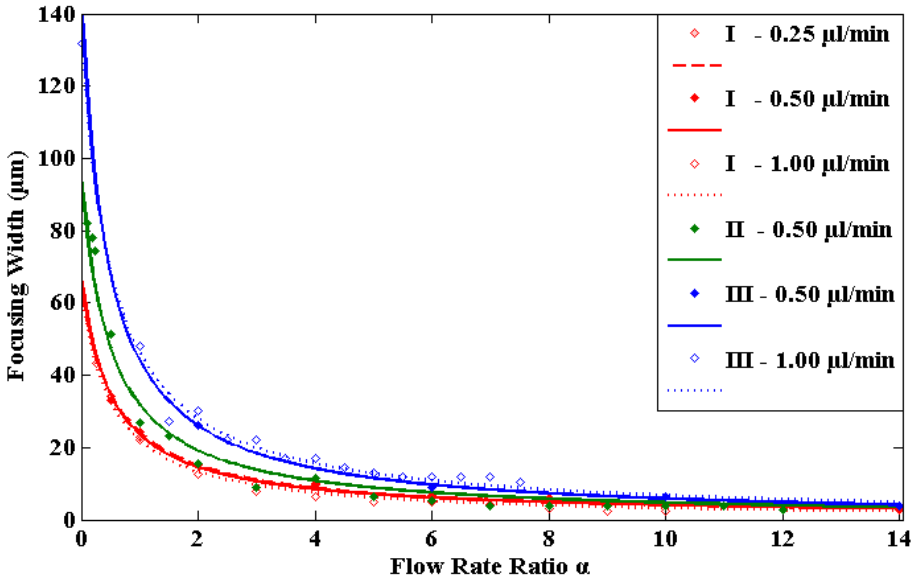

Figure 3.15. Focusing width versus side-to-central inlet flow rate ratio α for chip designs I, II and III and central inlet flow rate of 0.25 µl/min, 0.5 µl/min and 1 µl/min.

As the outlet channel width decreased from 131.5 µm in design III to 93 µm and 65.5 µm in designs II and I respectively (channel height constant at 50 µm), tighter focusing was achieved (figure 3.15). The effect of the outlet channel dimensions on the hydrodynamically focused stream width has been studied by Lee et al., who concluded that smaller normalised focusing width w_f/w_o is obtained for channels with higher aspect ratio ε [26]. For the chips used herein $\varepsilon_{III}<\varepsilon_{II}<\varepsilon_I$, therefore design I was expected to yield narrower focusing.

This is illustrated in figure 3.16 where the focusing width is expressed as a percentage of the outlet channel width. According to equation 3.3, w_f/w_o versus α data was fitted using equation 3.4 (χ_R^2=0.975-0.999). Unlike results presented by Lee at al. which indicated a more significant effect of ε under low ratios α, the largest difference in focusing between designs I, II and III was observed for α>6 (figure 3.16). This was the region where the fits plateaued and the lowest possible w_f/w_o values were obtained. The minimum focusing ratios achieved were 2.1%, 2.7% and 5%, corresponding to focusing width values of 1.4 µm, 2.6 µm and 6.5 µm, for chip designs I, II and III respectively.

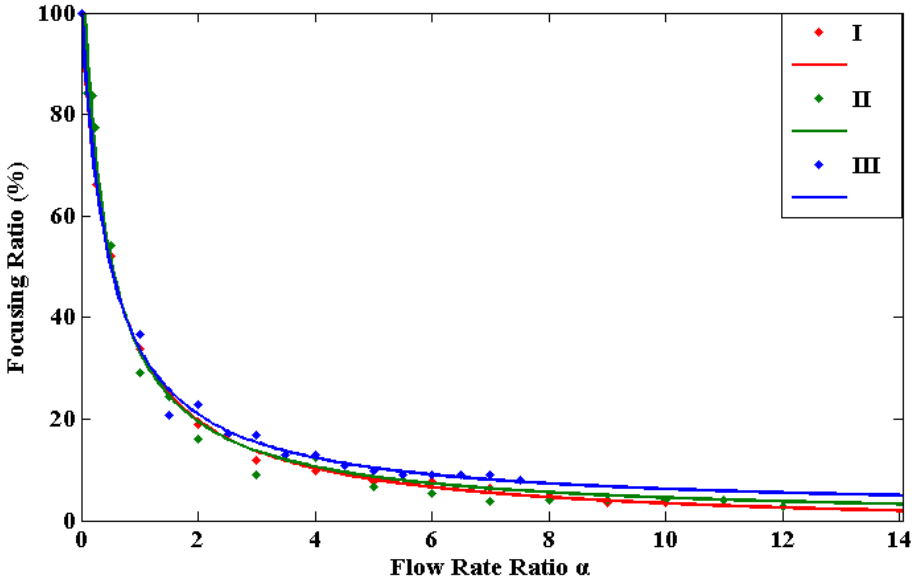

Figure 3.16. Focusing ratio w_f/w_o (%) versus flow rate ratio α for chip designs I, II and III.

Chip design with nozzles

Focusing width versus ratio α measurements were also performed using the improved chip design with smaller channel dimensions and nozzles shown in figure 3.2b [21, 22]. Reducing the dimensions ensured a higher aspect ratio compared to designs I, II and III ($\varepsilon_{nozzle}\approx1.03$ along the outlet channel length). Thus, a significant drop in both the focusing width and focusing ratio was expected for this design. Additionally, the introduction of the nozzles further decreased the channel width at the junction yielding even lower w_f and w_f/w_o values ($\varepsilon_{nozzle}\approx1.76$ at the intersection).

Due to the small dimensions of this design, slower absolute flow rates were used during these measurements to ensure low linear flow velocities within the microchannels. More specifically, the central inlet flow rate was kept constant at 0.20 μl/min, while the side inlet flow rate varied between 0.05-0.35 μl/min yielding ratios α from 0.25 up to 1.75, after which focusing was lost. The experimentally determined α_{min} and α_{max} values were not in very good agreement with the theoretically calculated ones (0.6 and 1.5 respectively), possibly due to the difficulty in accurately determining the fluidic resistance R for the nozzles.

Figure 3.17 shows the extracted focusing width values versus α for the design with nozzles in comparison with w_f obtained in chip design II (without nozzles). The central inlet width in the two chips was approximately the same. The measured focused stream width was much lower for the design with the nozzles as a result of the small dimensions. w_f values of as little as 1 μm were acquired at α=1.75, while an α value of approximately 12 was required to obtain the minimum w_f=2.6 μm in chip design II. This is beneficial in cases where minimizing valuable sample consumption is crucial as small values of α yield lower total volume flow rates.

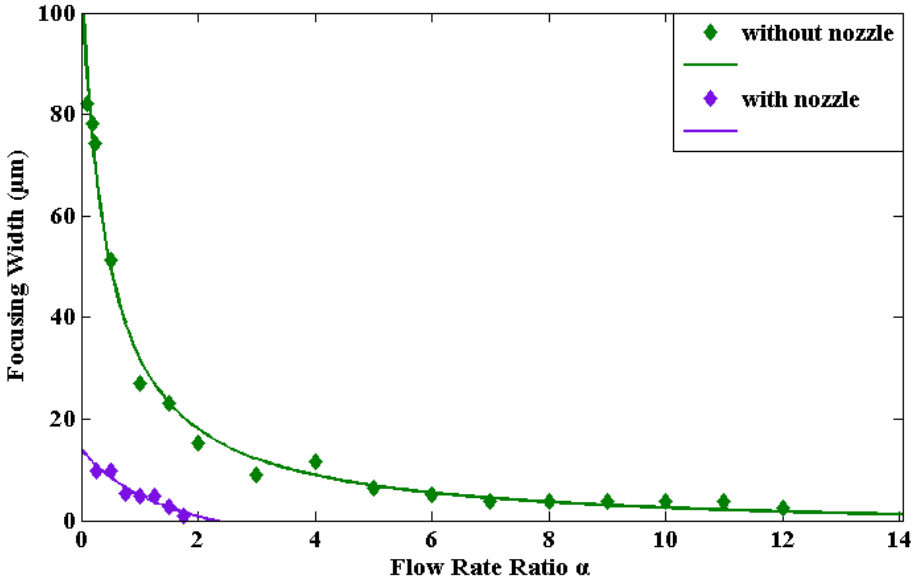

Figure 3.17. Focusing width versus side-to-central inlet flow rate ratio α for design II (green) and for the improved design with smaller dimensions and nozzles (purple).

The benefit of introducing the nozzles becomes more evident in figure 3.18, where the focusing ratio, as opposed to the absolute focusing width, was plotted versus α. The percentage of focusing for the two designs was approximately the same for values up to $\alpha \approx 1$. For $\alpha > 1$ however, the fit corresponding to the design with the nozzles in figure 3.18 (purple line) became much sharper. Thus, significantly tighter focusing was achieved for the same α in the presence of the nozzles. The minimum w_f/w_o obtained using this design was 7.1% (1 μm) for $\alpha_{max}=1.75$.

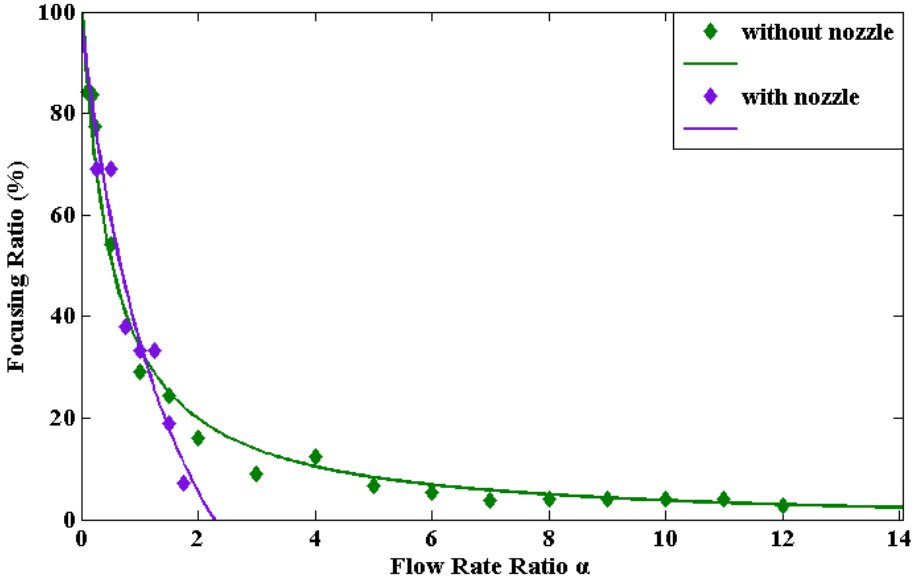

Figure 3.18. Focusing ratio w_f/w_o (%) versus side-to-central inlet flow rate ratio α for design II (green) and for the improved design with smaller dimensions and nozzles (purple).

The importance of achieving tighter focusing at lower ratios α is illustrated in figure 3.19, where the focusing ratio was plotted with respect to the normalised total flow rate $f_{tot,n}$. $f_{tot,n}$ expressed the total sample consumption and equalled $(f_c+2f_s)/f_c$. It was therefore independent of the absolute values of the central and side inlet flow rates and depended only on their ratio α. Based on equation 3.3, w_f/w_o versus $f_{tot,n}$ was fitted using the form:

$$\frac{w_f}{w_o} = \frac{p_1}{p_2 \times f_{tot,n}} + p_3 \tag{3.6}$$

where parameters p_1, p_2 and p_3 were adjusted according to the channel geometry. Figure 3.19 clearly indicates that the nozzle introduction was a significant improvement on the simple design II. In order to obtain a focusing ratio of ~7% in the design with the nozzles, the total sample consumption (all 3 inlets) required was approximately 4.5 times the central inlet flow rate as opposed to the $11.5f_c$ needed to achieve the same focusing performance in chip II (figure 3.19).

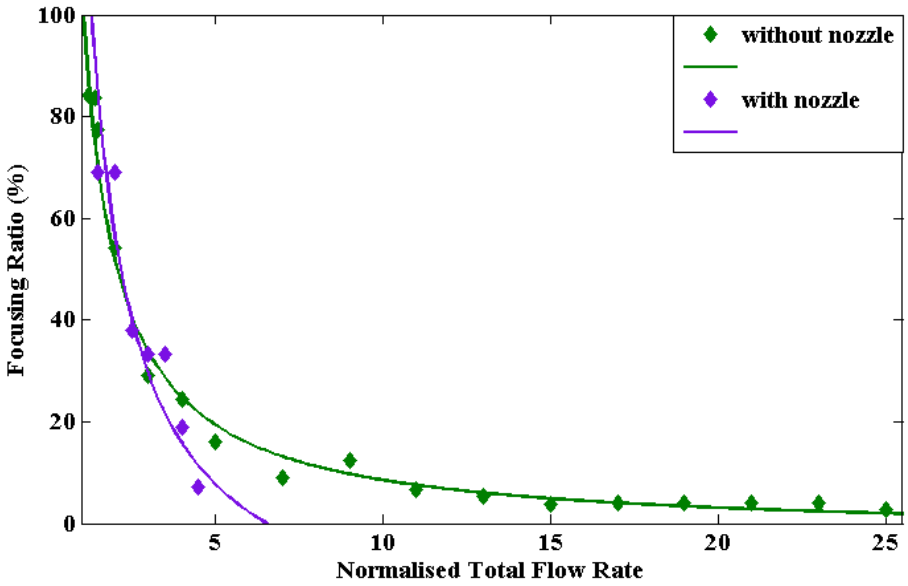

Figure 3.19. Focusing ratio w_f/w_o (%) versus normalised total flow rate $f_{tot,n}$ for chip designs with and without nozzles. w_f/w_o is independent of the absolute outlet channel width and $f_{tot,n}$ is independent of the absolute central and side inlet flow rates. Thus, the improved focusing performance resulted solely from the nozzle introduction.

Despite the benefits of the improved chip tested above, the small dimensions occasionally resulted in the channels being blocked. Bubbles accidentally entering the channels caused unstable flow and resulted in the channels having to be regenerated. With this in mind, in spite of the narrow focusing widths obtained, in following experiments these devices were used with extra care and only when the sample allowed it. Instead, the advantages of introducing the nozzles were exploited by maintaining the chip design but in larger channel scale.

3.3.1.3. Focusing width measurements under constant side inlet flow rate f_s

One of the key factors in experiments employing hydrodynamic focusing is to minimize the sample consumption. In most cases, the molecule under investigation is introduced into the device via the central inlet. Hence, when measurements under a range of ratios α are required, it is preferable to obtain higher values of α, and thus tighter focusing, by reducing the central inlet flow rate under constant side inlet flow rate. f_c is decreased until the α_{max} limit is reached and the ideal flow rate combination for narrow focusing with minimum sample consumption can be determined. When plotting w_f with respect to f_c for constant f_s, equation 3.3 yields a data fitting equation of the following form:

$$w_f = p_1 \times \frac{f_c}{f_c \times 2p_2} + p_3 \tag{3.7}$$

This kind of fits can be seen in figure 3.20 whereby the focusing width and focusing ratio within chip design I were extracted for constant f_s and varying f_c.

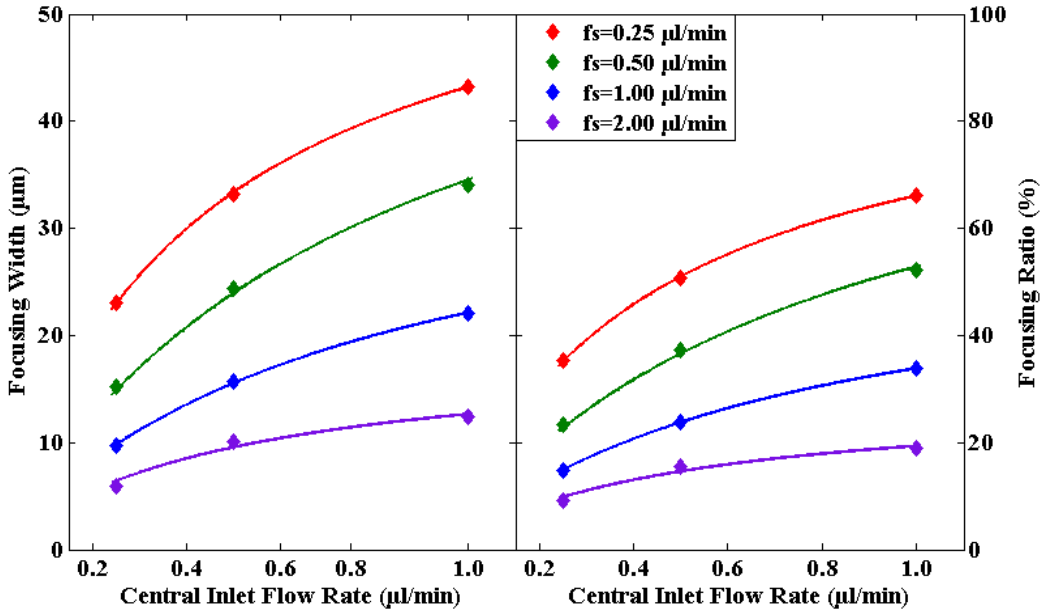

Figure 3.20. Focusing width and focusing ratio w_f/w_o (%) versus central inlet flow rate under constant side inlet flow rate of 0.25, 0.5, 1 and 2 µl/min, using chip design I.

3.3.2. Diffusion from the focused stream

One of the purposes for employing hydrodynamic focusing in experiments is to increase the detection efficiency by forcing as many sample molecules as possible to pass through the detection volume. All images shown in this chapter were acquired using 512×512 pixel scans and 1.12 s per scan. However, in order to successfully detect molecules as they flow down the

length of the outlet channel, the scanning time has to be decreased. This can be achieved by limiting the scanning area to within that of the focused sample stream (figure 3.21).

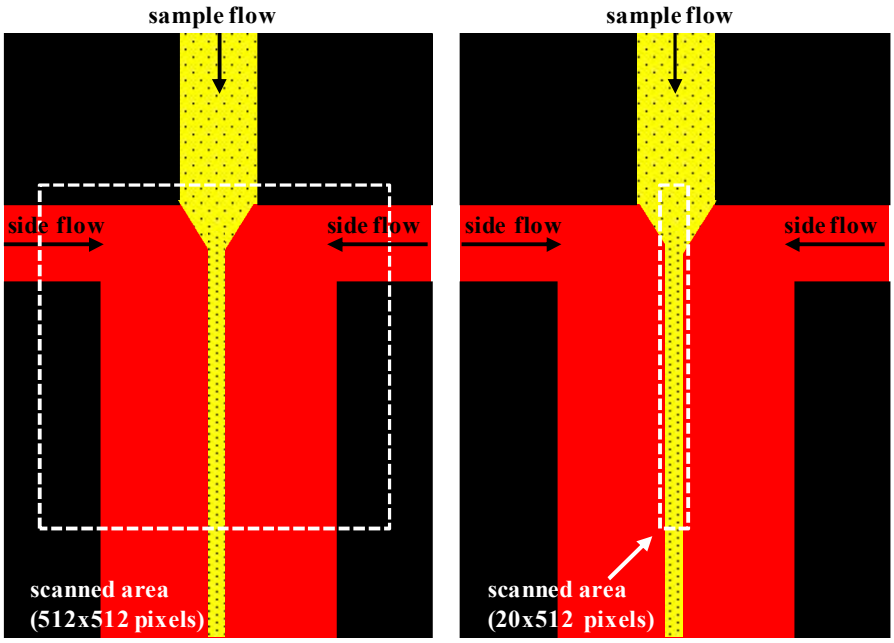

Figure 3.21. By scanning only the area around the focused stream (right) the acquisition time per scan is decreased.

For example, by performing scans of only 20 pixels in the x-direction, corresponding to approximately 9 µm (comparable to the focussed stream width), a scanning rate of approximately 42 µs/line could be achieved. It was therefore important to ensure that the central stream remained focused down the length of the channel, minimizing the loss of molecules escaping out of the scanned area via diffusion.

The distance d that a molecule diffuses in the x-direction at time t is given by:

$$d = \sqrt{2Dt} \qquad \text{with} \qquad D = \frac{kT}{6\pi\eta r} \tag{3.8}$$

where D is the molecular diffusion coefficient usually expressed in cm^2/s, k is the Boltzmann constant, T is the temperature in Kelvin, r the hydrodynamic radius and η is the solvent viscosity. By substituting time t with y/v (v being the flow velocity and y the distance traversed by the molecule in the y-direction), equation 3.8 yields:

$$d = \sqrt{\frac{2Dy}{v}} \tag{3.9}$$

It is obvious that for a given molecule (fixed D), d is affected by flow velocity, which in turn is determined by the flow rates and the channel cross section. In cases whereby diffusion is on the order of hundreds of nanometres, focused streams of only a couple of micrometres are not applicable, as d is comparable to the stream dimension and focusing is rapidly lost.

To demonstrate that the central stream remained focused down the length of the outlet channel, the fluorescence lifetimes along the x-direction were plotted for different distances from the intersection of the side inlet-outlet channels. Observation by eye as well as results shown in figure 3.22 verified that the width of the focused stream remained constant within the scanned area with little observable diffusion occurring.

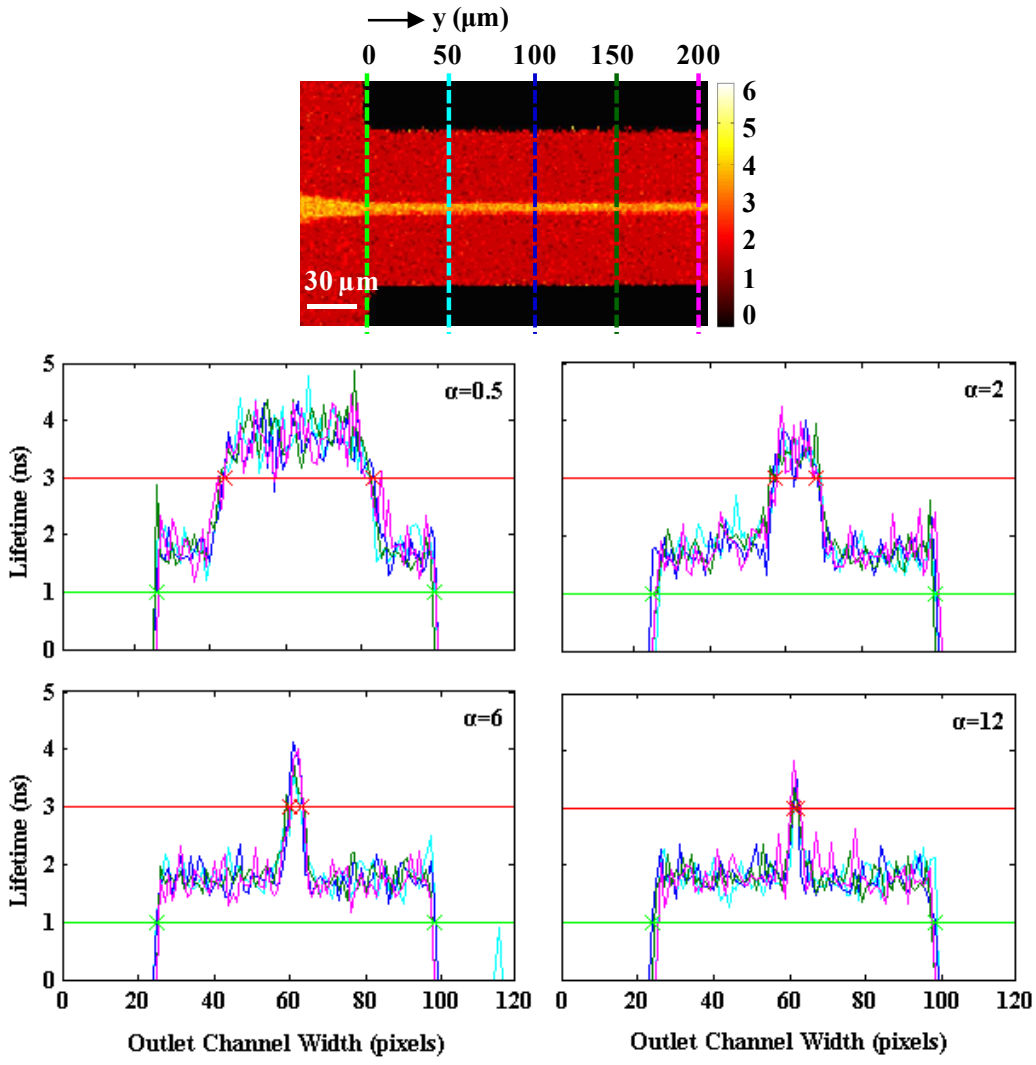

Figure 3.22. The width of the focused stream was measured at distances of 50, 100, 150 and 200 µm from the junction (cyan, blue, green and magenta respectively). Very similar w_f values were extracted along the length of the outlet channel indicating that only little diffusion occurred within the scanned area (α=0.5, 2, 6 and 12). The colourbar represents fluorescence lifetimes in ns.

3.3.3. Imaging method and fluorescence lifetime determination

In order to demonstrate hydrodynamic focusing and characterize the mixing performance of various microchannel designs, nearly all studies to date have used fluorescence intensity measurements [8, 21, 22, 29-34]. As it was previously mentioned (section 1.1.2), although differences in the intensity level allow discrimination amongst fluorescent species, fluorescence intensity is prone to artefacts originating by variations in fluorophore concentration and illumination intensity.

Fluorescence intensity images shown in figure 3.23a illustrate such artefacts. The interface between the flow streams appeared less bright due to changes in dye concentration. Additionally, some areas within the AcrOr flow in figure 23a (right) appeared brighter than the surrounding pixels, possibly due to non-uniform illumination. Unlike intensity measurements, images based on fluorescence lifetime data provided much better discrimination between molecular species eliminating the above artefacts (figure 3.23b).

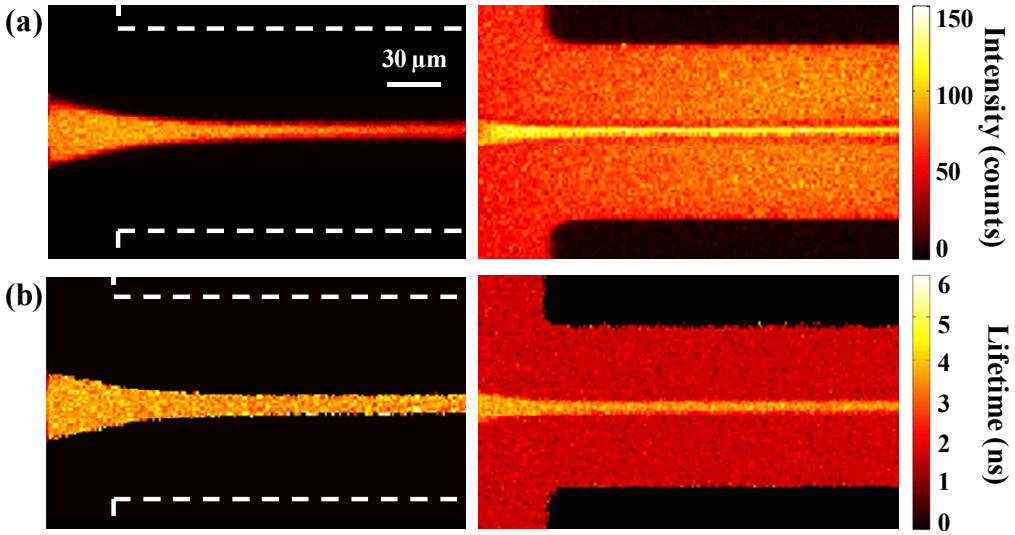

Figure 3.23. (a) Fluorescence intensity and (b) fluorescence lifetime images produced with central and side flows consisting of Fsc and buffer (left) or Rd110 and AcrOr (right). Intensity image artefacts due to changes in fluorophore concentration and non-uniform illumination are eliminated in the lifetime images.

In addition, a common for all images threshold was applied to easily distinguish between the two dyes (section 3.2.7), thus, an accurate determination of the focused stream width was facilitated (figure 3.24b). On the contrary, setting an appropriate intensity threshold was problematic (figure 3.24a). Occasionally, a number of repeats were required before a suitable threshold was selected and images often had to be handled individually in order to obtain accurate results.

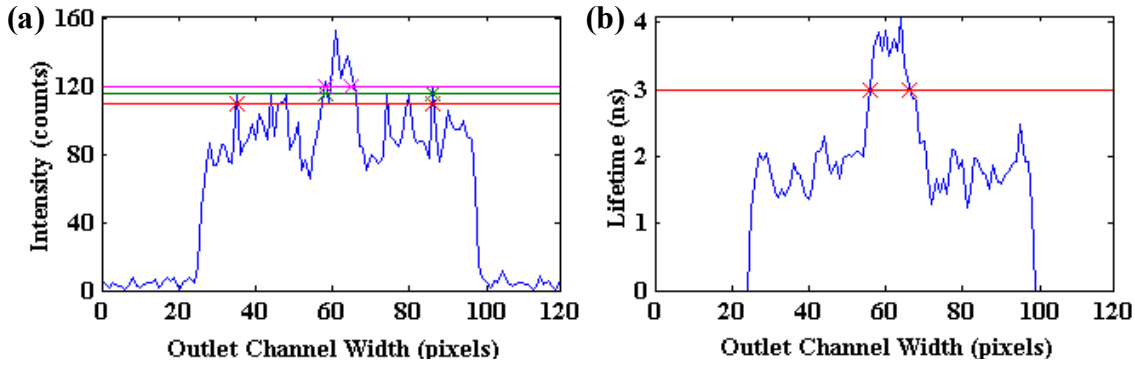

Figure 3.24. (a) Fluorescence intensity and (b) fluorescence lifetime plots across the outlet channel width at a distance of 100 μm from the junction, for α=2. A threshold of 3 ns was applied to the lifetime data to easily distinguish between the two dyes. On the contrary, for intensity measurements the threshold choice was problematic. Three different thresholds of 110, 116 and 120 counts (shown in red, green and magenta respectively) were tested. All three attempts however yielded incorrect focusing width results.

The minimum number of photons used for extracting pixel fluorescence lifetimes was 10. The lifetime for pixels with less than 10 corresponding photons was set to zero, since lower event numbers would result in significant statistical error. This limitation was directly related to the time required for data acquisition. There was an inevitable compromise between error and time resolution. For the specific scanning conditions (512×512 pixels, 1.12 s/scan), it was found that a data acquisition time of at least 20 s was necessary for collecting sufficient photons per pixel and producing well-defined images. Reducing the acquisition time or the applied MLE threshold led to either image deterioration or significant statistical error (figure 3.25). It was therefore important that the appropriate experimental conditions and optical components (laser excitation line, filters etc.) were employed to maximise the photon collection efficiency and accomplish high image quality as well as short acquisition times.

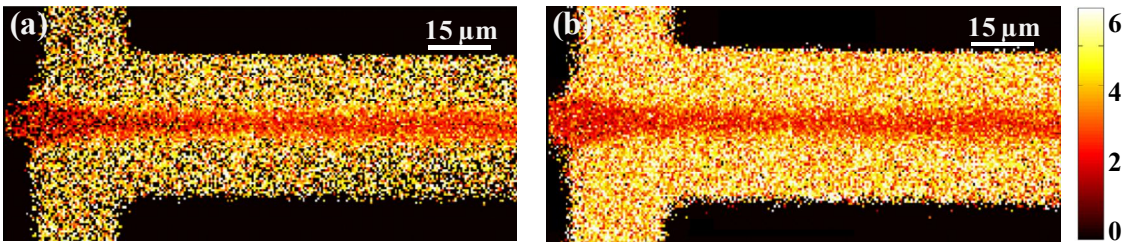

Figure 3.25. The minimum number of photons required for fluorescence lifetime determination using the MLE approach was set to 10. (a) For short acquisition times (10 s), insufficient photons were collected for the extraction of fluorescence lifetimes. Pixels with less than 10 corresponding photon events appeared black. (b) By setting the MLE limit to 5 photons, the images were improved, the statistical error however increased. The colourbar represents fluorescence lifetimes in ns.

3.4. Summary and conclusion

A 3-inlet 1-outlet device was used to demonstrate hydrodynamic focusing within microfluidic channels with dimensions varying between approximately 8-132 μm. The central inlet flow was confined into a narrow stream and it was established that the width was dependent on the flow rate ratio between the sheath and the analyte streams. FLIM was applied in combination with a MLE approach to construct fluorescence lifetime maps visualizing the focusing behaviour of the devices. Although the majority of hydrodynamic focusing studies up to date have used fluorescence intensity measurements, the superiority of the fluorescence lifetime technique was clearly illustrated by the improved quality of the obtained images. Furthermore, with the use of the MLE routine, fluorescence lifetimes were successfully calculated using as little as 10 photons indicating that the lifetime determination technique used herein is a powerful tool for studies that require extraction of information from systems where low photon counts are obtained. In addition, the combination of a scanning system with confocal imaging enabled fast and simple data acquisition with the high resolution and sensitivity of confocal microscopy.

A custom-written algorithm was applied to determine the width of the focused stream and the extracted values were successfully fitted to equations derived from theoretical calculations. Thus, the focusing behaviour of similar microfluidic designs and for a variety of channel dimensions in future experiments could be estimated according to the acquired fits. The analysis resulted in determining an optimum side-to-central inlet flow rate ratio α. Focusing width values of only a couple of micrometres were achieved for ratios α near the upper permitted by channel geometry limit. Considering the sample consumption and velocity however, it was concluded that an α of approximately 6 would be the ideal choice for achieving tight focusing as well as low sample consumption under stable flow of a suitable speed.

3.5. References

1. Wabuyele, M.B., S.M. Ford, W. Stryjewski, J. Barrow and S.A. Soper, *Single molecule detection of double-stranded DNA in poly(methylmethacrylate) and polycarbonate microfluidic devices.* Electrophoresis, 2001. **22**(18): p. 3939-3948.
2. Haab, B.B. and R.A. Mathies, *Single-molecule detection of DNA separations in microfabricated capillary electrophoresis chips employing focused molecular streams.* Analytical Chemistry, 1999. **71**(22): p. 5137-5145.
3. Dittrich, P.S. and P. Schwille, *An integrated microfluidic system for reaction, high-sensitivity detection, and sorting of fluorescent cells and particles.* Analytical Chemistry, 2003. **75**(21): p. 5767-5774.
4. Wang, T.H., Y.H. Peng, C.Y. Zhang, P.K. Wong and C.M. Ho, *Single-molecule tracing on a fluidic microchip for quantitative detection of low-abundance nucleic acids.* Journal of the American Chemical Society, 2005. **127**(15): p. 5354-5359.
5. Hill, E.K. and A.J. de Mello, *Single-molecule detection using confocal fluorescence detection: Assessment of optical probe volumes.* Analyst, 2000. **125**(6): p. 1033-1036.
6. Brody, J.P., P. Yager, R.E. Goldstein and R.H. Austin, *Biotechnology at low Reynolds numbers.* Biophysical Journal, 1996. **71**(6): p. 3430-3441.
7. de Mello, A.J. and J.B. Edel, *Hydrodynamic focusing in microstructures: Improved detection efficiencies in subfemtoliter probe volumes.* Journal of Applied Physics, 2007. **101**(8).
8. Knight, J.B., A. Vishwanath, J.P. Brody and R.H. Austin, *Hydrodynamic focusing on a silicon chip: Mixing nanoliters in microseconds.* Physical Review Letters, 1998. **80**(17): p. 3863-3866.
9. Nguyen, D.C., R.A. Keller, J.H. Jett and J.C. Martin, *Detection of single molecules of phycoerythrin in hydrodynamically focused flows by laser-induced fluorescence.* Analytical Chemistry, 1987. **59**(17): p. 2158-2161.
10. Castro, A., F.R. Fairfield and E.B. Shera, *Fluorescence detection and size measurement of single DNA-molecules.* Analytical Chemistry, 1993. **65**(7): p. 849-852.
11. Demas, J.N., M. Wu, P.M. Goodwin, R.L. Affleck and R.A. Keller, *Fluorescence detection in hydrodynamically focused sample streams: Reduction of diffusional defocusing by association of analyte with high-molecular-weight species.* Applied Spectroscopy, 1998. **52**(5): p. 755-762.
12. Goodwin, P.M., M.E. Johnson, J.C. Martin, W.P. Ambrose, B.L. Marrone, J.H. Jett and R.A. Keller, *Rapid sizing of individual fluorescently stained DNA fragments by flow-cytometry.* Nucleic Acids Research, 1993. **21**(4): p. 803-806.
13. Petty, J.T., M.E. Johnson, P.M. Goodwin, J.C. Martin, J.H. Jett and R.A. Keller, *Characterization of DNA size determination of small fragments by flow-cytometry.* Analytical Chemistry, 1995. **67**(10): p. 1755-1761.

14. Huang, Z.P., J.T. Petty, B. Oquinn, J.L. Longmire, N.C. Brown, J.H. Jett and R.A. Keller, *Large DNA fragment sizing by flow cytometry: Application to the characterization of P1 artificial chromosome (PAC) clones.* Nucleic Acids Research, 1996. **24**(21): p. 4202-4209.

15. Huang, Z.P., J.H. Jett and R.A. Keller, *Bacteria genome fingerprinting by flow cytometry.* Cytometry, 1999. **35**(2): p. 169-175.

16. Kim, Y.S., J.H. Jett, E.J. Larson, J.R. Penttila, B.L. Marrone and R.A. Keller, *Bacterial fingerprinting by flow cytometry: Bacterial species discrimination.* Cytometry, 1999. **36**(4): p. 324-332.

17. Van Orden, A., R.A. Keller and W.P. Ambrose, *High-throughput flow cytometric DNA fragment sizing.* Analytical Chemistry, 2000. **72**(1): p. 37-41.

18. Godin, J., C.-H. Chen, S.H. Cho, W. Qiao, F. Tsai and Y.-H. Lo, *Microfluidics and photonics for Bio-System-on-a-Chip: A review of advancements in technology towards a microfluidic flow cytometry chip.* Journal of Biophotonics, 2008. **1**(5): p. 355-376.

19. Lin, C.H. and G.B. Lee, *Micromachined flow cytometers with embedded etched optic fibers for optical detection.* Journal of Micromechanics and Microengineering, 2003. **13**(3): p. 447-453.

20. Pamme, N., R. Koyama and A. Manz, *Counting and sizing of particles and particle agglomerates in a microfluidic device using laser light scattering: application to a particle-enhanced immunoassay.* Lab on a Chip, 2003. **3**(3): p. 187-192.

21. Hertzog, D.E., B. Ivorra, B. Mohammadi, O. Bakajin and J.G. Santiago, *Optimization of a microfluidic mixer for studying protein folding kinetics.* Analytical Chemistry, 2006. **78**(13): p. 4299-4306.

22. Yao, S. and O. Bakajin, *Improvements in mixing time and mixing uniformity in devices designed for studies of protein folding kinetics.* Analytical Chemistry, 2007. **79**(15): p. 5753-5759.

23. Gosch, M., H. Blom, J. Holm, T. Heino and R. Rigler, *Hydrodynamic flow profiling in microchannel structures by single molecule fluorescence correlation spectroscopy.* Analytical Chemistry, 2000. **72**(14): p. 3260-3265.

24. Hung, C.I., B.J. Ke, G.R. Huang, B.H. Hwei, H.F. Lai and G.B. Lee, *Hydrodynamic focusing for a micromachined flow cytometer.* Journal of Fluids Engineering-Transactions of the Asme, 2001. **123**(3): p. 672-679.

25. Stiles, T., R. Fallon, T. Vestad, J. Oakey, D.W.M. Marr, J. Squier and R. Jimenez, *Hydrodynamic focusing for vacuum-pumped microfluidics.* Microfluidics and Nanofluidics, 2005. **1**(3): p. 280-283.

26. Lee, G.B., C.C. Chang, S.B. Huang and R.J. Yang, *The hydrodynamic focusing effect inside rectangular microchannels.* Journal of Micromechanics and Microengineering, 2006. **16**(5): p. 1024-1032.

27. Morris, C.J. and F.K. Forster, *Oscillatory flow in microchannels - Comparison of exact and approximate impedance models with experiments.* Experiments in Fluids, 2004. **36**(6): p. 928-937.

28. Fuerstman, M.J., A. Lai, M.E. Thurlow, S.S. Shevkoplyas, H.A. Stone and G.M. Whitesides, *The pressure drop along rectangular microchannels containing bubbles.* Lab on a Chip, 2007. **7**(11): p. 1479-1489.

29. Hertzog, D.E., X. Michalet, M. Jager, X.X. Kong, J.G. Santiago, S. Weiss and O. Bakajin, *Femtomole mixer for microsecond kinetic studies of protein folding.* Analytical Chemistry, 2004. **76**(24): p. 7169-7178.

30. Nguyen, N.T. and X.Y. Huang, *Mixing in microchannels based on hydrodynamic focusing and time-interleaved segmentation: modelling and experiment.* Lab on a Chip, 2005. **5**(11): p. 1320-1326.

31. Park, H.Y., X.Y. Qiu, E. Rhoades, J. Korlach, L.W. Kwok, W.R. Zipfel, W.W. Webb and L. Pollack, *Achieving uniform mixing in a microfluidic device: Hydrodynamic focusing prior to mixing.* Analytical Chemistry, 2006. **78**(13): p. 4465-4473.

32. Matsumoto, S., A. Yane, S. Nakashima, M. Hashida, M. Fujita, Y. Goto and S. Takahashi, *A rapid flow mixer with 11-mu s mixing time microfabricated by a pulsed-laser ablation technique: Observation of a barrier-limited collapse in cytochrome c folding.* Journal of the American Chemical Society, 2007. **129**(13): p. 3840-3841.

33. Pan, X., H. Yu, X. Shi, V. Korzh and T. Wohland, *Characterization of flow direction in microchannels and zebrafish blood vessels by scanning fluorescence correlation spectroscopy.* Journal of Biomedical Optics, 2007. **12**(1).

34. Schafer, D., E.A. Gibson, W. Amir, R. Erikson, J. Lawrence, T. Vestad, J. Squier, R. Jimenez and D.W.M. Marr, *Three-dimensional chemical concentration maps in a microfluidic device using two-photon absorption fluorescence imaging.* Optics Letters, 2007. **32**(17): p. 2568-2570.

CHAPTER 4
MIXING WITHIN MICROFLUIDIC DEVICES

4.1. Introduction

A large number of microfluidics applications involve the study of molecular interactions and reaction kinetics in the microscale [1]. Processes, such as protein folding/unfolding [2-8], enzymatic activity [9-11], nucleic acid interactions [12-14] etc., can be observed in real-time within a microfluidic platform. Considering that the time scale for activation and completion of the above interactions can be on the order of seconds, milliseconds or even microseconds, it is crucial to reduce the time required for mixing of the interacting molecules to the same order or less than the respective reaction time. This way, the dead time for observation is minimised and real reaction kinetics can be measured [15]. A variety of methods and chip configurations have been proposed with the aim to achieve thorough and rapid mixing of multiple molecular species in the microscale [16-20].

Microfluidic mixers can be categorized as either active, whereby an external field is applied to induce flow disturbance, or passive, which do not require external energy supply. In active mixing, the external actuators used for perturbing the flow often introduce a considerable degree of additional complexity and cost. On the contrary, passive mixers do not require additional components. They are robust, stable in operation and can be easily integrated into complex systems. Hence, for a variety of microfluidics applications, passive mixing is preferred [16]. The mixing process within these devices relies on molecular diffusion and chaotic advection, which can be enhanced by increasing the contact surface and contact time of the sample species through specially designed microchannel configurations.

Turbulent flow (high Reynolds number) and vortex formation (intermediate Reynolds number) can be used to improve the mixing performance of passive micromixers [16]. These, however, require large flow velocities to obtain the values of Reynolds number needed. In contrast, mixing under laminar flow conditions (low Reynolds number) significantly reduces the sample consumption due to the low flow rates used. In laminar flow micromixers whereby no flow manipulation is applied to induce chaotic advection, mixing occurs solely via molecular diffusion. In such devices, the inherently slow process of diffusion can be improved by decreasing the diffusion path between the mixing species. In this context, hydrodynamic

focusing has been proposed as a way to reduce the diffusion length under laminar flow conditions [21, 22]. The principle of hydrodynamic focusing was described in detail in chapter 3. By confining one of the interacting species within a narrow focused stream, the distance to be traversed by the diffusing molecules is diminished, resulting in rapid mixing.

The time t required for a molecule to diffuse through distance d can be calculated by rearranging equation 3.8. Diffusion time scales as the square of the distance [21, 23]. When hydrodynamic focusing is employed, substituting w_f for d yields that the time required for diffusion through the focused stream is proportional to w_f^2/D. Thus, for a specific molecule (fixed D), the diffusion time depends solely on the focusing width, which, in turn, is determined by the channel geometry and the side-to-central inlet flow rate ratio α (equation 3.3). The time t_{mix} required for complete mixing of the central and side inlet flow species is determined by the simultaneous diffusion of the molecules constituting the focused stream towards the surrounding flow and reverse.

Since it was first proposed [21, 22], hydrodynamic focusing has been employed in a variety of applications as a means to enhance micromixing and sub-millisecond mixing times have been reported [2-4, 7, 8, 24-30]. This method is particularly popular in protein folding and unfolding studies whereby hydrodynamic focusing is used as a mechanism for denaturant introduction or dilution; the resulting conformational change of the protein is then monitored within the outlet channel and kinetic information as well as intermediate state characteristics can be extracted [2-4, 7, 24, 31, 32]. Interactions between nucleic acids and other species introduced via the inlets of a microfluidic chip have also been investigated with the use of hydrodynamic focusing for micromixing initiation and enhancement. For example, the reaction between the fluorescent protein R-phycoerythrin and a mixture of live bacterial cells exhibiting or lacking the respective surface antigens has be followed by introducing the cell suspension into the main channel and adding R-phycoerythrin solution via the side inlets [33]. In a similar way, the irreversible cleavage reaction of double stranded DNA by the enzyme exonuclease III [26] and the binding of uracil DNA glycosylase repair enzyme to a fluorescently labelled DNA substrate [34] has be monitored using hydrodynamic focusing within a continuous flow ultrafast micromixer.

In the majority of these studies, molecules with low diffusion coefficient are introduced into the central inlet, while the side inlet flows consist of molecules with high D. This way, the central inlet flow remains confined in the focused stream for long periods of time, while the molecules supplied via the side inlets rapidly diffuse towards the centre of the mixing channel [21]. In a slightly different experimental configuration, a mixture of species may be introduced

via the central inlet and molecules diffuse away from the focused stream at different rates depending on their diffusion coefficient [4, 7]. Either way, the degree of mixing between the central and side inlet flows can be evaluated by calculating the concentration of the high *D* species within the focused stream. There is no strict definition for the mixing time, it is common however to define t_{mix} as the time required for the rapidly diffusing species concentration within the focused stream to change from 10% to 90% (or the reverse) of the final (or the initial) concentration [4, 35].

Several approaches have been applied for characterising mixing within microchannels, including fluorescence-based techniques [17, 36]. Although fluorescence intensity methods are commonly used in mixing experiments [4, 7, 8, 22, 23, 25, 26, 28-30, 37], these measurements are prone to artefacts associated with fluorophore concentration, sample illumination, choice of filters, detection efficiency etc. On the contrary, a fluorescence lifetime approach removes the above artefacts [13, 35, 38-40].

A way to characterize the mixing performance of a microfluidic device using fluorescence lifetime measurements is via exploiting the quenching of a fluorescent dye, typically fluorescein or rhodamine, by iodide ions (I^-) in the form of either sodium iodide (NaI) or potassium iodide (KI). The presence of the quencher results in a reduction of the fluorophore lifetime, which is related to the quenching ions concentration [I^-] via the Stern-Volmer equation:

$$\frac{\tau_0}{\tau} = 1 + k_q \tau_0 \left[I^-\right] \tag{4.1}$$

where τ_0 and τ is the dye lifetime in the absence and presence of the quencher respectively and k_q is the biomolecular quenching rate coefficient. When fluorescent dye and quencher are introduced into the device inlets, [I^-], which expresses the degree of mixing, can be determined by measuring the fluorophore lifetime τ and solving equation 4.1. The presence of the quenching ions also reduces the fluorescence intensity of the dye. However, an intensity-base method for monitoring the mixing process requires two separate measurements whereby the intensity of the quenched and unquenched fluorophore is recorded and subsequently compared [4, 7].

In this chapter, hydrodynamic focusing and a fluorescence lifetime approach were employed to characterise mixing within two microfluidic chip designs. Fluorescein and KI quencher were introduced into the central and side inlet channels respectively and mixing was visualized using FLIM. In continuous flow microfluidic devices, such as the ones used herein, positions

along the outlet channel length correspond to time. Therefore, the mixing time was extracted via appropriate analysis of the acquired FLIM images.

4.2. Experimental methods

4.2.1. Chemicals

Fluorescein and KI solutions were prepared in buffer pH 8.0 and filtered with 0.2 µm syringe filters (Pall Corporation, UK) to avoid device blockage. Fsc exhibits an absorption maximum at 490 nm, therefore a laser line of 488 nm (excitation path 2, section 2.1.1.2) was used for sample excitation. The fluorescence lifetime of Fsc at pH 8.0 is approximately 4 ns [41], the accurate τ_0 value however was experimentally determined using the current optical arrangement and analysis method (see section 4.2.4).

4.2.2. Microfluidic chip designs

The microfluidic devices were designed according to potential future applications, such as protein-protein binding, protein folding etc. The designs used for the experiments are shown in figure 4.1a and figure 4.1b and will be referred to as designs *a* and *b* respectively.

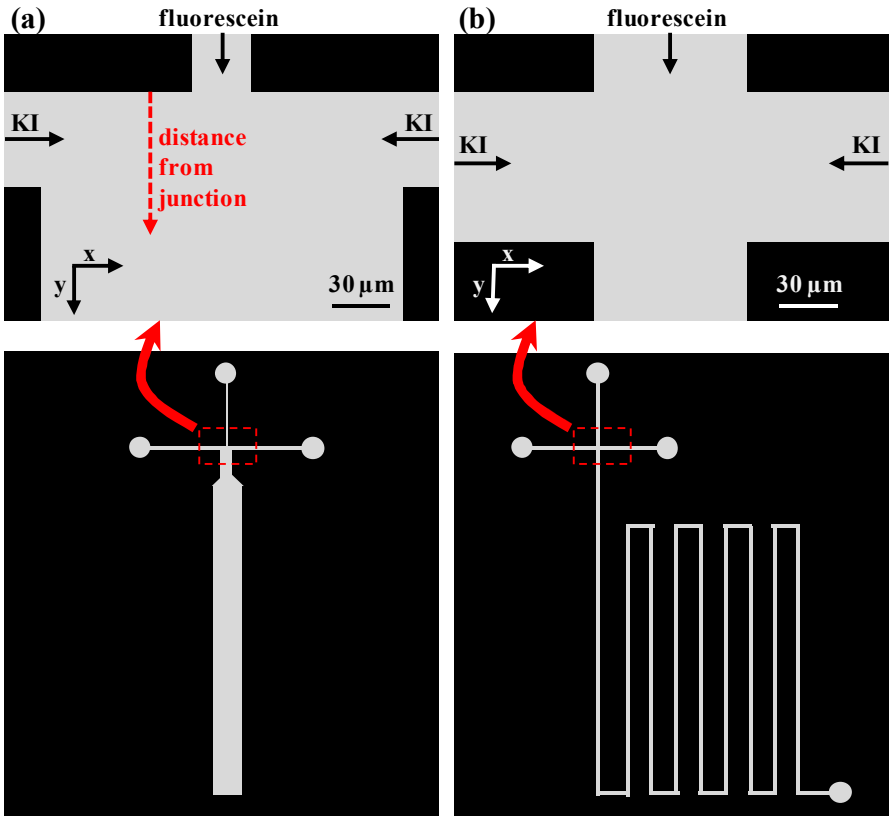

Figure 4.1. Microfluidic chip designs used in mixing characterisation experiments (also in Appendix A).

When the molecular interaction under investigation is characterized by kinetics in the order of tens or hundreds of milliseconds, it is important that similar timescale periods can be observed along the outlet channel. Given the small channel dimensions and the range of flow rates commonly used for the experiments, the resulting sample outlet velocity was in the order of tens of micrometres per millisecond. In order to ensure that the reaction of interest (post-mixing) occurred before the sample exited the chip and was directed to waste, the outlet channel in the above designs was modified in terms of either width (design *a*) or length (design *b*). The resulting devices allowed for visualisation of approximately 1 second, depending on the applied inlet flow rates.

In order to achieve rapid mixing, small focusing width values are desired. At the same time, the need for sample consumption minimization demands that the tightly focused stream is obtained under low side-to-central inlet flow rate ratio α and low total flow rate f_{tot}. With this in mind, the junction area in design *a* was essentially the design tested in chapter 3 (designs I, II and III). In order to avoid blockage, the smallest channel dimension (central inlet) was set to 29 μm. The side inlets were 46 μm and the outlet was 174 μm wide for the first 1mm and 435 μm thereafter. All channels were 50 μm deep.

In design *b*, the additional outlet length significantly increased the fluidic resistance of the channel (equation 3.5). Therefore, the channel cross-section was increased to reduce the pressure and facilitate the flow. All channels in this design were 75 μm wide and 100 μm deep. Detailed dimensions of the designs can be found in appendix A (figure A.3 and figure A.4).

4.2.3. Experimental procedure

In order to characterize mixing, 500 μM Fsc and 0.6 M KI were introduced into the central and side inlets respectively. As found by trial and error, the above concentrations ensured adequate Fsc quenching as well as sufficient photon counts for accurate fluorescence lifetime determination even under high fluorescence quenching conditions. Similarly to the focusing width measurement experiments (chapter 3), the same pump was used for both side inlets to ensure focusing symmetry, while a separate pump was used to deliver Fsc into the central inlet. Measurements were performed under constant central inlet flow rate for different side-to-central inlet flow rate ratios α, as well as under constant α while varying the central and side inlet flow rates. Depending on the chip design and the α limits set by the channel dimensions (see section 3.3.1.2), the flow rates varied between 0.2-10 μl/min.

The laser spot was positioned approximately at the intersection of the inlet channels and 512x512 pixel x-y scans were performed corresponding to an imaged area of 235x235 μm^2. Photon arrival data were acquired using the TimeHarp 200 TTTR mode. Subsequently, the microscope stage was moved 200 μm in the y-direction using the Prior Scientific software and a second image along the outlet was acquired (figure 4.2). In the same manner, up to 5 images were obtained along the outlet channel length corresponding to a total visualized area of approximately 235x1000 μm^2 (the last few pixels of the images in the y-direction overlapped). In most occasions, the mixing process was complete within the first ~550 μm from the junction, therefore only the first 3 images were used for extracting t_{mix} (figure 4.2).

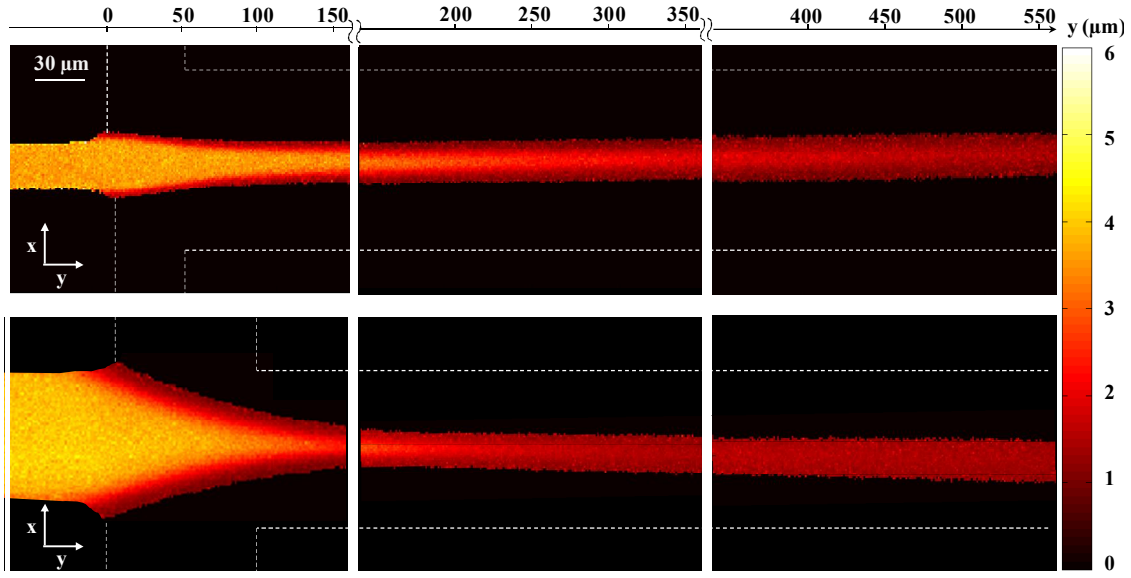

Figure 4.2. Fluorescence lifetime images acquired along the outlet channel length. The lifetimes represented by the colourbar (in ns) correspond to KI concentration via equation 4.1. Top: chip design *a*, α=1, f_c=f_s=1 μl/min. Bottom: chip design *b*, α=1, f_c=f_s=0.4 μl/min.

4.2.4. Quenched fluorescein lifetime calibration

As it was previously mentioned, the presence of the quenching ions decreased the fluorescence lifetime of Fsc. In order to match measured lifetimes to quencher concentrations via equation 4.1, the quenching rate coefficient k_q for the Fsc-KI system had to be determined. For this purpose, the fluorescence lifetime of 500 μM Fsc solutions in 0-0.6 M KI was determined using FLIM under equilibrium conditions. The lifetime for each KI concentration ([KI]=0 M corresponds to τ_0) was extracted by averaging values within the imaged area. For increasing [KI], the obtained lifetimes dropped from τ_0=3.88 ns down to 0.76 ns when [KI]=0.6 M (figure 4.3).

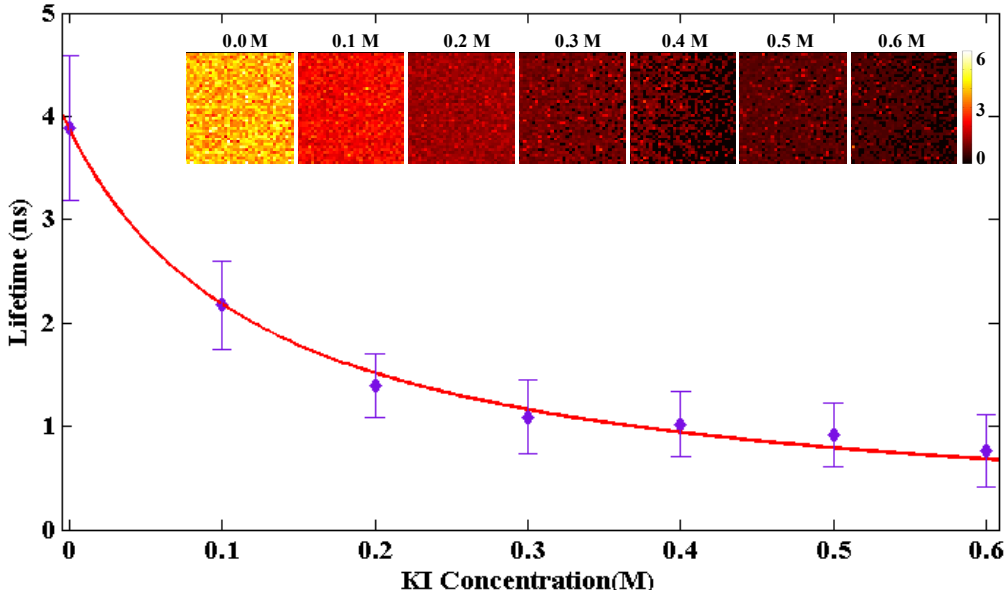

Figure 4.3. The fluorescence lifetime of fluorescein upon quenching dropped from τ_0=3.88 ns ([KI]=0) to 0.76 ns for [KI]=0.6 M. Error bars represent standard deviation. The colourbar for the FLIM images represents fluorescence lifetime in ns.

The ratio τ_0/τ was plotted against [KI] (figure 4.4) and, according to equation 4.1, fitted using the linear form:

$$\frac{\tau_0}{\tau} = 1 + k_q \times 3.88 \times 10^{-9} \times [\mathrm{KI}] \tag{4.2}$$

The extracted k_q was 1.82×10^9 $M^{-1}s^{-1}$. In the subsequent real-time mixing experiments, this value was replaced in equation 4.2 to calculate the KI concentration for various lifetimes τ.

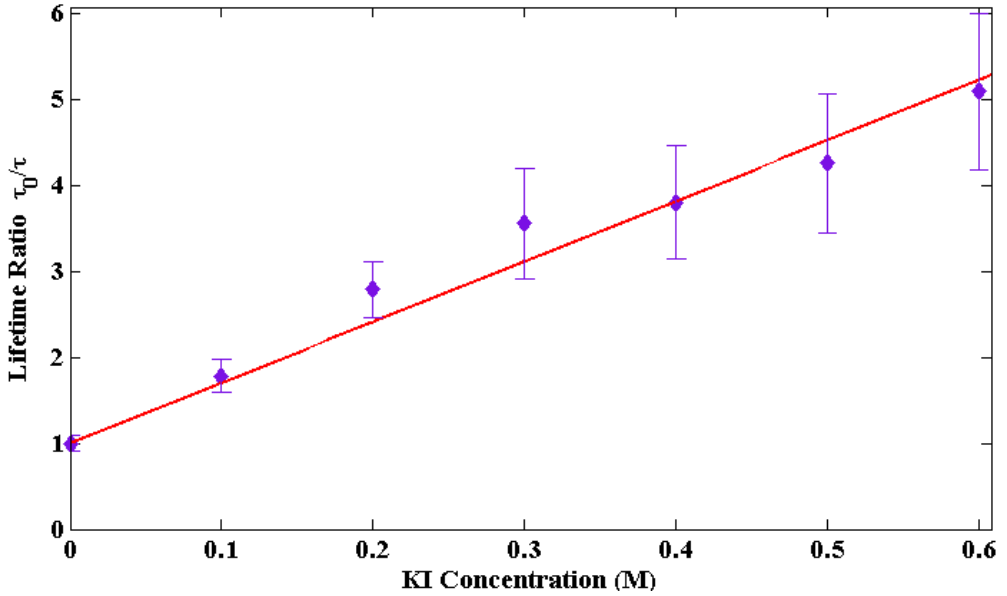

Figure 4.4. τ_0/τ ratio versus KI concentration and linear fit (χ_R^2 =0.964). The extracted quenching rate coefficient k_q was 1.82×10^9 $M^{-1}s^{-1}$.

4.2.5. FLIM analysis and mixing time extraction

The fluorescence lifetime maps shown in figure 4.2 were obtained by processing TTTR data as described in section 2.3.3. For the 30 s acquisition time used herein, the minimum number of photon events per pixel required for lifetime determination via the MLE routine was set to 30.

As KI diffused into the central Fsc stream, the KI concentration, and thus the Fsc lifetime, across the focused stream width varied with x (figure 4.2). A custom-written Matlab algorithm was used to locate the 3 central pixels of the focused stream for each y position along the outlet length. The Fsc lifetime for a specific distance y from the junction was represented by the average lifetime value of the corresponding 3 pixels (figure 4.5).

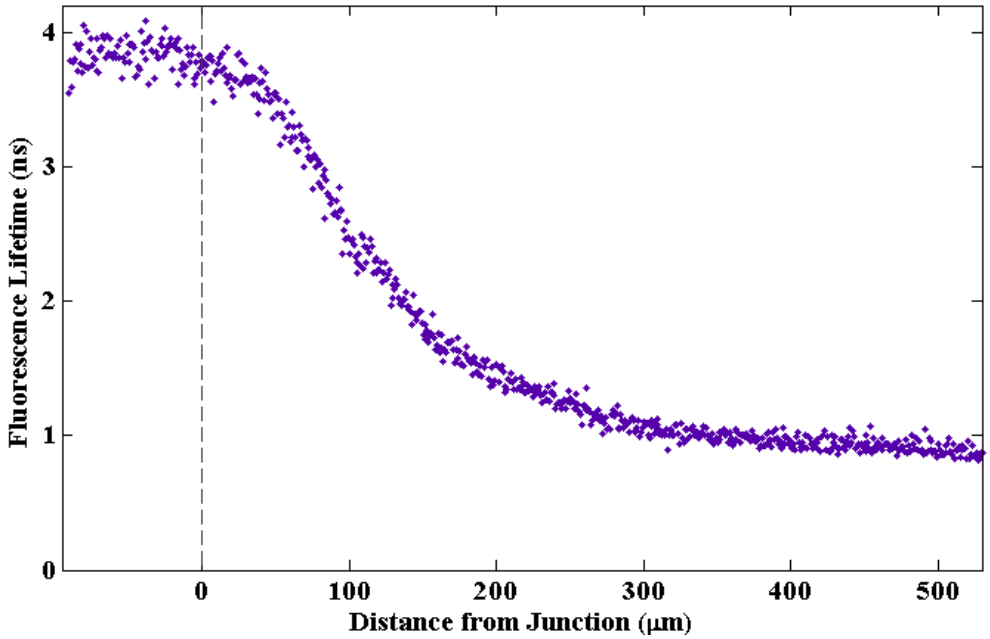

Figure 4.5. Fluorescence lifetime at the centre of the focused stream along the outlet channel. The lifetime of fluorescein decreased as mixing progressed. The dashed vertical line represents the intersection of the inlet channels. Chip design b, α=1, f_c=f_s=0.4 μl/min.

Subsequently, the distance y from the junction was translated into time based on the channel geometry and the total flow rate, and fluorescence lifetimes were matched to the corresponding [KI] values via equation 4.2. As expected, [KI] along the device centreline was zero before the fluidic streams were brought into contact at the junction and increased as mixing progressed, until a saturation [KI] was reached when mixing was complete. Hence, the resulting [KI]-time curve appeared to have a sigmoidal shape (figure 4.6) and it was therefore modelled using an adapted Boltzmann sigmoid function, described by equation:

$$[\mathrm{KI}] = p_1 + \frac{p_2 - p_1}{1 + \exp\left(-\frac{t - p_3}{p_4}\right)} \tag{4.3}$$

where p_1, p_2 were the initial and final KI concentrations, p_3 was the time when [KI] became 50% of the final [KI] and p_4 was the slope of the curve at time p_3. As discussed in section 4.1 [4, 35], the mixing time was defined as the time required for the KI concentration within the focused stream to change from 10% to 90% of the equilibrium [KI] value (figure 4.6).

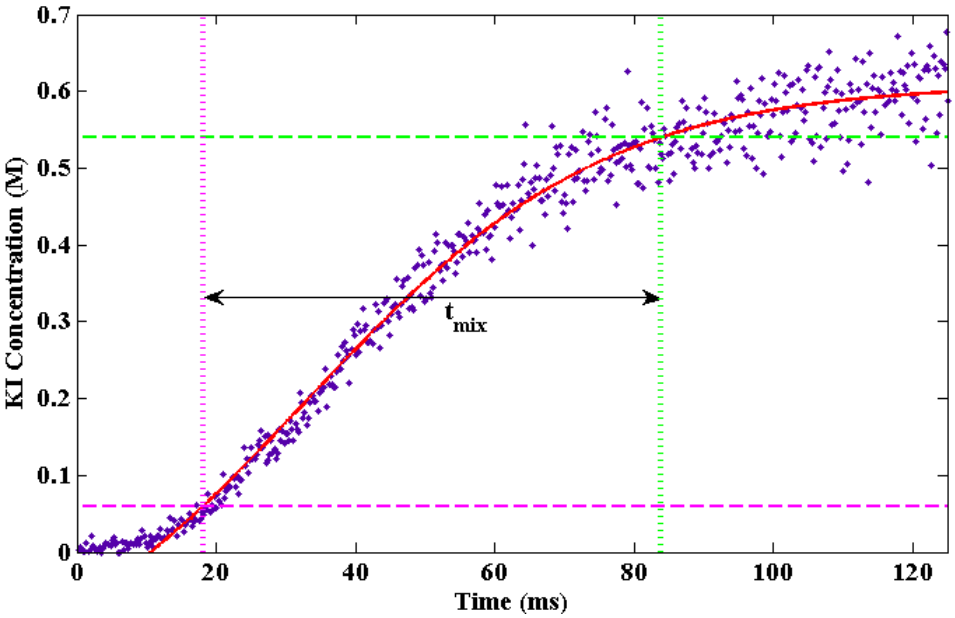

Figure 4.6. KI concentration versus time along the outlet channel. The sigmoid fit is shown in red. Mixing time t_{mix} was defined as the time required for the [KI] to increase from 10% to 90% of the final concentration (magenta/green dashed lines respectively). Chip design *b*, α=1, f_c=f_s=0.4 µl/min.

4.3. Results and Discussion

4.3.1. Mixing time versus flow rate ratio α

As it was discussed in section 4.1, in mixing experiments whereby hydrodynamic focusing is employed the diffusion time scales as the square of the focused stream width. In turn, w_f depends on the side-to-central inlet flow rate ratio α, thus, the mixing time for specific channel geometry and molecular species is determined by α.

In order to characterize the mixing performance of design *a* with respect to ratio α, the central inlet flow rate (Fsc) was kept constant at 1 µl/min while the side inlet flow rate (KI) varied between 1-10 µl/min. The resulting α values also varied from 1 to 10. The obtained fluorescence lifetime maps are shown in figure 4.7.

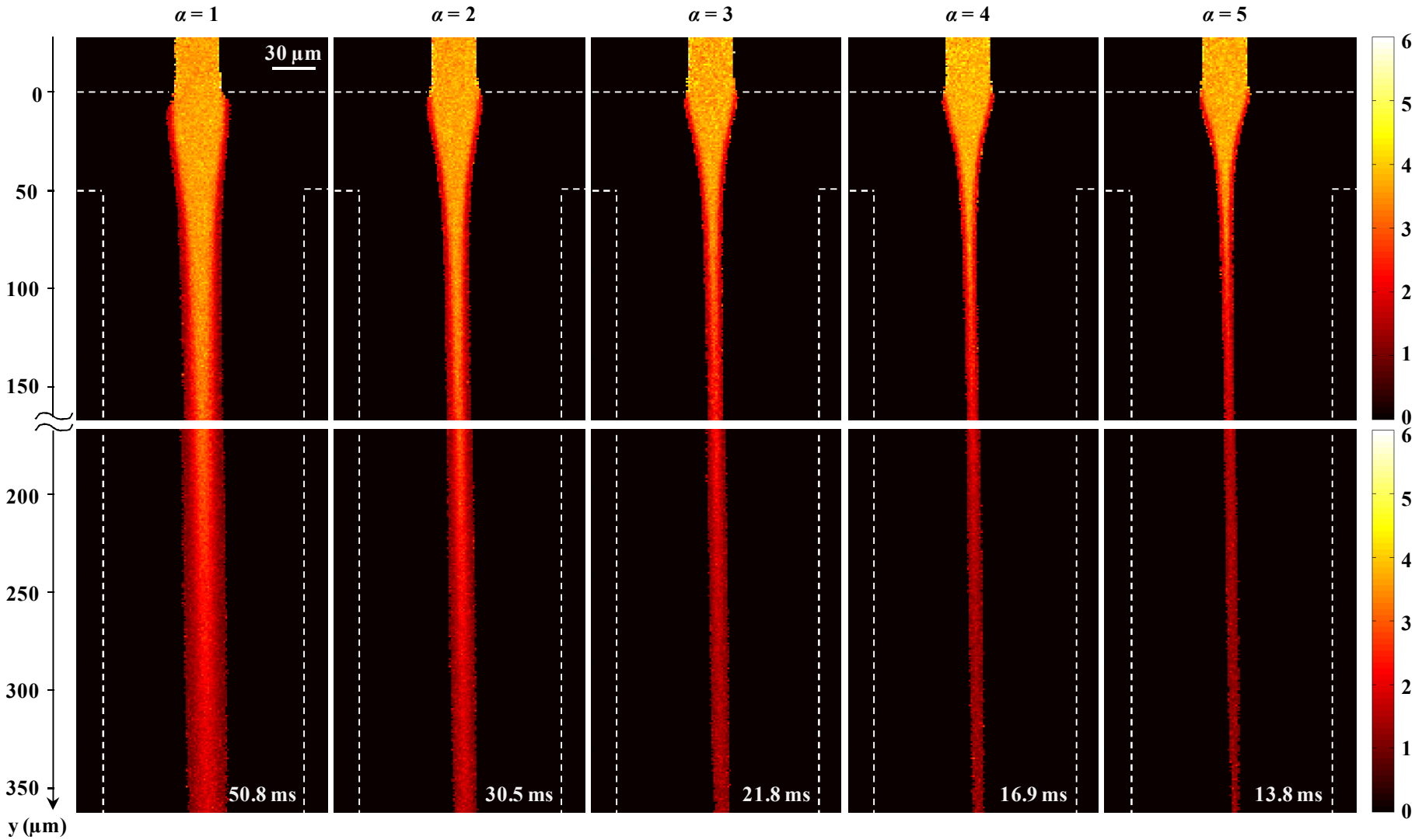
α = 1
α = 2
α = 3
α = 4
α = 5
30 µm
0
50
100
150
200
250
300
350
y (µm)
50.8 ms
30.5 ms
21.8 ms
16.9 ms
13.8 ms
6
5
4
3
2
1
0

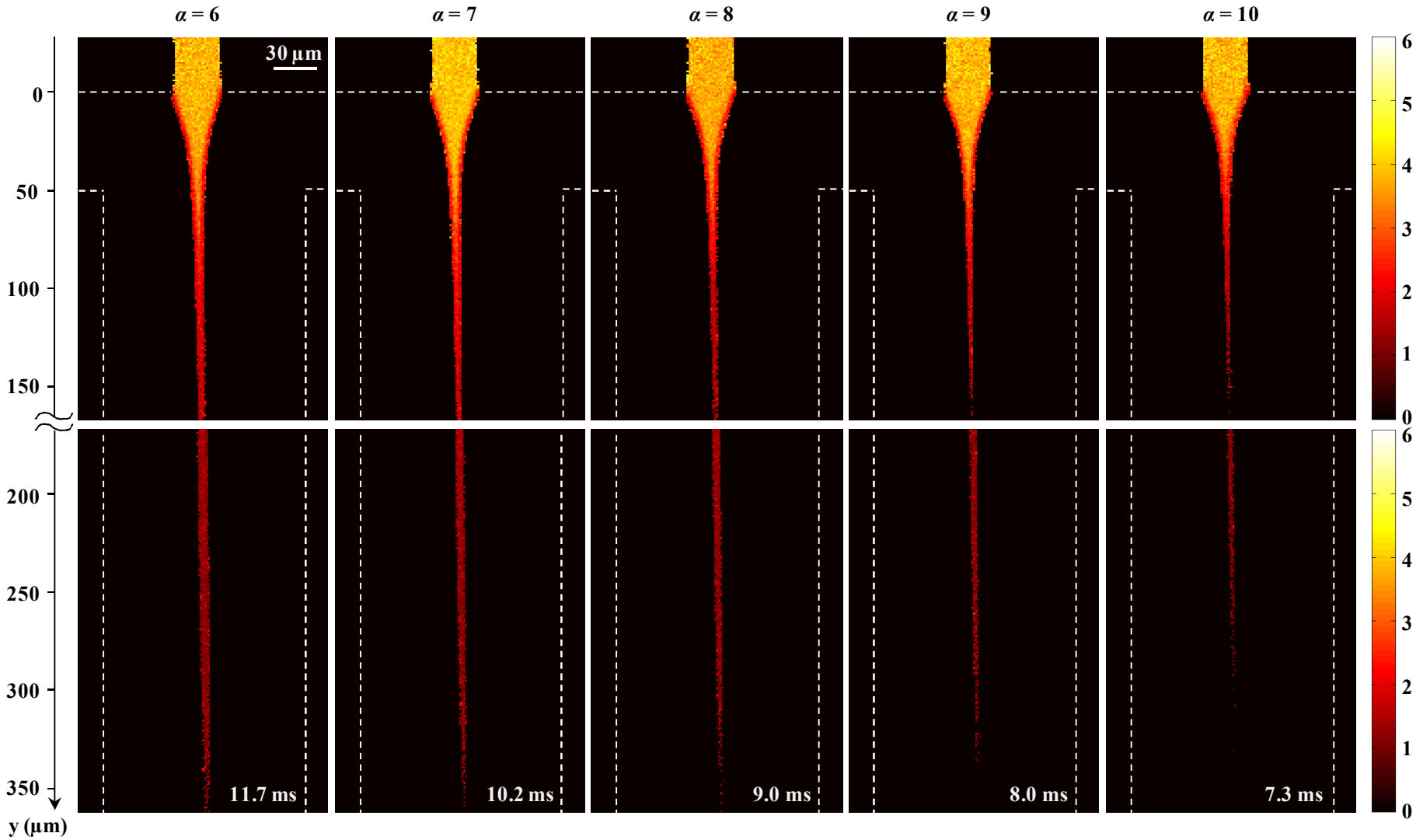

Figure 4.7. Fluorescence lifetime maps visualising mixing within microchannels for various values of side-to-central inlet flow rate ratio α. Chip design a, f_c=1 µl/min, α=1-10, imaged time reduced from 50.8 to 7.3 ms. Central and side inlet flows consisted of 500 µM Fsc and 0.6 M KI respectively. Colourbar represents fluorescence lifetimes in ns.

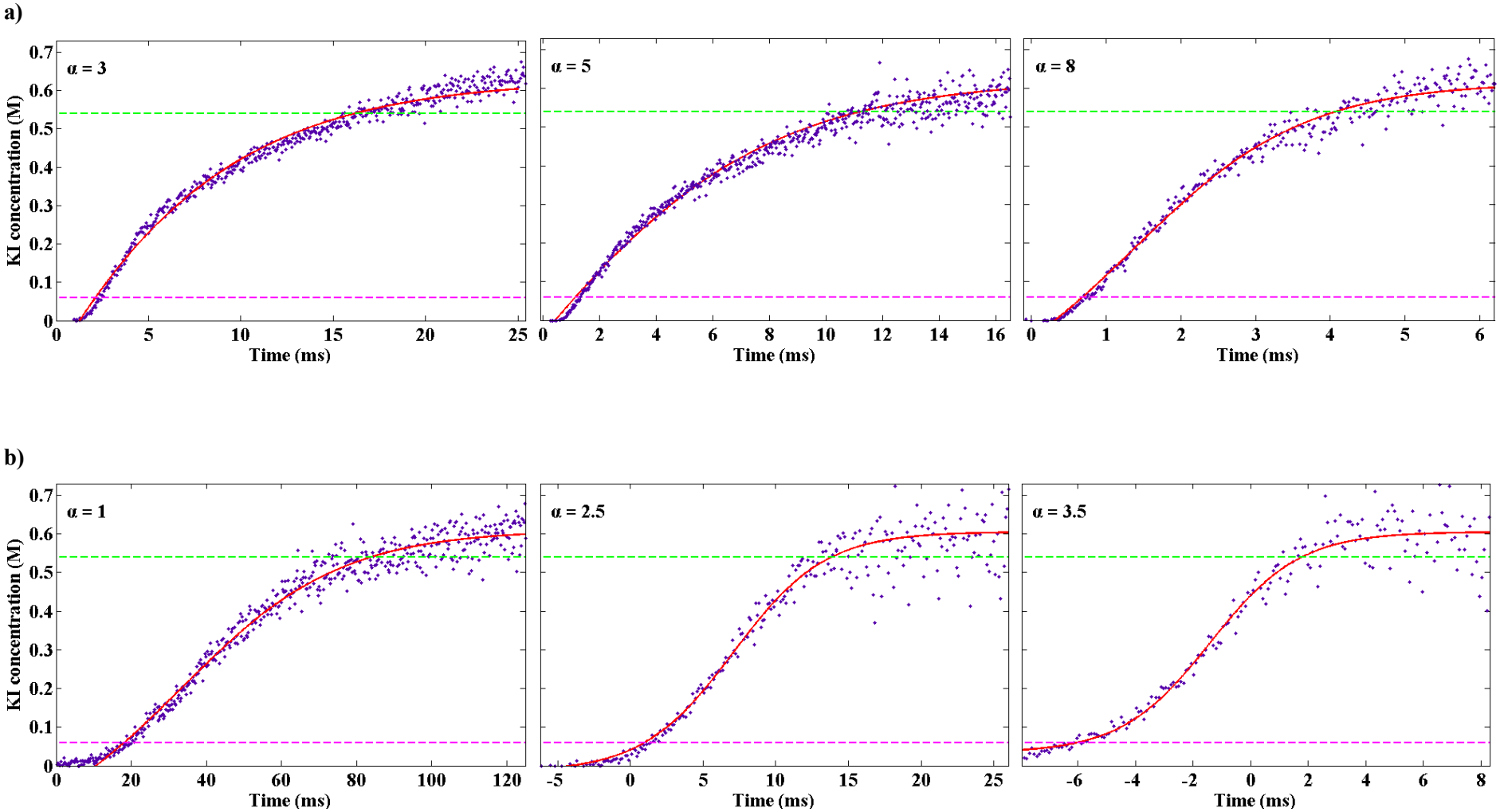

Figure 4.8. Representative KI concentration versus time plots and sigmoid fits along the outlet channel (a) Chip design *a*, f_c=1 µl/min, α=3, 5, 8 (b) Chip design *b*, f_c=0.4 µl/min, α=1, 2.5, 3.5.

It is evident that as mixing progressed, Fsc lifetime decreased. For $\alpha \geq 3$, Fsc lifetime reached its final value within the first 350 μm from the intersection of the inlet channels. Therefore, acquisition of 2 images along the outlet length was sufficient to fully monitor and characterize the mixing process. The diffusion coefficient of fluorescein is larger than that of KI hence the central stream remained focused while KI diffused towards it. By taking into account the channel dimensions, the flow rates used and a diffusion coefficient of $\sim 4.25 \times 10^{-6}$ cm^2/s for Fsc (provided by supplier), the total time imaged within the first ~350 μm from the junction (2 images) and the Fsc diffusion distance at the same point were calculated. For comparison, the focusing ratio (see figure 3.16 in section 3.3.1.2) and focused stream width for the specific channel dimensions were also extracted and it was noticed that for $\alpha \geq 8$, Fsc diffusion distance at 350 μm from the junction and focusing width became comparable ($d > 0.25 w_f$). As a result, the focusing was rapidly lost as it is shown in figure 4.7 for $\alpha = 10$, whereby the focused stream disappeared after approximately 6.2 ms (~300 μm from the junction).

It should be noted that towards the bottom of each image less photon events per pixel were recorded and a number of pixels appeared dark as the minimum threshold for the MLE was not reached. This was possibly due to non-uniform illumination or reduced detection efficiency for photons originating from the specific area. The above observation was more evident for $\alpha > 6$, whereby the number of emitted photons was already low due to fluorescence quenching (figure 4.7, α=7-10). This was a systematic error affecting the last ~35 μm (in the y-direction) of all images and should not be confused with the loss of focusing due to the Fsc diffusion described earlier. The difference is illustrated in figure 4.7, where for $\alpha = 10$ the focused stream appeared to fade out at the end of the top image but became visible again in the second image until focusing was lost around the middle of the same image (~300 μm from the junction). In order to compensate for the loss of data in the poorly illuminated region, the scanning was performed in such way that the first 35 μm (in the y-direction) of each 235x235 μm^2 acquired image overlapped with the final 35 μm of the previous image. Increasing the data acquisition time or reducing the MLE threshold could also compensate for the lack of photons but would inevitably prolong the experimental procedure and data analysis or increase the statistical error. The superiority of a fluorescence lifetime as opposed to a fluorescence intensity approach becomes apparent as in intensity measurements the low photon count due to inadequate excitation or detection could be mistaken for additional fluorescein quenching. Similarly, the reduced Fsc concentration and, thus, photon emission, due to diffusion could also be interpreted as fluorescence quenching. Therefore, an additional experiment with the side flow consisting of plain buffer instead of KI would be required in a fluorescence intensity method for comparison purposes.

The images shown in figure 4.7 were processed and the lifetime of fluorescein at the centre of the focused stream was converted into KI concentration. Representative [KI] versus time plots together with sigmoid fits described by equation 4.3 (section 4.2.5) are shown in figure 4.8a. As mixing progressed, fluorescence quenching by KI led to reduced photon emission, therefore fewer photons were used by the MLE routine for lifetime determination. As a result, the statistical error increased (more disperse calculated lifetimes) and the KI concentrations extracted via equation 4.2 were more scattered, for times t close to mixing completion (figure 4.8).

The [KI] versus time fits for α=1-10 are shown in figure 4.9. A strong dependence of the KI diffusion time with respect to ratio α was observed for values up to α=3. The same trend continued up to a value of α=6 while increasing α beyond 6 did not have a significant effect on the mixing process. These results were in perfect agreement with the focusing width results presented in chapter 3 as the time required for diffusion through the focused stream is proportional to w_f^2/D.

Similar measurements were also performed using design *b*. In this design, the outlet channel was narrower (75 μm) than that in design *a* (174 μm) and the aspect ratio ε was larger due to the channels being deeper (ε is 0.29 and 1.33 for designs *a* and *b* respectively). Consequently, the focused stream width and, thus, the mixing times acquired for this design were expected to be similar or smaller than for design *a*. In order to characterize the mixing performance of this device, the central inlet flow rate was kept constant at 0.4 μl/min, whilst the KI flow rate varied from 0.4-1.4 μl/min with a step of 0.2 μl/min. The resulting ratios α varied between 1 and 3.5. α values above 3.5 were not achieved due to the chip geometry. KI concentration versus time plots are presented in figures 4.8b and 4.10. As it is illustrated in figure 4.10, for $\alpha \geq 2.5$, mixing began within the central inlet (negative t) due to pressure from the side flows.

The calculated mixing times t_{mix} for both designs were plotted against ratio α (figure 4.11). Taking into account that the KI diffusion time scales as the square of the focused stream width and that w_f versus α plots can be fitted using equation 3.4, t_{mix} versus ratio α data were fitted using the following form:

$$t_{mix} = \frac{p_1}{\left(p_2 + p_3 \times \alpha\right)^2} + p_4 \tag{4.4}$$

where parameters p_1, p_2, p_3 and p_4 were appropriately estimated according to the channel geometry (via w_f) and the species used (via D). The χ_R^2 values for the fits were 0.997 and 0.980 for designs *a* and *b* respectively.

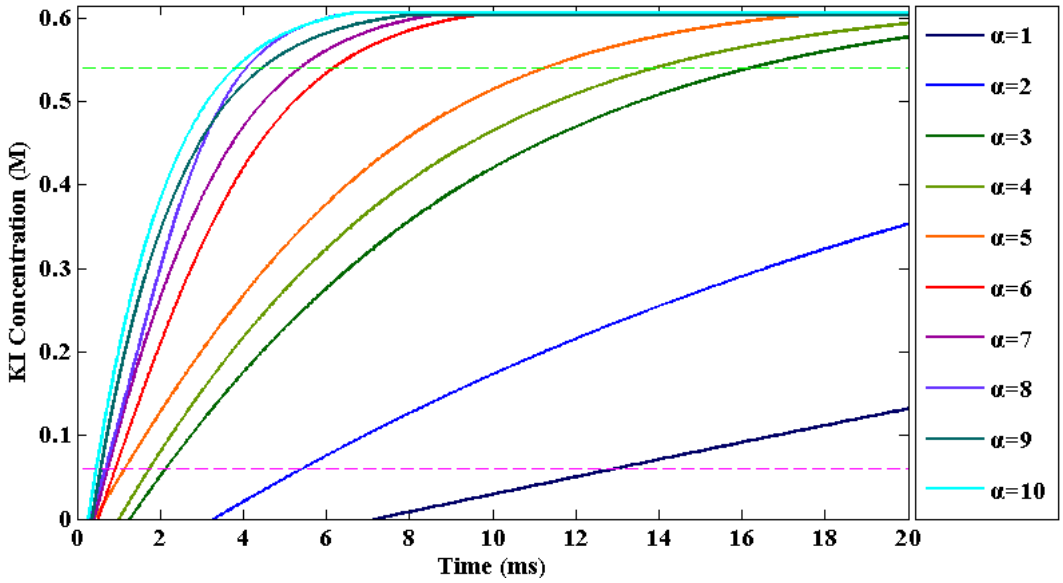

Figure 4.9. KI concentration versus time sigmoid fits in chip design *a*, α=1-10 (constant f_c=1 µl/min). The magenta and green dashed lines represent the 10% and 90% of the final [KI] respectively.

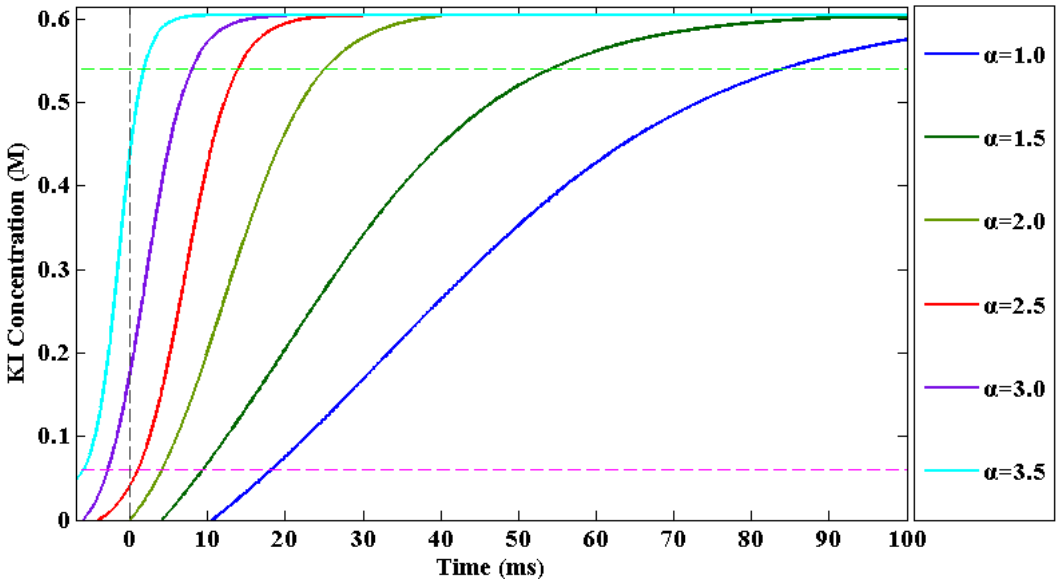

Figure 4.10. KI concentration versus time sigmoid fits in chip design *b*, α=1-3.5 (constant f_c=0.4 µl/min). The magenta and green dashed lines represent the 10% and 90% of the final [KI] respectively.

Similarly to figure 4.9, figure 4.11 illustrates that in chip design *a*, a slight increase in the flow rate ratio resulted in significantly faster mixing for $\alpha \leq 3$, while increasing α beyond 6 did not notably decrease t_{mix}. An analogous trend was observed in design *b* for α values up to 2.5. As discussed earlier, due to the different channel geometry, design *b* yielded slightly shorter mixing times than design *a* for the same side-to-centre flow rate ratio. However, the loss of focusing at α=2.5 in design *b* as opposed to α=10 in design *a*, resulted in the minimum mixing time being achieved in design *a* (2.8 ms). The minimum t_{mix} obtained in design *b* was 7.8 ms for α=2.5.

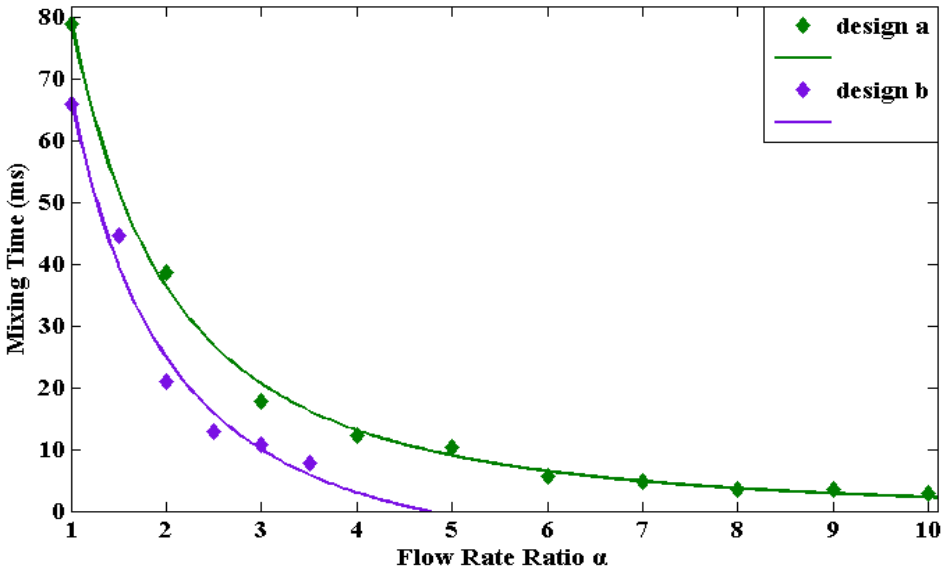

Figure 4.11. Mixing time versus side-to-central inlet flow rate ratio α for chip designs *a* (green) and *b* (purple).

4.3.2. Mixing time under constant flow rate ratio α

As illustrated in the previous section, increasing the side-to-central inlet flow rate ratio beyond 6 and 2.5 in chip designs *a* and *b* respectively, did not yield a significant improvement in t_{mix}. In addition, greater values of α result in unwanted increase of the, potentially valuable, side inlet sample consumption and in higher outlet flow velocities which decrease the total time period that can be observed within the outlet. Finally, the use of α values yielding extremely small w_f may lead to rapid loss of focusing and complicate the experimental procedure. Therefore, α=6 and α=2.5 were considered as ideal working flow rate ratios for designs *a* and *b* respectively. By fixing ratio α at these values and varying the central and side inlet flow rates, an optimum f_c-f_s combination could be determined, in order to achieve fast mixing as well as small f_{tot} and, thus, low sample consumption and outlet flow velocity.

The fluorescence lifetime maps obtained from these experiments in chip design *a* are shown in figure 4.12. In these images the inlet flow rate ratio remained the same (α=6) while f_{tot} increased from 2.6 μl/min to 13.0 μl/min. As a result, the corresponding time per pixel decreased from 134 μs/pixel for f_{tot}=2.6 μl/min to 31 μs/pixel for f_{tot}=13.0 μl/min. It becomes apparent that there was an inevitable trade-off between resolution and acquisition/analysis complexity. At slow flow rates the mixing process was complete within ~150 μm from the junction corresponding to a single image (~25 ms for f_{tot}=2.6 μl/min). On the contrary, as the flow rate increased, more images along the outlet (~5 ms each for f_{tot}=13 μl/min) were required to fully monitor the mixing process, leading to longer acquisition and data analysis procedures. The time resolution however was significantly improved. The most appropriate flow rate combination can be selected depending on the demands of a specific application.

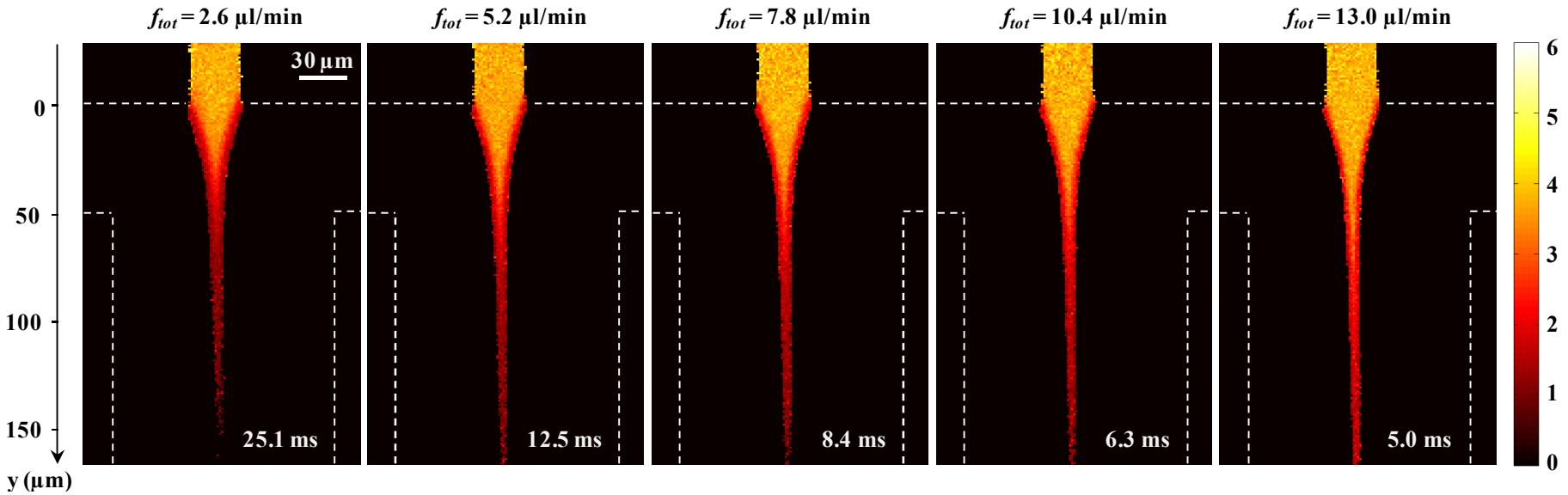

Figure 4.12. Fluorescence lifetime maps visualising mixing within microchannels under constant side-to-central inlet flow rate ratio α. Chip design *a*, α=6, f_{tot}=2.6-13.0 µl/min, imaged time reduced from 25.1 to 5.0 ms. The central and side inlet flows consist of 500 µM Fsc and 0.6 M KI respectively. Colourbar represents fluorescence lifetimes in ns.

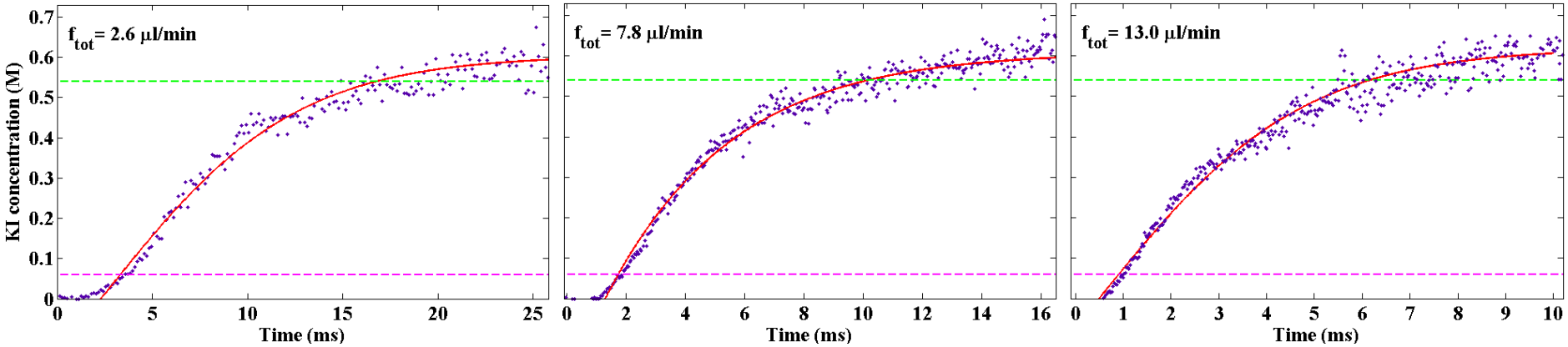

Figure 4.13. Representative KI concentration versus time plots and sigmoid fits along the outlet channel. Chip design *a*, α=6, f_{tot}=2.6, 7.8, 13.0 µl/min.

Representative [KI] versus time plots and the acquired via equation 4.3 fits are given in figures 4.13 and 4.14. Fits obtained by similar measurements within chip design *b* under constant α of 2.5 are shown in figure 4.15.

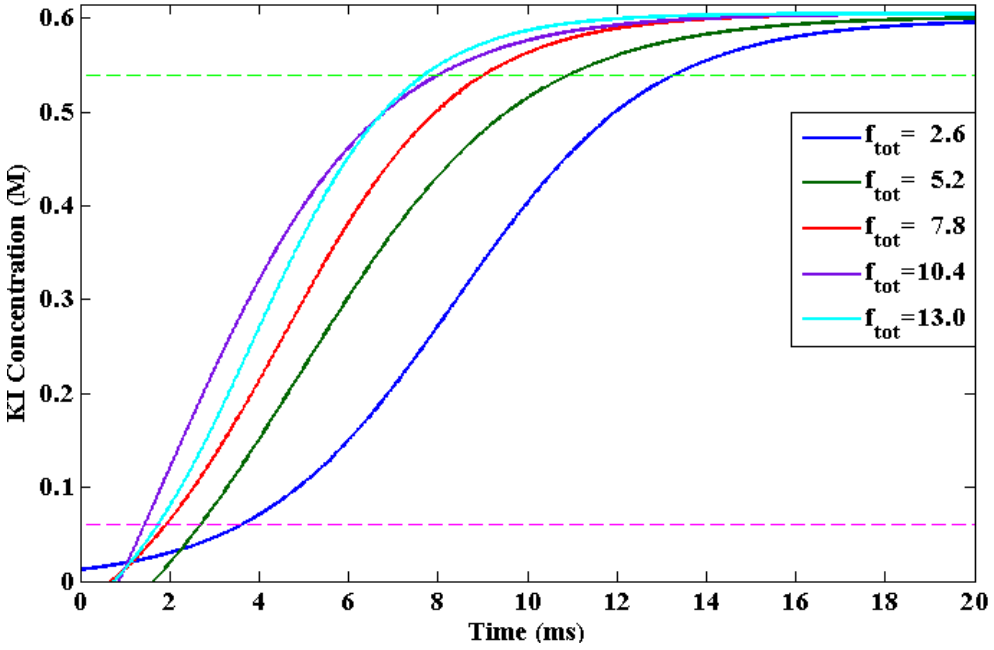

Figure 4.14. KI concentration versus time sigmoid fits in chip design *a*, f_{tot}=2.6-13.0 µl/min (constant α=6). The magenta and green dashed lines represent the 10% and 90% of the final [KI] respectively.

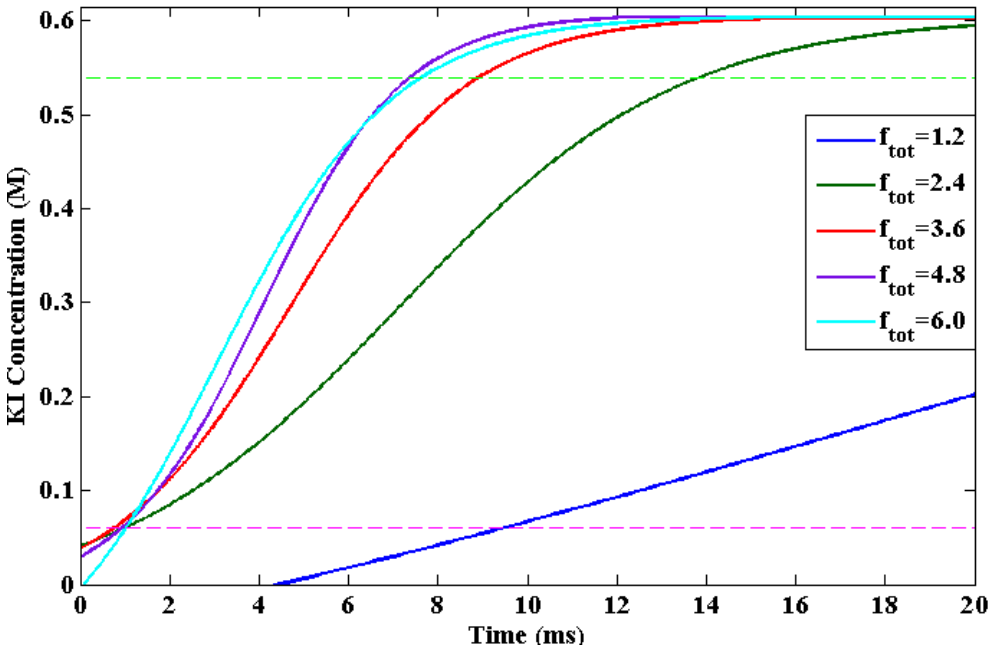

Figure 4.15. KI concentration versus time sigmoid fits in chip design *b*, f_{tot}=1.2-6.0 µl/min (constant α=2.5). The magenta and green dashed lines represent the 10% and 90% of the final [KI] respectively.

Figures 4.14 and 4.15 illustrate that although during these measurements the inlet flow rate ratio remained unchanged, the variation of the total flow rate affected the time required for KI

diffusion into the focused stream. This was more pronounced in chip design *b*, whereby decreasing f_{tot} below 3.6 µl/min significantly decelerated the mixing process. These results were consistent with simulation and experimental data presented by other researchers [35]. For f_{tot}>3.6 µl/min and for chip design *a*, increasing f_{tot} appeared to shift the mixing process to earlier points in time without, however, necessarily reducing the mixing time. The extracted t_{mix} values for both chip designs are presented with respect to the total flow rate f_{tot} in figure 4.16. t_{mix} versus f_{tot} data were fitted using a power equation ($t_{mix}=p_1+p_2\times f_{tot}^{p3}$) yielding χ_R^2 values of 0.998 and 0.999 for designs *a* and *b* respectively.

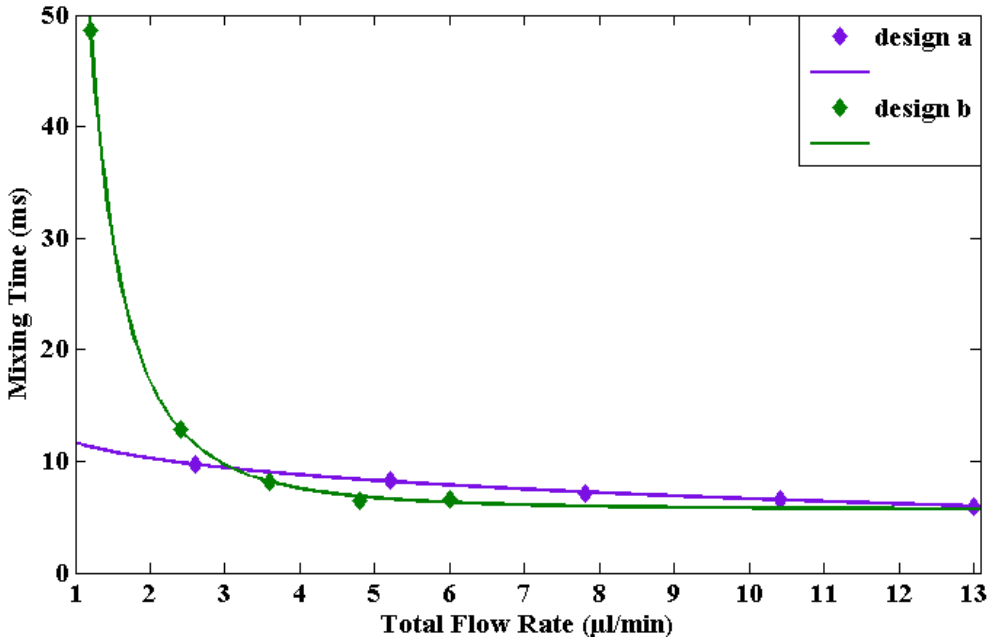

Figure 4.16. Mixing time versus total flow rate for chip designs *a* (green) and *b* (purple). The side-to-central inlet flow rate ratio α is 6 and 2.5 for designs *a* and *b* respectively.

Figure 4.16 shows that the total flow rate had a minor effect on the time required for Fsc-KI mixing. With the exception of cases whereby f_{tot}<3.6 µl/min in chip design *b*, increasing f_{tot} led to slightly shorter t_{mix}. This could possibly be connected to a similar trend observed for the focused stream width (section 3.3.1.1). As the diffusion time is proportional to w_f^2, the effect of the flow rate on the focusing width discussed in chapter 3 was expected to be larger in terms of mixing time.

The dependence of the mixing time on the total flow rate could also be related to the fact that the Fsc quenching started the moment the central and side inlet flows were brought in contact, before the final w_f was reached. As the inlet flow rates decreased, especially for f_{tot}<3.6 µl/min in chip design *b*, the time required for the focused stream to obtain its final width increased. During this period, the distance to be traversed by diffusing quencher molecules until they

reached the centre of the focused stream was larger. Therefore, longer mixing times were obtained at low f_{tot}. For the same reason, the whole mixing process was shifted to earlier times when the flow rates used were increased. Similar variations in the mixing progress due to mixing prior to the formation of the focused stream have been previously reported [28]. The addition of sheath flows to create a barrier between the central and side inlet samples was proposed as a way to address such 'premixing' issues.

4.4. Summary and conclusion

The mixing performance of two 3-inlet 1-outlet microfluidic chip designs was characterised using hydrodynamic focusing and FLIM. For this purpose, fluorescein and KI were introduced into the central and side inlets respectively and mixing occurred via KI diffusion towards the focused Fsc stream. As mixing progressed, fluorescein lifetime reduction was observed due to fluorescence quenching. The mixing process along the outlet channel length was imaged using FLIM and a MLE approach was employed to construct two-dimensional fluorescence lifetime maps with a threshold of 30 photons for lifetime determination. Changes in Fsc lifetime were translated into KI concentrations via the Stern-Volmer equation and pixels in the direction of the flow were converted into time. The extracted mixing time was found to decrease for increasing side-to-central inlet flow rate ratio α and t_{mix} values as short as ~3 ms were achieved. Similar mixing times were acquired by reducing the total flow rate while keeping ratio α constant. This way the sample consumption was minimised. According to data presented herein, the most appropriate chip design and inlet flow rates to be employed for an experiment should be selected depending on the samples used and the specific application requirements.

Similarly to results presented in the previous chapter and unlike the majority of microfluidic mixing studies, the combination of a fluorescence lifetime instead of a fluorescence intensity approach and a MLE method for lifetime determination ensured improved image quality and accurate population discrimination (Fsc-KI) under very low photon count conditions. Nonetheless, with the use of a scanning confocal configuration data were acquired rapidly and a ~250×250 μm^2 area (0.5-1.0 μm spatial resolution) could be imaged at a single acquisition, while the temporal resolution depended on the applied flow rates. Finally, the use of mathematical equations to successfully fit the mixing procedure within the microchannels as well as the mixing times obtained at different flow rate ratios rendered these measurements valuable for estimating microfluidic mixing characteristics in future experiments after performing an appropriate adjustment based on the different sample diffusion coefficients.

4.5. References

1. Jeong, G.S., S. Chung, C.-B. Kim and S.-H. Lee, *Applications of micromixing technology.* Analyst, 2010. **135**(3): p. 460-473.
2. Pollack, L., M.W. Tate, N.C. Darnton, J.B. Knight, S.M. Gruner, W.A. Eaton and R.H. Austin, *Compactness of the denatured state of a fast-folding protein measured by submillisecond small-angle x-ray scattering.* Proceedings of the National Academy of Sciences of the United States of America, 1999. **96**(18): p. 10115-10117.
3. Pollack, L., M.W. Tate, A.C. Finnefrock, C. Kalidas, S. Trotter, N.C. Darnton, L. Lurio, R.H. Austin, C.A. Batt, S.M. Gruner, and S.G.J. Mochrie, *Time resolved collapse of a folding protein observed with small angle x-ray scattering.* Physical Review Letters, 2001. **86**(21): p. 4962-4965.
4. Hertzog, D.E., X. Michalet, M. Jager, X.X. Kong, J.G. Santiago, S. Weiss and O. Bakajin, *Femtomole mixer for microsecond kinetic studies of protein folding.* Analytical Chemistry, 2004. **76**(24): p. 7169-7178.
5. Roder, H., K. Maki, H. Cheng and M.C.R. Shastry, *Rapid mixing methods for exploring the kinetics of protein folding.* Methods, 2004. **34**(1): p. 15-27.
6. Bilsel, O., C. Kayatekin, L.A. Wallace and C.R. Matthews, *A microchannel solution mixer for studying microsecond protein folding reactions.* Review of Scientific Instruments, 2005. **76**(1).
7. Hertzog, D.E., B. Ivorra, B. Mohammadi, O. Bakajin and J.G. Santiago, *Optimization of a microfluidic mixer for studying protein folding kinetics.* Analytical Chemistry, 2006. **78**(13): p. 4299-4306.
8. Yao, S. and O. Bakajin, *Improvements in mixing time and mixing uniformity in devices designed for studies of protein folding kinetics.* Analytical Chemistry, 2007. **79**(15): p. 5753-5759.
9. Bianco, P.R., L.R. Brewer, M. Corzett, R. Balhorn, Y. Yeh, S.C. Kowalczykowski and R.J. Baskin, *Processive translocation and DNA unwinding by individual RecBCD enzyme molecules.* Nature, 2001. **409**(6818): p. 374-378.
10. van Oijen, A.M., P.C. Blainey, D.J. Crampton, C.C. Richardson, T. Ellenberger and X.S. Xie, *Single-molecule kinetics of lambda exonuclease reveal base dependence and dynamic disorder.* Science, 2003. **301**(5637): p. 1235-1238.
11. Jung, S.-Y., Y. Liu and C.P. Collier, *Fast mixing and reaction initiation control of single-enzyme kinetics in confined volumes.* Langmuir, 2008. **24**(9): p. 4439-4442.
12. Amitani, I., R.J. Baskin and S.C. Kowalczykowski, *Visualization of Rad54, a chromatin remodeling protein, translocating on single DNA molecules.* Molecular Cell, 2006. **23**(1): p. 143-148.
13. Benninger, R.K.P., O. Hofmann, B. Onfelt, I. Munro, C. Dunsby, D.M. Davis, M.A.A. Neil, P.M.W. French and A.J. de Mello, *Fluorescence-lifetime imaging of DNA-dye interactions within continuous-flow microfluidic systems.* Angewandte Chemie-International Edition, 2007. **46**(13): p. 2228-2231.

14. Schaerli, Y., R.C. Wootton, T. Robinson, V. Stein, C. Dunsby, M.A.A. Neil, P.M.W. French, A.J. deMello, C. Abell and F. Hollfelder, *Continuous-Flow Polymerase Chain Reaction of Single-Copy DNA in Microfluidic Microdroplets.* Analytical Chemistry, 2009. **81**(1): p. 302-306.

15. Nguyen, N.T., *Micromixers. Fundamentals, designs and fabrication, 2nd edition.* Elsevier Inc., Oxford, 2012.

16. Hardt, S., K.S. Drese, V. Hessel and F. Schonfeld, *Passive micromixers for applications in the microreactor and mu TAS fields.* Microfluidics and Nanofluidics, 2005. **1**(2): p. 108-118.

17. Hessel, V., H. Lowe and F. Schonfeld, *Micromixers - a review on passive and active mixing principles.* Chemical Engineering Science, 2005. **60**(8-9): p. 2479-2501.

18. Nguyen, N.T. and Z.G. Wu, *Micromixers - a review.* Journal of Micromechanics and Microengineering, 2005. **15**(2): p. R1-R16.

19. Mansur, E.A., M. Ye, Y. Wang and Y. Dai, *A state-of-the-art review of mixing in microfluidic mixers.* Chinese Journal of Chemical Engineering, 2008. **16**(4): p. 503-516.

20. Lee, C.-Y., C.-L. Chang, Y.-N. Wang and L.-M. Fu, *Microfluidic Mixing: A Review.* International Journal of Molecular Sciences, 2011. **12**(5): p. 3263-3287.

21. Brody, J.P., P. Yager, R.E. Goldstein and R.H. Austin, *Biotechnology at low Reynolds numbers.* Biophysical Journal, 1996. **71**(6): p. 3430-3441.

22. Knight, J.B., A. Vishwanath, J.P. Brody and R.H. Austin, *Hydrodynamic focusing on a silicon chip: Mixing nanoliters in microseconds.* Physical Review Letters, 1998. **80**(17): p. 3863-3866.

23. Stroock, A.D., S.K.W. Dertinger, A. Ajdari, I. Mezic, H.A. Stone and G.M. Whitesides, *Chaotic mixer for microchannels.* Science, 2002. **295**(5555): p. 647-651.

24. Kauffmann, E., N.C. Darnton, R.H. Austin, C. Batt and K. Gerwert, *Lifetimes of intermediates in the beta-sheet to alpha-helix transition of beta-lactoglobulin by using a diffusional IR mixer.* Proceedings of the National Academy of Sciences of the United States of America, 2001. **98**(12): p. 6646-6649.

25. Pabit, S.A. and S.J. Hagen, *Laminar-flow fluid mixer for fast fluorescence kinetics studies.* Biophysical Journal, 2002. **83**(5): p. 2872-2878.

26. Dittrich, P.S., B. Muller and P. Schwille, *Studying reaction kinetics by simultaneous FRET and cross-correlation analysis in a miniaturized continuous flow reactor.* Physical Chemistry Chemical Physics, 2004. **6**(18): p. 4416-4420.

27. Nguyen, N.T. and X.Y. Huang, *Mixing in microchannels based on hydrodynamic focusing and time-interleaved segmentation: modelling and experiment.* Lab on a Chip, 2005. **5**(11): p. 1320-1326.

28. Park, H.Y., X.Y. Qiu, E. Rhoades, J. Korlach, L.W. Kwok, W.R. Zipfel, W.W. Webb and L. Pollack, *Achieving uniform mixing in a microfluidic device: Hydrodynamic focusing prior to mixing.* Analytical Chemistry, 2006. **78**(13): p. 4465-4473.

29. Schafer, D., E.A. Gibson, W. Amir, R. Erikson, J. Lawrence, T. Vestad, J. Squier, R. Jimenez and D.W.M. Marr, *Three-dimensional chemical concentration maps in a*

microfluidic device using two-photon absorption fluorescence imaging. Optics Letters, 2007. **32**(17): p. 2568-2570.

30. Gambin, Y., C. Simonnet, V. VanDelinder, A. Deniz and A. Groisman, *Ultrafast microfluidic mixer with three-dimensional flow focusing for studies of biochemical kinetics.* Lab on a Chip, 2010. **10**(5): p. 598-609.

31. Lipman, E.A., B. Schuler, O. Bakajin and W.A. Eaton, *Single-molecule measurement of protein folding kinetics.* Science, 2003. **301**(5637): p. 1233-1235.

32. Hamadani, K.M. and S. Weiss, *Nonequilibrium single molecule protein folding in a coaxial mixer.* Biophysical Journal, 2008. **95**(1): p. 352-365.

33. Dittrich, P.S. and P. Schwille, *An integrated microfluidic system for reaction, high-sensitivity detection, and sorting of fluorescent cells and particles.* Analytical Chemistry, 2003. **75**(21): p. 5767-5774.

34. Robinson, T., H.B. Manning, C. Dunsby, M.A.A. Neil, G.S. Baldwin, A.J. de Mello and P.M.W. French, *Investigating fast enzyme-DNA kinetics using multidimensional fluorescence imaging and microfluidics*, in *Microfluidics, Biomems, and Medical Microsystems Viii*. 2010.

35. Robinson, T., P. Valluri, H.B. Manning, D.M. Owen, I. Munro, C.B. Talbot, C. Dunsby, J.F. Eccleston, G.S. Baldwin, M.A.A. Neil, A.J. de Mello, and P.M.W. French, *Three-dimensional molecular mapping in a microfluidic mixing device using fluorescence lifetime imaging.* Optics Letters, 2008. **33**(16): p. 1887-1889.

36. Aubin, J., M. Ferrando and V. Jiricny, *Current methods for characterising mixing and flow in microchannels.* Chemical Engineering Science, 2010. **65**(6): p. 2065-2093.

37. Lu, Z., J. McMahon, H. Mohamed, D. Barnard, T.R. Shaikh, C.A. Mannella, T. Wagenknecht and T.-M. Lu, *Passive microfluidic device for submillisecond mixing.* Sensors and Actuators B-Chemical, 2010. **144**(1): p. 301-309.

38. Magennis, S.W., E.M. Graham and A.C. Jones, *Quantitative spatial mapping of mixing in microfluidic systems.* Angewandte Chemie-International Edition, 2005. **44**(40): p. 6512-6516.

39. Redford, G.I., Z.K. Majumdar, J.D.B. Sutin and R.M. Clegg, *Properties of microfluidic turbulent mixing revealed by fluorescence lifetime imaging.* Journal of Chemical Physics, 2005. **123**(22).

40. Matthews, S.M., A.D. Elder, K. Yunus, C.F. Kaminski, C.M. Brennan and A.C. Fisher, *Quantitative kinetic analysis in a microfluidic device using frequency-domain fluorescence lifetime imaging.* Analytical Chemistry, 2007. **79**(11): p. 4101-4109.

41. Baker, G.A., A.N. Watkins, S. Pandey and F.V. Bright, *Static and time-resolved fluorescence of fluorescein-labeled dextran dissolved in aqueous solution or sequestered within a sol-gel-derived hydrogel.* Analyst, 1999. **124**(3): p. 373-379.

CHAPTER 5
SINGLE MOLECULE DETECTION WITHIN MICROFLUIDIC CHANNELS

5.1. Introduction

Fluorescence microscopy has been extensively used in numerous scientific fields, the majority of applications, however, are related to biology and medicine. The increasing need for high sensitivity detection in biological and biomedical analysis has been the main motivation for performing measurements with single molecule resolution [1]. Applications, such as DNA analysis, immunoassays and forensics, require rapid measurements at very low concentrations. Moreover, in pathology and diagnostic medicine, the identification of a single copy of a protein or gene within a cell might be crucial. Single molecule measurements are ideal for such applications, as they represent the ultimate level of detection sensitivity. Unlike ensemble measurements, whereby only average properties of the studied population can be extracted, a single molecule approach allows for observations of individual molecular characteristics to be made [2]. No assumption of how the bulk population might vary is required. Therefore, direct comparison with theory and computer simulations can be much more efficient. Furthermore, ensemble experiments studying fast kinetics may require the initial synchronization of many molecules. For example, in protein folding studies, the folding of many molecules must be synchronized by a starting event, which inevitably introduces a dead time for observation [3]. This can make it impossible to investigate early kinetic events. Such synchronization is not needed at the single molecule level, hence, reactions or folding kinetics can be monitored with much shorter dead times. In addition to high sensitivity, single molecule experiments can also provide information about the local environment of the molecule with extremely high spatial resolution, as an individual fluorophore can probe its surroundings via the decay rate k_{nr} within only a few cubic nanometres [1].

In single molecule detection (SMD) experiments, it is important to ensure that the collected signal originates from a single molecule. This can typically be achieved by working at low sample concentrations, so that at most one molecule of interest is present in the excitation volume within any given time period. At the same time, special optical arrangements can be employed to improve the signal-to-noise ratio *S/N*. Amongst the various optical configurations proposed [4], factors that hold common are the necessity to enable the reduction of the

excitation and detection volumes, improved delivery of the excitation light and increased rejection of the background light interfering with the original signal.

The most commonly used approach fulfilling the above criteria is confocal microscopy. The principle and advantages of a confocal configuration were presented in detail in section 1.1.3. Since it was applied at the single molecule level for the first time [5], confocal microscopy has been extensively used in SMD fluorescence spectroscopy. A variety of related applications can be found in references [1, 6, 7] and examples of home-built scanning units for SMD are given in references [8-10].

Apart from confocal microscopy, total internal reflection fluorescence microscopy (TIRFM) has also been employed as an efficient method for minimizing background levels. A number of studies employing TIRFM are presented in references [11] and [12]. Although this technique results in high *S/N*, the short penetration depth (typically around 150 nm) renders this method suitable mainly for applications whereby the molecules of interest are immobilised on a surface. Elegant exceptions have been demonstrated by Hollars et al. [13] and Le at al. [14], who used TIRFM for monitoring DNA molecules flowing within appropriately configured microchannels. An alternative method for effectively reducing the focal volume involves modifying the sample illumination profile with the use of zero mode waveguides (ZMWs) [15]. ZMWs reduce the effective observation volume down to 10^{-21} l and allow for SMD at concentrations as high as 200 μM [16]. Examples of studies employing ZMWs for measurements at the single molecule level can be found in references [16-18].

As mentioned above, a common method employed for performing measurements at the single molecule level involves immobilisation of the molecule of interest on a surface and observing the signal over time. Although this is readily achieved for nucleic acids, it appears to be problematic for proteins and other biomolecules. The degree to which the immobilised molecule is perturbed by the nearby surface as well as by the overall immobilisation protocol is not always straightforward. Also, extended illumination may lead to early fluorescence photobleaching. Measurements of molecules in solution while they freely diffuse or flow through the detection volume can overcome these problems. Furthermore, as discussed in section 1.2.1, the use of a microfluidic platform instead of performing measurements on freely diffusing molecules can be beneficial in terms of acquisition time and statistical accuracy. A large number of biological applications combining microfluidics and SMD techniques have been proposed and for a detailed review the reader is directed to some very good review articles available within this field [19-21].

Flow of individual molecules through the probe volume gives rise to a stochastic series of fluorescence bursts and useful information can be extracted via appropriate burst analysis. For example, straightforward counting of the fluorescence bursts has been used for enumeration and concentration estimation purposes [22-24] or to evaluate the detection ability and limits of a specific experimental arrangement [25]. Moreover, in applications whereby species are distinguishable by the quantity of fluorophore labelled to them, the burst width and burst area distributions can be directly related to the molecule size [26]. In DNA fragment sizing applications, SMD and microfluidics techniques have been attractive due to their sensitivity and the ability for quick analysis with very low sample consumption. The quantity of fluorescent dye intercalated into a DNA fragment is directly proportional to its length [27]. Thus, assuming that all fragments experience the same excitation intensity, the number of photons detected per fragment has been used as a direct measure of its size [28-32]. Combined burst size and burst frequency analysis can be used to extract the relative proportions of individual species within a mixture of molecules [33] and perform molecular separations within microchannels [34, 35].

Discrimination between the components of a mixture of molecules has also been achieved based on differences in the molecule transit times extracted via fluorescence correlation spectroscopy (FCS) [36, 37]. FCS entails the statistical analysis of fluctuations in the fluorescence intensity emitted by single molecules traversing the detection volume and can be used to obtain parameters such as local concentrations, mobility coefficients and time constants of internal fluctuations [38]. In this manner, binding ratios and reaction kinetics within microchannels can be determined based on the different mobility of flowing molecular complexes [39].

SMD techniques combined with microfluidics have been employed for studying a variety of interactions between different reactants and species [30, 40-44] including cell biology applications [45, 46]. Hydrodynamic flow profiling and construction of three-dimensional velocity maps within microchannels have also been demonstrated by performing measurements at the single molecule level [47-49].

Apart from experiments whereby the molecules of interest are flowing down the length of a microfluidic channel, alternative applications combining SMD and microfluidic methods have been suggested. DNA sequencing was demonstrated by anchoring a DNA strand with distinguishably labelled nucleotides within an exonuclease flow stream and subsequently detecting the sequentially cleaved single nucleotides [50, 51]. Furthermore, a flow stream containing appropriate reagents, can be used to stretch single DNA molecules immobilised on the channel surface, with the purpose to investigate DNA-protein interactions and enzymatic

reactions at the single molecule level [21, 52-55]. DNA stretching has also been achieved by employing hydrodynamic focusing in microfluidic channels [56] or with the use of nanochannels with dimensions smaller than the radius of gyration of the DNA molecule [15]. A different approach entails encapsulation of single molecules into droplets and carrying out reaction kinetics measurements within the droplet on the single molecule scale [57].

It is clear that employing an appropriate optical arrangement together with a specially configured microfluidic platform, can maximize the detection efficiency and improve the *S/N* enabling measurements at the single molecule level. In this chapter, the custom-built optical detection system was used in conjunction with microfluidic channels to detect freely flowing single DNA molecules in real time. Photon arrival events were recorded using TCSPC and fluorescence burst analysis was performed under a wide range of flow rates. Subsequently, hydrodynamic focusing was employed as a molecular confinement mechanism to investigate the benefits on single molecule detection efficiency.

5.2. Experimental description and methodology

5.2.1. Sample preparation

Double stranded λ-DNA (~48 kbp) was purchased from New England Biolabs Ltd. and labelled with the intercalating dye YOYO-1 (Invitrogen) at a ratio of 1 dye molecule per 5 base pairs [58]. λ-DNA and YOYO-1 solutions were prepared in filtered 1×Tris-Acetate EDTA buffer (40 mM Tris-Acetate and 1 mM EDTA) at pH 8.0 and mixed to a final λ-DNA concentration of 1 nM. The λ-DNA was allowed to stain for 1 hour before use. λ-DNA solutions of 20 pM were then prepared in the same buffer for use in the SMD experiments.

5.2.2. Experimental procedure and data analysis

In order to detect single molecules in flow, 20 pM λ-DNA solution was introduced in a channel at flow rates varying between 0.01-0.25 μl/min. The flow rates were kept as low as possible to minimise DNA sample consumption as well as to ensure linear flow velocities within the single molecule detection limits of the system. The microfluidic device used was the design III tested during focusing experiments (figure 3.3 in chapter 3), with the addition of 15 μm wide nozzles (50 μm deep, details in Appendix A, figure A.5). During the experiments the side inlets were kept blocked. Excitation path 1 along with pulsed diode laser LDH-P-C-470 (section 2.1.1.1) were used for YOYO-1 excitation. Single point-excitation mode was used to detect λ-DNA molecules traversing the probe volume (no imaging). Photon arrival data were

acquired using the TimeHarp 200 TTTR mode (acquisition time 120 s) and analysed as described in section 2.3.4, using a re-sampling time of 1 ms. A threshold of 20 photon counts was applied by the peak locating algorithm in order to distinguish between single molecule bursts and background noise. The same number of photons was set as the minimum limit for fluorescence lifetime determination by the MLE routine. Burst height, width and area, as well as fluorescence lifetime histograms were produced and appropriately analysed.

In experiments whereby hydrodynamic focusing was employed for sample confinement, the central and side flows consisted of 20 pM λ-DNA and Tris-Acetate EDTA buffer respectively. The central inlet flow rate varied between 0.025-0.7 μl/min, while the side inlet flow rate was adjusted to achieve side-to-central inlet flow rate ratios of 1 and 4. The laser spot was carefully positioned approximately in the middle of the outlet channel to ensure that single DNA molecules flowing within the focused stream were detected. Data were acquired and analysed as before, with respect to the central inlet flow rate (related to the sample consumption) as well as the outlet flow rate, which is a measure of the detected molecules velocity.

5.3. Results and Discussion

5.3.1. Detection of single molecules freely flowing within a microchannel

5.3.1.1. Single molecule detection frequency

Representative fluorescence burst scans for different sample flow rates within a microfluidic channel are shown in figure 5.1. The blue circles indicate bursts exceeding the background threshold (green dashed line) and correspond to single DNA molecule events.

As seen in figure 5.1, the number of detected DNA molecules increased with volumetric flow rate. This was directly related to the number of molecules available for detection. At high volumetric flow rates, a larger number of molecules were introduced into the channel, and hence traversed the probe volume, in the unit of time.

The number of located peaks, and thus the number of detected molecules, per second for each flow rate followed a normal distribution. Both mean and spread of the distribution increased with flow rate (figure 5.2). The normal distribution probability density function (pdf) is:

$$y = f(x \mid p_1, p_2) = \frac{1}{p_1\sqrt{2\pi}} e^{-\frac{1}{2}\left(\frac{x-p_2}{p_1}\right)^2} \tag{5.1}$$

where p_1, p_2 are the standard deviation and the mean of the distribution respectively.

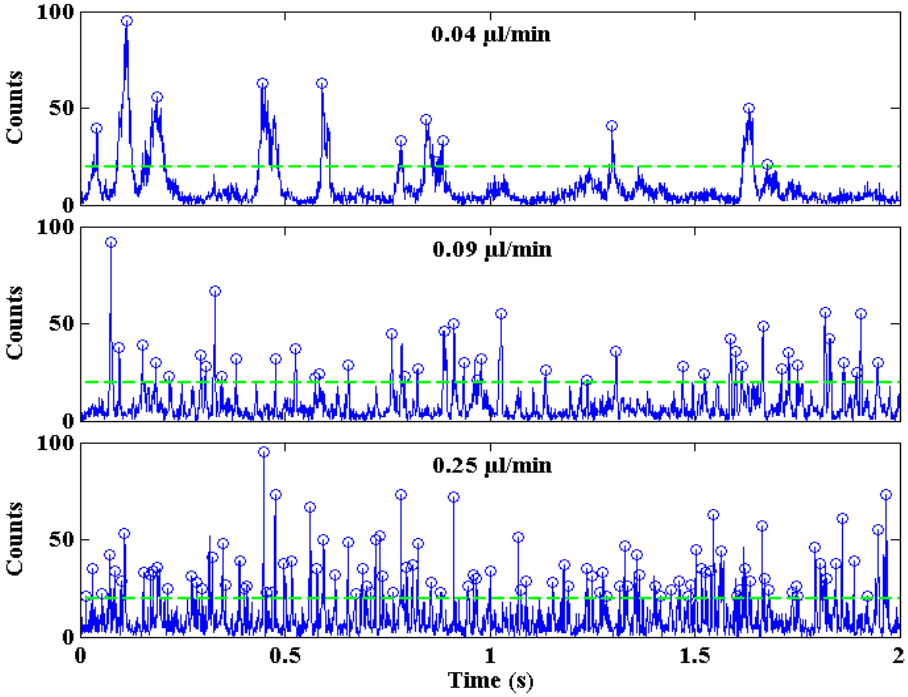

Figure 5.1. Representative single molecule burst scans for flow rates of 0.04, 0.09 and 0.25 µl/min. The applied threshold for distinguishing between single molecule bursts and noise is represented by the green dashed line. The blue circles indicate located peaks.

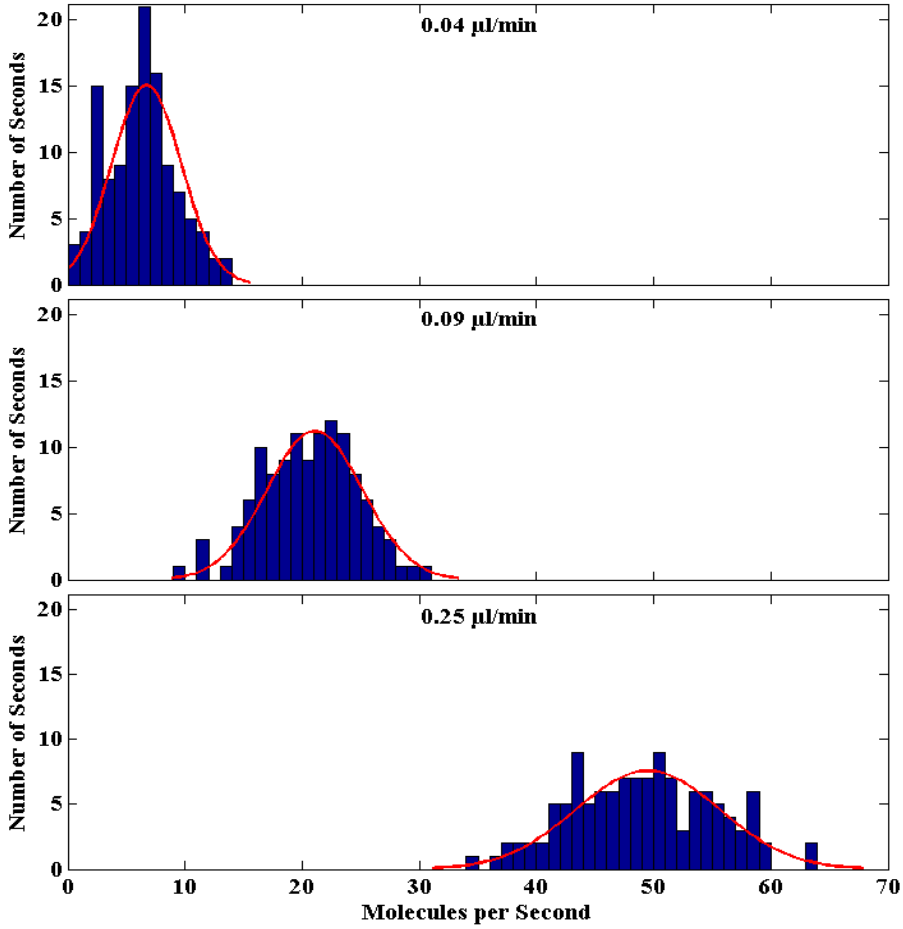

Figure 5.2. Fluorescence burst frequency histograms and normal distribution fits for flow rates of 0.04, 0.09 and 0.25 µl/min.

Figure 5.3 illustrates that the mean fluorescence burst frequency was proportional to the flow speed, the extrapolated value at a flow rate of 0 µl/min, however, did not yield zero molecules because of the natural diffusive behaviour of the DNA molecules through the probe volume [59]. The large standard deviation observed for flow rates below 0.04 µl/min was possibly due to the molecular diffusion through the probe volume at these flow rates being significant with respect to bulk flow velocities [26]. For a flow rate of 0.01 µl/min for example the linear flow velocity was ~0.33 µm/ms while the theoretically calculated diffusion distance (equation 3.8) at the detection point (~50 µm from the junction) was ~0.30 µm. At high flow rates, diffusion became negligible. At the timescale of the measurement however, it is possible that a number of molecules traversed the probe volume undetected; at the same time a proportion of bursts were not fully resolved. As a result, the standard deviation of the burst frequency distribution slightly increased with flow rate in the region between 0.04 and 0.25µl/min (figure 5.3, inset).

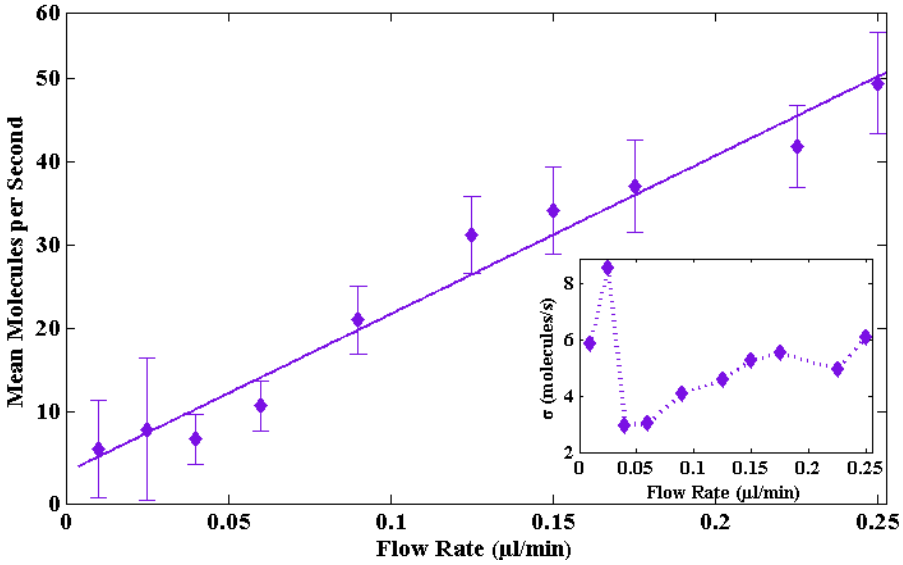

Figure 5.3. Mean number of molecules detected per second versus flow rate, error bars represent standard deviation σ. Inset: Standard deviation versus flow rate.

5.3.1.2. Burst height distribution analysis

The burst height is defined as the maximum photon count occurring within the boundaries of a burst and the higher height obtained herein was 126 photon counts. Representative burst height histograms for flow rates of 0.04, 0.09 and 0.25 µl/min are given in figure 5.4. Observation of the burst height histograms yields that the peak height followed an exponential distribution with generalised pdf:

$$y = f(x \mid p_1, p_2) = \frac{1}{p_1} e^{-\frac{x-p_2}{p_1}} \tag{5.2}$$

where p_1 and p_2 relate to the mean and the location of the distribution respectively.

More specifically, p_2 represents the starting point of the distribution (first value on the x axis) and, in the case that p_2=0, p_1 is the distribution mean. Otherwise, the mean is given by p_1+p_2. Although the exponential distribution is usually used to model time-related variables, burst height data were successfully fitted using appropriate Matlab code (figure 5.4).

Figure 5.5 shows the resulting fits for flow rates of 0.01-0.25 µl/min, all characterised by χ_R^2 above 0.97, with the exception of flow rates 0.01 µl/min and 0.05 µl/min, which corresponded to χ_R^2 of 0.83 and 0.82 respectively. The starting point of the distribution (p_2) was the 20 photon counts threshold applied for burst-background discrimination. It is evident that the distributions followed a similar pattern for all flow rates and a greater number of molecules corresponded to each burst height bin under high flow rates. This was expected, as the overall number of molecules detected at fast flow rates was larger, and was more pronounced for peak heights between 20 and 40 photon counts.

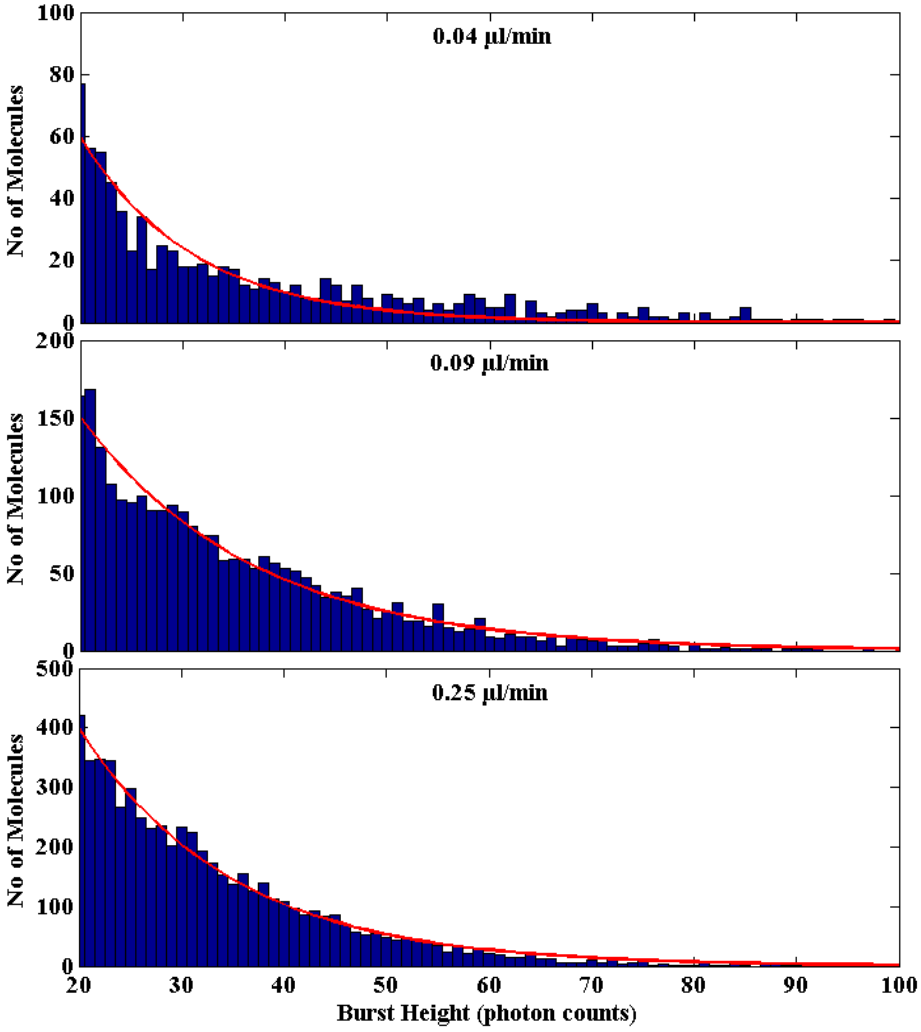

Figure 5.4. Burst height histograms and exponential distribution fits for flow rates of 0.04, 0.09 and 0.25 µl/min.

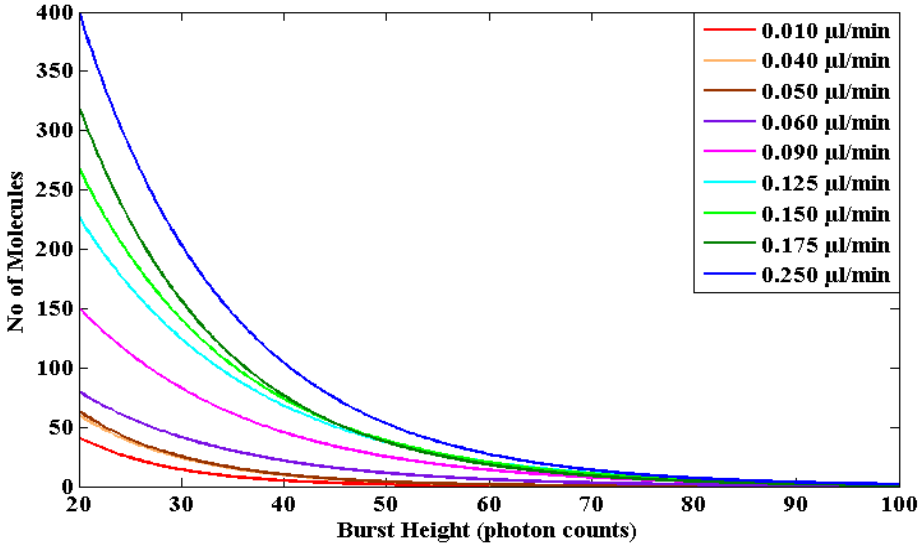

Figure 5.5. Exponential burst height distribution fits for flow rates between 0.01-0.25 µl/min.

The significant variation in burst height under the same volumetric flow rate was partially due to the many possible molecular trajectories through the detection volume [26, 60]. Since the probe volume had a non-uniform illumination intensity distribution, the emitted fluorescence was strongly dependent on the location of the molecule within the beam [60]. Given that all λ-DNA molecules had the same size and, therefore, contained the same amount of fluorescence dye molecules, the average burst height was not expected to be significantly affected by the sample flow rate. For the acquisition and plotting resolution used herein, combined with the applied flow velocities, variations in molecular transit times due to different volumetric flow rates were generally represented by changes in the burst width and area. This was confirmed in figure 5.6, where the mean burst height (p_1+p_2) was plotted versus volumetric flow rate. Error bars represent standard deviation (p_1).

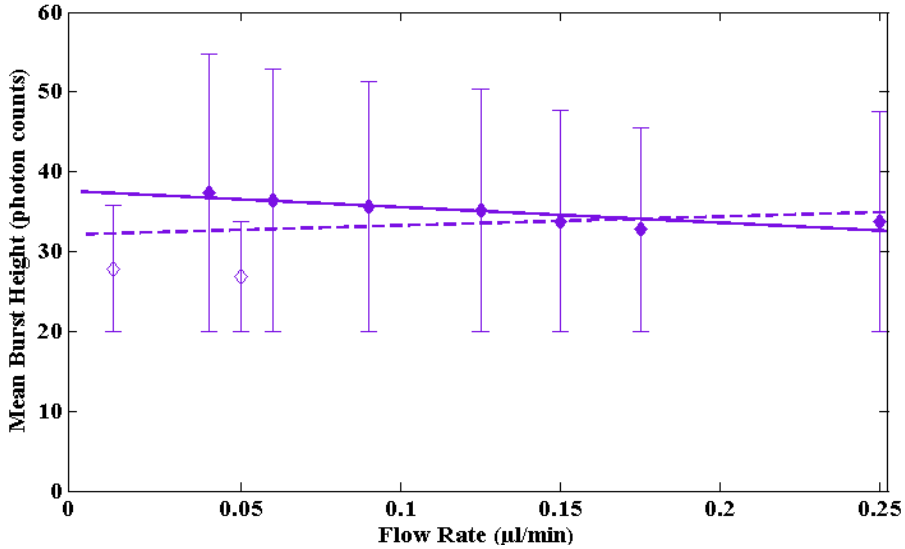

Figure 5.6. Mean fluorescence burst height versus flow rate. Open markers represent anomalous points which were not taken into account for the final fit (solid line). The fit represented by the dashed line includes all flow rates.

The extracted mean burst height appeared approximately constant if all data points were taken into account (figure 5.6, dashed line). However, due to the problematic distribution fitting for flow rates 0.01 and 0.05 μl/min, these two conditions were considered as anomalous (figure 5.6, open diamond markers). Excluding flow rates 0.01 and 0.05 μl/min, a slight decrease in the mean burst height was observed for increasing volumetric flow rate (figure 5.6, solid line), which could possibly be the result of molecules traversing the probe volume faster. The same trend was observed for the standard deviation, which in exponential distributions equals the mean parameter p_1. Assuming this change insignificant, the mean peak height varied between 33 and 37 counts (at 0.175 and 0.04 μl/min respectively) and the average value was 35 photon counts with a standard deviation of ~2 photon counts.

5.3.1.3. Burst width distribution analysis

Fluorescence burst duration is directly related to the flow rate [26]. This can be noticed in figure 5.1 and is clearly illustrated in figure 5.7, where burst width histograms are shown for flow rates of 0.04, 0.09 and 0.25 μl/min. Burst duration typically varied between 1 ms (the resampling time) and 100 ms, but isolated events with duration above 100 ms were also observed at flow rates below 0.06 μl/min. The maximum burst width recorded was 669 ms.

Burst width variation under the same flow rate was partially due to the Gaussian profile of the focused beam and the curved contribution to the probe volume (chapter2, figure 2.8). As a result, molecules of the same size and speed traversed the detection volume in different times depending on their location in the probe volume. Although the Gaussian probe volume was symmetrical, it can be seen in figure 5.7 that fluorescence burst width histograms were positively skewed, especially at low flow rates. Hence, they were better approximated using a gamma distribution, characterised by the following pdf:

$$y = f(x \mid p_1, p_2) = \frac{1}{{p_2}^{p_1}\Gamma(p_1)} x^{p_1-1} e^{-\frac{x}{p_2}} \tag{5.3}$$

where $\Gamma(p_1)$ is the gamma function. p_1 is the shape parameter and the skewness of the distribution is defined as $\frac{2}{\sqrt{p_1}}$ (positive). Thus, as p_1 increases, the gamma distribution becomes less skewed and approaches the normal distribution. p_2 is a parameter associated with the spread of the distribution and large values of p_2 yield wider spread. The distribution mean and standard deviation are given by $p_1 \times p_2$ and $\sqrt{p_1} \times p_2$ respectively. The fits obtained for flow rates between 0.01-0.25 μl/min are shown in figure 5.8.

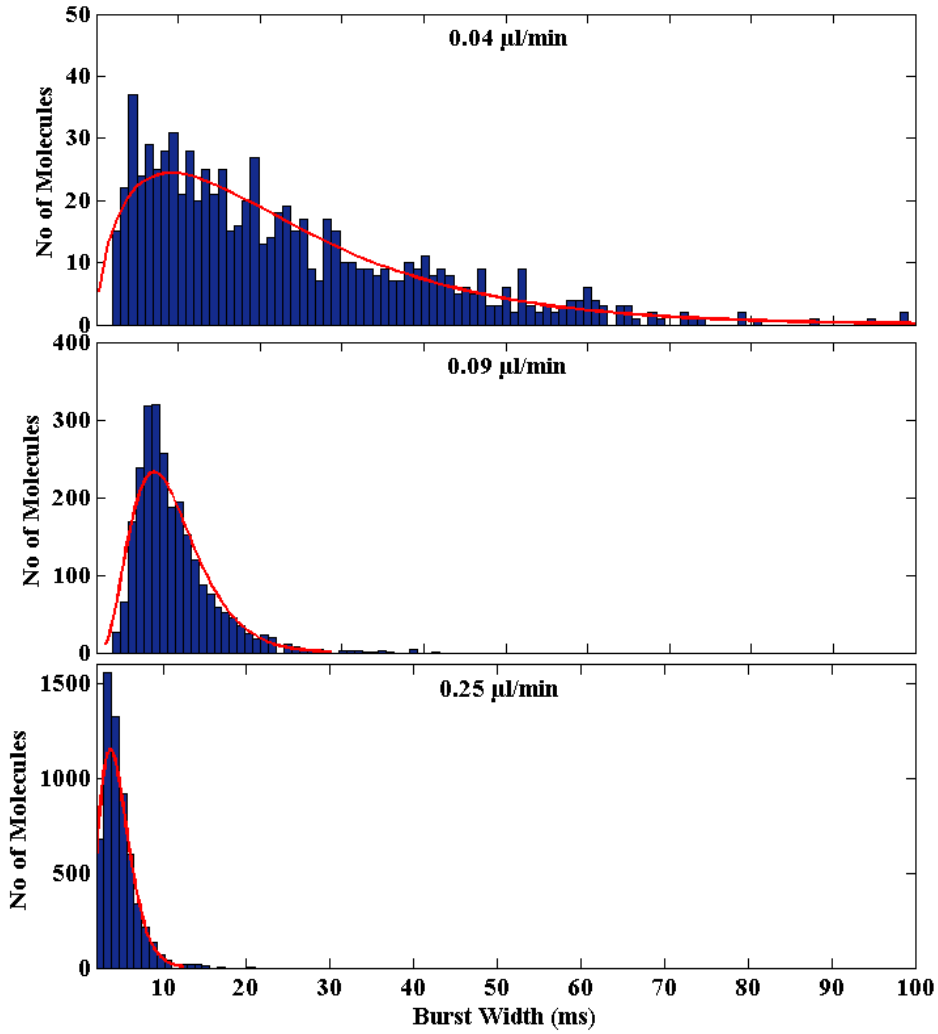

Figure 5.7. Fluorescence burst width histograms and gamma distribution fits for flow rates of 0.04, 0.09 and 0.25 µl/min.

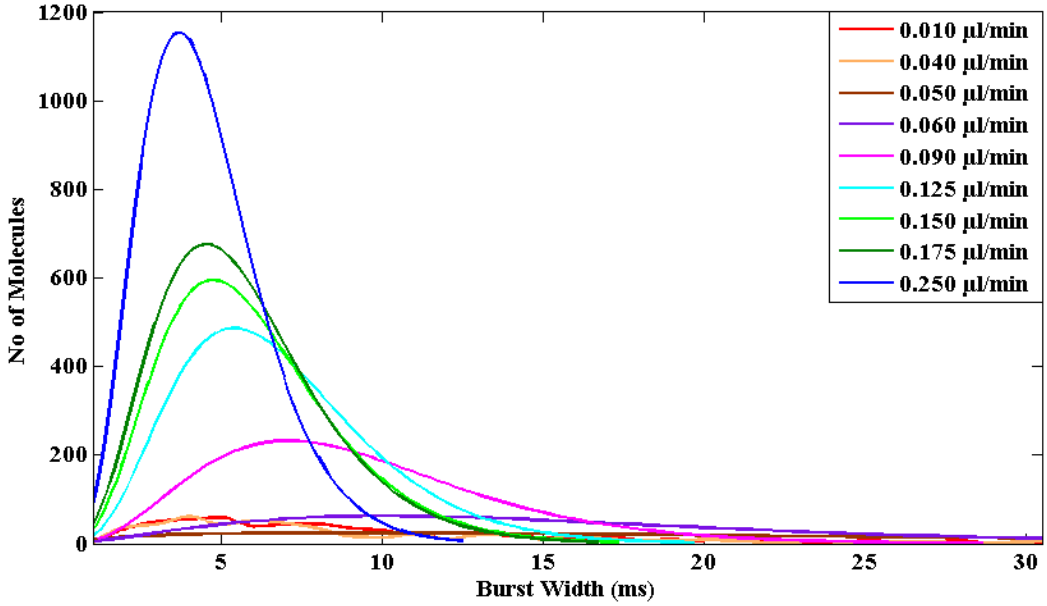

Figure 5.8. Gamma burst width distribution fits for flow rates between 0.01-0.25 µl/min.

It is evident that at high volumetric flow rates, the distribution peak shifted towards shorter burst widths and less spread was observed. At the same time, the distribution became less skewed due to the higher values of parameter p_1 obtained (figure 5.9), and approximated the Gaussian shape as the 'tail' slowly disappeared.

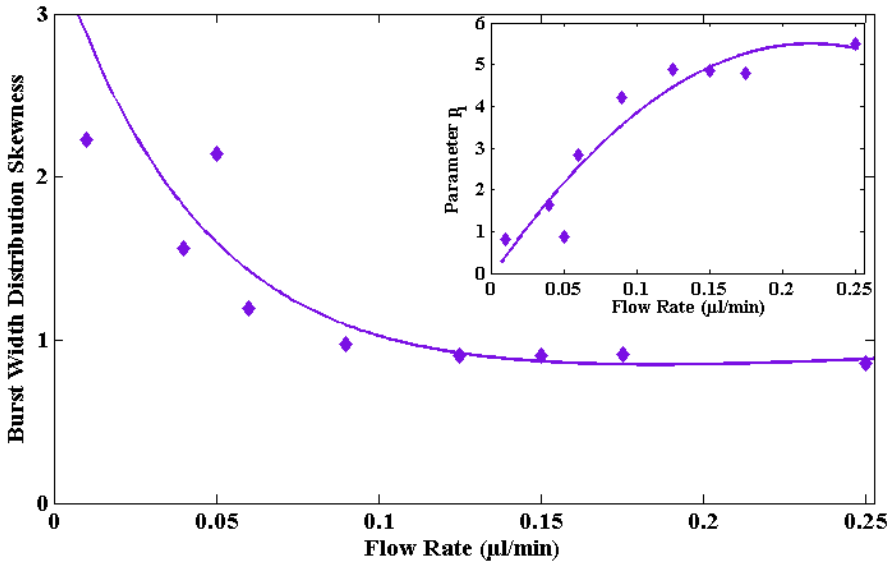

Figure 5.9. Burst width distribution skewness versus flow rate. The skewness was calculated via parameter p_1 (inset).

The extracted mean burst width values for each flow rate are shown in figure 5.10. Taking into account the microfluidic channel dimensions and the flow rates used, as well as the parabolic velocity profile within the microchannels [61, 62], the flow velocity increased from 0.33 µm/ms (for flow rate 0.01 µl/min) to 8.33 µm/ms (for flow rate 0.25 µl/min). For a given molecule shape and size, molecules flowing at high velocities were associated with the probe volume for a shorter period of time, therefore, the mean burst duration decreased when the volumetric flow rate increased.

It should be noted that, according to data presented in figure 5.10, this relationship was not linear. At low flow rates, the trajectory of the molecules within the probe volume was significantly affected by molecular diffusion. Hence, single molecules travelling through the detection volume potentially followed a range of different paths, prolonging or shortening the molecular transit time. This was partially the reason for the wide spread and high standard deviation of the distributions observed at low volumetric flow rates (figure 5.11). As it was previously mentioned, at high flow rates diffusion became negligible compared to the flow velocity and molecules traversed the detection volume with approximately constant trajectory [26]. As a result, a more even distribution of fluorescence burst widths was acquired, as indicated by smaller skewness and standard deviation (figures 5.9 and 5.11).

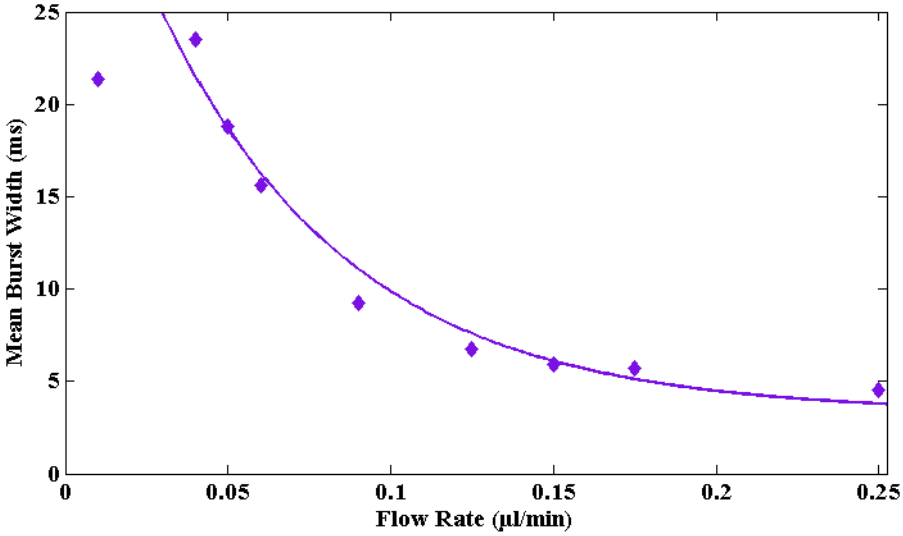

Figure 5.10. Mean burst width versus flow rate extracted from gamma distribution fits. Standard deviation is shown in figure 5.11.

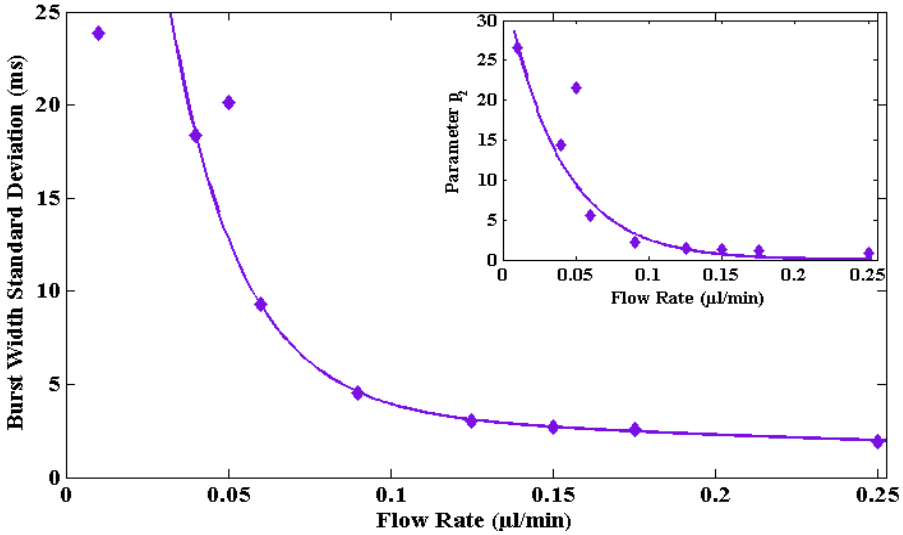

Figure 5.11. Burst width distribution standard deviation versus flow rate. The gamma distribution standard deviation is mainly determined by fitting parameter p_2 (inset).

In addition, at high flow velocities, it is possible that a fraction of the detected molecules were not fully resolved, yielding longer than the expected fluorescence burst duration. This limitation, together with the 1 ms resampling time used for the analysis, could possibly be factors affecting the linearity of the burst width-flow rate relationship and leading to the burst width plateau observed for high flow rates in figure 5.10.

Furthermore, it is not totally clear to what degree the conformation of the λ-DNA molecule was affected by the flow velocity. The presence of the nozzle at the exit of the inlet channel accelerated the fluid and an elongational flow was generated along the channel centreline, causing the initially coiled λ-DNA molecules to (partially) stretch [63]. Depending on the molecular velocity, and thus on the applied flow rate, the degree of DNA relaxation at the location of the measurement (within the outlet nozzle, at approximately 50 µm from the

junction) was different. It is possible that the length of the λ-DNA molecules at the position of the measurement was larger under high flow rates, leading to longer burst duration times as indicated by the plateau of the acquired burst width values in figure 5.10.

In terms of burst width spread under the same flow rate, a primary reason for the small burst width standard deviation at high flow rates was the detection and subsequent analysis of a greater number of single molecule events within the acquisition time. For example, mean burst duration for flow rate of 0.01 μl/min was extracted via analysis of 667 fluorescence peaks as opposed to the 5954 peaks used for the 0.25 μl/min flow rate. A higher number of bursts was certainly favourable for statistical analysis and accuracy.

5.3.1.4. Burst area distribution

The fluorescence burst area is defined as the total number of photons composing one intensity peak and is closely related to both peak height and duration. In the experiments performed herein, the burst height exhibited only a slight decrease when the volumetric flow rate increased, thus, variations in the burst area were expected to be mainly determined by changes in fluorescence peak width. Representative burst area histograms are shown in figure 5.12.

Similarly to burst width histograms, the total number of photon counts recorded per fluorescence peak was smaller when high flow rates were applied. For flow rates up to 0.04 μl/min, large spread of the peak area was observed, with values typically varying between 20-2500 photon counts, but bursts with areas above 2500 counts also occasionally appeared. The maximum area recorded was $\sim 20 \times 10^3$ photon counts (at flow rate of 0.01 μl/min). At flow rates above 0.09 μl/min, the total photon counts per burst did not exceed ~450.

The obtained burst area histograms (figure 5.12) revealed that there were two burst area 'populations' detected, indicated by two separate peaks in the histograms. The one 'population' followed a normal distribution around approximately the same mean value for all flow rates, while the other one could be described using a gamma distribution, similar to that, characterising the fluorescence burst width.

Fitting histograms to a mixed normal-gamma distribution can be complicated. Therefore, a threshold of 40 photon counts per burst was applied to distinguish between the two distributions, which were subsequently fitted individually via equations 5.1. and 5.3. Nevertheless, this method could possibly lead to slight statistical discrepancies because the shift of the gamma distribution towards lower burst areas resulted in an overlapping region for

flow rates below 0.06 µl/min. This region was taken into account only as a part of the normal distribution. The calculated distribution fits are shown in figure 5.13.

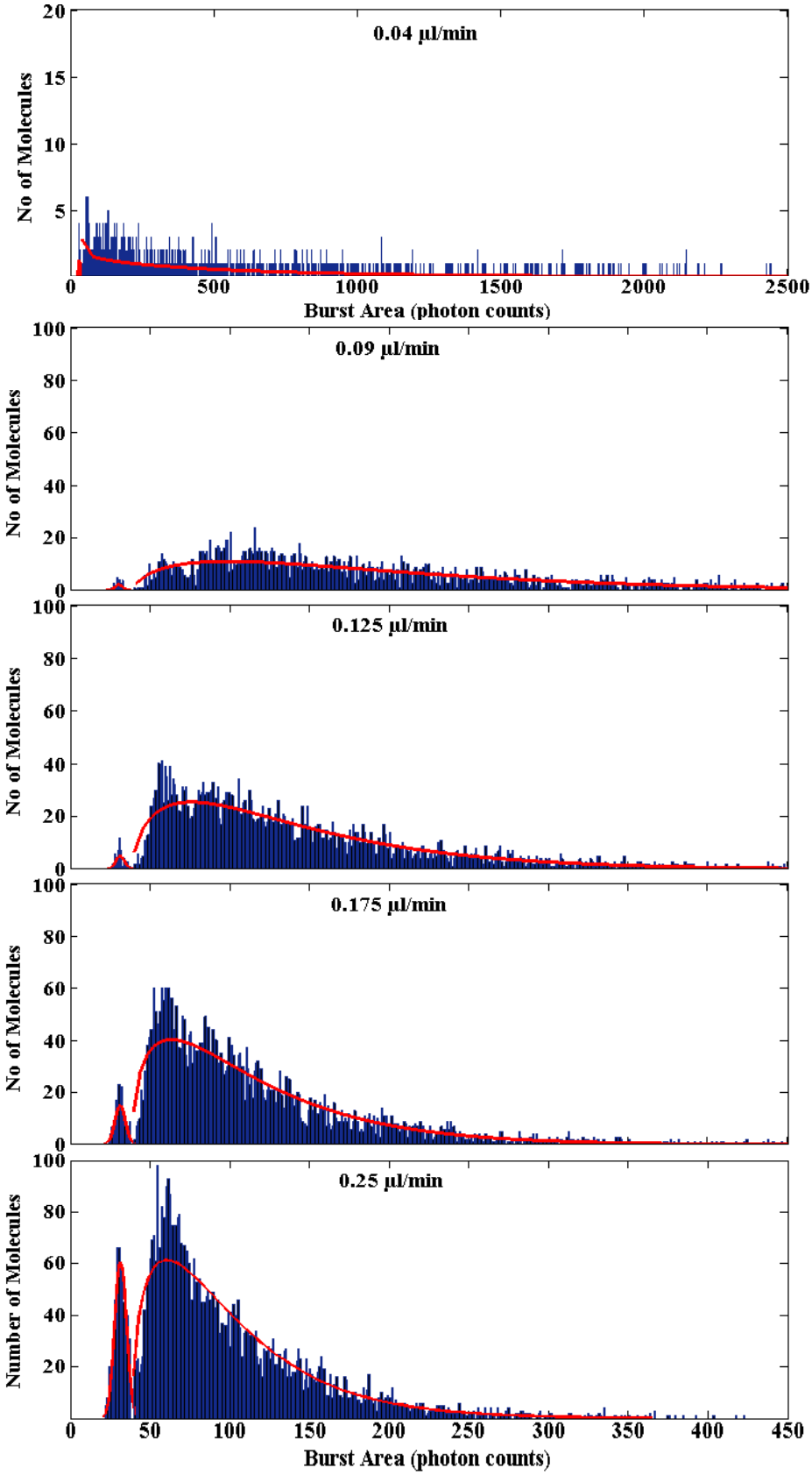

Figure 5.12. Fluorescence burst area histograms and mixed normal-gamma distribution fits.

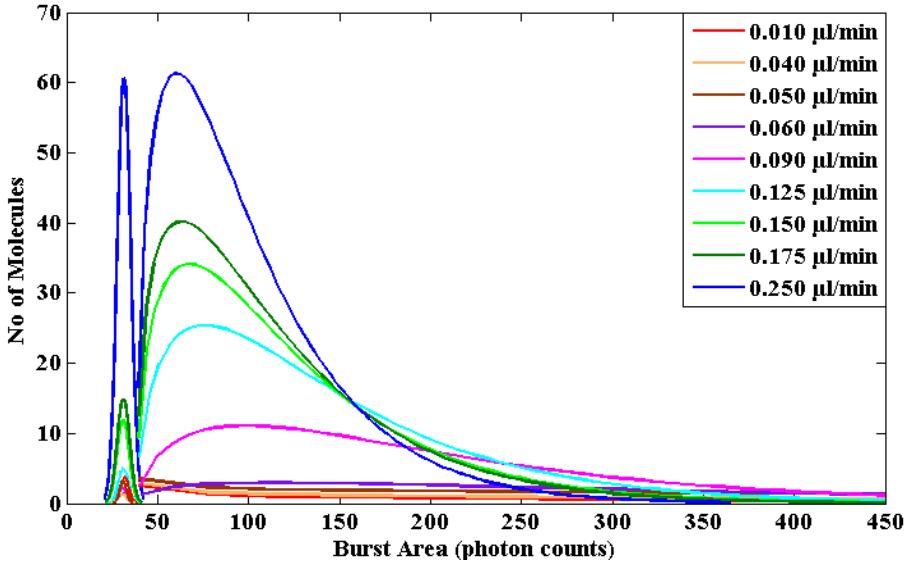

Figure 5.13. Normal and gamma burst area distribution fits at flow rates of 0.01-0.25 µl/min.

The mean of the normal distribution together with its standard deviation for various flow rates is shown in Figure 5.14. The distribution mean did not change with flow rate and yielded an average of 31 photon counts per burst with standard deviation of less than 1 photon (0.46 photon counts).

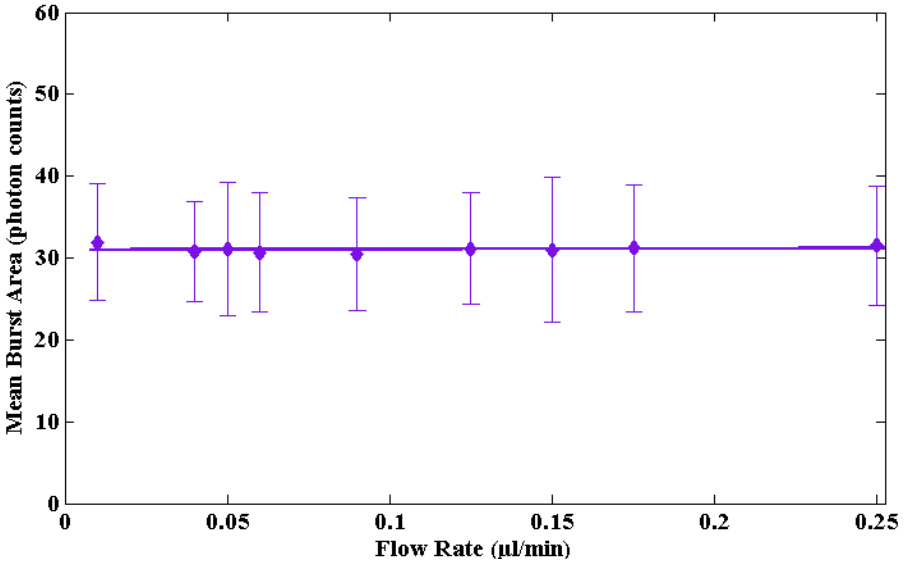

Figure 5.14. Mean burst area extracted from the normal distribution part of the area histograms versus flow rate. Error bars represent standard deviation.

Comparing the average burst area to the mean burst height extracted in section 5.3.1.2 (35±2 photon counts), it was safely assumed that the part of the burst area histogram represented by the normal distribution corresponded to fluorescence bursts which, although they exceeded the peak locating algorithm threshold, they exhibited very small duration. These bursts could probably be attributed to single molecules traversing the probe volume in times shorter than the resampling time used during analysis. Therefore, they appeared as individual spikes in the fluorescence burst scan. This opinion was supported by the fact that the number of bursts composing the normal distribution significantly increased with the flow rate, indicating that the spikes most probably corresponded to rapidly moving single DNA molecules and were not related to noise or failure of the selected signal-background discrimination threshold.

The mean, the standard deviation and the skewness of the gamma distributions are given in figure 5.15. These properties followed the same trends described in section 5.3.1.3 for burst width distributions. This was expected, as for a given molecule and approximately constant mean burst height, the burst width and area distributions should vary in a similar manner.

It becomes apparent that fluorescence burst analysis can be used to distinguish between populations within a sample. For example, fluorophores with different extinction coefficient and quantum yield emit different number of photons per molecule and, thus, in a burst area histogram they should yield separate distributions. Similar observations could possibly be made using burst height histograms.

Furthermore, in applications whereby the quantity of fluorophore labelled on a molecule is proportional to the molecule size, the photon counts recorded per burst are directly related to the size of the molecule [26]. For example, when intercalating dyes are used to label DNA, the amount of fluorescent molecules attached on a DNA fragment is proportional to its length [27]. Scanning a mixture of differently sized DNA fragments should yield a burst area histogram, whereby each fragment length is represented by an individual distribution. Differently sized fluorescent or fluorescently labelled molecules can also be distinguished and separated using burst width histogram analysis, as larger molecules are associated with the detection volume for a longer time. Finally, the absolute size of a molecule, in terms of length, can be estimated based on the burst width distribution, on condition that the linear velocity and the probe volume dimensions can be accurately determined.

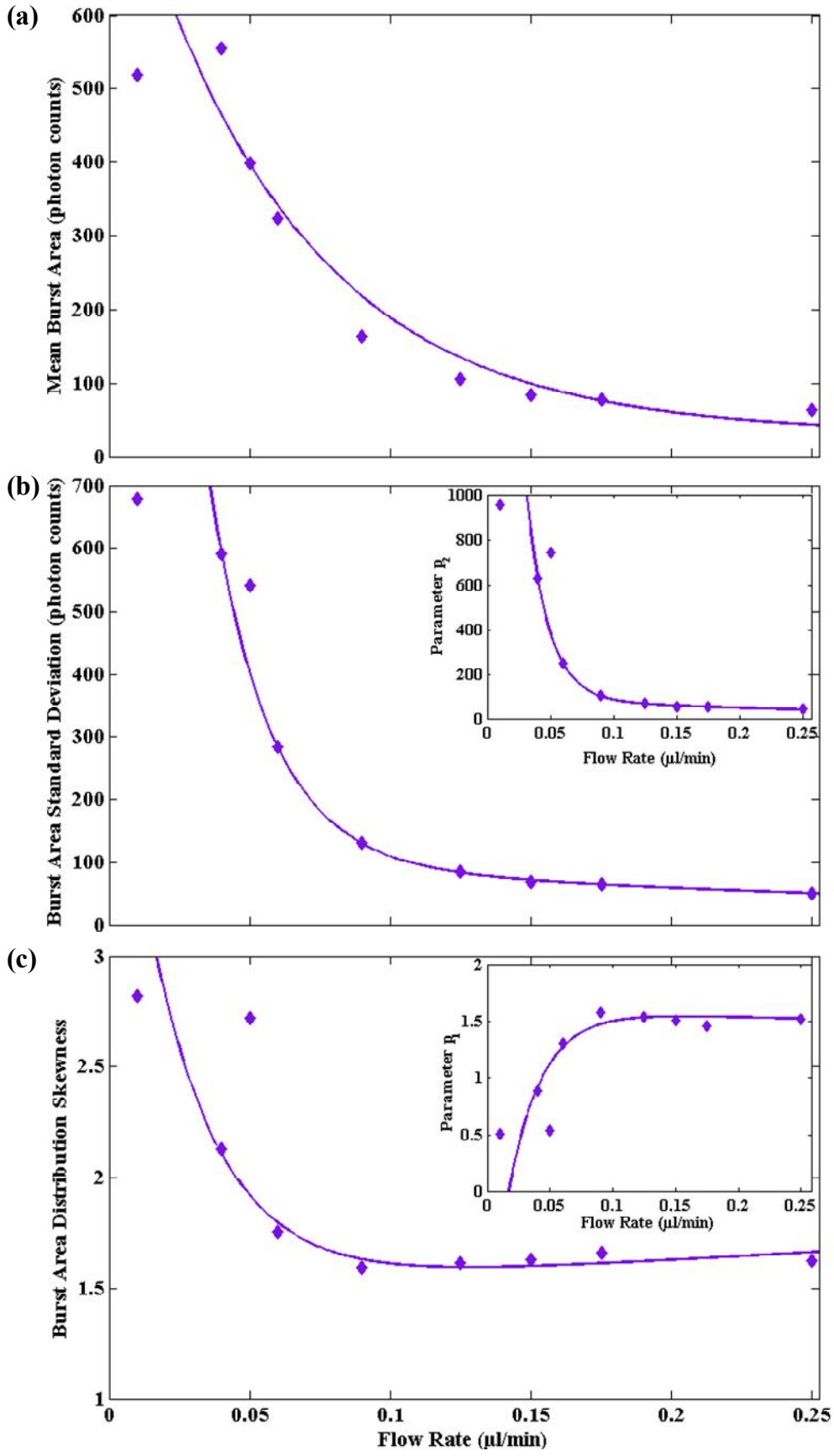

Figure 5.15. (a) Mean (b) standard deviation and (c) skewness of the gamma distribution part of the burst area histograms versus flow rate. Fitting parameters p_2 and p_1, related to standard deviation and skewness respectively, are shown in the insets ((b) and (c) respectively).

5.3.1.5. Single molecule fluorescence lifetime

Fluorescence lifetimes derived from single molecules typically follow a normal distribution. Figure 5.16 shows representative single molecule lifetime histograms. Distribution fits (equation 5.1) for flow rates between 0.01-0.25 µl/min are given in figure 5.17.

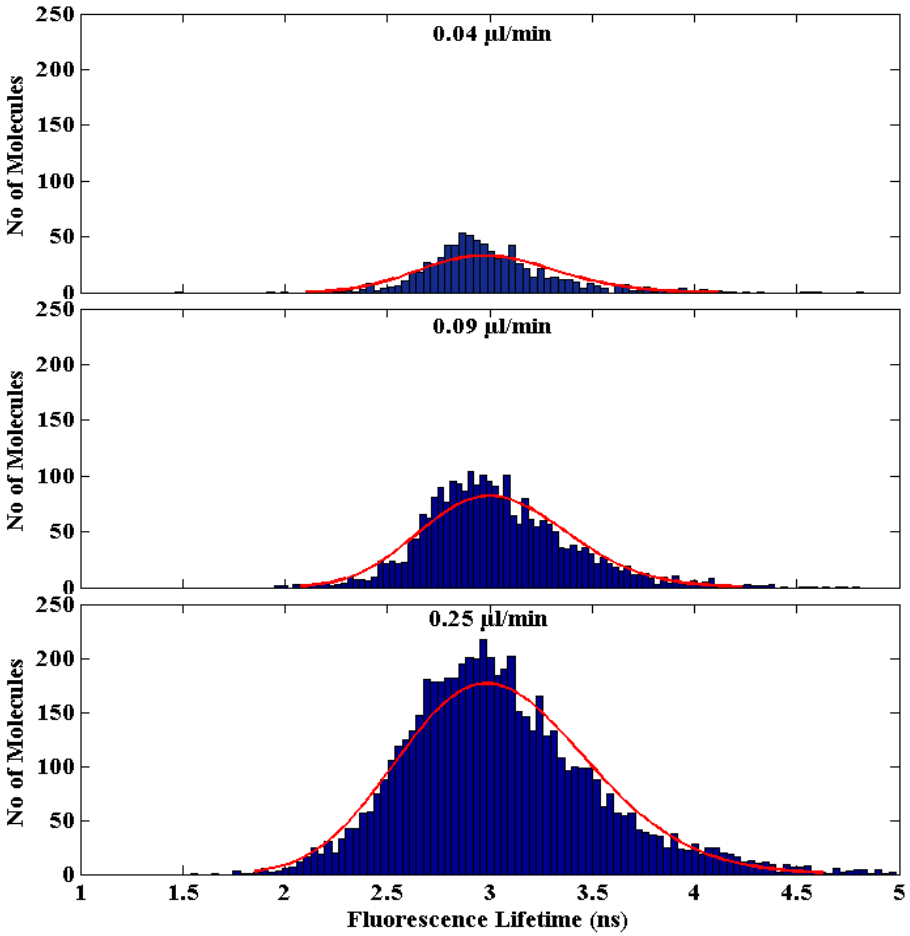

Figure 5.16. Single molecule fluorescence lifetime histograms and normal distribution fits.

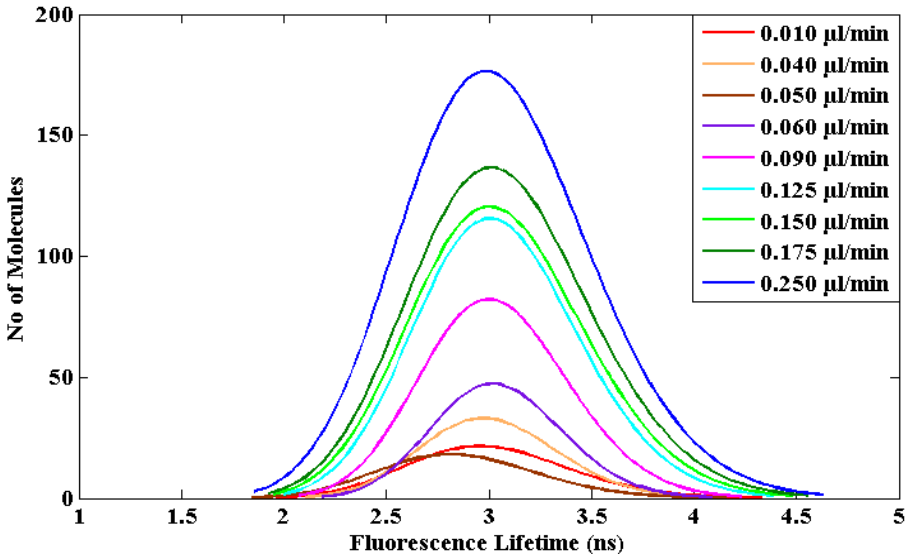

Figure 5.17. Normal fluorescence lifetime distribution fits for flow rates between 0.01-0.25 µl/min.

For all flow rates, apart from 0.05 µl/min which could be considered as an anomalous measurement, an almost identical distribution shape was observed, with slightly wider spread at high flow rates. The extracted lifetime mean was approximately constant (figure 5.18), yielding an average fluorescence lifetime of ~3 ns with a standard deviation of 0.02 ns (excluding the anomalous flow rate of 0.05 µl/min).

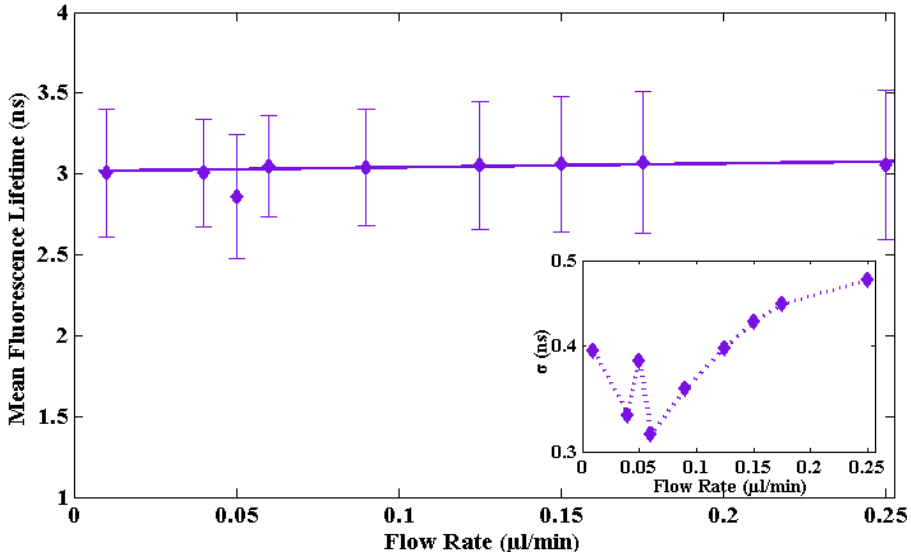

Figure 5.18. Mean single molecule fluorescence lifetime versus flow rate, error bars represent standard deviation σ. Inset: Standard deviation versus flow rate.

In order to interpret the slight increase in the lifetime standard deviation with flow rate, the histograms were also fitted to a gamma distribution (equation 5.3). As expected, the acquired p_1 parameter values were above 10 resulting in minimal skewness, which however exhibited a subtle increase with flow rate (figure 5.19). This could possibly be due to enhanced over-representation of early photons (section 2.2.2) at high molecule velocities.

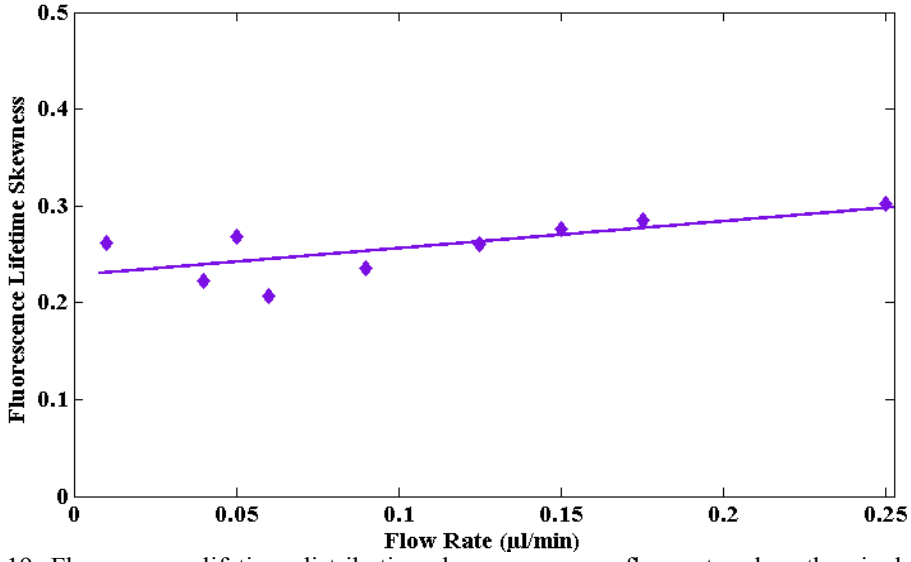

Figure 5.19. Fluorescence lifetime distribution skewness versus flow rate when the single molecule lifetime histograms were fitted to a gamma distribution.

5.3.2. Hydrodynamic focusing for single molecule detection within microchannels

5.3.2.1. Molecular detection efficiency

As described in chapter 3, hydrodynamic focusing within microchannels can be employed for confining the sample flow to a narrow stream with dimensions comparable to the detection volume. This way, a larger portion of the sample is forced through the probe volume and the molecular detection efficiency is increased. Hydrodynamic focusing has been widely used in SMD applications in order to ensure that the majority of the molecules contained in the sample are screened [25, 28, 30, 34, 35, 40, 64, 65].

SMD measurements using hydrodynamic focusing were performed under side-to-central inlet flow rate ratio α of 1 and 4. Ratio α=7 was also tested, but the extremely narrow and non-stable focused stream acquired, combined with the very high outlet flow velocity, resulted in a decrease in the number of molecules detected and rendered these measurements problematic.

Molecule detection frequency followed a normal distribution (equation 5.1) and the extracted mean frequencies for α=0 (no focusing, section 5.3.1), α=1 and α=4 are plotted against flow rate in figure 5.20. As it was discussed in section 5.3.1.1, the number of molecules detected per second increased with flow rate. However, although the relationship was linear for α=0 and DNA flow rates up to 0.25 μl/min, it became strongly non-linear for α=1 and α=4. This was not due to the hydrodynamic focusing being employed as a method, but it was rather the result of the increased molecular velocity imposed by the side inlet flows. The flow rate in the detection channel (outlet) was 3 times and 9 times the central inlet flow rate, for α=1 and α=4 respectively. In addition, assuming that the laser spot was positioned approximately at the centre of the focused stream, molecules travelled through the probe volume at velocities 1.5 times higher than the total outlet flow velocity due to the parabolic flow profile. At such high velocities, a large proportion of the fluorescence bursts could not be fully resolved. At the same time, it was possible that a number of molecules were not detected at all. Consequently, at high flow speeds, although more molecules traversed the probe volume in the unit of time, a smaller fraction of these were detected and resolved and the linearity of the relationship between flow rate and molecule detection frequency was lost.

It is evident that, for sample inlet flow rates up to 0.25 μl/min, employing hydrodynamic focusing increased the number of molecules detected per second. For the same inlet flow rate (same sample consumption), ratio α=4 resulted in more molecules being detected than for ratio α=1. For the optical setup used herein, the Gaussian probe volume cross section (x-z surface, where y is the direction of the flow) was estimated to be approximately 1.4 μm^2. Taking into

account the channel dimensions and the expected focusing ratio achieved for α=1 and α=4 (estimation according to results presented in chapter 3), it was calculated that only ~0.26%, 0.55% and 1.68% of the molecules flowing in the detection channel would traverse the probe volume for α=0 (no focusing), α=1 and α=4 respectively. It was therefore expected that applying a side-to-central inlet flow rate ratio of 1 and 4, would increase the detection efficiency by a factor of approximately 2 and 6.4 respectively, with respect to experiments where no focusing was employed.

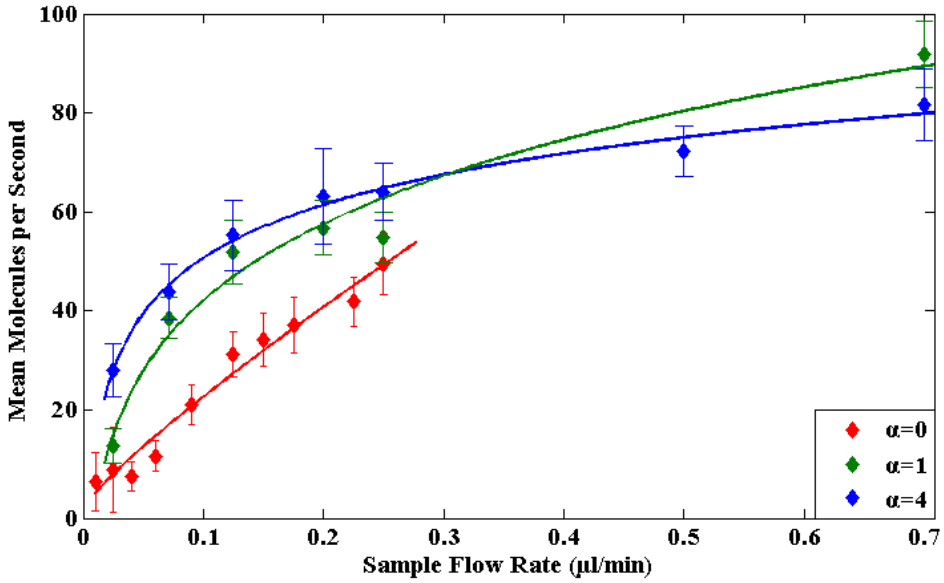

Figure 5.20. Mean molecule detection frequency versus sample inlet flow rate (central inlet) when no focusing was employed (α=0) and for hydrodynamic focusing under side-to-central inlet flow rate ratio α of 1 and 4. Error bars represent standard deviation.

Measured molecular detection efficiencies, calculated based on the DNA concentration and the flow rates used, are shown in figure 5.21. These are expressed as the ratio (%) of the detected DNA molecules per second over the introduced via the inlet channel molecules per second. It can be seen that, for central inlet flow rate up to 0.25 µl/min, higher detection efficiency was achieved for the same sample consumption, when hydrodynamic focusing was employed.

It should be noted that the detection efficiency improvement by a factor of 2 and 6.4 for α=1 and α=4 respectively, was calculated based only on the probe volume and sample stream (outlet channel for α=0, focused stream for α=1 and α=4) cross sectional area ratio. Hence, it should be valid for molecules flowing at the same velocity. However, as discussed above, employing hydrodynamic focusing increased the molecular velocity within the outlet with respect to the velocity within the inlet channel. Therefore, a direct comparison between

experimentally measured and theoretically calculated detection efficiency values for different ratios α can only be done under the same total flow rate (the same DNA flow velocity within the outlet).

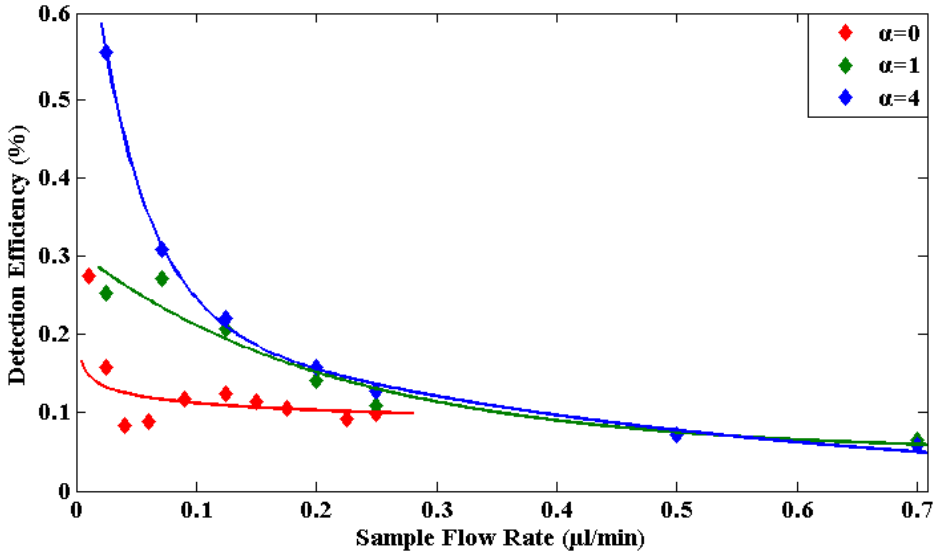

Figure 5.21. Molecular detection efficiency (%) versus sample inlet flow rate (central inlet) when no focusing was employed (α=0) and for hydrodynamic focusing under side-to-central inlet flow rate ratio α of 1 and 4.

Figure 5.22 depicts measured detection efficiencies versus outlet flow rate. The light green and blue dashed lines represent the theoretically calculated efficiencies for α=1 and α=4 respectively, which correspond to the experimentally determined efficiencies for α=0, under the same sample velocity. The measurement at 0.01 µl/min for α=0 (detection efficiency 0.28%) was considered problematic as it will be discussed further down.

A very good agreement between theory and experiment was observed for ratio α=1 (figure 5.22, solid green and dashed light green lines almost overlap). For α=4, experimental efficiency values appeared to match the theoretical values at low total flow rates. For high flow rates however, the measured detection efficiency became significantly smaller than the theoretically expected efficiency. This was possibly due to very high molecule velocities combined with the extremely small focused stream width (~1.6 µm). The 1.6 µm focusing width was comparable to the probe volume diameter (~1 µm), therefore a very stable flow was required to locate and maintain the focal spot within the sample stream. Furthermore, for ratio α=4, diffusion of DNA molecules away from the focused stream could be considered as significant and possibly reduced the number of molecules available for detection within the stream. More specifically, the calculated diffusion distances at the detection point (~50 µm

from the junction) for central inlet flow rates 0.025-0.7 μl/min varied between 63 nm and 12 nm. The respective diffusion distances for ratio α=1 were between 110 nm and 20 nm, which were however considered negligible compared to the acquired focusing width (~5.2 μm).

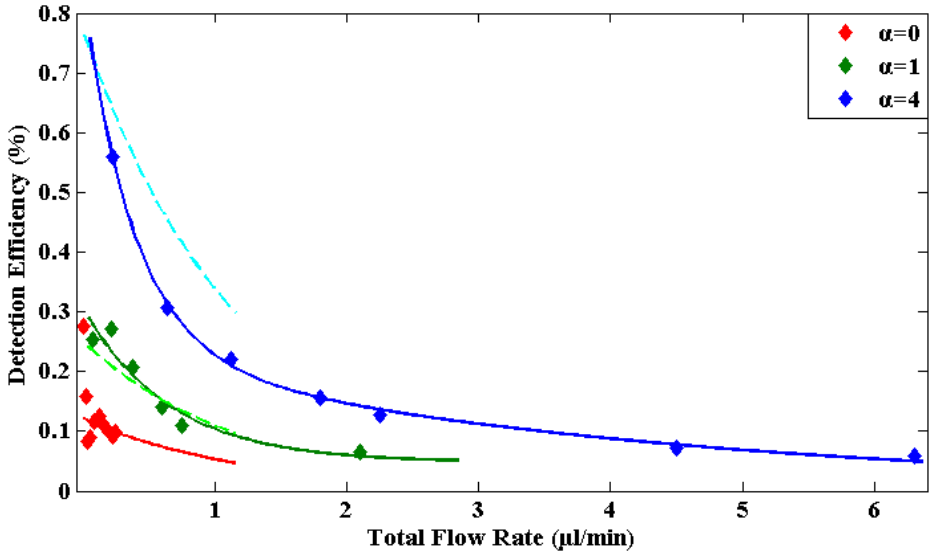

Figure 5.22. Molecular detection efficiency versus total flow rate (outlet) when no focusing was employed (α=0) and for hydrodynamic focusing under side-to-central inlet flow rate ratio α of 1 and 4. The green and blue dashed lines represent the expected detection efficiency values extracted via theoretical calculations for ratios α=1 and α=4 respectively.

The effect of the total flow rate (or the molecular flow velocity) on the detection efficiency is illustrated in figure 5.23. The 'corrected' detection efficiency was expressed as the ratio (%) of the detected molecules per second to the estimated number of molecules entering the probe volume per second. Thus, it did not account for the hydrodynamic focusing benefit and solely expressed the relationship between detection efficiency and velocity of molecules. Considering the effect of the focused stream width (flow stability and diffusion) insignificant, all data points were incorporated into a relatively good common fit (χ_R^2=0.934). The measurement at 0.01 μl/min for α=0 was not taken into account for this fit, as calculations showed that a greater number of molecules were detected than the molecules which entered the probe volume per second, yielding a detection efficiency of ~104% (not shown in figure 5.23). Similar observations have been previously reported and were attributed to diffusional re-crossings or to uncertainty in sample concentration and loading [35].

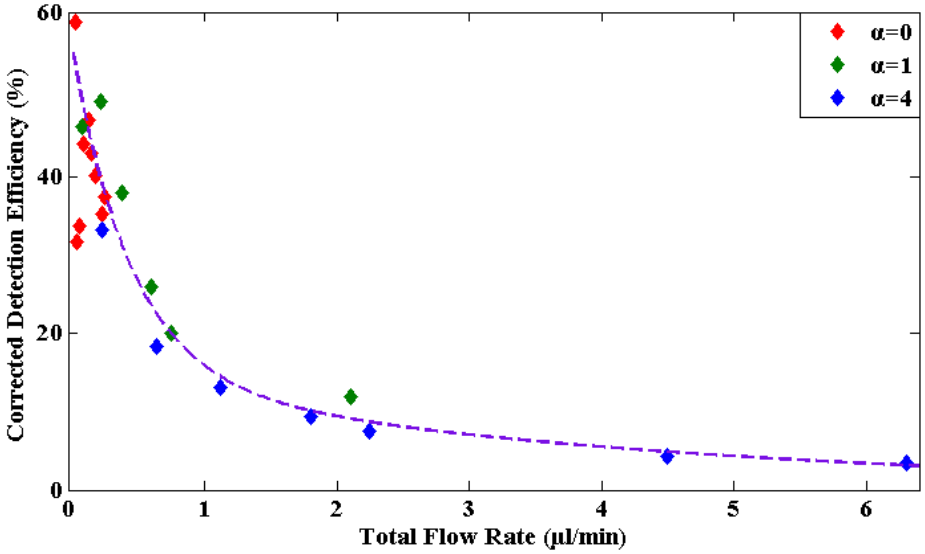

Figure 5.23. Corrected molecular detection efficiency (%) versus total flow rate (outlet) when no focusing was employed (α=0) and for hydrodynamic focusing under side-to-central inlet flow rate ratio α of 1 and 4. Corrected efficiencies do not depend on ratio α and thus the common fit shown above corresponds to the relationship between molecular velocity and detection efficiency.

5.3.2.2. Fluorescence burst analysis

Fluorescence burst analysis in terms of burst height, width, area and lifetime was performed in an identical way as described in sections 5.3.1.2-5.3.1.5 and all trends were consistent with those observed when no focusing was employed.

Mean burst height remained nearly constant for all flow rates and approximately the same as the mean of the normal distribution part of the burst area histogram. As discussed in section 5.3.1.4, the mean of the gamma distribution of the burst area histogram decreased for high flow rates. Very similar mean burst height and area values were acquired for both ratios α=1 and α=4 and when these data were plotted against the total flow rate, they were integrated in common fits (figure 5.24a). It should be noted that a higher signal-background discrimination threshold was applied during these measurements, therefore the absolute values acquired for α=1 and α=4 were different to those obtained for α=0.

Burst width and burst fluorescence lifetime results under hydrodynamic focusing conditions were also perfectly consistent with data acquired without employing focusing (figure 5.24b and figure 5.24c). The possible stretching of the λ-DNA molecule at high flow rates was more pronounced when focusing was employed, not only because of the higher flow velocities obtained, but also due to the confinement of the sample within a focused stream with dimensions comparable to the relatively large λ-DNA molecule (coiled length ~1.5 µm) [63, 66, 67].

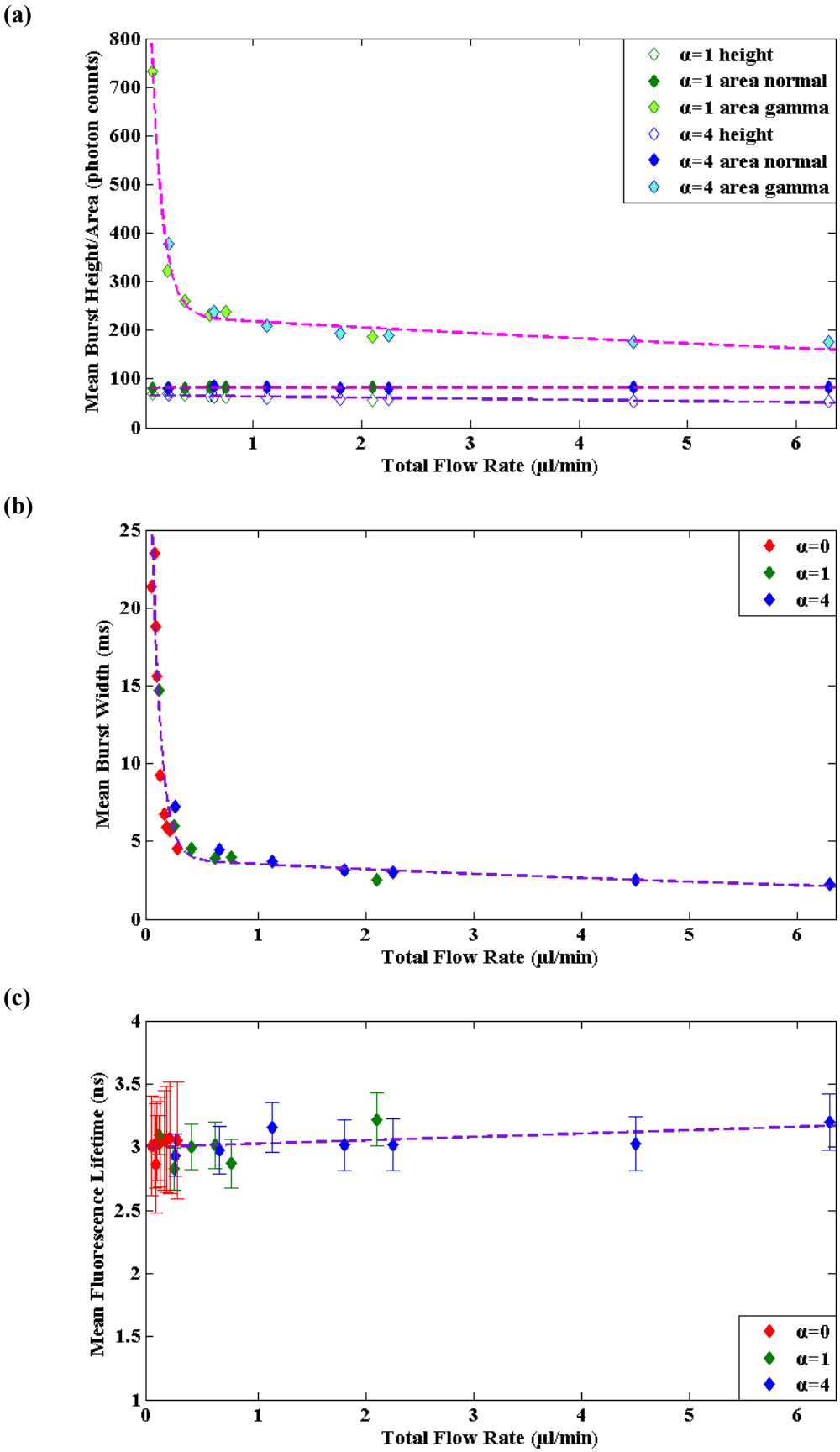

Figure 5.24. (a) Mean burst height and area extracted by normal and gamma distributions for α=1 and α=4 (b) Mean burst width extracted by gamma distributions for α=0, 1 and 4 (c) Mean fluorescence lifetime extracted by normal distributions for α=0, 1 and 4. Error bars represent standard deviation.

5.4. Summary and considerations

The home-built optical detection system was successfully used to detect single λ-DNA molecules fluorescently labelled with YOYO-1 while freely flowing down the length of a microfluidic channel, as well as when confined into a narrow fluidic stream, formed with the use of hydrodynamic focusing. In the latter case a significant improvement in the molecular detection efficiency was achieved. Fluorescence burst analysis was performed and useful trends were extracted. For flow rates within the limits that allowed for the majority of molecules to be detected and fully resolved, the detection frequency was found to increase with flow rate, whilst burst duration and area decreased. Burst height and fluorescence lifetime remained approximately the same for all flow rates.

Under constant flow velocity, the burst width relates to the size of a molecule as it expresses the time that the molecule is associated with the probe volume and burst height is related to the intrinsic fluorophore properties (extinction coefficient, quantum yield). Fluorescence lifetime is also characteristic of the fluorophore. Burst area represents the total photon counts obtained by a molecule traversing the probe volume and is therefore connected to both burst width and height. It becomes apparent that burst height, width, area and lifetime histograms provide useful information about the characteristics of a molecule and via appropriate analysis can be used to distinguish between fluorophores or different states/sizes of the same species, which should yield separate distributions within the acquired histograms. In the current work, burst characteristics and trends were not only observed or pointed out but mainly they were interpreted within a well-defined context by using accurate mathematical equations to successfully fit the obtained distributions.

The experiments presented herein illustrated that performing measurements at the single molecule level is extremely challenging and a series of factors should be taken into account to achieve maximum molecular detection efficiency as well as statistical accuracy. Some of the considerations and possible improvements are listed below:

- Fluorophores with appropriate characteristics, such as high extinction coefficient and quantum yield, should be used to obtain high fluorescence emission and signal to noise ratio.
- The optical setup and experimental conditions should be optimised in terms of excitation wavelength and power, probe volume reduction, background suppression, filters, photon detection efficiency etc.

- In microfluidics applications, the choice of the flow rate to be used is crucial and highly depends on the specific sample (size, diffusion coefficient) and experimental purposes (low sample consumption, high throughput, rapid measurements). It became evident by results presented herein that at low sample velocities, it is possible that molecular diffusion interferes with the trajectory of molecules through the probe volume, introducing discrepancy amongst the obtained single molecule transit times and photon counts. In addition, when low flow rates are used, fewer molecules traverse the probe volume and are being detected within the acquisition time, thus, statistical analysis is not favoured. On the other hand, at high sample velocities, a proportion of the molecules flowing through the probe volume are not detected and at the same time a fraction of those detected cannot be fully resolved. Hence, the detection efficiency is significantly reduced. For a given acquisition time however, more molecules are detected, allowing for high throughput measurements with fast acquisition times and reliable statistical analysis.
- An efficient way to perform SMD at high flow rates and benefit from the lack of diffusional effects and the narrower histograms obtained, is to further decrease the sample concentration. This also reduces the sample consumption.
- As it was illustrated by measurements performed in this work, hydrodynamic focusing significantly improves the molecular detection efficiency by increasing the probe volume over sample flow stream cross sectional area ratio and, thus, forcing a larger proportion of the sample to travel through the detection volume. However, when a very narrow focused stream is obtained, it is possible that a significant number of molecules rapidly diffuse away from the focused stream and remain undetected. In addition, positioning the focal spot within the focused flow might be problematic. Finally, hydrodynamic focusing increases the molecular velocity under constant sample consumption, with all the related advantages and disadvantages mentioned above. It becomes evident that side-to-central inlet flow rate ratio and absolute inlet flow rate values should be carefully balanced.
- Decreasing the channel width and depth can act as an additional sample confinement mechanism, improving the detection efficiency and minimising the sample consumption. Three dimensional flow focusing could also be employed to further decrease the ratio of probe volume and sample stream cross sectional areas. For example, by achieving a 3-D focussed stream with a z-dimension of approximately 10 μm (channel depth ~50 μm, probe volume depth ~1 μm), five times more molecules could be forced through the probe volume compared to the respective 2-D focusing condition resulting in significant improvement of the molecular detection efficiency. It should be noted however that downsizing the channel dimensions as well as employing 3-D focusing induce additional complexity in terms of device fabrication as well as experimental procedure.

5.5. References

1. Gell, C., D. Brockwell and A. Smith, *Handbook of single molecule fluorescence spectroscopy* University Press, Oxford, 2006.
2. Weiss, S., *Fluorescence spectroscopy of single biomolecules.* Science, 1999. **283**(5408): p. 1676-1683.
3. Roder, H., K. Maki, H. Cheng and M.C.R. Shastry, *Rapid mixing methods for exploring the kinetics of protein folding.* Methods, 2004. **34**(1): p. 15-27.
4. Patra, D., *Application and new developments in fluorescence spectroscopic techniques in studying individual molecules.* Applied Spectroscopy Reviews, 2008. **43**(5): p. 389-415.
5. Eigen, M. and R. Rigler, *Sorting single molecules - appplication to diagnostics and evolutionary biotechnology.* Proceedings of the National Academy of Sciences of the United States of America, 1994. **91**(13): p. 5740-5747.
6. Michalet, X. and S. Weiss, *Single-molecule spectroscopy and microscopy.* Comptes Rendus Physique, 2002. **3**(5): p. 619-644.
7. Pawley, J.B., *Handbook of biological confocal microscopy, 3rd edition.* Springer Science and Business Media, New York, 2006.
8. Segers-Nolten, G.M.J., C. Wyman, N. Wijgers, W. Vermeulen, A.T.M. Lenferink, J.H.J. Hoeijmakers, J. Greve and C. Otto, *Scanning confocal fluorescence microscopy for single molecule analysis of nucleotide excision repair complexes.* Nucleic Acids Research, 2002. **30**(21): p. 4720-4727.
9. Sabanayagam, C.R., J.S. Eid and A. Meller, *High-throughput scanning confocal microscope for single molecule analysis.* Applied Physics Letters, 2004. **84**(7): p. 1216-1218.
10. Zheng, H., L.S. Goldner and S.H. Leuba, *Homebuilt single-molecule scanning confocal fluorescence microscope studies of single DNA/protein interactions.* Methods, 2007. **41**(3): p. 342-352.
11. Ishijima, A. and T. Yanagida, *Single molecule nanobioscience.* Trends in Biochemical Sciences, 2001. **26**(7): p. 438-444.
12. Wazawa, T. and M. Ueda, *Total internal reflection fluorescence microscopy in single molecule nanobioscience*, in *Microscopy Techniques*. 2005. p. 77-106.
13. Hollars, C.W., J. Puls, O. Bakajin, B. Olsan, C.E. Talley, S.M. Lane and T. Huser, *Bio-assay based on single molecule fluorescence detection in microfluidic channels.* Analytical and Bioanalytical Chemistry, 2006. **385**(8): p. 1384-1388.
14. Le, N.C.H., R. Yokokawa, D.V. Dao, T.D. Nguyen, J.C. Wells and S. Sugiyama, *Versatile microfluidic total internal reflection (TIR)-based devices: Application to microbeads velocity measurement and single molecule detection with upright and inverted microscope.* Lab on a Chip, 2009. **9**(2): p. 244-250.
15. Mannion, J.T. and H.G. Craighead, *Nanofluidic structures for single biomolecule fluorescent detection.* Biopolymers, 2007. **85**(2): p. 131-143.

16. Levene, M.J., J. Korlach, S.W. Turner, M. Foquet, H.G. Craighead and W.W. Webb, *Zero-mode waveguides for single-molecule analysis at high concentrations.* Science, 2003. **299**(5607): p. 682-686.

17. Liao, D., P. Galajda, R. Riehn, R. Ilic, J.L. Puchalla, H.G. Yu, H.G. Craighead and R.H. Austin, *Single molecule correlation spectroscopy in continuous flow mixers with zero-mode waveguides.* Optics Express, 2008. **16**(14): p. 10077-10090.

18. Eid, J., A. Fehr, J. Gray, K. Luong, J. Lyle, G. Otto, P. Peluso, D. Rank, P. Baybayan, B. Bettman, A. Bibillo, K. Bjornson, B. Chaudhuri, F. Christians, R. Cicero, S. Clark, R. Dalal, A. deWinter, J. Dixon, M. Foquet, A. Gaertner, P. Hardenbol, C. Heiner, K. Hester, D. Holden, G. Kearns, X. Kong, R. Kuse, Y. Lacroix, S. Lin, P. Lundquist, C. Ma, P. Marks, M. Maxham, D. Murphy, I. Park, T. Pham, M. Phillips, J. Roy, R. Sebra, G. Shen, J. Sorenson, A. Tomaney, K. Travers, M. Trulson, J. Vieceli, J. Wegener, D. Wu, A. Yang, D. Zaccarin, P. Zhao, F. Zhong, J. Korlach, and S. Turner, *Real-Time DNA Sequencing from Single Polymerase Molecules.* Science, 2009. **323**(5910): p. 133-138.

19. Dittrich, P.S. and A. Manz, *Single-molecule fluorescence detection in microfluidic channels - the Holy Grail in mu TAS?* Analytical and Bioanalytical Chemistry, 2005. **382**(8): p. 1771-1782.

20. Craighead, H., *Future lab-on-a-chip technologies for interrogating individual molecules.* Nature, 2006. **442**(7101): p. 387-393.

21. Brewer, L.R. and P.R. Bianco, *Laminar flow cells for single-molecule studies of DNA-protein interactions.* Nature Methods, 2008. **5**(6): p. 517-525.

22. Ferris, M.M., M.O. McCabe, L.G. Doan and K.L. Rowlen, *Rapid enumeration of respiratory viruses.* Analytical Chemistry, 2002. **74**(8): p. 1849-1856.

23. Ferris, M.M. and K.L. Rowlen, *Detection and enumeration of single nanometric particles: A confocal optical design for fluorescence flow cytometry.* Review of Scientific Instruments, 2002. **73**(6): p. 2404-2410.

24. Chao, S.-Y., Y.-P. Ho, V.J. Bailey and T.-H. Wang, *Quantification of low concentrations of DNA using single molecule detection and velocity measurement in a microchannel.* Journal of Fluorescence, 2007. **17**(6): p. 767-774.

25. Wang, T.H., Y.H. Peng, C.Y. Zhang, P.K. Wong and C.M. Ho, *Single-molecule tracing on a fluidic microchip for quantitative detection of low-abundance nucleic acids.* Journal of the American Chemical Society, 2005. **127**(15): p. 5354-5359.

26. Edel, J.B. and A.J. de Mello, *Single particle confocal fluorescence spectroscopy in microchannels: Dependence of burst width and burst area distributions on particle size and flow rate.* Analytical Sciences, 2003. **19**(7): p. 1065-1069.

27. Yan, X.M., W.K. Grace, T.M. Yoshida, R.C. Habbersett, N. Velappan, J.H. Jett, R.A. Keller and B.L. Marrone, *Characteristics of different nucleic acid staining dyes for DNA fragment sizing by flow cytometry.* Analytical Chemistry, 1999. **71**(24): p. 5470-5480.

28. Kim, Y.S., J.H. Jett, E.J. Larson, J.R. Penttila, B.L. Marrone and R.A. Keller, *Bacterial fingerprinting by flow cytometry: Bacterial species discrimination.* Cytometry, 1999. **36**(4): p. 324-332.

29. Van Orden, A., R.A. Keller and W.P. Ambrose, *High-throughput flow cytometric DNA fragment sizing.* Analytical Chemistry, 2000. **72**(1): p. 37-41.

30. Wabuyele, M.B., S.M. Ford, W. Stryjewski, J. Barrow and S.A. Soper, *Single molecule detection of double-stranded DNA in poly(methylmethacrylate) and polycarbonate microfluidic devices.* Electrophoresis, 2001. **22**(18): p. 3939-3948.

31. Ferris, M.M., R.C. Habbersett, M. Wolinsky, J.H. Jett, T.M. Yoshida and R.A. Keller, *Statistics of single-molecule measurements: Applications in flow-cytometry sizing of DNA fragments.* Cytometry Part A, 2004. **60A**(1): p. 41-52.

32. Ferris, M.M., X.M. Yan, R.C. Habbersett, Y.L. Shou, C.L. Lemanski, J.H. Jett, T.M. Yoshida and B.L. Marrone, *Performance assessment of DNA fragment sizing by high-sensitivity flow cytometry and pulsed-field gel electrophoresis.* Journal of Clinical Microbiology, 2004. **42**(5): p. 1965-1976.

33. Foquet, M., J. Korlach, W. Zipfel, W.W. Webb and H.G. Craighead, *DNA fragment sizing by single molecule detection in submicrometer-sized closed fluidic channels.* Analytical Chemistry, 2002. **74**(6): p. 1415-1422.

34. Fister, J.C., S.C. Jacobson, L.M. Davis and J.M. Ramsey, *Counting single chromophore molecules for ultrasensitive analysis and separations on microchip devices.* Analytical Chemistry, 1998. **70**(3): p. 431-437.

35. Haab, B.B. and R.A. Mathies, *Single-molecule detection of DNA separations in microfabricated capillary electrophoresis chips employing focused molecular streams.* Analytical Chemistry, 1999. **71**(22): p. 5137-5145.

36. Fogarty, K. and A. Van Orden, *Two-beam fluorescence cross-correlation spectroscopy for simultaneous analysis of positive and negative ions in continuous-flow capillary electrophoresis.* Analytical Chemistry, 2003. **75**(23): p. 6634-6641.

37. Bi, R., P.D. Zhang, C.Q. Dong and J.C. Ren, *Combination of micro-fluidic chip with fluorescence correlation Spectroscopy for single molecule detection.* Chinese Chemical Letters, 2006. **17**(4): p. 521-524.

38. Magde, D., W.W. Webb and E.L. Elson, *Fluorescence correlation spectroscopy. 3. Uniform translationnand laminar flow.* Biopolymers, 1978. **17**(2): p. 361-376.

39. LeCaptain, D.J., M.A. Michel and A. Van Orden, *Characterization of DNA-protein complexes by capillary electrophoresis-single molecule fluorescence correlation spectroscopy.* Analyst, 2001. **126**(8): p. 1279-1284.

40. Dittrich, P. and P. Schwille, *Single molecule reactions and sorting in microfluidic channels.* Biophysical Journal, 2003. **84**(2): p. 473A-474A.

41. Lipman, E.A., B. Schuler, O. Bakajin and W.A. Eaton, *Single-molecule measurement of protein folding kinetics.* Science, 2003. **301**(5637): p. 1233-1235.

42. Dittrich, P.S., B. Muller and P. Schwille, *Studying reaction kinetics by simultaneous FRET and cross-correlation analysis in a miniaturized continuous flow reactor.* Physical Chemistry Chemical Physics, 2004. **6**(18): p. 4416-4420.

43. Dittrich, P.S., S.P. Schafer and P. Schwille, *Characterization of the photoconversion on reaction of the fluorescent protein kaede on the single-molecule level.* Biophysical Journal, 2005. **89**(5): p. 3446-3455.

44. Hamadani, K.M. and S. Weiss, *Nonequilibrium single molecule protein folding in a coaxial mixer.* Biophysical Journal, 2008. **95**(1): p. 352-365.

45. Dittrich, P.S. and P. Schwille, *An integrated microfluidic system for reaction, high-sensitivity detection, and sorting of fluorescent cells and particles.* Analytical Chemistry, 2003. **75**(21): p. 5767-5774.

46. Wang, M.M., E. Tu, D.E. Raymond, J.M. Yang, H.C. Zhang, N. Hagen, B. Dees, E.M. Mercer, A.H. Forster, I. Kariv, P.J. Marchand, and W.F. Butler, *Microfluidic sorting of mammalian cells by optical force switching.* Nature Biotechnology, 2005. **23**(1): p. 83-87.

47. Gosch, M., H. Blom, J. Holm, T. Heino and R. Rigler, *Hydrodynamic flow profiling in microchannel structures by single molecule fluorescence correlation spectroscopy.* Analytical Chemistry, 2000. **72**(14): p. 3260-3265.

48. Kunst, B.H., A. Schots and A. Visser, *Detection of flowing fluorescent particles in a microcapillary using fluorescence correlation spectroscopy.* Analytical Chemistry, 2002. **74**(20): p. 5350-5357.

49. Shelby, J.P. and D.T. Chiu, *Mapping fast flows over micrometer-length scales using flow-tagging velocimetry and single-molecule detection.* Analytical Chemistry, 2003. **75**(6): p. 1387-1392.

50. Sauer, M., B. Angerer, W. Ankenbauer, Z. Foldes-Papp, F. Gobel, K.T. Han, R. Rigler, A. Schulz, J. Wolfrum and C. Zander, *Single molecule DNA sequencing in submicrometer channels: state of the art and future prospects.* Journal of Biotechnology, 2001. **86**(3): p. 181-201.

51. Werner, J.H., H. Cai, J.H. Jett, L. Reha-Krantz, R.A. Keller and P.M. Goodwin, *Progress towards single-molecule DNA sequencing: a one color demonstration.* Journal of Biotechnology, 2003. **102**(1): p. 1-14.

52. Bianco, P.R., L.R. Brewer, M. Corzett, R. Balhorn, Y. Yeh, S.C. Kowalczykowski and R.J. Baskin, *Processive translocation and DNA unwinding by individual RecBCD enzyme molecules.* Nature, 2001. **409**(6818): p. 374-378.

53. van Oijen, A.M., P.C. Blainey, D.J. Crampton, C.C. Richardson, T. Ellenberger and X.S. Xie, *Single-molecule kinetics of lambda exonuclease reveal base dependence and dynamic disorder.* Science, 2003. **301**(5637): p. 1235-1238.

54. Amitani, I., R.J. Baskin and S.C. Kowalczykowski, *Visualization of Rad54, a chromatin remodeling protein, translocating on single DNA molecules.* Molecular Cell, 2006. **23**(1): p. 143-148.

55. Galletto, R., I. Amitani, R.J. Baskin and S.C. Kowalczykowski, *Direct observation of individual RecA filaments assembling on single DNA molecules.* Nature, 2006. **443**(7113): p. 875-878.

56. Larson, J.W., G.R. Yantz, Q. Zhong, R. Charnas, C.M. D'Antoni, M.V. Gallo, K.A. Gillis, L.A. Neely, K.M. Phillips, G.G. Wong, S.R. Gullans, and R. Gilmanshin, *Single DNA molecule stretching in sudden mixed shear and elongational microflows.* Lab on a Chip, 2006. **6**(9): p. 1187-1199.

57. Beer, N.R., K.A. Rose and I.M. Kennedy, *Monodisperse droplet generation and rapid trapping for single molecule detection and reaction kinetics measurement.* Lab on a Chip, 2009. **9**(6): p. 841-844.

58. Chansin, G.A.T., R. Mulero, J. Hong, M.J. Kim, A.J. deMello and J.B. Edel, *Single-molecule Spectroscopy using nanoporous membranes.* Nano Letters, 2007. **7**(9): p. 2901-2906.

59. Edel, J.B., E.K. Hill and A.J. de Mello, *Velocity measurement of particulate flow in microfluidic channels using single point confocal fluorescence detection.* Analyst, 2001. **126**(11): p. 1953-1957.

60. Hill, E.K. and A.J. de Mello, *Single-molecule detection using confocal fluorescence detection: Assessment of optical probe volumes.* Analyst, 2000. **125**(6): p. 1033-1036.

61. Brody, J.P., P. Yager, R.E. Goldstein and R.H. Austin, *Biotechnology at low Reynolds numbers.* Biophysical Journal, 1996. **71**(6): p. 3430-3441.

62. Lee, G.B., C.C. Chang, S.B. Huang and R.J. Yang, *The hydrodynamic focusing effect inside rectangular microchannels.* Journal of Micromechanics and Microengineering, 2006. **16**(5): p. 1024-1032.

63. Shrewsbury, P.J., S.J. Muller and D. Liepmann, *Flow of lambda-DNA in microfluidic devices*, in *1st Annual International Ieee-Embs Special Topic Conference on Microtechnologies in Medicine & Biology, Proceedings*. 2000. p. 415-420.

64. Yan, X.M., R.C. Habbersett, T.M. Yoshida, J.P. Nolan, J.H. Jett and B.L. Marrone, *Probing the kinetics of SYTOX orange stain binding to double-stranded DNA with implications for DNA analysis.* Analytical Chemistry, 2005. **77**(11): p. 3554-3562.

65. Godin, J., C.-H. Chen, S.H. Cho, W. Qiao, F. Tsai and Y.-H. Lo, *Microfluidics and photonics for Bio-System-on-a-Chip: A review of advancements in technology towards a microfluidic flow cytometry chip.* Journal of Biophotonics, 2008. **1**(5): p. 355-376.

66. Wong, P.K., Y.K. Lee and C.M. Ho, *Deformation of DNA molecules by hydrodynamic focusing.* Journal of Fluid Mechanics, 2003. **497**: p. 55-65.

67. Shaqfeh, E.S.G., *The dynamics of single-molecule DNA in flow.* Journal of Non-Newtonian Fluid Mechanics, 2005. **130**(1): p. 1-28.

CHAPTER 6
ACCURATE DISTANCE DETERMINATION VIA FÖRSTER RESONANCE ENERGY TRANSFER

6.1. Introduction

Förster resonance energy transfer (FRET) is a process that involves non-radiative energy transfer from a donor molecule to an acceptor molecule via dipole-dipole interactions [1]. The efficiency of the energy transfer is extremely sensitive to the distance between the donor and acceptor molecules and can be used to extract inter-molecular distances. Since it was first proposed by Stryer and Haugland as a 'spectroscopic ruler' [2], FRET has been extensively used to investigate various biological systems for both intramolecular rearrangements as well as for intermolecular interactions. In a typical FRET experiment, the donor and acceptor dyes are attached to known sites within a macromolecule or within the interacting molecules. Changes in the relative position of the fluorophores are detected as changes in the efficiency of the energy transfer. Inter-dye distances, and thus information about the molecules under investigation, can be subsequently extracted. Detailed descriptions of the numerous FRET applications and techniques can be found in references [3-11].

The main principle of FRET can be illustrated by a simplified Jablonski diagram (figure 6.1). FRET requires a significant overlap between the emission spectrum of the donor and the absorption spectrum of the acceptor and for the distance separating the two molecules to be less than 10 nm [1, 5]. Under these conditions, a part of the excited donor energy may be transferred to the acceptor, which subsequently relaxes to its ground state by emitting a photon of lower energy. The rate of the energy transfer is given by [1]:

$$k_{FRET} = \frac{1}{\tau_D}\left(\frac{R_0}{R_{DA}}\right)^6 \tag{6.1}$$

where τ_D is the fluorescence lifetime of the donor in the absence of the acceptor, R_{DA} is the distance between the donor and acceptor molecules and R_0 is the characteristic Förster distance at which 50% FRET occurs. The efficiency of the energy transfer E_{FRET} is strongly dependent on the centre-to-centre distance between the two molecules and is given by [1]:

$$E_{FRET} = \frac{R_0^6}{R_0^6 + R_{DA}^6} \tag{6.2}$$

The characteristic distance R_0, and therefore E_{FRET}, depends on the extent of the donor-acceptor spectral overlap, with large overlap resulting in higher efficiency. Other factors affecting R_0 are the relative orientation between the donor and acceptor molecules and the fluorescence quantum yield Q_D of the donor in the absence of the acceptor. The dependence of R_0 on the factors above is illustrated in equation 6.3, which gives R_0 for any dye pair [1]:

$$R_0 = \left[8.79 \times 10^{23} \times \frac{\kappa^2 Q_D J(\lambda)}{n^4} \right]^{1/6} \text{(in Å)} \qquad \text{with} \qquad J(\lambda) = \int f_D(\lambda) \varepsilon_A(\lambda) \lambda^4 d\lambda \tag{6.3}$$

κ^2 in equation 6.3 is related to the angle between the two fluorophore dipoles and is usually assumed to be 2/3 and n is the refractive index of the medium, which is generally assumed to be 1.4 [1]. $J(\lambda)$ represents the donor-acceptor spectral overlap as a function of the wavelength λ, $f_D(\lambda)$ is the fluorescence emission intensity of the donor as a fraction of the total integrated intensity and $\varepsilon_A(\lambda)$ is the extinction coefficient of the acceptor in the absence of the donor. Typical values of R_0 for common dye pairs range from 2 to 6 nm [5, 12, 13].

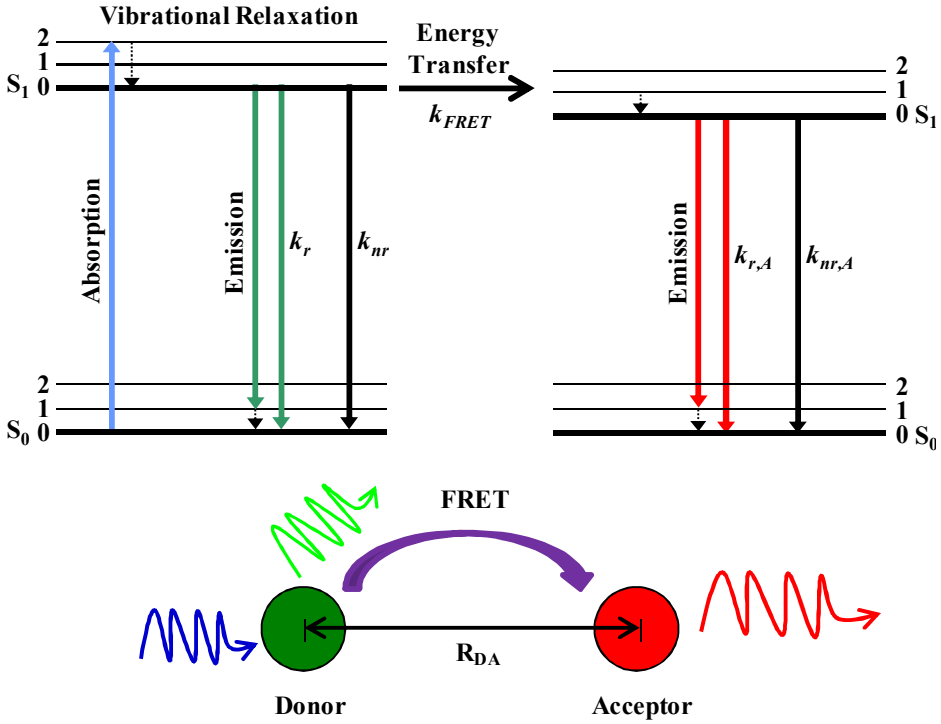

Figure 6.1. Simplified Jablonski diagram and FRET cartoon. Upon donor excitation a part of the donor energy may be transferred to the acceptor via dipole-dipole interaction. Thus emission is detected in both green and red regions, originating from donor and acceptor molecules respectively.

Equation 6.2 gives a theoretical estimation for E_{FRET}. Experimentally, E_{FRET} cannot be directly measured and, therefore, it is determined by exploiting changes in the photophysical properties of the donor and acceptor molecules when FRET occurs. During FRET, the energy of a fraction of the photons absorbed by the donor is transferred to the acceptor molecule. As a result, the quantum yield of the donor is diminished, which leads to reduced donor fluorescence intensity. At The same time, the acceptor intensity increases due to excitation caused by the non-radiative energy transfer by the donor. Given that FRET serves as an additional mechanism for depopulating the excited state of the donor, the fluorescence lifetime of the donor also decreases in the presence of the acceptor.

A variety of FRET techniques have been proposed which are based on either fluorescence intensity or fluorescence lifetime measurements [3, 5, 9, 11]. Choosing the best technique depends on factors such as the available instrumentation, the specific biomolecule(s) used and the selected dye pair.

A commonly employed FRET method aims at qualifying the change in the donor emission introduced by FRET. The fluorescence intensity I_{DA} of the donor in the presence of the acceptor is measured (FRET conditions) and after the acceptor is photobleached the donor intensity I_D is re-measured (non-FRET conditions). Subsequently, E_{FRET} is obtained by [3, 9]:

$$E_{FRET} = 1 - \frac{I_{DA}}{I_D} \tag{6.4}$$

In such experiments, the molecule labelled with the acceptor dye is typically immobilised on a surface. This however, induces additional complexity as well as uncertainty about the degree of perturbation due to the immobilisation protocol. Alternatively, I_D can be extracted via a separate, donor-only measurement. In this case however, it is difficult to ensure that the two experiments are performed under identical conditions, due to factors other than FRET affecting fluorescence intensity, such as fluorophore concentration, excitation power fluctuations etc.

An alternative FRET method depends on the measurement of the acceptor instead of the donor intensity. The acceptor intensities I_{AD} and I_A under FRET (in the presence of the donor) and non-FRET (in the absence of the donor) conditions respectively, can be related to the FRET efficiency via [3, 9]:

$$E_{FRET} = \frac{\varepsilon_A}{\varepsilon_D}\left(\frac{I_{AD}}{I_A} - 1\right) \tag{6.5}$$

where ε_A and ε_D are the extinction coefficients of the acceptor and the donor respectively at the excitation wavelength. This technique requires additional measurements in order to accurately determine ε_A and ε_D as well as I_A, inducing similar issues to those mentioned above for I_D determination. An advantage of this method is that the change in the acceptor signal directly represents the energy transferred by the donor, with no regard to non-FRET quenching processes that could possibly affect the donor intensity.

FRET efficiency can be described as the fraction of photons absorbed by the donor, whose energy is transferred to the acceptor molecule. In experiments whereby two detection channels are available, the use of appropriate filters allows for simultaneous monitoring of the donor and acceptor intensities. As fluorescence intensity is expressed in photon counts, the above relationship, in terms of intensity, yields [3, 8, 9, 13]:

$$E_{FRET} = \frac{I_{AD}}{I_{AD} + \gamma I_{DA}} \tag{6.6}$$

In equation 6.6, I_{AD} and I_{DA} are the acceptor and donor intensities measured simultaneously during FRET and they should both be corrected for emission leakage of the one fluorophore into the detection channel of the other. In addition, I_{AD} should be further corrected for direct excitation of the acceptor. γ is a parameter given by [8, 13]:

$$\gamma = \frac{\eta_A Q_A}{\eta_D Q_D} \tag{6.7}$$

where η_A and η_D are the detection efficiencies of the acceptor and the donor channels and Q_A, Q_D are the acceptor and donor quantum yields respectively. Although the need for two detection channels induces complexity to the optical setup, this method has been extensively used, especially in single molecule studies, due to its ability to simultaneously provide information about the emission of donor and acceptor fluorophores. Even though the leakage of the donor emission into the acceptor detection channel (red channel) is determined via a separate, donor-only measurement, it can be expressed as a percentage of the donor emission in the green channel. Thus, it is not susceptible to fluorophore concentration and sample illumination and the requirement for identical experimental conditions is no longer needed. Similarly, the leakage of the acceptor dye emission within the green detection region can also be expressed as a percentage instead of absolute photon counts. This method can be implemented under any conditions without the need for molecule immobilisation and is ideal for the study of freely diffusing or flowing molecules in bulk as well as at the single molecule level.

An alternative approach to intensity measurements is the extraction of FRET efficiency via changes in the fluorescence lifetime of the donor. In terms of lifetime, E_{FRET} is expressed by [1, 3, 9]:

$$E_{FRET} = 1 - \frac{\tau_{DA}}{\tau_D} \tag{6.8}$$

where τ_{DA} and τ_D is the fluorescence lifetime of the donor in the presence and absence of the acceptor respectively. This is essentially a restatement of equation 6.4, with the advantage that τ_D can be determined more accurately than I_D, as it is characteristic for the donor fluorophore. This method is generally equipped with all the advantages of fluorescence lifetime-based as opposed to the intensity-based techniques, such as independence of fluorophore concentration, illumination intensity and detector efficiency. Given that emission leakage is normally observed in the acceptor detection channel (originating from the donor dye), this method is not prone to cross talk artefacts, as it monitors only the donor detection channel. Another important attribute of the lifetime-based FRET technique is that, in cases of multispecies samples, although the decay fitting procedure might be complicated, it enables the detection, to some extent, of multiple FRET populations in bulk, which is impossible for intensity based methods.

Considering the techniques mentioned above, it becomes apparent that the choice of the FRET dye pair is significant. Relatively photostable fluorophores with high quantum yields and large spectral overlap are generally preferred. It is important however, especially in intensity-based measurements, to minimise the donor emission leakage into the acceptor detection channel and reverse. Therefore, the FRET dye pair should be carefully chosen so that the spectral overlap and leakage are balanced. In addition, in order to reduce contributions resulting from direct excitation of the acceptor, the excitation line should be chosen to coincide with the minimum of the acceptor absorption spectrum, providing at the same time enough excitation energy for the donor.

An increasing interest in resonance energy transfer applications has emerged within the last decades and FRET has been widely used in biological research for the investigation of intramolecular and intermolecular interactions [14]. FRET methods are particularly popular in nucleic acid studies. For example, the denaturation of a DNA hairpin with respect to urea concentration has been investigated [15] and timescales for the lifetime of open and closed states have been obtained via FRET [16]. By labelling two of the four helices of a four-way (Holliday) DNA junction with a proper donor-acceptor pair, structural characteristics and related kinetics can be extracted [17, 18]. By labelling three arms of the same junction with

one donor and two acceptor fluorophores, distances between the junction components can be determined via three-colour FRET [19]. The Mg^{2+}-facilitated conformational change of an immobilised RNA three-helix junction has been studied via FRET and fluctuations in E_{FRET} were interpreted as transitions of the RNA junction between open and folded conformation [20]. FRET has also been employed to investigate intranucleosomal DNA dynamics of immobilised molecules [21].

FRET measurements have been extensively used to gain insight into the complex aspects of enzymatic catalysis [22] and DNA enzymatic cleavage [15]. The irreversible cleavage reaction of a double-stranded DNA oligomer by the enzyme exonuclease III has been monitored in real time by combining FRET and hydrodynamic focusing within a microfluidic reactor [23]. Protein-DNA interactions, such as interactions between DNA and escherichia coli catabolite activator protein [24] or single-stranded DNA binding protein [25], RecA filament growth dynamics [26], as well as molecular binding interactions [27], have also been investigated using FRET methods.

Furthermore, FRET is a powerful tool in the study of protein conformational dynamics. By appropriately labelling a protein at known sites, variations in FRET efficiency indicate changes in the inter-dye distance and thus in the molecular structure. For example, FRET measurements have been used to demonstrate the reversible denaturation-renaturation of immobilised ribonuclease H molecules upon exposure to guanidinium chloride [28] and to investigate the timescale for transitions between folded and unfolded states [29]. Conformational changes of freely diffusing chymotrypsin inhibitor 2 [30], cold-shock protein [31] and calmodulin [32, 33] molecules due to the presence of appropriate chemical reagents have also been studied using FRET. Furthermore, protein folding FRET studies have been performed in combination with microfluidics systems. More specifically, FRET measurements have been employed to characterize the performance of microfluidic mixers specially designed for protein folding kinetic studies [34, 35] and conformational changes of cold-shock protein labelled with the FRET pair Alexa488-Alexa594 have been monitored in real time within a microfluidic channel with the use of hydrodynamic focusing as a denaturant dilution mechanism [36]. Protein folding studies combining FRET and three-dimensional hydrodynamic focusing have also been performed [37]. In addition, flow focusing has been employed to achieve rapid reagent mixing and to enable monitoring of the early kinetics of protein folding inside a chaperonin cavity [38].

The common objective in experiments employing FRET is to accurately determine nanometre range distances, which are subsequently used to extract information about the biomolecule(s)

under investigation. Before doing so however, it is important to develop and optimize an analysis method with verified validity for the specific experimental arrangement and FRET dye pair used. The current chapter deals with the development of such a method. For this purpose, complementary DNA oligos were labelled with FRET donor and acceptor fluorophores. Following hybridisation, the distance between the two dyes on the resulting double stranded DNA molecules was known. Upon FRET, fluorescence emission was detected in both green (donor) and red (acceptor) regions and the extracted FRET efficiency was used to confirm the distance between the donor and acceptor fluorophores. Two FRET dye pairs were tested; the well-known AlexaFluor488-AlexaFluor647 pair and the less common DyLight549-DyLight633 pair. The latter was tested in order to verify that the technique was suitable for fluorophores with larger than normally spectral overlap, which are more difficult to resolve.

6.2. Experimental methods

6.2.1. The AlexaFluor488-AlexaFluor647 FRET pair

6.2.1.1. Oligonucleotides and DNA hybridisation

Oligonucleotides were purchased from Eurofins Operon (Germany). A biotinylated DNA strand was internally labelled with AlexaFluor488 (AF488), while AlexaFluor647 (AF647) was internally labelled on the complementary strand, so that after hybridisation the dye molecules would be 12 base pairs (bp) apart. The two sequences, each containing 40 bases, were:

Biotin-5'-TAGTGTAACTTAAGCCTAGGATAAGAGC**[AF488]**AGTAATCGGTA-3'
3'-ATCACATTGAATTCGG**[AF647]**TCCTATTCTCGGTCATTAGCCAT-5'

For the remainder of this chapter the sequences above will be referred to as *DNA488B* and *DNA647* respectively. The DNA samples were prepared in tris(hydroxymethyl) aminomethane hydrochloride (Tris-HCl) pH 8.0 buffer (Fluka) with the use of de-ionized water. Buffer and water were filtered with 0.2 μm syringe filters (Pall Corporation, UK) before use for sample preparation.

The DNA hybridisation was performed at pH 8.0 using a binding buffer consisting of 10 mM Tris-HCl and 50 mM NaCl. The single-stranded DNA (ssDNA) mixture (*DNA488B* and *DNA647*) was prepared by pipetting 50 μl of 200 nM of each DNA solution into 200 μl

Eppendorf tubes, which resulted in a final concentration of 100 nM for the hybridised DNA. The hybridisation was performed using a Genius Thermal Cycler (Techne, UK). The process was carried out by rapidly increasing the temperature to 92ºC, holding at this temperature for 2 minutes and then slowly decreasing to 4ºC at a rate of 1.6 ºC/min.

The hybridisation process yielded a double-stranded DNA (dsDNA) molecule consisting of 40 bp, with the donor (AF488) and acceptor (AF647) dye molecules being 12 bp apart. The dsDNA sample will be referred to as *HybrDNA*.

6.2.1.2. Experimental procedure

For fluorescence intensity and fluorescence lifetime FRET measurements, a drop (~8 µl) of 10 nM *HybrDNA* was positioned on a 24×50 mm, 160 µm thick glass cover slip (thickness No 1, VWR International) and excited using point excitation mode. According to the spectral properties of the AF488-AF647 dye pair (figure 6.2), a 488 nm excitation line of ~44 µW at 20 MHz was chosen (excitation path 2, section 2.1.1.2). Fluorescence emission in the green (donor) and red (acceptor) channels was collected using filters HQ540/80 and LP640 respectively. Fluorescence intensity and fluorescence lifetime analysis was performed as described in sections 2.3.1 and 2.3.2 (*JLife* program) respectively. *DNA488B* and *DNA647* solutions at a concentration of 10 nm were used as controls for carrying out the necessary corrections.

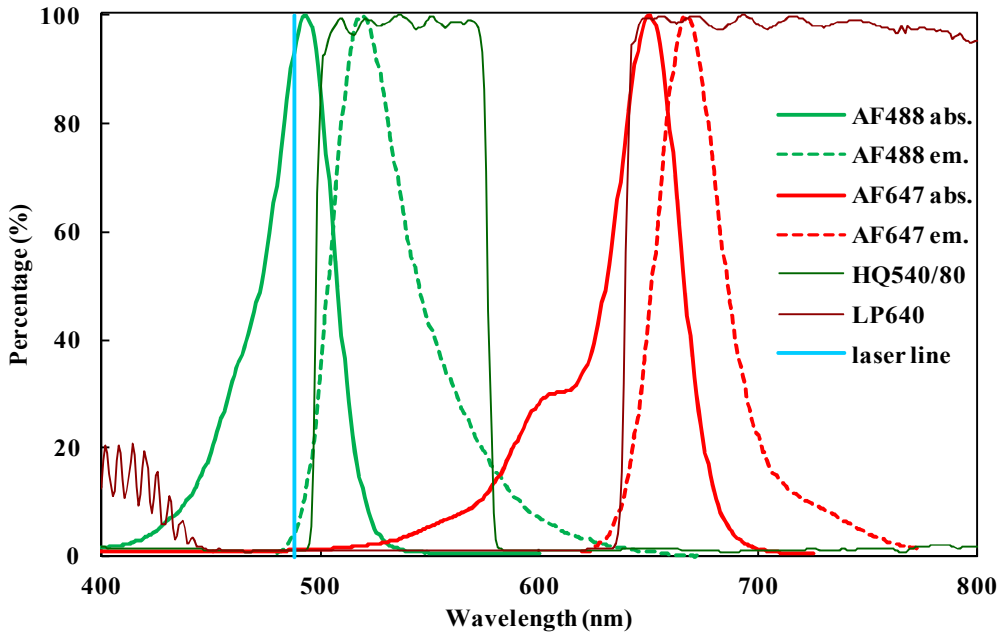

Figure 6.2. AF488-AF674 spectra, excitation line and emission filters. A 488 nm laser line matched well the AF488 absorption maximum, avoiding at the same time direct AF647 excitation. The emission spectra of the two dyes hardly overlapped, therefore they were easily resolved using appropriate filters (HQ540/80 and LP640 for the green and red channels respectively). The y-axis represents normalised absorption/emission or filter transmission.

6.2.1.3. Inter-dye distance and theoretical E_{FRET} calculation

Considering the helical molecular geometry of dsDNA, the distance R_{DA} between the donor and acceptor fluorophores is not proportional to the number of base pairs n separating the two molecules. In a simple cylindrical description of the DNA helix the typical diameter is 2 nm, the length per bp is approximately 0.34 nm and 10 bp make a turn [39, 40]. The inter-dye distance R_{DA} is given by the vector sum of two components parallel ($R_{DA,a}$) and perpendicular ($R_{DA,b}$) to the cylinder axis (figure 6.3).

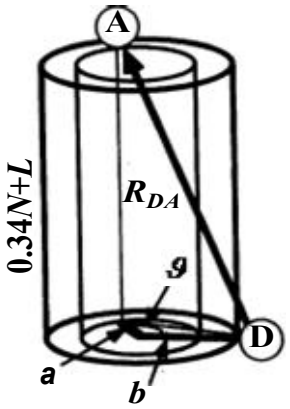

Figure 6.3. Schematic representation of the DNA molecule helical geometry. The donor-acceptor distance R_{DA} is given by the vector sum of two components parallel and perpendicular to the cylinder axis. Adapted with permission from [40], copyright 1993, National Academy of Sciences.

The length of $R_{DA,a}$ is $R_{DA,a}=0.34N+L$, where $N=n-1$ and L is the distance between the dyes for $n=1$. $R_{DA,b}$ can be calculated as $R_{DA,b}=(a^2+b^2-2ab\cos\vartheta)^{1/2}$, with ϑ being the angular separation between the fluorophores ($\vartheta=36N+\varphi$) and φ the angular separation if donor and acceptor were attached on the same base pair ($n=1$). Based on the structural properties of the dyes and their tethers, a good approximation for the parameters above could be $a=b\approx1.5$ nm, $L\approx0.5$ nm and $\varphi\approx225°$ [15, 40]. Using these values and $n=12$ bp, the distance between the donor and acceptor on the *HybrDNA* molecule was calculated to be approximately 4.81 nm. Substituting this distance in equation 6.2 together with a R_0 value of 5.6 nm for the AF488-AF647 FRET pair (R_0 provided by supplier), the resulting expected E_{FRET} for the sample was ~0.71.

6.2.2. The DyLight549-DyLight633 FRET pair

The not commonly used DyLight549-DyLight633 FRET pair was tested to confirm that the developed technique provided accurate results for fluorophores with relatively large spectral overlap which may lead to significant leakage between the green and red detection channels.

6.2.2.1. FRET sample preparation

The DNA samples labelled with the DyLight549-DyLight633 (DL549-DL633) FRET dye pair were provided by collaborator Tim Wilson, Imperial College London. Briefly, the oligo

sequences shown below were synthesised by Eurogentec, the forward having a 5' primary amine modification and the reverse sequence having a primary amine attached to a thymine via a C6 linkage. The position of the amine modified thymine, counting from the 3' end, determined the number of base pairs separating the donor and acceptor fluorophores in the final dsDNA molecule. Three reverse sequences were synthesised with modified amines at positions 5, 10 and 15:

H2N-5'-CAGTAGCAGATTCCAGTAGACCTTAGCACGAG-3'
3'-GTCA**T**CGTC**T**AAGG**T**CATCTGGAATCGTGCTC-5'

To attach the fluorescence molecules to the DNA, DL549 and DL633 with N-hydroxysuccinimide esters (NHS esters) modifications were purchased from Pierce. The NHS ester reacted with the primary amines to form a covalent linkage between dye and DNA. In a typical reaction, 50 µg of dye were solubilised in 10 µl of anhydrous dimethylformamide. To this, a mixture of 5.5 µl of 200 mM borate buffer at pH 8.5 and 6.4 µl of DNA at 1 mM was added. After mixing with a micropipette, the solution was left at room temperature for 1-4 hours. The labelled DNA was separated from the un-reacted components by reverse phase chromatography using a HiChrome 5 C18 column (HI-5C18-250A). After purification, the forward and reverse strands were combined in a 1:1 ratio, heated to 80ºC and then allowed to cool slowly to room temperature. This was to ensure the maximum possible yield of dsDNA. The dsDNA was isolated by ion-exchange chromatography using a TOSOH Bioscience TSKgel DNAE-NPR column.

The above procedure yielded three FRET DNA samples, with 4, 9 and 14 bp separation between the donor and acceptor molecules (see section 6.2.2.3 for spacing in nm). These will be referred to as *FRET04*, *FRET09* and *FRET14* respectively, while the donor-only or acceptor-only labelled oligos will be mentioned as *DNA549* and *DNA633* respectively.

6.2.2.2. Experimental procedure

The excitation and emission spectra of DL549 and DL633 are significantly different to those of the fluorescence dyes used in the rest of this work (figure 6.4). Therefore, some optical components had to be replaced. More specifically, a laser line of ~543 nm (~100 µW at 20 MHz, excitation path 2) was chosen to provide the necessary energy for donor excitation whilst minimising direct excitation of the acceptor and the excitation dichroic mirror was changed to the AH/FV1000/DM/11 (section 2.1.2), allowing excitation at the selected laser line. A relatively high overlap between the emission spectra of the two dyes was observed (figure 6.4). In order to avoid leakage of the donor emission into the red detection channel,

LP640 was used to filter the signal detected by the red APD, resulting however in a significant part of the acceptor fluorescence emission being lost. This loss was partially balanced by replacing HQ540/80 with ET585/40 filter for the green APD, which transmits in a fairly narrow region (565-605 nm).

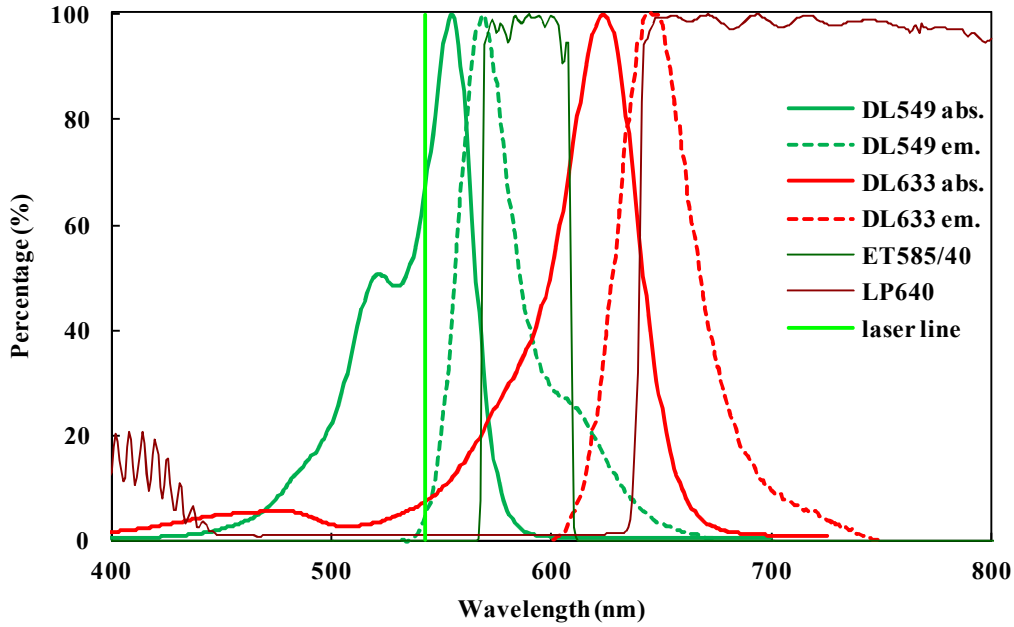

Figure 6.4. DL549-DL633 spectra, excitation line and emission filters. Due to the overlap of the fluorophore absorption spectra, a 543 nm laser line was considered as the best choice to achieve significant donor excitation without leading to large direct excitation of the acceptor. ET585/40 and LP640 were used to filter the signal detected by the green and red APDs respectively. The y-axis represents normalised absorption/emission or filter transmission.

Fluorescence intensity and lifetime measurements and analysis were performed as previously described (section 6.2.1.2), using *FRET04*, *FRET09* and *FRET14* samples as well as *DNA549* and *DNA633* as controls (100 nM and 10 nM concentrations, chosen based on trial and error). Fluorescence lifetime measurements at the same DNA concentration were also performed on samples freely flowing within a 50×50 μm^2 microfluidic channel. Finally, the samples were observed on cover slip at the single molecule level (500 pM concentration) and analysis was performed as described in section 2.3.4.

6.2.2.3. Inter-dye distance and theoretical E_{FRET} calculation

The inter-dye distance for the three FRET samples was determined as described in section 6.2.1.3. The calculated distances were 1.65 nm, 4.34 nm and 4.97 nm for *FRET04*, *FRET09* and *FRET14* respectively. Substituting these in equation 6.2, together with 5.87 nm as R_0 for the DL549-DL633 pair (R_0 provided by Pierce), resulted in theoretically estimated FRET efficiencies of 0.99, 0.86 and 0.73 for samples *FRET04*, *FRET09* and *FRET14* respectively.

6.3. Results

6.3.1. The AlexaFluor488-AlexaFluor647 FRET pair

Upon *HybrDNA* excitation, fluorescence intensity data acquired simultaneously in the green and red detection channels were used for calculating E_{FRET} via equation 6.6. Independent measurements on *DNA488* and *DNA647* were carried out to perform the necessary corrections. In order to compensate for leakage of the acceptor emission into the green detection channel, I_{DA} was calculated by:

$$I_{DA} = I_{H,g} - \alpha_l I_{H,r} \qquad \text{with} \qquad \alpha_l = I_{A,g} / I_{A,r} \tag{6.9}$$

where $I_{H,g}$, $I_{H,r}$ were the measured intensities for *HybrDNA* in the green and red detection channels respectively and $I_{A,g}$, $I_{A,r}$ were the measured intensities for the acceptor-only sample (*DNA647*) in the green and red detection channels respectively. Hence, factor α_l was a measure of the emission detected by the green APD that originated from acceptor excitation. Leakage was chosen to be expressed as a ratio of intensities instead of absolute photon counts, in order to eliminate errors associated with possible deviations in the sample concentration or other experimental conditions that could affect the fluorescence intensity. It was found that the leakage of the acceptor emission into the green detection channel was negligible, therefore $I_{DA} \approx I_{H,g}$. In a similar way, I_{AD} in equation 6.6 was calculated by:

$$I_{AD} = I_{H,r} - \beta_l I_{DA} - I_{A,r} \qquad \text{with} \qquad \beta_l = I_{D,r} / I_{D,g} \tag{6.10}$$

where $I_{D,r}$, $I_{D,g}$ were the measured intensities for the donor-only sample (*DNA488B*) in the red and green detection channels respectively. $\beta_l I_{DA}$ represented the photons detected in the red channel, which originated from donor instead of acceptor excitation. The corrected value I_{DA} was used here (instead of $I_{H,g}$) for better accuracy. In addition, in order to correct for direct AF647 excitation, $I_{A,r}$ was subtracted from the photon counts detected in the red channel ($I_{H,r}$). It should be noted that before any calculations were performed, all measured intensities were corrected for background noise. Finally, the correction parameter γ in equation 6.6 (given by equation 6.7) for the specific dye pair and detection arrangement was:

$$\gamma = \frac{0.33}{0.92} \times 0.9913 \tag{6.11}$$

with 0.33, 0.92 being the acceptor and donor quantum yields respectively (provided by Invitrogen) and 0.9913 the red-to-green APD detection efficiency derived from equation 2.6.

By combining equations 6.6 and 6.9-6.11, the extracted FRET efficiency for *HybrDNA* was 0.37±0.02. This was not consistent with the theoretically expected E_{FRET} of 0.71 (figure 6.5). Additional measurements were performed at a variety of concentrations and laser powers, which yielded similar results (data not shown).

Subsequently, fluorescence lifetime data collected from the donor (green) channel were used for calculating E_{FRET} according to equation 6.8. The donor lifetime in the absence of the acceptor (τ_D) was determined via *DNA488B* excitation. More specifically, the donor decay was fitted to a double exponential function (χ_R^2=1.11) yielding two lifetime components. The slow component (3.50±0.09 ns) was identified as the fluorophore-DNA conjugate lifetime τ_D, while the fast component (0.20±0.002 ns) was more likely related to the optical arrangement and background noise and not linked to the sample. This component remained constant (lifetime and amplitude) throughout the experiments and, therefore, it was fixed during all fluorescence decay fitting processes. This will be referred to as *setup component*.

Upon *HybrDNA* excitation, τ_{DA} values were initially extracted via a double exponential fit (*setup component* fixed). The obtained lifetimes however (non-fixed component), showed very little decrease with respect to τ_D, resulting in E_{FRET} no higher than 0.1 (~0.09±0.02).

The extremely low E_{FRET} was interpreted as evidence that the extracted τ_{DA} did not represent solely hybridised DNA molecules. It was more likely that an additional component, with lifetime higher than the expected under FRET, was present in the *HybrDNA* sample, contributing to the fluorescence decay. This was attributed to donor molecules which did not undergo FRET, considering that during sample preparation an assessment step was not performed to evaluate the efficiency of the hybridisation process. Consequently, it was possible that not all DNA oligos were successfully hybridised and thus, a fraction of the donor molecules in the solution did not possess respective acceptors in close proximity. This could also offer an explanation for the discrepancy between the theoretically calculated and the experimentally extracted from intensity measurements FRET efficiencies. For the latter, only the emission of donors attached to hybridised molecules should be taken into account during FRET calculation. As a result, I_{DA} (equations 6.6 and 6.9) should be further adjusted.

In order to correctly represent the *HybrDNA* sample as a mixture of donor-only (no FRET) and donor-acceptor (experiencing FRET) molecules, the fluorescence decay was fitted to a triple exponential function. During this fit, in addition to the *setup component*, the lifetime of a

second component was fixed, at the lifetime of the donor τ_D. According to equation 1.3, the equation used for the fitting was:

$$I(t) = \alpha_D \exp\left(-t/\tau_D\right) + \alpha_{DA} \exp\left(-t/\tau_{DA}\right) + \alpha_S \exp\left(-t/\tau_S\right) \quad (6.12)$$

where α_D, α_{DA}, α_S and τ_D, τ_{DA}, τ_S were the amplitudes and lifetimes of the donor-only component, the donor-acceptor component (FRET) and the *setup component* respectively (τ_D, α_S, τ_S fixed). The obtained value for τ_{DA} was 1.17±0.05 ns. Substituting τ_{DA} and τ_D on equation 6.8 resulted in an average E_{FRET} of ~0.67±0.01 (6 repeats performed, figure 6.5). This was in satisfying agreement with the theoretically estimated E_{FRET} (~0.71).

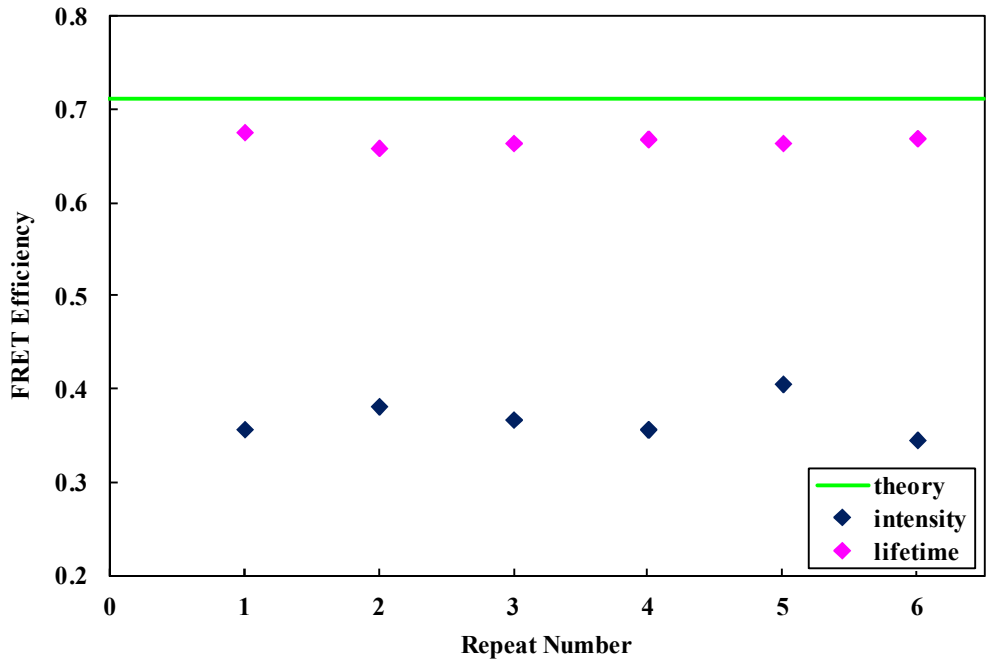

Figure 6.5. FRET efficiencies for *HybrDNA* at 10 nM, extracted via fluorescence intensity (blue) and fluorescence lifetime (magenta) measurements. The theoretically predicted E_{FRET} is represented by the green line.

6.3.2. The DyLight549-DyLight633 FRET pair

6.3.2.1. Bulk FRET measurements on cover slip

Identical experiments to those described in section 6.3.1 were carried out using *FRET04*, *FRET09* and *FRET14* samples. Measurements on *DNA549* and *DNA633* were also performed, in order to correct for direct acceptor excitation and cross talk artefacts in intensity calculations (equations 6.9 and 6.10). The ratio Q_A/Q_D in the expression for γ (equation 6.7) was 1.427 (quantum yields provided by Pierce). The FRET efficiencies extracted via equation 6.6 varied

between 0.14 and 0.37 for 100 nM and 10 nM samples, which, similarly to results presented in section 6.3.1, were significantly lower than the theoretically expected efficiencies (figure 6.6). This implied that, as before, the FRET samples possibly contained donor molecules with no respective acceptors, due to labelling efficiency mismatch for the two fluorophores, reduced hybridisation efficiency or free donor dye molecules that were not completely removed during sample preparation.

For fluorescence lifetime-based E_{FRET} calculation, *DNA549* was excited and the donor lifetime was found using a double exponential fit with the *setup component* fixed. The extracted τ_D was 1.16±0.01 ns. A triple exponential fit, with the donor and *setup component* lifetimes fixed, was used to extract fluorescence lifetimes upon FRET (τ_{DA} in equation 6.12). Subsequently, FRET efficiencies were calculated via substitution in equation 6.8. The resulting E_{FRET} values were 0.69±0.02, 0.86±0.01 and 0.99±0.01 for *FRET14*, *FRET09* and *FRET04* respectively (figure 6.6). These were in excellent agreement with the respective theoretically calculated efficiencies of 0.73, 0.86 and 0.99 (section 6.2.2.3).

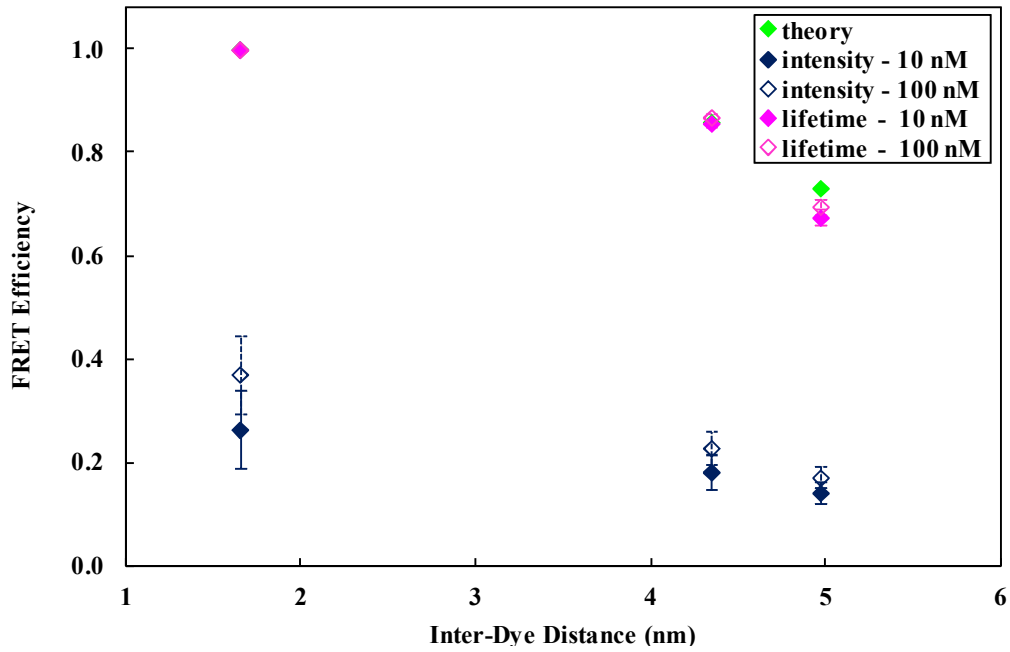

Figure 6.6. Bulk FRET efficiencies versus inter-dye distance at 10 nM (filled markers) and 100 nM (open markers) DNA concentration, extracted via fluorescence intensity (blue) and fluorescence lifetime (magenta) measurements. Theoretically predicted efficiencies are shown in green (where not visible they overlap with the lifetime magenta points). Error bars represent standard deviation. Distances of 1.65 nm, 4.34 nm and 4.97 nm correspond to *FRET04*, *FRET09* and *FRET14* respectively.

6.3.2.2. FRET measurements in flow

Fluorescence lifetime measurements were performed on 10 nM FRET samples, freely flowing down the length of a microfluidic channel. The aim of these measurements was to confirm the

suitability of the FRET technique described above for microfluidic experiments, as well as to investigate possible effects of the flow rate on the calculated efficiencies.

FRET14, *FRET09* and *FRET04* were introduced in the channel and data were collected at flow rates of 1.00, 0.50, 0.10 and 0.05 µl/min, using point and laser scanning excitation modes. Fluorescence decays were fitted to equation 6.12 and E_{FRET} values were calculated as previously described (section 6.3.2.1). Table 6.1 and figure 6.7 show the resulting E_{FRET} for each condition together with the theoretically expected values.

Table 6.1. FRET efficiencies for *FRET14*, *FRET09* and *FRET04* measured within a microchannel.

10 nM DNA in flow			point excitation mode				laser scanning excitation mode			
sample	dist.(nm)	theory	1µl/min	0.5µl/min	0.1µl/min	0.05µl/min	1µl/min	0.5µl/min	0.1µl/min	0.05µl/min
FRET14	4.97	0.731	0.667	0.668	0.670	0.667	0.717	0.713	0.734	0.695
FRET09	4.34	0.859	0.848	0.870	0.857	0.861	0.877	0.870	0.871	0.870
FRET04	1.65	0.999	0.999	0.999	0.999	0.999	0.999	0.999	0.999	0.999

E_{FRET} calculations in flow were consistent with the efficiencies obtained via bulk measurements on cover slip and with the theoretical estimations. In addition, no particular trend was observed with respect to the flow rate. The mode of excitation, point or laser scanning, did not have a significant effect on the results, with scanning mode yielding slightly higher E_{FRET}. *FRET14* exhibited more disperse FRET efficiencies than *FRET09* and *FRET04*, these however were well scattered around the average.

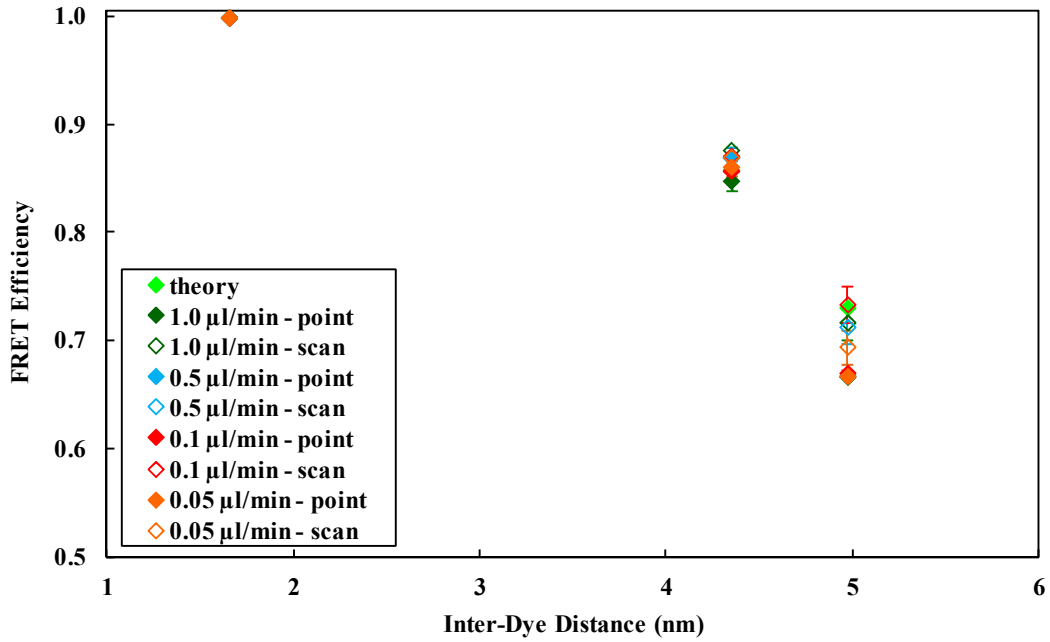

Figure 6.7. FRET efficiencies versus inter-dye distance, extracted via fluorescence lifetime measurements within a microfluidic channel (10 nM), using point (filled markers) and laser scanning (open markers) excitation modes. Theoretically predicted efficiencies are shown in light green. Distances of 1.65 nm, 4.34 nm and 4.97 nm correspond to FRET04, FRET09 and FRET14 respectively. Non-visible data points overlap.

6.3.2.3. FRET measurements at the single molecule level

Single molecule FRET measurements were performed using *DNA549*, *FRET14*, *FRET09* and *FRET04* at 500 pM concentration. Unlike experiments presented in chapter 5, whereby single DNA molecules labelled with an intercalated dye were detected (many dye molecules per DNA molecule), the results provided herein refer to single dye molecule detection. Therefore, the fluorescence signal during these experiments was much weaker. In addition, under high FRET conditions, photon counts obtained in the donor channel were further reduced. A typical burst scan under high FRET is shown in figure 6.8.

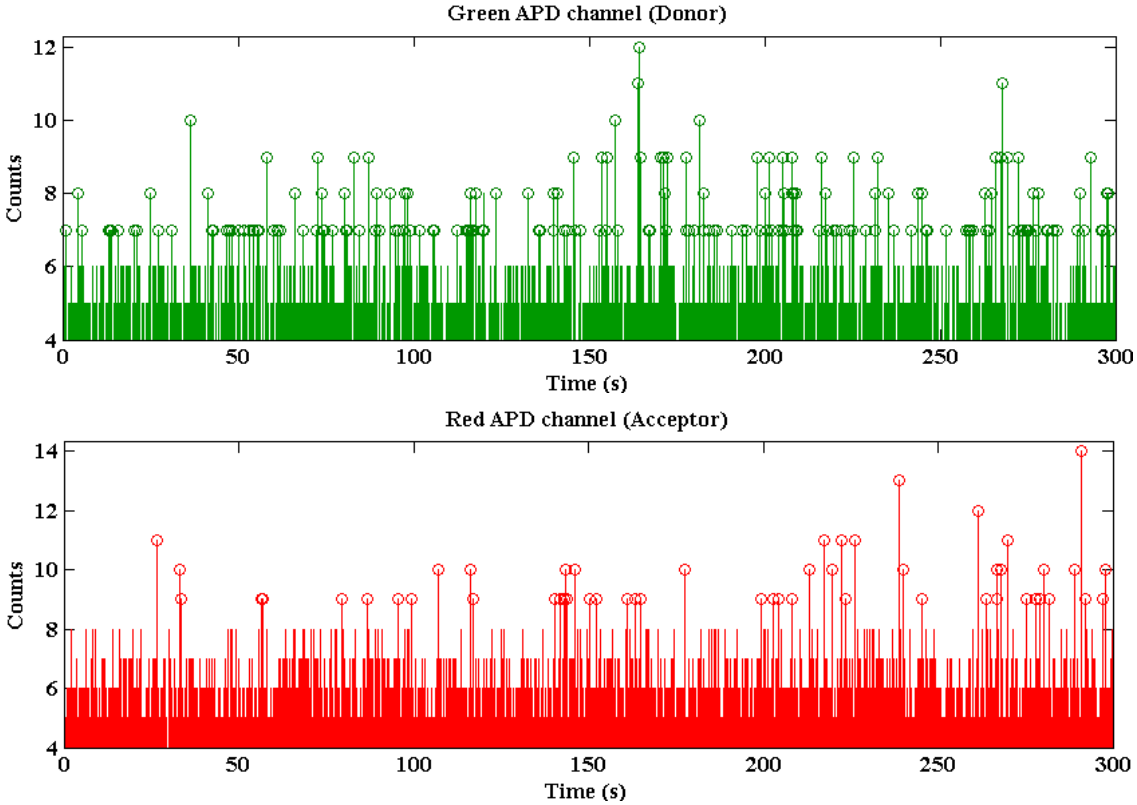

Figure 6.8. Single molecule burst scan for *FRET04* in the green (top) and red (bottom) detection channels over a 300 s acquisition period. Based on background levels and control measurements, the threshold for the peak locating logarithm was set to 7 photon counts.

In order to distinguish between fluorescence originating from dye molecules and background noise, the thresholds for peak height and peak area were set at 7 and 10 photons respectively. The number of peaks detected for each sample in the green and red channels during a 300 s period can be seen in table 6.2. Peak height and peak area histograms are given in figures 6.9 and 6.10 respectively.

In the green detection channel, the number of peaks exceeding the height and area thresholds for the three FRET samples was significantly lower than the respective number of peaks for

the donor-only sample (*DNA549*). However, there was only small variation between *FRET14*, *FRET09* and *FRET04* (table 6.2). Additionally, in terms of peak height and peak area, the observed values for FRET samples and *DNA549* were very similar (figures 6.9a and 6.10a). This could possibly indicate that the detected in the green channel molecules represented only the non-fretting components of each sample. Due to energy transfer, the molecules undergoing FRET did not emit enough photons to overcome the peak height and peak area thresholds. Therefore, they could not be resolved from the background and were not detected. As a result, the peak height and area histograms for *FRET14*, *FRET09*, *FRET04* and *DNA549* displayed high resemblance, as all the detected peaks corresponded to non-experiencing FRET donors. As mentioned in previous sections, these could be molecules labelled only with the donor dye, non-hybridised oligos or free DL549 residue.

Table 6.2. Number of bursts exceeding the height and area thresholds in green and red channels.

500 pM DNA		**peak height>7 photon counts**		**peak area>10 photon counts**	
sample	**distance (nm)**	**green**	**red**	**green**	**red**
DNA549	-	629	0	324	0
FRET14	4.97	86	30	32	5
FRET09	4.34	84	104	32	33
FRET04	1.65	70	159	20	70

On the contrary, in the red detection channel, there were no peaks above the threshold for *DNA549* and *DNA633*, thus, photons detected in the red region directly corresponded to molecules experiencing FRET. According to data acquired in the red channel, a greater number of molecules were detected as the inter-dye distance decreased (table 6.2). At the same time, the height and area of the detected peaks also slightly increased, indicating that more energy was transferred to the acceptor molecules (figures 6.9b and 6.10b). However, equation 5.6 could not be used for the intensity-based FRET efficiency calculation, due to the lack of fretting molecules detected in the green channel.

It becomes apparent that the lack of fretting molecules in the green detection channel also prevented the calculation of lifetime-based E_{FRET}, as this requires the decays of FRET experiencing donors. Setting a threshold of 10 photons for the MLE routine (the same as the peak area threshold), the fluorescence lifetime of donor-only molecules (*DNA549*) was extracted. Figure 6.11 shows a single molecule *DNA549* lifetime histogram, which confirms the ~1.16 ns τ_D extracted from bulk experiments (section 6.3.2.1).

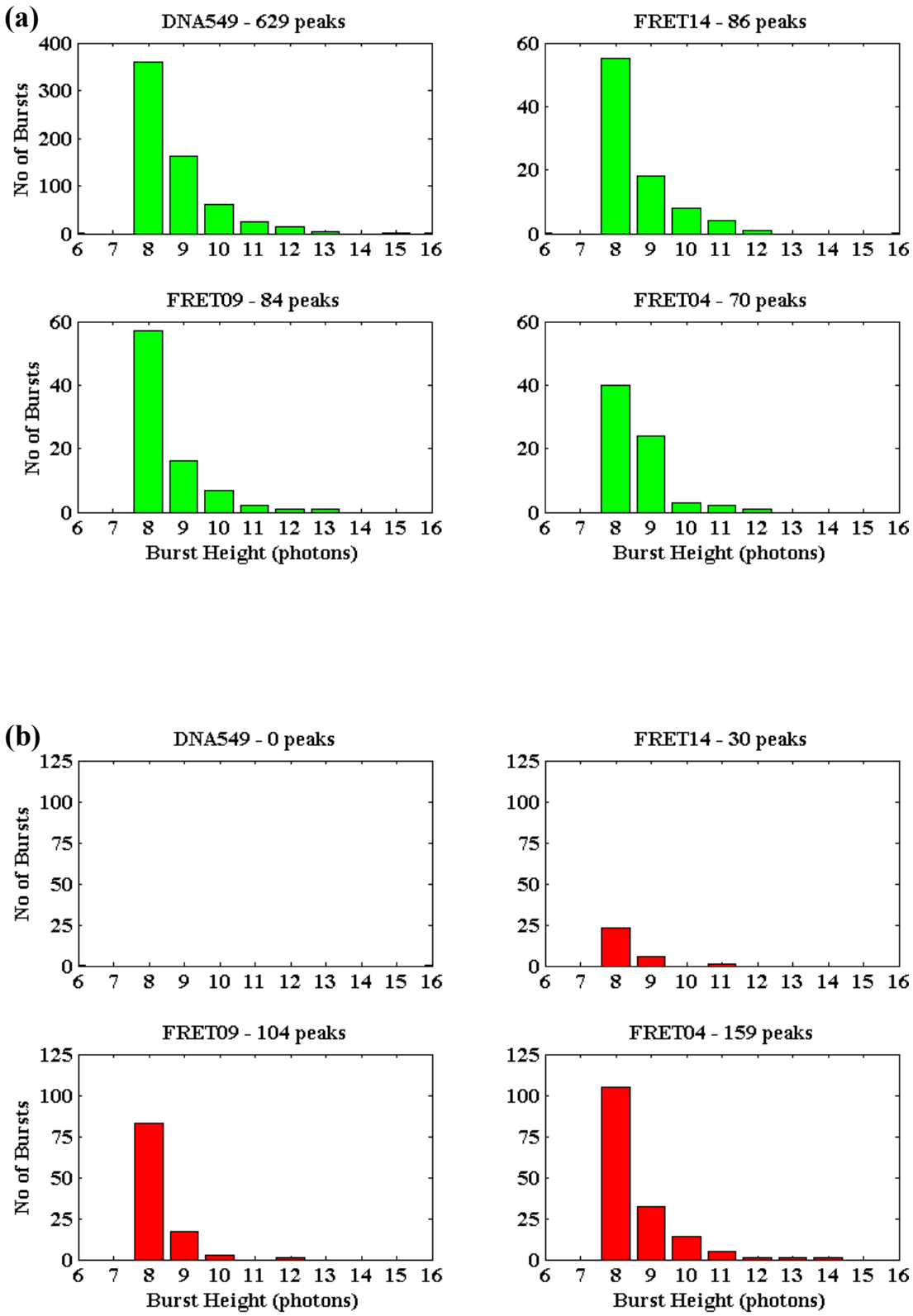

Figure 6.9. Burst height histograms for (a) green and (b) red detection channels, obtained from measurements of *DNA549*, *FRET14*, *FRET09* and *FRET04* at the single molecule level.

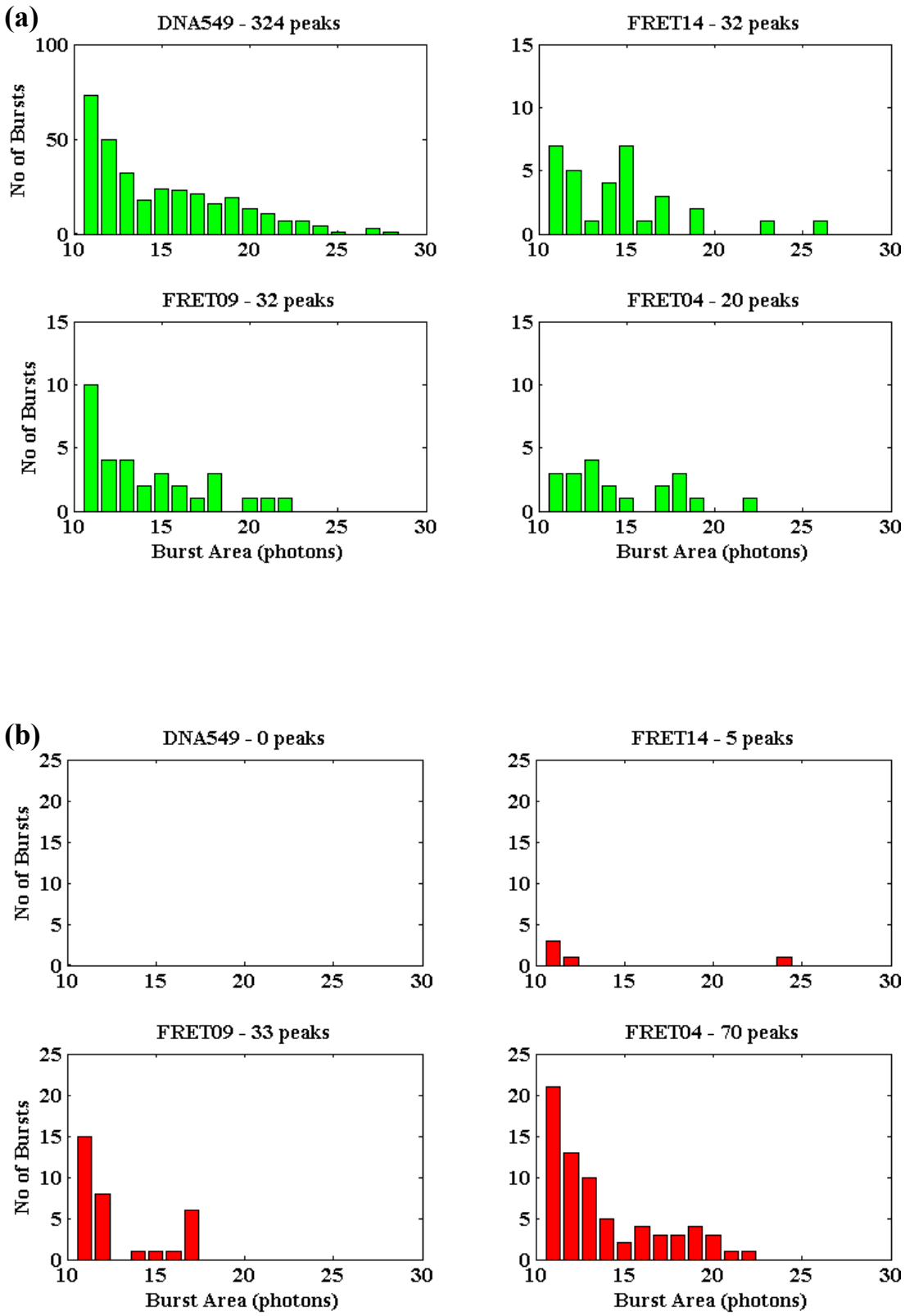

Figure 6.10. Burst area histograms for (a) green and (b) red detection channels, obtained from measurements of *DNA549*, *FRET14*, *FRET09* and *FRET04* at the single molecule level.

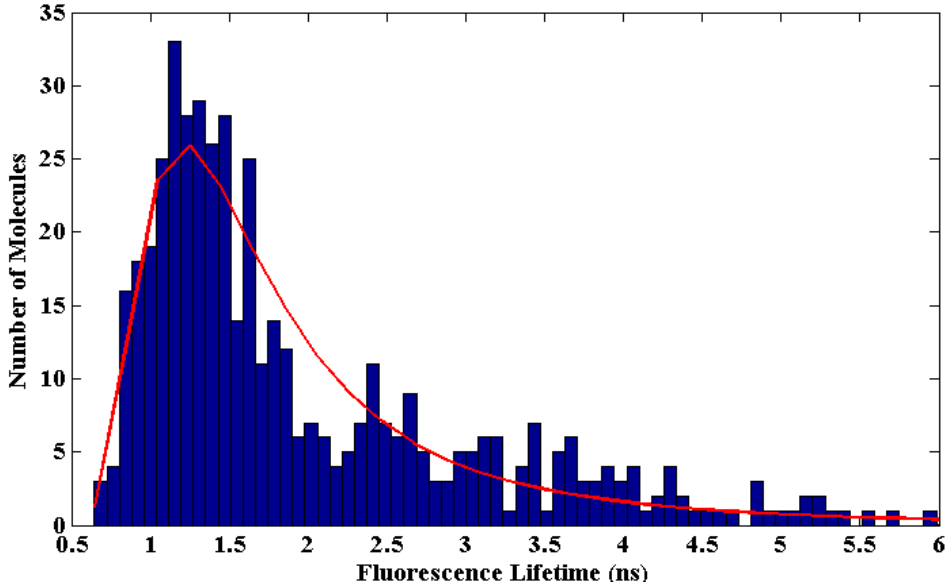

Figure 6.11. Single molecule fluorescence lifetime histogram for *DNA549*. The extracted donor lifetime was approximately 1.16 ns.

6.4. Discussion

6.4.1. Error analysis

Comparing the experimentally determined values of a quantity to the respective theoretically calculated values, the absolute and relative errors, ε_{abs} and ε_{rel}, can be extracted using:

$$\varepsilon_{abs} = value_{\exp eriment} - value_{theory} \quad \text{and} \quad \varepsilon_{rel} = \frac{\varepsilon_{abs}}{value_{theory}} \times 100\% \tag{6.13}$$

Six repeats were performed on the HybrDNA sample (section 6.3.1), yielding an average E_{FRET} of 0.67, with a standard deviation of 0.006. Comparing this to the theoretically calculated E_{FRET}, the absolute and relative errors were -0.05 and -6.36%. Yet, a more meaningful evaluation of the method used herein can be obtained by expressing the above errors in terms of distances. By reverse solving of equation 6.2, the experimentally extracted FRET efficiencies yielded an average fluorophore separation distance of 4.99 nm, with a standard deviation of 0.02 nm. Substitution on equation 6.13 resulted in ε_{abs} and ε_{rel} of 0.17 nm and 3.16% respectively.

Regarding the DL549-DL633 dye pair, results presented in sections 6.3.2.1 and 6.3.2.2 illustrate that flowing and freely diffusing molecules exhibited almost identical E_{FRET} for the same inter-dye distance. In addition, the flow rate and excitation mode (point/laser scanning) did not affect the extracted E_{FRET}. Hence, bulk and flow experiments could be safely

considered as repeats of the same measurement and the extracted average E_{FRET} for *FRET14*, *FRET09* and *FRET04* was 0.69, 0.87 and 0.99 respectively (standard deviations 0.024, 0.009 and 0.001 respectively). Comparing to the theoretically expected FRET efficiencies, the average ε_{abs} and ε_{rel} were -0.04 and -5.6%, 0.01 and 0.7%, 0.001 and -0.04%, for *FRET14*, *FRET09*, *FRET04* respectively.

The average experimentally determined inter-dye distances for the above samples were 5.14 nm, 4.31 nm and 1.83 nm, with standard deviation of 0.10 nm, 0.05 nm and 0.02 nm respectively (figure 6.12). It is evident that the standard deviation for short inter-dye distances was smaller, possibly due to the DNA construct being more rigid over a dye separation of only a few base pairs. For longer inter-dye separations, the intramolecular distances are less stable and a greater number of repeats are required to minimise the standard deviation.

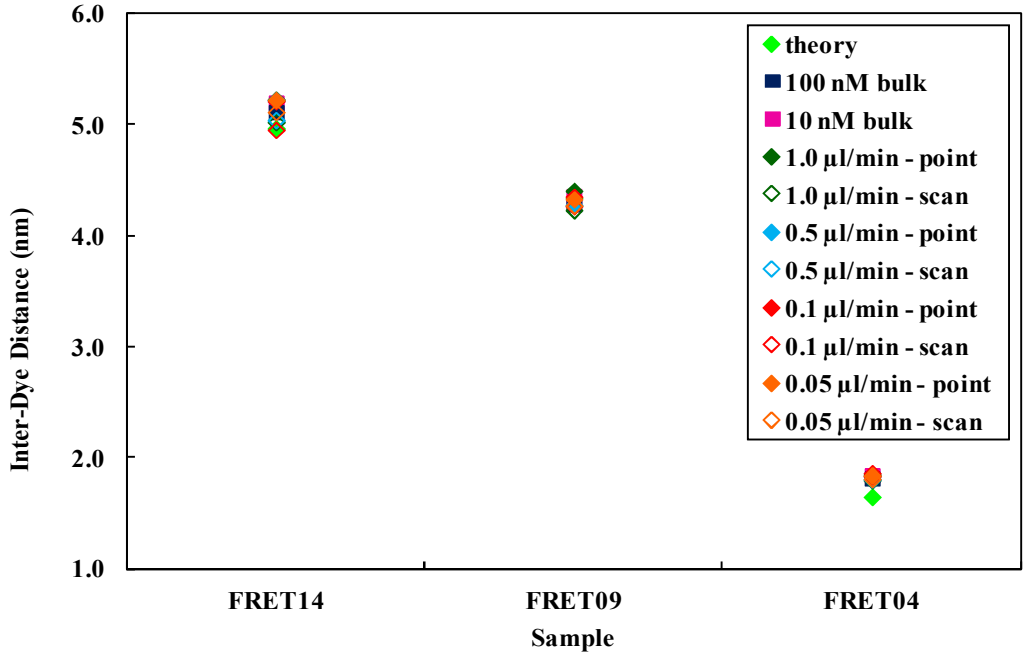

Figure 6.12. Experimentally determined donor-acceptor separation distances via fluorescence lifetime measurements, for *FRET14*, *FRET09* and *FRET04*. Experiments were performed on freely diffusing (10 nM and 100 nM) as well as on flowing (10 nM) molecules, under various flow rates and using point or laser scanning excitation mode. The theoretically predicted values are shown in light green. Non-visible data points overlap.

Comparison of the experimentally extracted donor-acceptor distances with the respective theoretical values, yielded average ε_{abs} and ε_{rel} of 0.17 nm and 3.35%, -0.04 nm and -0.87%, 0.18 nm and 11.06%, for *FRET14*, *FRET09*, *FRET04* respectively. These indicated that, unlike efficiency-based errors, ε_{rel} expressed in terms of distance was larger for *FRET04*. This was expected as, for short distances, a deviation of even a few tenths of a nanometre were significant compared to the real inter-dye separation. Therefore, similar ε_{abs} values for *FRET14* and *FRET04* (0.17-0.18 nm) resulted in much higher ε_{rel} for *FRET04* than for *FRET14*.

According to the above calculations, the 9 bp fluorophore separation was determined more accurately than the 4 bp and 14 bp distances. In addition, data obtained from both AF488-AF647 and DL549-DL633 FRET dye pairs, indicated that a separation distance yielding E_{FRET} of approximately 0.72 (0.71 and 0.73 for *HybrDNA* and *FRET14* respectively), could be experimentally determined with absolute and relative errors of ~0.17 nm and ~3.2% respectively.

6.4.2. Data acquisition and analysis method: the fluorescence lifetime approach

Experiments conducted using either of the two systems tested (dsDNA labelled with either AF488-AF647 or DL549-DL633) showed that a part of the fluorescence detected in the green region did not originate from FRET-experiencing donor molecules. This was indicated by the low FRET efficiencies extracted from fluorescence intensity-based calculations, as well as from fluorescence lifetime analysis, when a single component (in addition to the *setup component*) was used for decay fitting. Instead, the use of two lifetime components (in addition to the *setup component*) illustrated that the samples contained two populations; one population characterised by the original donor lifetime (τ_D) and a second one, displaying a lifetime closely matched to the theoretically predicted lifetime under FRET (τ_{DA}). Thus, the samples essentially consisted of a mixture of fretting and non-fretting molecules.

As discussed in previous sections, a possible explanation for this could be that for a portion of the donor molecules contained in the sample, there were no corresponding acceptors present within close proximity. Thus, energy transfer did not occur. This could partially be due to the sample preparation procedure, which could possibly lead to donor-only labelled hybridised DNA molecules (mismatch between donor and acceptor labelling efficiency), non-hybridised ssDNA molecules labelled with the donor dye (hybridisation efficiency) or free dye residue (failure to completely remove the donor fluorophore from the final sample).

In addition to sample preparation related factors, the apparent non-FRET condition observed for a fraction of donor molecules could be attributed to processes other than energy transfer. More specifically, a number of studies on immobilised DNA molecules have reported significant donor intensity values, even for donor-acceptor separation distances that should theoretically yield nearly 100% energy transfer [41-43]. Sabanayagam et al. resolved the discrepancy by introducing a scaling factor to the E_{FRET} expression, which accounted for all de-excitation pathways competing FRET [42]. Large donor intensities under presumably high FRET conditions have also been attributed to inactive acceptors [21, 41, 43]. These studies, focus on cyanine acceptor dyes and prolonged excitation times (immobilised molecules), which was not the case in this work. However, similar effects could not be ruled out with

certainty for the dyes used herein. Especially the DyLight FRET pair has not been extensively studied in the past and the time scale for possible acceptor dark states is not known.

With no regard to the reasons causing a portion of the donor molecules not to transfer energy to acceptor molecules, experiments presented in this chapter showed that extracting FRET efficiency via bulk fluorescence intensity measurements can be highly problematic. Instead, experiments at the single molecule level are required to handle each molecule individually and to identify the 'zero' or 'near zero' FRET populations. In a typical SMD E_{FRET} histogram, these populations are represented by a characteristic peak close to zero, which has been described as an artefact [15]. On the contrary, fluorescence lifetime methods using multi-exponential decay fitting, allow for distinguishing, to some extent, between molecules, which exhibit different lifetimes and thus, represent different energy transfer states in bulk.

In addition to the ability for identifying different FRET populations within a sample, the superiority of a lifetime-based FRET technique also lies in the fact that fluorescence lifetime is hardly prone to inconsistencies, caused by sample concentration and optical arrangement features, such as illumination intensity/uniformity, emission filters, photon detection efficiency etc. Especially in calculations whereby the direct acceptor excitation must be taken into account, the intensity-induced discrepancy can be large, as direct acceptor emission can only be expressed in absolute, and not relative, photon counts. Thus, even slight variations in fluorophore concentration, illumination power or background signal levels may lead to false results. On the contrary, in a fluorescence lifetime approach, the error introduced by FRET correction measurements is minimised, rendering this method highly reproducible and, therefore, more reliable than a fluorescence intensity-based method.

6.4.3. FRET measurements at the single molecule level

Results presented in section 6.3.2.3 illustrated that for short inter-dye distances, the donor emission is significantly reduced due to energy transfer to the acceptor. For the specific FRET dye pair tested (DL549-DL633) combined with the current optical arrangement, donor molecules undergoing FRET could not be resolved from background noise. Therefore, these molecules were not detected in the green channel. It should be noted that the theoretically estimated FRET efficiencies were above 0.7 (inter-dye distances shorter than R_0). If the labelling of the *DNA633* oligo was performed on sites yielding fluorophore separation around or greater than R_0, donor molecules undergoing FRET would potentially provide enough photon counts to be detected in the green channel, as a result of lower energy transfer occurring.

Regarding fluorescence lifetime SMD measurements, besides the low number of photons emitted per molecule, an additional detection limitation was set by the range of fluorescence lifetimes that could be measured with the current optical arrangement. Due to the instrument response, individual molecules exhibiting lifetimes below ~0.7 ns could not be successfully detected. The extracted donor lifetime τ_D was ~1.16 ns, this however dropped below 0.7 ns during FRET. Thus, the specific τ_{DA} values could only be extracted via multi-exponential fitting of fluorescence decay data acquired from bulk measurements.

Emission detected in the red channel directly corresponded to energy transfer from donor to acceptor molecules. The increasing number, height and area of single molecule bursts in the red region for short inter-dye distances clearly indicated higher levels of energy transfer. However, single molecule E_{FRET} could not be extracted without the coincident donor bursts in the green channel. Also, a well-defined relationship between peak height/area and inter-dye distance could not be established based on the acquired data, due to the relatively small amount of molecules contributing to the histograms (figures 6.9b and 6.10b). By increasing the acquisition time, more conclusive histograms could be obtained and potentially provide quantitative relationships between peak characteristics and FRET efficiencies. Nevertheless, the number of molecules detected in the red channel per minute for each sample, appeared to be linearly related to the respective theoretically calculated E_{FRET} (figure 6.13).

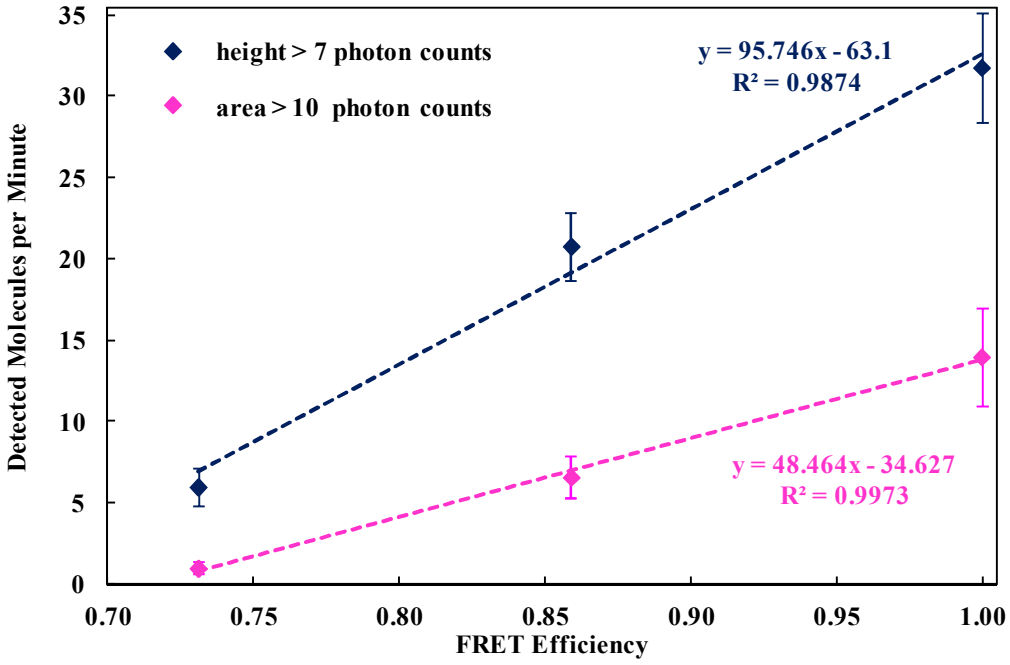

Figure 6.13. Number of bursts per minute which overcame the peak height (blue) and peak area (magenta) thresholds in the red detection channel versus theoretically estimated FRET efficiency. A linear relationship was observed.

6.5. Summary and conclusion

The fluorescence lifetime FRET analysis method presented herein was proved to be successful for estimating nanoscale distances with high accuracy. Although fluorescence lifetime-based FRET techniques are rarely found in literature, the advantages of such methods over a fluorescence intensity approach were clearly demonstrated in this work. In addition, unlike conventional methods which employ single molecule measurements to distinguish between different energy transfer states, the method used herein for lifetime fitting, keeping the *setup component* and the original donor lifetime τ_D fixed, allowed for discrimination, to some extent, between different FRET states in bulk. According to the results presented in this chapter, in a simple, single-FRET condition experiment, a triple exponential function could be used to fit the donor decay (*setup component* and τ_D fixed), while in cases whereby more than one fretting populations are expected, a multi-exponential fit can be applied to discriminate between different FRET levels. Following bulk measurements, experiments within microfluidic channels can be performed without the need for additional control measurements. The validity of the specific technique was verified by performing measurements on a commonly used FRET dye pair (Alexa Fluor dyes) as well as on a more challenging FRET pair (DyLight dyes) which has not been extensively studied in the past.

It was concluded that for the specific optical arrangement used herein, single dye-molecule experiments should only be attempted, provided that the expected fluorescence intensity and fluorescence lifetime of donor molecules undergoing FRET would be at levels allowing for successful detection, despite the system limitations.

6.6. References

1. Lakowicz, J.R., *Principles of fluorescence spectroscopy, 3rd edition.* Springer Science and Business Media, New York, 2006.
2. Stryer, L. and R.P. Haugland, *Energy transfer: a spectroscopic ruler.* Proceedings of the National Academy of Sciences of the United States of America, 1967. **58**(2): p. 719-26.
3. Zal, T. and N.R.J. Gascoigne, *Using live FRET imaging to reveal early protein-protein interactions during T cell activation (vol 16, pg 418, 2004).* Current Opinion in Immunology, 2004. **16**(5): p. 674-683.
4. Wallrabe, H. and A. Periasamy, *Imaging protein molecules using FRET and FLIM microscopy.* Current Opinion in Biotechnology, 2005. **16**(1): p. 19-27.
5. Piston, D.W. and G.-J. Kremers, *Fluorescent protein FRET: the good, the bad and the ugly.* Trends in Biochemical Sciences, 2007. **32**(9): p. 407-414.
6. Roy, R., S. Hohng and T. Ha, *A practical guide to single-molecule FRET.* Nature Methods, 2008. **5**(6): p. 507-516.
7. Schuler, B. and W.A. Eaton, *Protein folding studied by single-molecule FRET.* Current Opinion in Structural Biology, 2008. **18**(1): p. 16-26.
8. McCann, J.J., U.B. Choi, L. Zheng, K. Weninger and M.E. Bowen, *Optimizing Methods to Recover Absolute FRET Efficiency from Immobilized Single Molecules.* Biophysical Journal, 2010. **99**(3): p. 961-970.
9. Pietraszewska-Bogiel, A. and T.W.J. Gadella, *FRET microscopy: from principle to routine technology in cell biology.* Journal of Microscopy, 2010. **241**(2): p. 111-118.
10. Varghese, S.S., Y. Zhu, T.J. Davis and S.C. Trowell, *FRET for lab-on-a-chip devices - current trends and future prospects.* Lab on a Chip, 2010. **10**(11): p. 1355-1364.
11. Fruhwirth, G.O., L.P. Fernandes, G. Weitsman, G. Patel, M. Kelleher, K. Lawler, A. Brock, S.P. Poland, D.R. Matthews, G. Keri, P.R. Barber, B. Vojnovic, S.M. Ameer-Beg, A.C.C. Coolen, F. Fraternali, and T. Ng, *How Forster Resonance Energy Transfer Imaging Improves the Understanding of Protein Interaction Networks in Cancer Biology.* Chemphyschem, 2011. **12**(3): p. 442-461.
12. Wu, P.G. and L. Brand, *Resonance energy-transfer - Methods and Applications.* Analytical Biochemistry, 1994. **218**(1): p. 1-13.
13. Michalet, X., S. Weiss and M. Jager, *Single-molecule fluorescence studies of protein folding and conformational dynamics.* Chemical Reviews, 2006. **106**(5): p. 1785-1813.
14. Joo, C., H. Balci, Y. Ishitsuka, C. Buranachai and T. Ha, *Advances in single-molecule fluorescence methods for molecular biology*, in *Annual Review of Biochemistry*. 2008. p. 51-76.
15. Deniz, A.A., M. Dahan, J.R. Grunwell, T.J. Ha, A.E. Faulhaber, D.S. Chemla, S. Weiss and P.G. Schultz, *Single-pair fluorescence resonance energy transfer on freely diffusing molecules: Observation of Forster distance dependence and subpopulations.*

Proceedings of the National Academy of Sciences of the United States of America, 1999. **96**(7): p. 3670-3675.

16. Grunwell, J.R., J.L. Glass, T.D. Lacoste, A.A. Deniz, D.S. Chemla and P.G. Schultz, *Monitoring the conformational fluctuations of DNA hairpins using single-pair fluorescence resonance energy transfer.* Journal of the American Chemical Society, 2001. **123**(18): p. 4295-4303.

17. McKinney, S.A., A.C. Declais, D.M.J. Lilley and T. Ha, *Structural dynamics of individual Holliday junctions.* Nature Structural Biology, 2003. **10**(2): p. 93-97.

18. McKinney, S.A., A.D.J. Freeman, D.M.J. Lilley and T.J. Ha, *Observing spontaneous branch migration of Holliday junctions one step at a time.* Proceedings of the National Academy of Sciences of the United States of America, 2005. **102**(16): p. 5715-5720.

19. Hohng, S., C. Joo and T. Ha, *Single-molecule three-color FRET.* Biophysical Journal, 2004. **87**(2): p. 1328-1337.

20. Kim, H.D., G.U. Nienhaus, T. Ha, J.W. Orr, J.R. Williamson and S. Chu, *Mg2+-dependent conformational change of RNA studied by fluorescence correlation and FRET on immobilized single molecules.* Proceedings of the National Academy of Sciences of the United States of America, 2002. **99**(7): p. 4284-4289.

21. Koopmans, W.J.A., A. Brehm, C. Logie, T. Schmidt and J. van Noort, *Single-pair FRET microscopy reveals mononucleosome dynamics.* Journal of Fluorescence, 2007. **17**(6): p. 785-795.

22. Ha, T.J., A.Y. Ting, J. Liang, W.B. Caldwell, A.A. Deniz, D.S. Chemla, P.G. Schultz and S. Weiss, *Single-molecule fluorescence spectroscopy of enzyme conformational dynamics and cleavage mechanism.* Proceedings of the National Academy of Sciences of the United States of America, 1999. **96**(3): p. 893-898.

23. Dittrich, P.S., B. Muller and P. Schwille, *Studying reaction kinetics by simultaneous FRET and cross-correlation analysis in a miniaturized continuous flow reactor.* Physical Chemistry Chemical Physics, 2004. **6**(18): p. 4416-4420.

24. Kapanidis, A.N., N.K. Lee, T.A. Laurence, S. Doose, E. Margeat and S. Weiss, *Fluorescence-aided molecule sorting: Analysis of structure and interactions by alternating-laser excitation of single molecules.* Proceedings of the National Academy of Sciences of the United States of America, 2004. **101**(24): p. 8936-8941.

25. Roy, R., A.G. Kozlov, T.M. Lohman and T. Ha, *Dynamic structural rearrangements between DNA binding modes of E. coli SSB protein.* Journal of Molecular Biology, 2007. **369**(5): p. 1244-1257.

26. Joo, C., S.A. McKinney, M. Nakamura, I. Rasnik, S. Myong and T. Ha, *Real-time observation of RecA filament dynamics with single monomer resolution.* Cell, 2006. **126**(3): p. 515-527.

27. Srisa-Art, M., E.C. Dyson, A.J. deMello and J.B. Edel, *Monitoring of real-time streptavidin-biotin binding kinetics using droplet microfluidics.* Analytical Chemistry, 2008. **80**(18): p. 7063-7067.

28. Groll, J., E.V. Amirgoulova, T. Ameringer, C.D. Heyes, C. Rocker, G.U. Nienhaus and M. Moller, *Biofunctionalized, ultrathin coatings of cross-linked star-shaped*

poly(ethylene oxide) allow reversible folding of immobilized proteins. Journal of the American Chemical Society, 2004. **126**(13): p. 4234-4239.

29. Kuzmenkina, E.V., C.D. Heyes and G.U. Nienhaus, *Single-molecule Forster resonance energy transfer study of protein dynamics under denaturing conditions.* Proceedings of the National Academy of Sciences of the United States of America, 2005. **102**(43): p. 15471-15476.

30. Deniz, A.A., T.A. Laurence, G.S. Beligere, M. Dahan, A.B. Martin, D.S. Chemla, P.E. Dawson, P.G. Schultz and S. Weiss, *Single-molecule protein folding: Diffusion fluorescence resonance energy transfer studies of the denaturation of chymotrypsin inhibitor 2.* Proceedings of the National Academy of Sciences of the United States of America, 2000. **97**(10): p. 5179-5184.

31. Schuler, B., E.A. Lipman and W.A. Eaton, *Probing the free-energy surface for protein folding with single-molecule fluorescence spectroscopy.* Nature, 2002. **419**(6908): p. 743-747.

32. Slaughter, B.D., M.W. Allen, J.R. Unruh, R.J.B. Urbauer and C.K. Johnson, *Single-molecule resonance energy transfer and fluorescence correlation spectroscopy of calmodulin in solution.* Journal of Physical Chemistry B, 2004. **108**(29): p. 10388-10397.

33. Slaughter, B.D., J.R. Unruh, M.W. Allen, R.J.B. Urbauer and C.K. Johnson, *Conformational substates of calmodulin revealed by single-pair fluorescence resonance energy transfer: Influence of solution conditions and oxidative modification.* Biochemistry, 2005. **44**(10): p. 3694-3707.

34. Hertzog, D.E., X. Michalet, M. Jager, X.X. Kong, J.G. Santiago, S. Weiss and O. Bakajin, *Femtomole mixer for microsecond kinetic studies of protein folding.* Analytical Chemistry, 2004. **76**(24): p. 7169-7178.

35. Yao, S. and O. Bakajin, *Improvements in mixing time and mixing uniformity in devices designed for studies of protein folding kinetics.* Analytical Chemistry, 2007. **79**(15): p. 5753-5759.

36. Lipman, E.A., B. Schuler, O. Bakajin and W.A. Eaton, *Single-molecule measurement of protein folding kinetics.* Science, 2003. **301**(5637): p. 1233-1235.

37. Hamadani, K.M. and S. Weiss, *Nonequilibrium single molecule protein folding in a coaxial mixer.* Biophysical Journal, 2008. **95**(1): p. 352-365.

38. Hofmann, H., F. Hillger, S.H. Pfeil, A. Hoffmann, D. Streich, D. Haenni, D. Nettels, E.A. Lipman and B. Schuler, *Single-molecule spectroscopy of protein folding in a chaperonin cage.* Proceedings of the National Academy of Sciences of the United States of America, 2010. **107**(26): p. 11793-11798.

39. Dickerson, R.E., *DNA-structure from A to Z.* Methods in Enzymology, 1992. **211**: p. 67-111.

40. Clegg, R.M., A.I.H. Murchie, A. Zechel and D.M.J. Lilley, *Observing the helical geometry of double-stranded DNA in solution by fluorescence resonance energy-transfer.* Proceedings of the National Academy of Sciences of the United States of America, 1993. **90**(7): p. 2994-2998.

41. Heilemann, M., E. Margeat, R. Kasper, M. Sauer and P. Tinnefeld, *Carbocyanine dyes as efficient reversible single-molecule optical switch.* Journal of the American Chemical Society, 2005. **127**(11): p. 3801-3806.

42. Sabanayagam, C.R., J.S. Eid and A. Meller, *Using fluorescence resonance energy transfer to measure distances along individual DNA molecules: Corrections due to nonideal transfer.* Journal of Chemical Physics, 2005. **122**(6).

43. Sabanayagam, C.R., J.S. Eid and A. Meller, *Long time scale blinking kinetics of cyanine fluorophores conjugated to DNA and its effect on Forster resonance energy transfer.* Journal of Chemical Physics, 2005. **123**(22).

CHAPTER 7
STUDYING BIOMOLECULES VIA FRET

7.1. Introduction

As discussed in chapter 6, FRET has been extensively used as a natural spectroscopic ruler to investigate conformations and dynamics of various biological systems. In a FRET configuration, changes in the measured energy transfer correspond to changes in the inter-dye distance, thus, are directly related to the relative position of known sites within the studied biomolecules. Specific FRET applications and techniques were discussed in detail in chapter 6. This chapter focuses on applying the previously described FRET analysis method in the study of molecular interactions and protein conformational changes. More specifically, two systems were tested; the well-known biotin-streptavidin binding model as well as the conformational change of bacterioopsin upon unfolding.

7.1.1. The streptavidin-biotin binding system

Streptavidin is a bacterial protein composed of four identical subunits, each capable of binding a single biotin with extremely high affinity and an exceptionally slow dissociation rate [1-3]. Hence, each streptavidin can bind up to four biotins. The streptavidin tetramer is organised in two symmetrical dimers, each containing a pair of binding sites (figure 7.1a) [2, 4, 5]. While the interface between the monomers of each dimer is maintained by over two-dozen hydrogen bonds, the dimer-dimer interaction is less strong and the quaternary integrity of the streptavidin tetramer is enhanced upon interaction with the biotin ligand. The biotin-streptavidin binding is often cited as one of the strongest known non-covalent protein-ligand interactions (association constant $K_a \approx 10^{15}$ M^{-1}) [1, 6, 7] and therefore it has been used in numerous studies for a wide range of bioanalytical applications [5, 8, 9]. For example, the strong bond between biotin and streptavidin can be exploited to firmly tether biomolecules, such as nucleic acids, on a surface or to attach them to other molecules [10-12]. A variety of engineering techniques have been proposed to modulate the streptavidin binding affinity and specificity and to alter its oligomeric and topological structure features as well as its physicochemical characteristics, with the aim to improve its value as a biotechnological tool [9].

Herein, a simple model was developed to investigate the effect of the ligand:streptavidin concentration ratio on the biotin-streptavidin binding. For this purpose, streptavidin and biotin were labelled with the donor and acceptor fluorophores respectively and fluorescence lifetime data were acquired at a variety of concentrations. Upon binding, the donor and acceptor molecules were brought into close proximity resulting in FRET and the efficiency of the energy transfer was associated with the number of biotins bound per streptavidin tetramer.

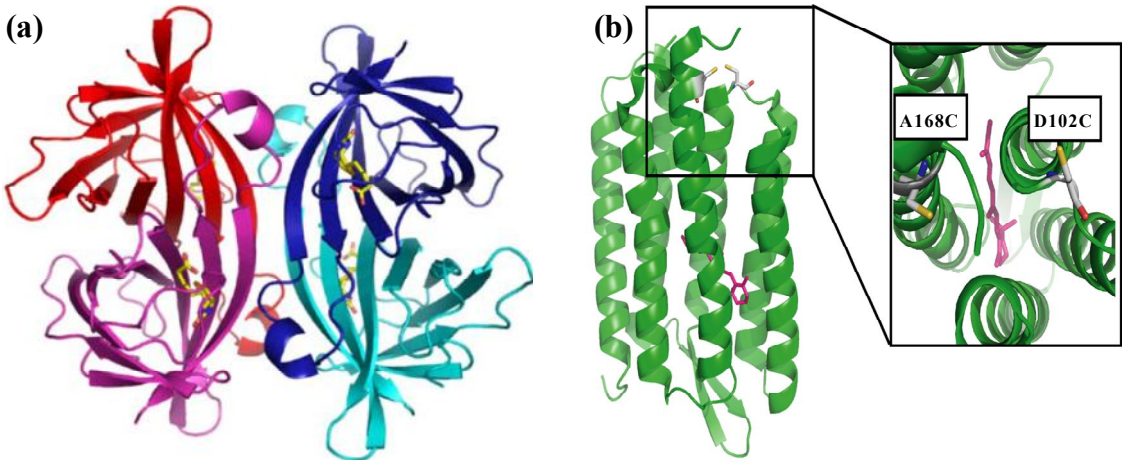

Figure 7.1. (a) The streptavidin tetramer structure, consisting of two dimers (red/magenta and blue/cyan). Bound biotins are shown in yellow. Adapted with permission from [5], copyright 2005, Elsevier. (b) Bacteriorhodopsin structure and cysteine mutations (A168C/D102C). Distance between side chains is approximately 1.2 nm. Retinal chromophore is shown in pink. Adapted with permission from [13], copyright 2010, Elsevier.

7.1.2. Bacterioopsin unfolding

Bacteriorhodopsin (bR) is a protein found in the membrane of *Halobacterium salinarium* which functions as a light-activated proton pump. Specifically, bR converts the energy of green light (500-650 nm) into an electrochemical proton gradient, which in turn is used for the production of chemical energy [14]. The protein consists of seven transmembrane alpha helices together with a covalently bound retinal chromophore (figure 7.1b) [15]. The retinal kinetically stabilizes bR by increasing its conformational rigidity and compactness [13]. Removing the retinal by bleaching with hydroxylamine results in a less compact apoprotein named bacterioopsin (bO). The native conformation (folded) of bR and bO can be reversibly unfolded by sodium dodecylsulfate (SDS) in mixed lipid-detergent micelles [16, 17].

Energy transfer to the retinal by an external dye has been used in the past to study bR [18] and mammalian rhodopsin [19], primarily to determine the molecular dimensions before the structure was accurately known. In addition, the folding and unfolding of bR and bO in mixed lipid-detergent micelles has been monitored by measuring changes in retinal absorbance [20],

tryptophan fluorescence [21] and secondary structure content [22], as well as via FRET between intrinsic protein tryptophan donors and an external acceptor [23, 24] and between a donor fluorophore and the retinal or an acceptor fluorophore attached to the protein [13]. Herein, the home-built optical detection system and the developed FRET analysis technique were used to investigate the effect of denaturant concentration on bO unfolding. A microfluidic device was also tested as a potential platform for extracting unfolding kinetics.

7.2. Experimental methods

7.2.1. The streptavidin-biotin binding system

7.2.1.1. Chemicals and DNA preparation

AlexaFluor488 streptavidin conjugate (*Str488*) was purchased from Invitrogen. The biotinylated dsDNA used for the experiments was provided by Dr. M. Srisa-Art [25]. Briefly, oligonucleotides were purchased from Eurofins Operon (Germany). Two strands, containing 46 base pairs each, were synthesized; one labelled with biotin on the 5' end and its complementary, internally labelled with AlexaFluor647:

Biotin-5'-GCGCTAAAATTATTTATTGATCGATTTTTTTTCGGGCGCGGCGGGC-3'
3'-CGCG**[AF647]**ATTTTAAAAATAACTAGCTAAAAAAAAGCCCGCGCCGCCCG-5'

The two sequences mainly consisted of C and G bases for stabilizing the dsDNA [26]. All samples were prepared in a pH 8.0 binding buffer, consisting of 100 mM Tris-HCl, 10 mM NaCl and 3 mM $MgCl_2$. The mixture of ssDNA (biotinylated ssDNA and AF647-labelled ssDNA) was prepared and hybridised as described in section 6.2.1.1. The distance between biotin and AF647 (acceptor dye) in the resulting dsDNA was 4 bp. The hybridised DNA will be referred to as *DNA647B*.

7.2.1.2. Experimental procedure

All measurements were performed on cover slip, as described in section 6.2.1.2. Similarly to experiments presented in chapter 6, excitation was achieved using a 488 nm laser line (figure 6.2) at point excitation mode and fluorescence lifetime data were analysed using *JLife*.

Experiments were performed using solutions of *Str488* and *DNA647B* at biotin/streptavidin concentration ratios *CR* (*CR*=[*DNA647B*]/[*Str488*]) varying between 0.3-3.3 Four sets of measurements were performed; two at constant *Str488* concentration of 22 nM and 14.7 nM

while *DNA647B* concentration varied between 6.6-72.6 nM and 4.4-48.5 nM respectively, and two at constant *DNA647B* concentration (16.7 nM and 13.3 nM) with varying *Str488* concentration (5.1-55.7 nM and 4.0-44.3 nM respectively). The concentrations were chosen according to sample brightness and to enable comparison with other work [25]. Measurements were also performed on *Str488*-only and *DNA647B*-only samples for carrying out the necessary corrections in FRET calculations.

7.2.1.3. Theoretical FRET efficiency calculations

Considering the helical molecular geometry of dsDNA, the biotin-AF647 distance (4 bp) was estimated to be 1.65 nm. Taking this into account, together with the radii of streptavidin (2.5 nm) and biotin (0.3 nm) [27], the distance R_{DA} between the donor and acceptor fluorophores, for a single-donor single-acceptor model, was approximately 4.45 nm.

The current system however, was more complicated. Specifically, each streptavidin molecule possessed four biotin binding sites. In addition, each streptavidin contained in the *Str488* sample was conjugated with, on average, 4 AF488 molecules. Thus, in a bound streptavidin-biotin complex, there was not a 1:1 analogy between donors and acceptors. Instead, this ratio could be 4:1, 4:2, 4:3 or 4:4, depending on the number of biotins bound per streptavidin (figure 7.2). Therefore, each donor could interact with multiple acceptors and each acceptor could interact with multiple donors. Energy transfer under these conditions was complex and determining E_{FRET}, theoretically and experimentally, was not straight forward [28].

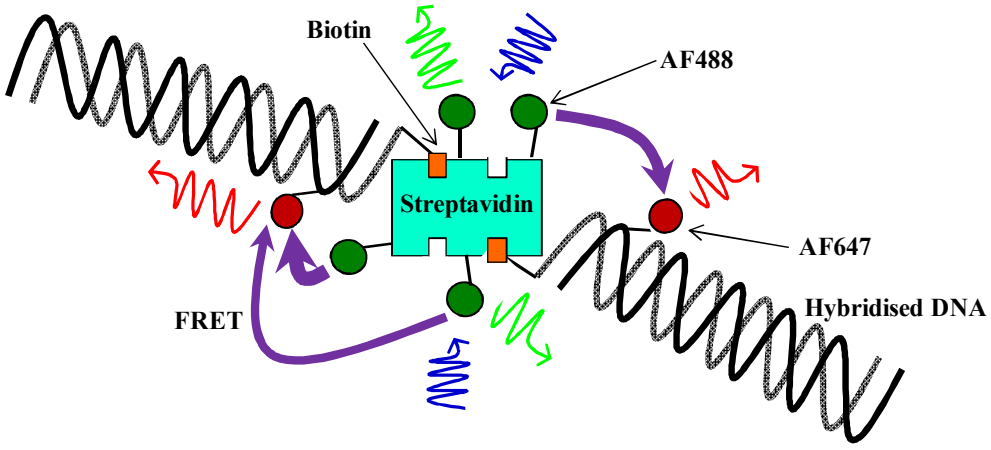

Figure 7.2. Cartoon showing one streptavidin/donor molecule with two biotin/DNA/acceptor complexes bound. In the presence of 4 donors (AF488) and 2 acceptors (AF647), E_{FRET} calculation is complex.

Assuming that the donor-acceptor fluorophore orientation was approximately the same for all pairs and R_{DA} was the average inter-dye distance, a theoretical expression for FRET efficiency, analogous to equation 6.2, could be [29]:

$$E_{FRET} = \frac{n_A R_0^6}{n_A R_0^6 + R_{DA}^6} \quad (7.1)$$

where n_A is the average number of acceptors interacting with one donor (herein: n_A=number of acceptors/number of donors). Taking into account equation 7.1, together with R_{DA} of approximately 4.45 nm and R_0 of 5.60 nm for the AF488-AF647 FRET pair, the calculated FRET efficiencies for 0-4 biotins bound to a streptavidin molecule are shown in table 7.1.

Table 7.1. Theoretical FRET efficiency calculation for 1, 2, 3 and 4 biotins bound per streptavidin.

Number of Molecules per Complex				R=4.45 nm, R_0=5.60 nm	
Streptavidins	AF488	Biotins	AF647	n_A	E_{FRET}
1	4	0	0	0.00	0.00
1	4	1	1	0.25	0.50
1	4	2	2	0.50	0.67
1	4	3	3	0.75	0.75
1	4	4	4	1.00	0.80

According to table 7.1 and calculations performed for 1 donor molecule (AF488) per streptavidin instead of 4, the presence of several acceptors in the current system increased the rate of energy transfer, while the presence of more than 1 donors decreased the overall FRET efficiency within the complex. As a result, additional biotin binding yielded higher E_{FRET} (table 7.1).

7.2.2. Bacterioopsin unfolding

7.2.2.1. Protein sample preparation

Buffer preparation

bR is a membrane protein, therefore all solutions were prepared in a buffer containing mixed lipid-detergent micelles. More specifically, 263.1 ml of 0.2 M sodium phosphate monobasic dihydrate solution ($NaH_2PO_4 \cdot 2H_2O$), 36.9 ml of 0.2 M sodium phosphate dibasic heptahydrate solution ($Na_2HPO_4 \cdot 7H_2O$) and 300 ml filtered de-ionised water were mixed to obtain 600 ml 0.1 M sodium phosphate buffer (NaP), pH 6.0. 1,2-dimyristoyl-*sn*-glycero-3-phosphocholine (DMPC) and 3-[(3-cholamidopropyl)dimethylammonio]-1-propanesulfonate (CHAPS) were purchased from Avanti Polar Lipids and Calbiochem respectively. 0.2 g DMPC, 1 ml 0.1 M NaP and 7 ml H_2O were added in a glass vial and stirred for 30 min. Subsequently, 2ml of 10% (w/v) CHAPS solution in water were added to the vial and stirred until clear (~15 min), then sonicated for 30 min. 2 ml 0.1 NaP, pH 6.0, and 8 ml H_2O were added to the DMPC/CHAPS mixture to obtain 20 ml of the working buffer.

Protein labelling and retinal removal

Labelled bR and bO were provided by Dr. P. Curnow (School of Biochemistry, University of Bristol). Detailed descriptions of protein expression, purification and labelling can be found in references [13, 20]. Briefly, wild-type bR was obtained using the methods of Krebs and co-workers [30, 31]. Two cysteine mutations, at alanine 168 (A168C) and at position 102 (D102C), were introduced to permit covalent labelling with donor AF488 (Alexafluor-488-C5-maleimide, Molecular Probes) and acceptor AF647 (Alexafluor-647-C2-maleimide, Molecular Probes). The two sites were selected based on their close proximity to the region that was expected to experience a conformational change upon unfolding (figure 7.1b). Site A168C could be labelled by both dyes, while site D102C could only be labelled with AF488. Thus, by labelling first with AF647 to fill A168C and subsequently introducing AF488 to label at D102C, mixed labelling populations were avoided. The extent of labelling for the resulting double mutant was 1.0±0.2 and 0.8±0.2 mole of label per mole of protein, for AF488 and AF647 respectively. Donor-only samples, containing AF488 in both A168C and D102C sites, were also prepared with labelling efficiency of 1.9±0.05 mole of label per mole of protein. All labelling reactions were performed on monomeric bR solubilised in the micelle buffer described above and the labelling efficiency was confirmed by absorbance spectroscopy.

In order to obtain bO, the retinal was removed by irradiating with >515 nm wavelength light for 1-5 min in the presence of excess hydroxylamine. Upon irradiation, bR went through the photocycle and the resulting conformational change increased solvent accessibility to the chromophore [32] and allowed hydroxylamine to strip the retinal from the binding pocket. The extent of retinal removal was confirmed by the loss of the chromophore band in absorbance spectra [13].

7.2.2.2. Equilibrium unfolding

Sample excitation and emission detection were as described in section 6.2.1.2 and fluorescence lifetime data were processed using *JLife*. The majority of the measurements were performed using bO (bR after retinal removal) at nM concentrations to minimise the sample consumption.

Equilibrium unfolding measurements at a variety of denaturant concentrations were performed on cover slip (as in section 6.2.1.2) as well as within a microfluidic channel. The protein was reconstituted into DMPC/CHAPS micelles at concentrations of 10-500 nM and aliquots of 20% (w/v) SDS (VWR International) were added to the protein solutions to obtain the desired denaturant concentrations. bR and bO unfolded within these mixed DMPC/CHAPS/SDS micelles, hence, denaturant concentration was expressed as dimensionless SDS mole fraction

(χ_{SDS}) rather than bulk molar concentration. This is considered to be the most appropriate metric for detergent concentration in mixed micelles [20, 33, 34]. Depending on the size of the added aliquot, SDS mole fraction varied between 0-0.96. Equilibrium measurements in flow were performed by introducing the mixed bO-SDS sample (10 nM bO, χ_{SDS}=0-0.82) into the central inlet of chip *design a* (section 4.2.2) while keeping the side inlets blocked, and data were acquired within the outlet, shortly after the junction. The flow rate was 0.5 μl/min.

7.2.2.3. Kinetic analysis

Kinetic data were acquired by introducing 200 nM bO into the central inlet of chip *design a* (figure 4.1a and Appendix A, figure A.3) while the side flows consisted of 6% (w/v) SDS (χ_{SDS} ~0.87, adequate for unfolding). The central and side inlet flow rates were 0.6 μl/min and 3.6 μl/min respectively (ratio α=6), which according to data presented in chapter 4, resulted in a mixing time of approximately 7.2 ms (not taking into account variations due to differences in diffusion coefficients D). Accordingly, bO-SDS mixing was estimated to be complete at ~195 μm from the junction (~9 ms). Therefore, fluorescence lifetime data were collected initially within the inlet (0 μm, χ_{SDS}=0) and subsequently along the outlet channel length at positions 200-6000 μm from the junction (200 μm step, χ_{SDS} ~0.87). Acquisition at different positions along the y-direction was achieved by moving the stage using the Prior Scientific software.

It should be noted that, unlike experiments described in section 4.2.3, point excitation mode was used herein instead of laser scanning. It was concluded via test experiments that the MLE routine used to extract pixel lifetimes and construct 2-dimensional fluorescence lifetime maps at scanning mode, provided adequate results only in the case of single-exponential fluorophore decays. Otherwise, the lifetimes extracted via the MLE routine corresponded to the average decay lifetime (similar to $\bar{\tau}$ calculated via equation 1.4). Therefore, although this method would be efficient to extract an average lifetime under FRET if all molecules were fretting, herein, a fraction of the donor molecules should be excluded from τ_{DA} calculation (equation 6.12 with τ_D fixed). Hence, constructing images using the MLE routine would lead to an overestimation of the donor lifetime as it would take into account both fretting and non-fretting populations. Combining FLIM with pixel lifetime extraction via exponential decay fitting instead of using the MLE routine could lead to significant error as the number of photons collected per pixel was typically low (section 2.3.3). In order to collect sufficient photon counts for accurate fluorescence lifetime determination, within reasonable acquisition times, point excitation mode and analysis via *JLife* were preferred. Nonetheless, a higher protein concentration was not used as that would significantly increase the consumption of the valuable sample.

7.3. Results and discussion

7.3.1. The streptavidin-biotin binding system

Fluorescence intensity and fluorescence lifetime analysis was performed in the same manner as described in chapter 6. Upon streptavidin-biotin binding, the donor and acceptor molecules were brought in close proximity and energy transfer occured. In order to calculate lifetime-based E_{FRET}, the fluorescence lifetime of the donor τ_D was determined via double exponential fitting of the *Str488* decay (*setup component* fixed). The extracted donor lifetime in the absence of the acceptor was τ_D=4.1±0.03 ns. Subsequently, fluorescence decays recorded in the donor channel (green) under FRET conditions were fitted using the triple exponential form described by equation 6.12 (donor lifetime τ_D and setup component α_S, τ_S fixed). The obtained donor in the presence of acceptor lifetimes τ_{DA} for *CR*=0.3-3.3 are shown in figure 7.3. A significant decrease in the donor lifetime was observed as an immediate result of the presence of the acceptor, even in small quantities, and the decrease continued, but became more subtle, as *CR* increased. This indicated that more FRET occurred at higher biotin:streptavidin concentration ratios as a result of more streptavidin binding sites being occupied.

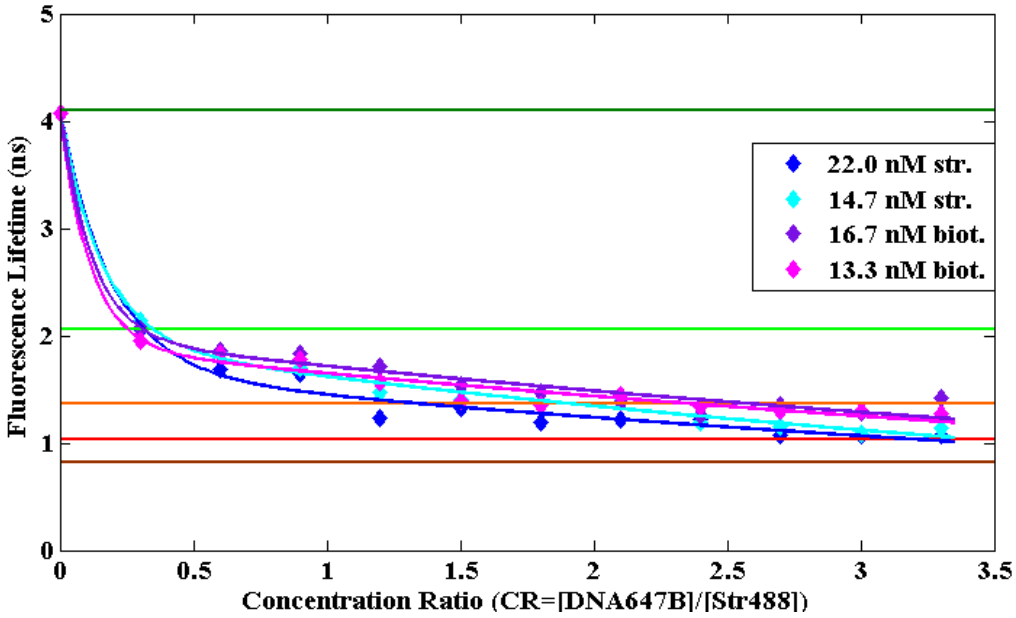

Figure 7.3. Donor fluorescence lifetime versus biotin/streptavidin concentration ratio *CR* for fixed streptavidin and fixed biotin concentrations. The horizontal lines correspond to theoretically calculated fluorescence lifetimes for donor-alone and 1, 2, 3 and 4 biotins bound per streptavidin (dark green, light green, orange, red and brown lines respectively).

Lifetime-based FRET efficiencies, obtained by substituting τ_D and τ_{DA} on equation 6.8, are shown in figure 7.4. The horizontal solid lines represent theoretical FRET levels for 1, 2, 3 and 4 biotins bound per streptavidin (green, orange, red and brown lines respectively), as estimated

in section 7.2.1.3 (table 7.1). The analysis method used herein for determining lifetime-based E_{FRET} took into account only the fretting donor molecules (non-fretting donors were excluded via τ_D in equation 6.12). Therefore, even small amounts of biotin in the mixture, yielded E_{FRET} of approximately 0.5, which was in perfect agreement with the theoretically estimated value for 1 biotin bound.

As *CR* increased, more biotins were available in the mixture for occupying the streptavidin binding sites and higher FRET efficiencies were obtained. It can be seen that for fixed streptavidin concentration the efficiency of ~0.67 estimated for 2 bound biotins (orange line in figure 7.4) was reached at *CR* below 2. This could potentially be attributed to streptavidin existing in forms of varying affinity, resulting in progressive biotin association with the highest affinity molecules [1, 8]. Hence, although initially binding sites were randomly occupied, it is possible that at higher *CR* a portion of streptavidin molecules associated with more than one biotins, without necessarily all streptavidins in the solution having at least one biotin bound.

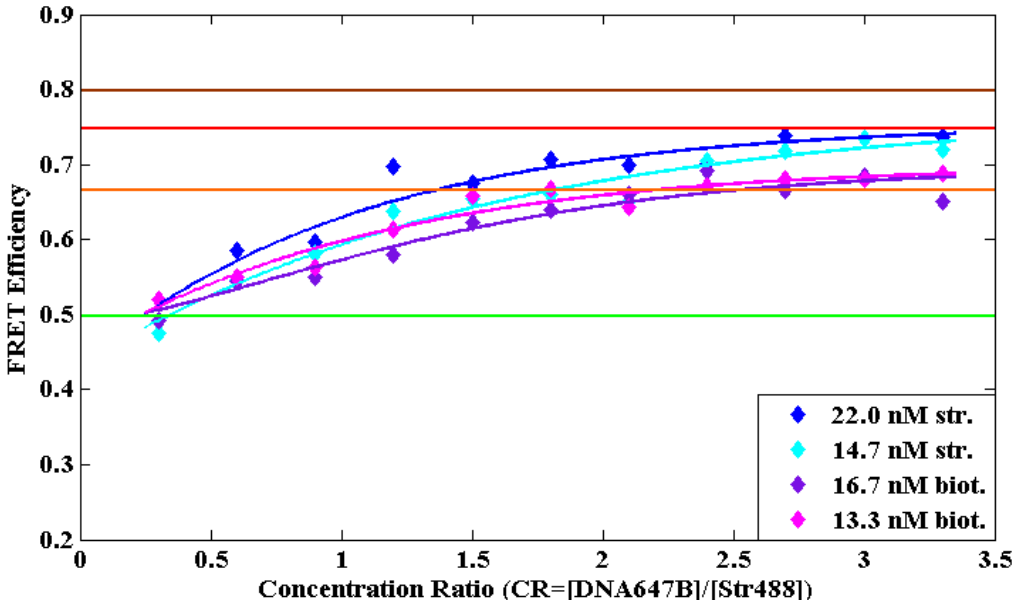

Figure 7.4. Lifetime-based FRET efficiency versus concentration ratio *CR* for fixed streptavidin and fixed biotin concentrations. The horizontal lines represent theoretical E_{FRET} for 1, 2, 3 and 4 biotins bound per streptavidin (green, orange, red and brown lines respectively).

For fixed biotin concentration, FRET efficiency plateaued at approximately 0.67 (2 biotins per streptavidin), even for CR>3, whilst, for fixed streptavidin concentration, efficiencies approximated the theoretically calculated E_{FRET} of 0.75 (3 biotins bound, red line in figure 7.4) for $CR \approx 2.7$. Increasing *CR* beyond 2.7 did not seem to further increase E_{FRET}.

It has been previously reported that in a streptavidin-biotin binding system, not all streptavidin binding sites are filled, even under ligand saturation conditions [8, 25, 35]. Although biotin appears to induce conformational changes in the streptavidin tetramer, it is believed that these structural changes do not substantially affect the binding affinity of the free pockets [3, 36, 37]. Instead, the loss in affinity, causing the fourth, and occasionally the third, sites to remain unfilled, has been attributed to steric hindrance, which inhibits the ability of biotin to settle in the most stable position inside the binding pocket [2, 8]. Adjacent binding sites are separated by a distance of approximately 2 nm, thus, the relatively large DNA molecule (~16 nm) attached to the biotin could potentially obstruct further binding on the same side of the streptavidin tetramer. In addition, bulky substituents have been shown to reduce the strength and stability of the biotin-streptavidin bond [37]. This possibly leads to high dissociation rates [8], which could be related to the unoccupied binding sites. It should be noted that in previous studies [8], streptavidins were tethered on a large bead and only two of the four sites were typically filled due to limited accessibility of the pockets near the bead surface as well as obstruction of incoming biotins as surface coverage increased. This was not the case herein hence binding of more than two biotins per streptavidin was also observed.

The calculation of the above FRET efficiencies (figure 7.4) took into account all fretting donors, with no regard to the number of biotins bound per streptavidin. Therefore, E_{FRET} expressed the average energy transfer for each concentration ratio *CR*. As a result, it is possible that, at high *CR*, a portion of the biotin-streptavidin complexes contained more than 3 biotins. However, combination with the 1-streptavidin 1-biotin and 1-streptavidin 2-biotins complexes, yielded FRET efficiencies which corresponded to an average of 3 biotins per streptavidin. In order to resolve the above complexes with certainty and determine the percentage of each complex within the solution, single molecule measurements would be required.

In an attempt to gain insight into the individual FRET 'populations' within the mixture in bulk, additional decay fitting was performed, using a four-components exponential equation, whereby, in addition to the setup component and the donor-only component, the lifetime of a third component was fixed to the estimated lifetime for a 1-streptavidin 1-biotin complex (~2.06 ns). The resulting component amplitudes, normalised to the donor-only amplitude α_D for *CR*=0.3, were plotted against *CR* in figure 7.5. It should be noted that the normalised values shown on the y-axis were a measure of the fraction of each component in the mixture and did not directly correspond to the contribution of each component to the fluorescence decay, which should also take into account the component lifetimes.

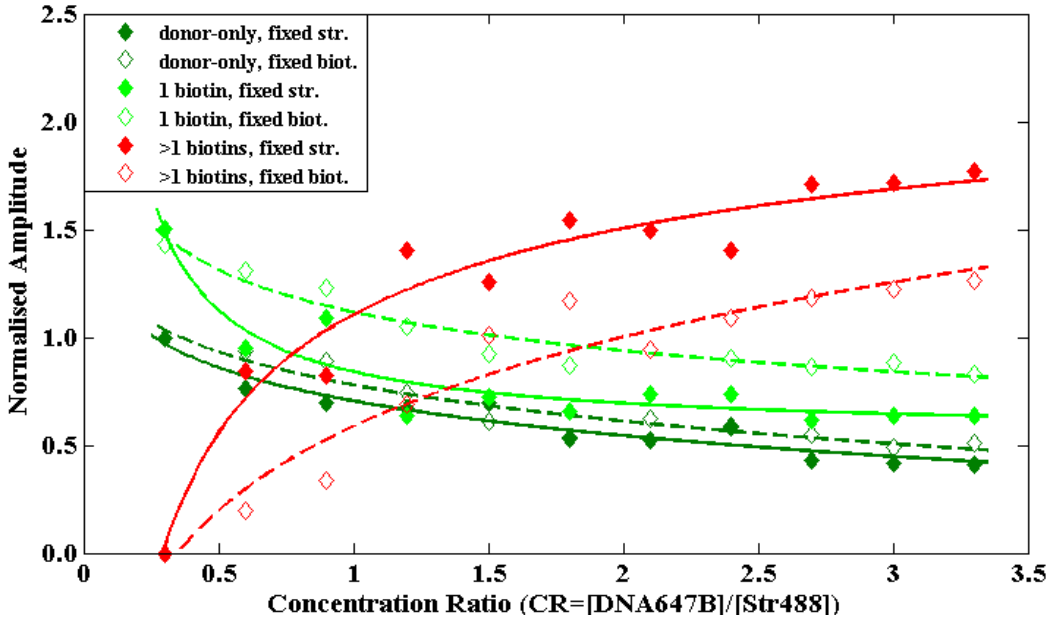

Figure 7.5. Normalised amplitudes for donor-only component, 1 biotin bound component and >1 biotins bound component versus concentration ratio CR. Fixed streptavidin concentration (22.0 nM, solid lines) and fixed biotin concentration (13.3 nM, dashed lines).

It can be seen that the donor-only component (dark green) was gradually reduced with *CR*, without however reaching zero, as, in addition to streptavidin with no biotins bound, it also represented free dye residue within the solution (chapter 6). For increasing *CR*, more biotins were present in the sample; therefore the portion of the 1-streptavidin 1-biotin complex (α_{1B}, light green) also decrease, as it was being replaced by the rising α_{DA} component (red). The latter represented all biotin-streptavidin complexes which contained more than 1 biotins (2, 3 or 4 biotins bound). It was observed that the α_{1B} decrease and the respective α_{DA} increase were more subtle for fixed biotin concentration than for fixed streptavidin concentration. As all samples were prepared individually and measured under equilibrium conditions, this should not be attributed to the lack of available binding sites or ligands, but rather on the low absolute concentrations used in experiments whereby *DNA647B* concentration was fixed.

Intensity-based FRET efficiencies for various *CR* under fixed streptavidin or fixed biotin concentrations were also extracted using equations 6.6 and 6.9-6.11 (figure 7.6). Comparison with the efficiencies presented in figure 7.4, clearly indicated the superiority of the lifetime-based technique for E_{FRET} extraction (figure 7.6). More specifically, although intensity- and lifetime-based E_{FRET} values were in good agreement for $CR>1.2$ at fixed streptavidin concentration of 22 nM, for $CR<1.2$ and for fixed biotin concentration (low absolute streptavidin concentration), FRET efficiencies obtained via intensity calculations were lower than expected. Under such concentration conditions, the contribution of the non-fretting donor fluorophores to the recorded decay was significant, therefore an additional correction factor should be added to the expression for I_{DA} (equation 6.9) to account for the donors not

experiencing FRET. Similar results were obtained for fixed [*Str488*]=14.7 nM and fixed [*DNA647B*]=16.7 nM (data not shown).

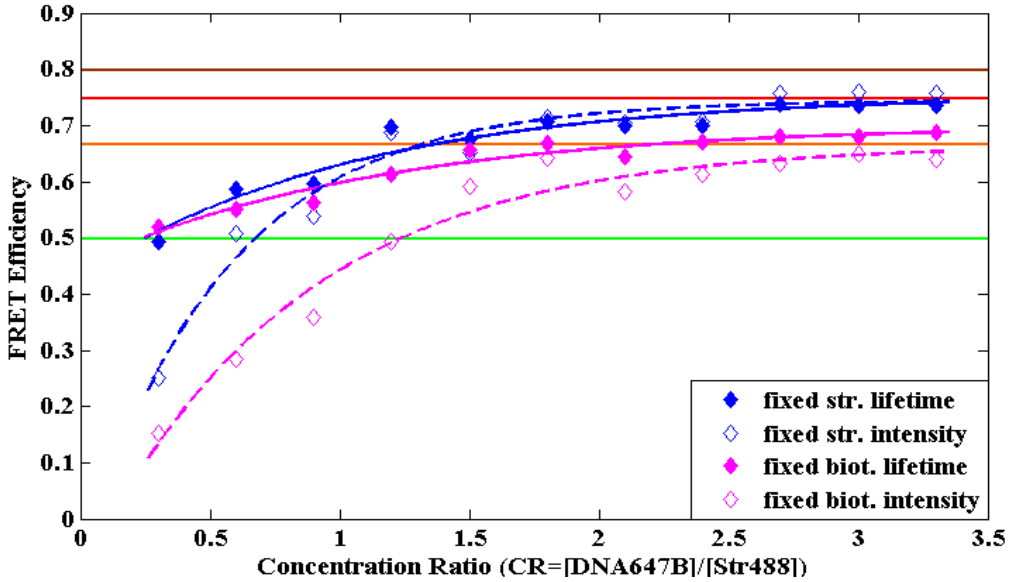

Figure 7.6. Intensity- and lifetime-based FRET efficiency versus concentration ratio CR for fixed streptavidin concentration (22.0 nM) and fixed biotin concentration (13.3 nM). The superiority of the lifetime-based technique is evident.

Finally, in order to investigate streptavidin-biotin binding kinetics, protein and ligand solutions were introduced in a microfluidic device (*device a*, section 4.2.2) and hydrodynamic focusing was employed to enhance mixing. Unfortunately, high streptavidin aggregation and absorption on the PDMS surface was observed (figure 7.7), which rendered these measurements unsuccessful. *n*-dodecyl-b-D-maltoside (DDM) has been reported to reduce non-specific protein absorption [38]. During control measurements performed on the present system however, DDM exhibited significant fluorescence count rate when excited with a 488 nm laser line, introducing background noise which could not be resolved from the donor signal. Therefore, these experiments were not further continued.

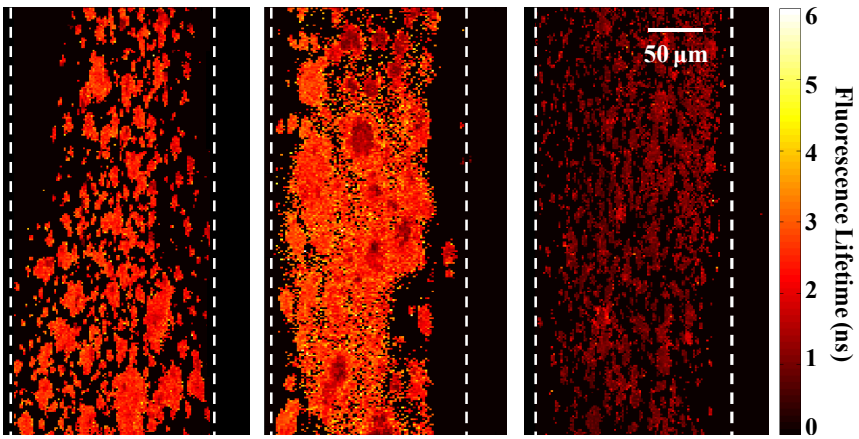

Figure 7.7. Biotin-streptavidin binding imaged at different positions along the outlet of a microfluidic device (the white dashed lines represent the channel walls). High streptavidin aggregation and absorption on the PDMS surface were observed. From left to right: low FRET (1 biotin bound), mixed low/high FRET and high FRET (3-4 biotins bound).

7.3.2. Bacterioopsin unfolding

7.3.2.1. Equilibrium unfolding

The folded and unfolded states of bR and bO

Initial experiments were performed using 10 nM bR and bO labelled with AF488/AF647. In the native form of the protein (folded state) the labelled sites were in close proximity and the extracted FRET efficiency was high (figure 7.8). In the presence of the retinal (bR), energy from the donor (AF488) was also transferred to the chromophore. Thus, more energy transfer occurred and, when using donor emission data to extract FRET efficiency (lifetime measurements), E_{FRET} was higher for bR than for bO. Intensity-based E_{FRET} calculation via equation 6.6 did not provide accurate results in the presence of the retinal as it took into account fluorescence signal from both donor (green) and acceptor (red) channels; the chromophore however did not emit in the red region, thus FRET towards the retinal was only depicted in the donor channel. In 10% (w/v) SDS (χ_{SDS} ~0.96), the protein unfolded and the distance between donor and acceptor molecules increased resulting in less energy transfer (figure 7.8). In addition, upon unfolding, the protein-retinal interactions were completely disrupted, as it was illustrated by almost identical results obtained for the unfolded states of bR and bO (figure 7.8, lifetime data). For both folded and unfolded states of bR and bO, fluorescence intensity-based calculations yielded significantly lower E_{FRET} than lifetime-based calculations (see below).

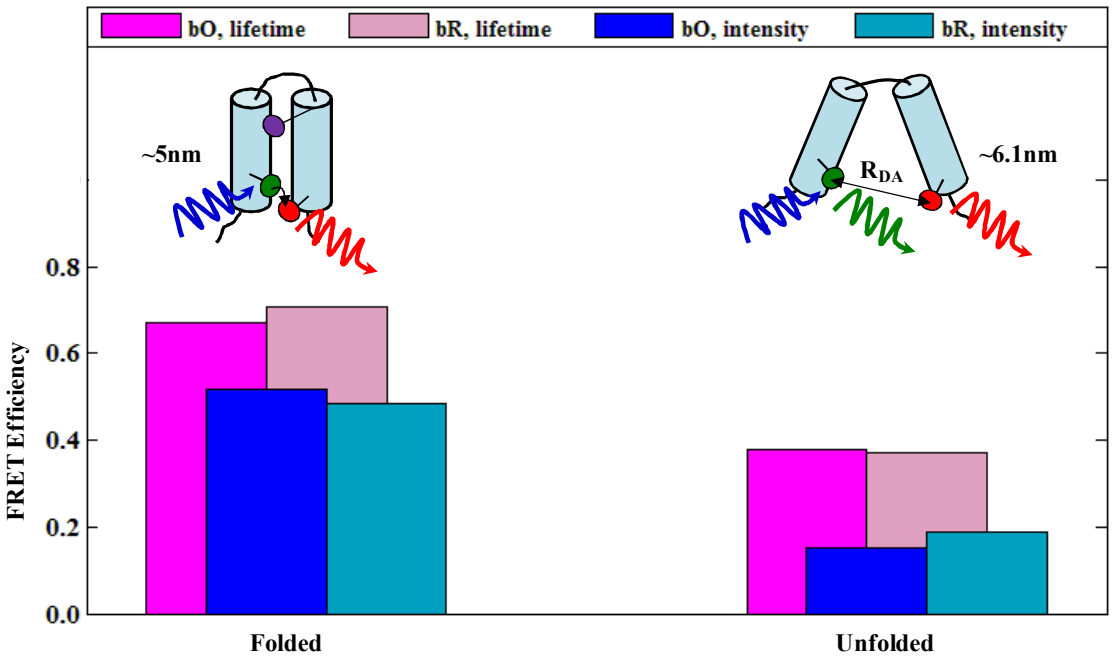

Figure 7.8. FRET cartoon and equilibrium intensity- and lifetime-based E_{FRET} for folded and unfolded bR (with retinal) and bO (after retinal removal).

Donor-acceptor distances for the folded and unfolded conformations of bO were extracted by substituting lifetime-based FRET efficiencies in equation 6.2. It was not possible to calculate

inter-dye distance for bR in the folded state, due to E_{FRET} representing energy transfer towards two acceptors, at different distances from the donor (AF647 and chromophore). Calculations for bO resulted in donor-acceptor distances of ~5 nm and 6.1 nm for the folded and unfolded states respectively (1.1 nm increase upon unfolding), which were in reasonable agreement with previously reported values. Specifically, Curnow and Booth [13] reported a 1.2 nm increase in the inter-dye distance upon unfolding (from 5 nm to 6.2 nm), using sensitised acceptor emission data. These however were not considered as absolutely accurate, due to the very small change in the acceptor signal observed during unfolding. Instead, they calculated FRET efficiencies via equation 6.4 (based on donor intensity) and extracted donor-acceptor distances of 4.6 nm and 5.4 nm for folded and unfolded bO states respectively. Structural inspection of bR suggests that the A168-D102 distance is approximately 1.1 nm, less is known however about the bO structure. The 0.8 nm distance change observed upon unfolding was consistent with both donor and acceptor dyes having extended linker arms as well as with potential protein structural changes upon retinal removal [13].

The distances calculated herein, and the change in distance upon unfolding, were in excellent agreement with sensitised acceptor emission results provided by Curnow and Booth, but were slightly higher than the respective values they obtained via donor intensity calculations. Nonetheless, equation 6.4 could not be used for E_{FRET} extraction in the present experiments, as determining the intensity of the donor in the absence of the acceptor (I_D) was problematic. Fluorescence intensity strongly depends on fluorophore concentration. The AF488/AF488 labelled sample (donor-only) possessed on average 1.9 moles of AF488 label per mole of protein. However, using this ratio to correct I_D and extract E_{FRET} via equation 6.4 did not yield plausible results (negative E_{FRET}). In order to accurately determine I_D, protein labelled with AF488 on A168C site only should be used (1:1 mole of AF488 per mole of protein). This however was not possible to obtain as AF488 would fill both A168C and D102C sites.

In addition, as it was previously discussed, extracting intensity-based FRET efficiencies via equation 6.6 is highly dependent on free donor dye residue and labelling efficiency. Moreover, it would require correction for direct acceptor excitation, which could only be estimated from measurements on free AF647 as an acceptor-only labelled protein sample was not provided. Thus, the resulting E_{FRET} shown in figure 7.8 (blue/light blue bars) yielded significantly higher inter-dye distances than the expected distances mentioned above. It becomes apparent that compared to fluorescence intensity calculations, the fluorescence lifetime approach provided the most satisfactory results, in reasonable agreement with previous studies [13].

Equilibrium bO unfolding on cover slip and in flow

Considering the complications related to the study of bR unfolding using FRET (multiple acceptor species, loss of chromophore in the unfolded state), experiments at varying SDS concentration were only performed using bO.

Control measurements revealed that the mixed DMPC/CHAPS/SDS micelles (without protein) yielded significant photon counts, interfering with the detected signal in the green and red regions. Normalised photon counts versus SDS mole fraction were approximated with a linear fit (figure 7.9, dashed lines) and the extracted slope was 0.206 (identical for green and red detection channels). The effect of the increasing DMPC/CHAPS/SDS-induced noise with SDS concentration, together with potential variations in donor emission due to structural changes upon unfolding, were quantified by exciting the AF488/AF488 bO sample and expressing the normalised intensity as a function of χ_{SDS} (figure 7.9, solid lines). Data were fitted to a cubic polynomial equation, which was used in intensity-based E_{FRET} calculations to correct the green and red signals for SDS contribution and intrinsic fluorescence emission variations due to unfolding. The extracted cubic polynomial fit for AF488/AF488 bO emission in the green channel was:

$$\frac{I(\chi_{SDS})}{I(0)} = 1 - 0.219\chi_{SDS} - 0.347\chi_{SDS}^2 + 1.238\chi_{SDS}^3 \qquad (7.2)$$

The contribution of SDS-originating emission to the detected donor signal also affected fluorescence lifetime-based FRET efficiencies, which were calculated using data recorded in the green channel. The SDS component exhibited a lifetime of approximately 1.3 ns. As shown in the inset of figure 7.9, the normalised fluorescence lifetime of AF488/AF488 bO with respect to χ_{SDS} was fitted to a cubic polynomial equation of the form:

$$\frac{\tau(\chi_{SDS})}{\tau(0)} = 1 - 0.112\chi_{SDS} - 0.111\chi_{SDS}^2 + 0.358\chi_{SDS}^3 \qquad 7.3$$

Equilibrium AF488/AF647 bO unfolding measurements were performed on cover slip as well as within a microfluidic channel. Donor fluorescence intensity and fluorescence lifetime increased with SDS concentration while acceptor fluorescence emission decreased, indicating reduction in FRET. The extracted intensity-based and lifetime-based FRET efficiencies plotted against SDS mole fraction are shown in figure 7.10. Error bars represent deviation from six individual measurements on cover slip and two individual measurements in flow. During bO preparation for these experiments, special care taken to minimise free dye residue, therefore

intensity (blue) and lifetime (magenta) calculated E_{FRET} were in good agreement. Measurements within the microchannel yielded slightly higher FRET efficiencies (open makers, dashed lines), the difference from measurements on cover slip however was not considered significant. Extracted E_{FRET} for folded (χ_{SDS}=0) and unfolded (approximately χ_{SDS}>0.75) states were consistent with previously obtained results (figure 7.8).

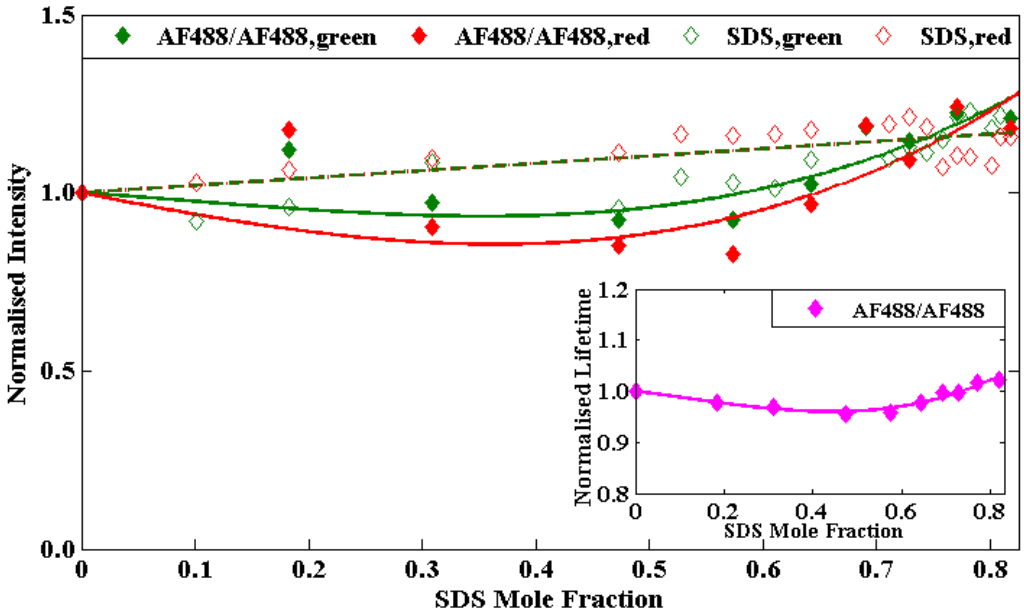

Figure 7.9. SDS (open markers) and AF488/AF488 bO (filled markers) normalised intensity versus SDS mole fraction. SDS data were fitted to a linear equation (dashed line) while cubic polynomial curves (solid lines) were used for bO fitting. Inset: AF488/AF488 bO normalised lifetime versus SDS mole fraction and cubic polynomial fit.

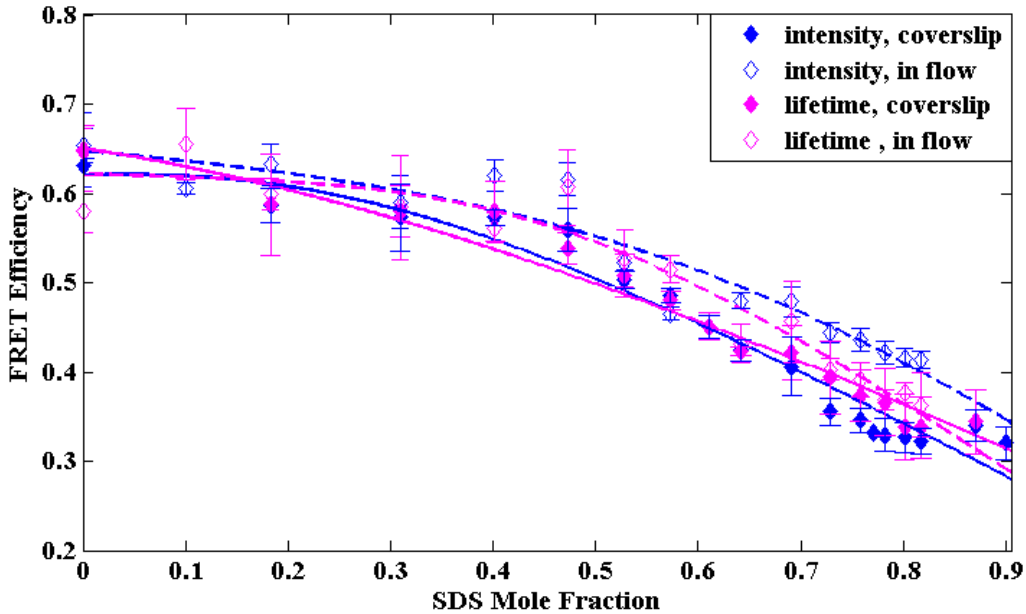

Figure 7.10. Equilibrium intensity- and lifetime-based FRET efficiency versus SDS mole fraction extracted from measurements on cover slip and in flow. Error bars represent deviation from six individual measurements on cover slip and two individual measurements in flow.

The transition between folded and unfolded states for bR, and to a satisfying degree for bO, is considered highly cooperative (all-or-nothing), hence unfolding can be modelled using simple two-state assumptions [13, 33]. In a two-state approximation, FRET efficiencies between the acquired E_{FRET} for folded and unfolded states correspond to an average E_{FRET} resulting from a mixture of folded and unfolded proteins (no partially unfolded states exist). Therefore, the observed decrease in E_{FRET} with χ_{SDS} (figure 7.10) indicated that the more SDS was added to the protein solution, the greater the fraction of the proteins that unfolded.

The fraction F_f of the proteins that remained folded at a given SDS concentration were estimated via changes in the normalised donor intensity and lifetime. For example, taking into account the overall change in donor fluorescence lifetime upon unfolding and assuming that in the folded state 100% of the proteins were folded while in the unfolded state 100% were unfolded, a 20% increase in τ_{DA} corresponded to approximately 78% of proteins in the sample remaining folded. In terms of efficiencies, calculations yielded that F_f could be expressed as:

$$F_f(\chi_{SDS}) = 1 - \frac{E_{FRET,f} - E_{FRET}(\chi_{SDS})}{E_{FRET,f} - E_{FRET,u}} \qquad 7.4$$

where subscripts f and u denoted the folded and unfolded states respectively. Using equation 7.4, the FRET efficiencies shown in figure 7.10 were translated into fraction of proteins in the sample that remained folded at each χ_{SDS} (figure 7.11). Fitting these data to a two-state model was used to provide useful information in terms of unfolding free energy and characteristics of the transition between folded and unfolded states.

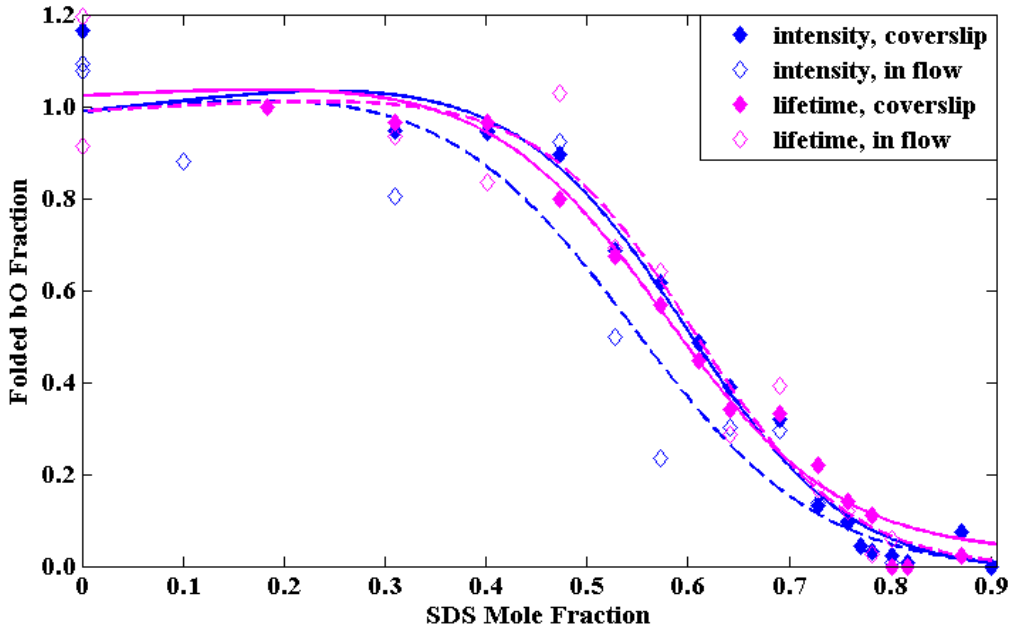

Figure 7.11. Fraction of bO proteins that remained folded versus SDS mole fraction together with two-state model fits. Equilibrium fluorescence intensity and lifetime measurements on cover slip and in flow.

A simple illustration of the two-state model used to fit the data is shown in figure 7.12. F_0 in figure 7.12 corresponded to the fraction of folded proteins when SDS was in excess and was considered to be zero, while F_c was a correction performed on the experimentally determined F_f. Combining equations 7.2 and 7.4 (intensity) or equations 7.3 and 7.4 (lifetime), F_c was given by equations 7.5 or 7.6 for fluorescence intensity or lifetime measurements respectively:

$$F_c(\chi_{SDS}) = 1 + 0.240\,\chi_{SDS} + 0.381\,\chi_{SDS}^2 - 1.362\,\chi_{SDS}^3 \quad 7.5$$

$$F_c(\chi_{SDS}) = 1 + 0.123\,\chi_{SDS} + 0.122\,\chi_{SDS}^2 - 0.394\,\chi_{SDS}^3 \quad 7.6$$

As it is shown in figure 7.12, the fraction of unfolded proteins F_u at a random χ_{SDS} was represented by $F_u=(F_c-F_f)/(F_c-F_0)$, which for $F_0=0$ yielded $F_f=F_c-F_c\times F_u$.

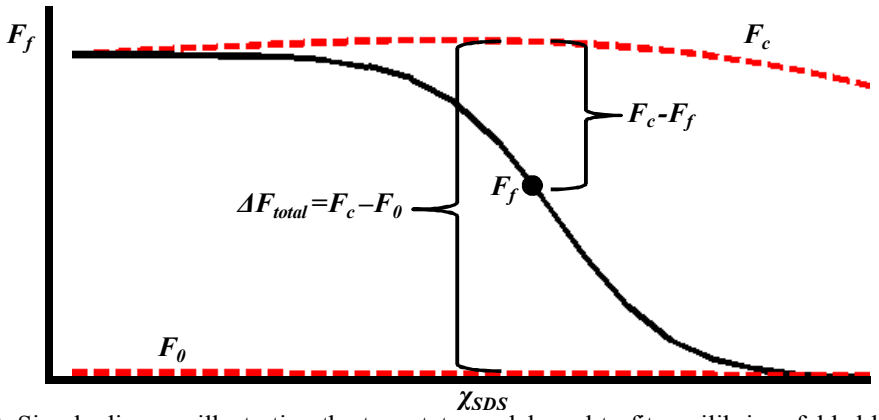

Figure 7.12. Simple diagram illustrating the two-state model used to fit equilibrium folded bO fraction versus SDS mole fraction data.

The ratio of the unfolded to folded protein was given by $F_u/(1-F_u)$ and the free energy of the unfolding reaction was $\Delta G_u = -R_gT\ln(F_u/(1-F_u))$ [39], with R_g and T being the gas constant and the temperature in Kelvin respectively. Thus $F_u=1/(1+\exp(\Delta G_u/R_gT))$. Assuming that ΔG_u was a linear function of χ_{SDS} [13, 20, 33], $\Delta G_u = p_1\times\chi_{SDS}+p_2$ and $F_u=1/(1+\exp((p_1\times\chi_{SDS}+p_2)/R_gT))$. In the expression for ΔG_u, parameter p_1 was the slope of the major transition in the equilibrium unfolding curves and was related to the cooperativity of the transition and parameter p_2 was the total free energy change upon unfolding at $\chi_{SDS}=0$ ($p_2=\Delta G_u^{H2O}$). Substituting F_u in the above expression for F_f ($F_f=F_c-F_c\times F_u$) yielded:

$$F_f(\chi_{SDS}) = F_c(\chi_{SDS}) - F_c(\chi_{SDS}) \times \frac{1}{1+\exp\left(\frac{p_1\times\chi_{SDS}+p_2}{R_gT}\right)} \quad 7.7$$

where $F_c(\chi_{SDS})$ was given by equation 7.5 or equation 7.6 (fluorescence intensity or lifetime calculations respectively). As χ_{SDS} was dimensionless, p_1 and p_2 were expressed in kcal/mol. The equilibrium unfolding curves in figure 7.11 were obtained by fitting folded fraction data (calculated via equation 7.4) to equation 7.7.

By allowing 5% freedom to the polynomial coefficients in the expression for $F_c(\chi_{SDS})$ and leaving parameters p_1 and p_2 free, the two-state model resulted in relatively good fits (χ_R^2 =0.93-0.98), with the main source of discrepancy being F_f variations at low χ_{SDS}. Similar p_1 and p_2 values were acquired via intensity and lifetime measurements on cover slip and in flow (table 7.2, free parameters columns). An average major transition slope (p_1) of 6.88±0.65 kcal/mol and an average total free energy upon unfolding at zero SDS concentration (p_2) of 4.06±0.56 kcal/mol were obtained, which were slightly lower than the respective values reported by Curnow and Booth (10.9±1 kcal/mol and 6.3±0.4 kcal/mol respectively) [13].

The major transition slope is generally a measure of the unfolding cooperativity and a smaller slope (small p_1) is associated with less cooperative unfolding (less all-or-nothing unfolding). As a part of the expression for ΔG_u ($\Delta G_u = p_1 \times \chi_{SDS} + p_2$), the free energy change upon unfolding at χ_{SDS}=0 ($\Delta G_u^{H2O} = p_2$) can be related to the activation energy required to initiate unfolding. Thus, low ΔG_u^{H2O} (small p_2) generally indicates that less activation energy is required for unfolding as a result of reduced stability of the protein structure and unfolding occurs at lower SDS concentrations.

Table 7.2. Major transition slope (p_1), free energy change upon unfolding at χ_{SDS}=0 (p_2), transition midpoint and χ_R^2 extracted via two-state model fits under equilibrium conditions.

Method		Free Parameters				Restricted Parameters			
		p_1 (kcal/mol)	p_2 (kcal/mol)	midpoint (χ_{SDS})	χ_R^2	χ_R^2	p_1 (kcal/mol)	p_2 (kcal/mol)	midpoint (χ_{SDS})
Intensity	Coverslip	7.04	4.33	0.60	0.98	0.97	9.90	6.06	0.61
	In Flow	6.08	3.36	0.55	0.92	0.91	10.95	5.90	0.54
Lifetime	Coverslip	6.75	3.90	0.59	0.97	0.95	10.05	5.90	0.60
	In Flow	7.65	4.65	0.61	0.93	0.94	9.90	6.21	0.62
Average		6.88	4.06	0.59			10.20	6.02	0.59
Standard Deviation		0.65	0.56	0.03			0.50	0.15	0.03

The extracted transition midpoint at which 50% of the proteins unfolded was χ_{SDS}=0.59±0.03, which was in excellent agreement with the χ_{SDS}=0.58±0.01 midpoint obtained by Curnow and Booth [13].

For the above fits, no limits were set for parameters p_1 and p_2. However, by adjusting the initial parameter guess and restricting p_1 and p_2 values within the previously reported estimated limits [13], the extracted average major transition slope and ΔG_u^{H2O} (10.20±0.50 kcal/mol and 6.02±0.15 kcal/mol respectively) were consistent with previous studies, while, as illustrated in table 7.2 (restricted parameters columns), the quality of the fits was not significantly affected (χ_R^2=0.91-0.97). In fact, in the case of fluorescence lifetime measurements in flow, adjusting the parameter limits resulted in an improved fit. It becomes evident that prior knowledge of the system can significantly assist a proper analysis. Nonetheless, integrating data from additional repeats could provide more conclusive results.

7.3.2.2. bO unfolding kinetics

Kinetic bO unfolding measurements were performed using hydrodynamic focusing within a microfluidic device with a ratio of 6 between side (denaturant) and centre (folded bO) inlet flow rates. As proteins were brought in contact with SDS they begin to unfold and the distance between the donor and acceptor fluorophores increased. Thus, less energy transfer occurred and the fluorescence lifetime along the outlet channel increased with distance (figure 7.13). The distance from the junction was converted into time according to the channel geometry and the total (outlet) flow rate and fluorescence lifetime-based FRET efficiency decreased with time (figure 7.14).

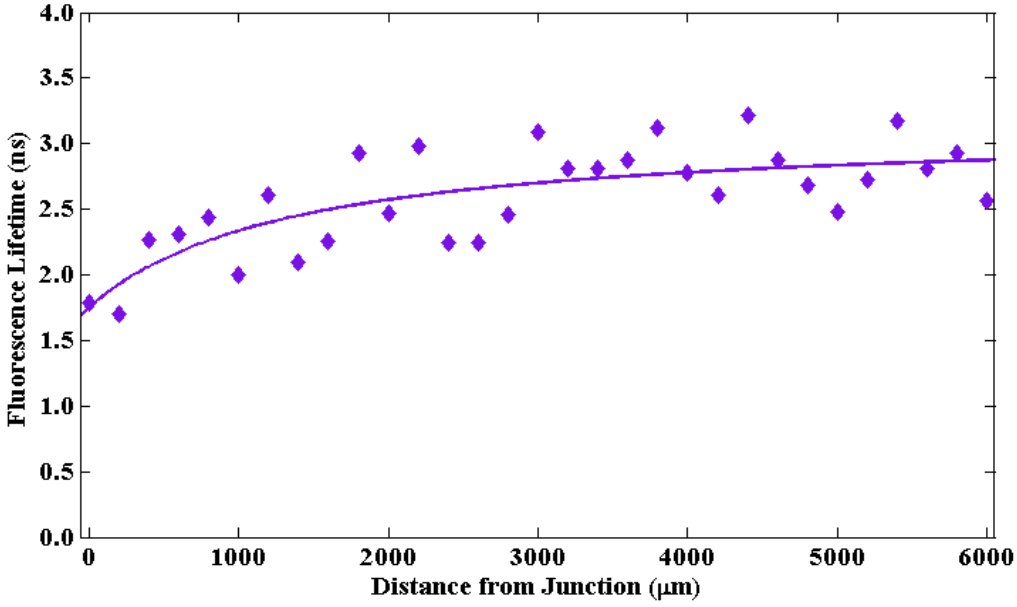

Figure 7.13. Fluorescence lifetime at the centre of the focused stream along the outlet channel of a microfluidic device (design a). The central and side flows consisted of 200 nM bO (0.6 μl/min) and ~0.87 SDS mole fraction (3.6 μl/min) respectively.

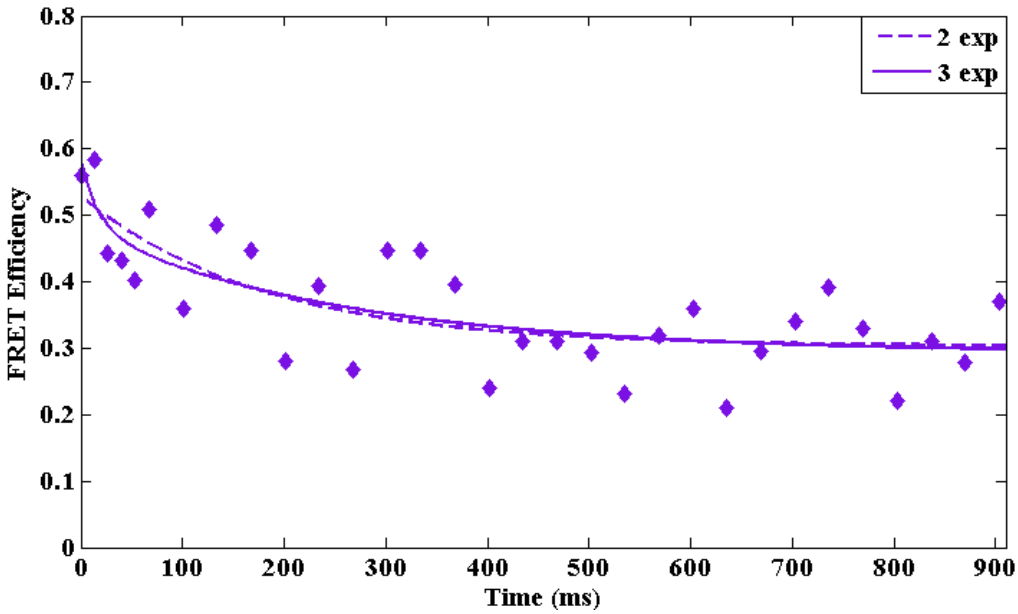

Figure 7.14. Lifetime-based FRET efficiency versus time together with double- and triple-exponential fits. Measurements were taken at the centre of the focused stream along the outlet channel with the central and side flows consisting of 200 nM bO (0.6 μl/min) and ~0.87 SDS mole fraction (3.6 μl/min) respectively. Mixing was estimated to be complete after ~9 ms.

As the bO-SDS mixing was estimated to be complete within ~9 ms, the SDS concentration along the outlet (from 200 μm from the junction onwards) was constant and equalled the SDS mole fraction within the side inlet (χ_{SDS}=0.87). According to equilibrium measurements (see previous section), at χ_{SDS}=0.87 approximately 100% of the proteins unfolded, therefore E_{FRET} along the outlet channel expressed the unfolding kinetics.

The observed rate constant k_{obs} for a molecular interaction or procedure can be extracted by appropriate fitting of FRET efficiency curves versus time [25]. Due to the small width of the focussed stream and noise within the microchannel, the obtained efficiencies were highly dispersed, rendering the fitting process problematic. Both double- and triple-exponential fits yield χ_R^2<0.75, the triple-exponential however seemed to provide better fitting for early events (figure 7.14).

When fitting the data to a sum of three exponential phases (triple-exponential fit), the first phase exhibited an observed rate constant of 55.2 s^{-1}, which contributed ~88% to the total E_{FRET} change and corresponded to the major unfolding transition. This was in satisfactory agreement with FRET data reported by Curnow and Booth (73.08±2.0 s^{-1}) and in excellent agreement with the observed rate constant obtained via intrinsic tryptophan fluorescence by the same authors (53.06±2.5 s^{-1}) [13]. The observed rate constant acquired herein (55.2 s^{-1}) for the major bO unfolding transition was remarkably higher than the respective constant for bR

(0.4±0.01 s^{-1}) [13], indicating that retinal removal significantly reduced protein stability and resulted in faster unfolding. The rate of the second phase (3.86 s^{-1}) most probably arose from residual bR within the bO sample as it seemed to result from the combination of the major transition rate for bR (0.52±0.02 s^{-1}) [13] and the rate of a phase associated with a shift in the chromophore band due to subtle conformational changes upon unfolding (7.54±0.30 s^{-1}) [13]. Finally, an extremely slow rate constant was obtained for the third phase with minor contribution to the E_{FRET} change, which probably corresponded to a solvent effect.

Inter-dye distances during unfolding, extracted via substituting E_{FRET} data from figure 7.14 on equation 6.2, are shown in figure 7.15.

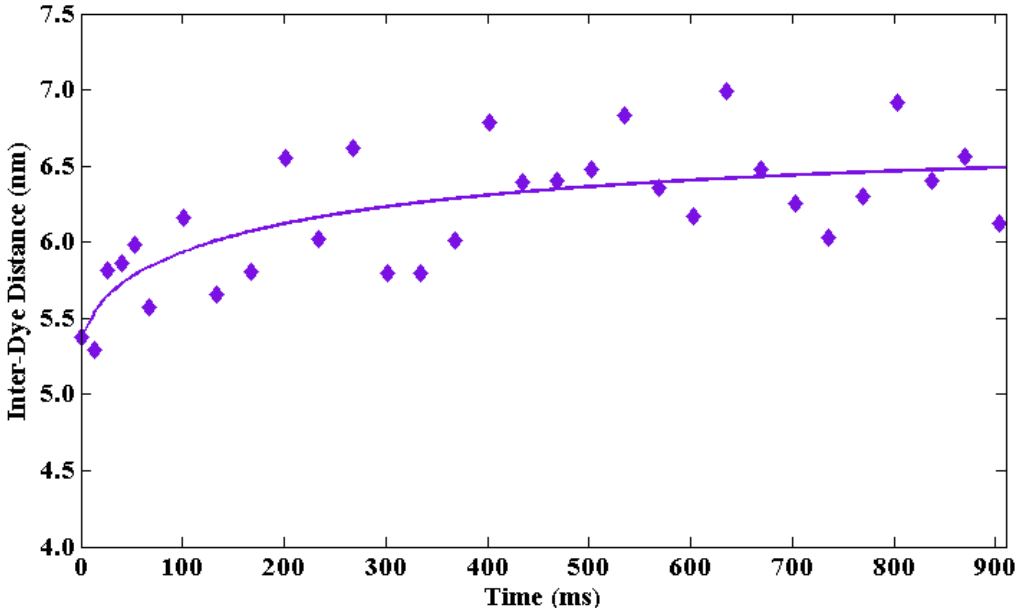

Figure 7.15. Inter-dye distances calculated from lifetime-based FRET efficiency measurements along the microfluidic device outlet, versus time.

7.4. Summary and conclusion

In this chapter, the previously developed FRET technique, based on fluorescence lifetime instead of fluorescence intensity measurements and on multi-exponential decay fitting, was successfully used as a tool for studying molecular interactions and protein conformational changes upon unfolding. More specifically, the effect of the concentration ratio on biotin-streptavidin binding was investigated and it was concluded that, in ligand excess, three biotins on average bound per streptavidin tetramer. Possible factors preventing the binding of a fourth biotin were discussed. In addition, equilibrium bacterioopsin unfolding under various

denaturant concentrations was characterised in terms of major transition slope, free energy change upon unfolding at zero SDS concentration and transition midpoint. Unfolding kinetic analysis was also performed within a microfluidic channel using hydrodynamic focusing to achieve fast mixing. Both equilibrium and kinetic measurements were in very good agreement with results reported by other researchers, the use of a confocal arrangement and microfluidics however significantly reduced the required sample concentration (from μM to nM) as well as the absolute sample consumption (only a few microlitres needed per condition), increasing at the same time the measurement sensitivity. Especially in terms of kinetic experiments, performing measurements within a microchannel minimises the dead time for observation and allows for real-time monitoring of the unfolding process. It becomes apparent that FRET measurements can give insight into complex biomolecular processes in the nanoscale and combined with a microfluidic platform can be an extremely attractive tool for a variety of bioanalytical applications.

7.5. References

1. Green, N.M., *Avidin. 1. The use of (14-c)biotin for kinetic studies and for assay.* The Biochemical journal, 1963. **89**: p. 585-91.
2. Hendrickson, W.A., A. Pahler, J.L. Smith, Y. Satow, E.A. Merritt and R.P. Phizackerley, *Crystal-structure of core streptavidin determined from multiwavelength anomalous diffraction of synchrotron radiation.* Proceedings of the National Academy of Sciences of the United States of America, 1989. **86**(7): p. 2190-2194.
3. Gonzalez, M., L.A. Bagatolli, I. Echabe, J.L.R. Arrondo, C.E. Argarana, C.R. Cantor and G.D. Fidelio, *Interaction of biotin with streptavidin - Thermostability and conformational changes upon binding.* Journal of Biological Chemistry, 1997. **272**(17): p. 11288-11294.
4. Livnah, O., E.A. Bayer, M. Wilchek and J.L. Sussman, *3-dimensional structures of avidin and the avidin-biotin complex.* Proceedings of the National Academy of Sciences of the United States of America, 1993. **90**(11): p. 5076-5080.
5. Wilchek, M., E.A. Bayer and O. Livnah, *Essentials of biorecognition: The (strept)avidin-biotin system as a model for protein-protein and protein-ligand interaction.* Immunology Letters, 2006. **103**(1): p. 27-32.
6. Green, N.M., *Avidin.* Advances in protein chemistry, 1975. **29**: p. 85-133.
7. Bayer, E.A. and M. Wilchek, *Biotin-binding proteins - overview and prospects.* Methods in Enzymology, 1990. **184**: p. 49-51.
8. Buranda, T., G.M. Jones, J.P. Nolan, J. Keij, G.P. Lopez and L.A. Sklar, *Ligand receptor dynamics at streptavidin-coated particle surfaces: A flow cytometric and spectrofluorimetric study.* Journal of Physical Chemistry B, 1999. **103**(17): p. 3399-3410.
9. Laitinen, O.H., H.R. Nordlund, V.P. Hytoenen and M.S. Kulomaa, *Brave new (strept)avidins in biotechnology.* Trends in Biotechnology, 2007. **25**(6): p. 269-277.
10. Grunwell, J.R., J.L. Glass, T.D. Lacoste, A.A. Deniz, D.S. Chemla and P.G. Schultz, *Monitoring the conformational fluctuations of DNA hairpins using single-pair fluorescence resonance energy transfer.* Journal of the American Chemical Society, 2001. **123**(18): p. 4295-4303.
11. McKinney, S.A., A.D.J. Freeman, D.M.J. Lilley and T.J. Ha, *Observing spontaneous branch migration of Holliday junctions one step at a time.* Proceedings of the National Academy of Sciences of the United States of America, 2005. **102**(16): p. 5715-5720.
12. Edel, J.B., J.S. Eid and A. Meller, *Accurate single molecule FRET efficiency determination for surface immobilized DNA using maximum likelihood calculated lifetimes.* Journal of Physical Chemistry B, 2007. **111**(11): p. 2986-2990.
13. Curnow, P. and P.J. Booth, *The Contribution of a Covalently Bound Cofactor to the Folding and Thermodynamic Stability of an Integral Membrane Protein.* Journal of Molecular Biology, 2010. **403**(4): p. 630-642.

14. Haupts, U., J. Tittor and D. Oesterhelt, *Closing in on bacteriorhodopsin: Progress in understanding the molecule.* Annual Review of Biophysics and Biomolecular Structure, 1999. **28**: p. 367-399.

15. Kim, J.M., P.J. Booth, S.J. Allen and H.G. Khorana, *Structure and function in bacteriorhodopsin: The role of the interhelical loops in the folding and stability of bacteriorhodopsin.* Journal of Molecular Biology, 2001. **308**(2): p. 409-422.

16. Huang, K.S., H. Bayley, M.J. Liao, E. London and H.G. Khorana, *Refolding of an integral membrane-protein - denaturation, renaturation, and reconstitution of intact bacteriorhodopsin and 2 proteolytic fragments.* Journal of Biological Chemistry, 1981. **256**(8): p. 3802-3809.

17. London, E. and H.G. Khorana, *Denaturation and renaturation of bacteriorhodopsin in detergents and lipid-detergent mixtures.* Journal of Biological Chemistry, 1982. **257**(12): p. 7003-7011.

18. Rehorek, M., N.A. Dencher and M.P. Heyn, *Fluorescence energy-transfer from diphenylhexatriene to bacteriorhodopsin in lipid vesicles.* Biophysical Journal, 1983. **43**(1): p. 39-45.

19. Wu, C. and L. Stryer, *Proximity relationships in rhodopsin.* Proceedings of the National Academy of Sciences of the United States of America, 1972. **69**(5): p. 1104-1108.

20. Curnow, P. and P.J. Booth, *Combined kinetic and thermodynamic analysis of alpha-helical membrane protein unfolding.* Proceedings of the National Academy of Sciences of the United States of America, 2007. **104**(48): p. 18970-18975.

21. Booth, P.J., S.L. Flitsch, L.J. Stern, D.A. Greenhalgh, P.S. Kim and H.G. Khorana, *Intermediates in the folding of the membrane-protein bacteriorhodopsin.* Nature Structural Biology, 1995. **2**(2): p. 139-143.

22. Riley, M.L., B.A. Wallace, S.L. Flitsch and P.J. Booth, *Slow alpha helix formation during folding of a membrane protein.* Biochemistry, 1997. **36**(1): p. 192-196.

23. Nannepaga, S.J., R. Gawalapu, D. Velasquez and R. Renthal, *Estimation of helix-helix association free energy from partial unfolding of bacterioopsin.* Biochemistry, 2004. **43**(2): p. 550-559.

24. Valluru, N., F. Silva, M. Dhage, G. Rodriguez, S.R. Alloor and R. Renthal, *Transmembrane helix-helix association: Relative stabilities at low pH.* Biochemistry, 2006. **45**(14): p. 4371-4377.

25. Srisa-Art, M., E.C. Dyson, A.J. deMello and J.B. Edel, *Monitoring of real-time streptavidin-biotin binding kinetics using droplet microfluidics.* Analytical Chemistry, 2008. **80**(18): p. 7063-7067.

26. Marko, J.F. and S. Cocco, *The micromechanics of DNA.* Physics World, 2003. **16**(3): p. 37-41.

27. Swift, J.L., R. Heuff and D.T. Cramb, *A two-photon excitation fluorescence cross-correlation assay for a model ligand-receptor binding system using quantum dots.* Biophysical Journal, 2006. **90**(4): p. 1396-1410.

28. Lakowicz, J.R., *Principles of fluorescence spectroscopy, 3rd edition.* Springer Science and Business Media, New York, 2006.

29. Clapp, A.R., I.L. Medintz, J.M. Mauro, B.R. Fisher, M.G. Bawendi and H. Mattoussi, *Fluorescence resonance energy transfer between quantum dot donors and dye-labeled protein acceptors.* Journal of the American Chemical Society, 2004. **126**(1): p. 301-310.

30. Krebs, M.P., T. Hauss, M.P. Heyn, U.L. Rajbhandary and H.G. Khorana, *Expression of the bacterioopsin gene in halobacterium-halobium using a multicopy plasmid.* Proceedings of the National Academy of Sciences of the United States of America, 1991. **88**(3): p. 859-863.

31. Krebs, M.P., R. Mollaaghababa and H.G. Khorana, *Gene replacement in halobacterium-halobium and expression of bacteriorhodopsin mutants.* Proceedings of the National Academy of Sciences of the United States of America, 1993. **90**(5): p. 1987-1991.

32. Oesterhe.D, Schuhman.L and H. Gruber, *Light-dependent reaction of bacteriorhodopsin with hydroxylamine in cell-suspensions of halobacterium-halobium-demonstration of an apo-membrane.* Febs Letters, 1974. **44**(3): p. 257-261.

33. Faham, S., D. Yang, E. Bare, S. Yohannan, J.P. Whitelegge and J.U. Bowie, *Side-chain contributions to membrane protein structure and stability.* Journal of Molecular Biology, 2004. **335**(1): p. 297-305.

34. Sehgal, P., J.E. Mogensen and D.E. Otzen, *Using micellar mole fractions to assess membrane protein stability in mixed micelles.* Biochimica Et Biophysica Acta-Biomembranes, 2005. **1716**(1): p. 59-68.

35. Green, N.M., *Avidin. 3. The nature of the biotin-binding site.* The Biochemical journal, 1963. **89**: p. 599-609.

36. Kurzban, G.P., G. Gitlin, E.A. Bayer, M. Wilchek and P.M. Horowitz, *Biotin binding changes the conformation and decreases tryptophan accessibility of streptavidin.* Journal of Protein Chemistry, 1990. **9**(6): p. 673-682.

37. Wilchek, M. and E.A. Bayer, *Introduction to avidin-biotin technology.* Methods in Enzymology, 1990. **184**: p. 5-13.

38. Huang, B., H.K. Wu, S. Kim and R.N. Zare, *Coating of poly(dimethylsiloxane) with n-dodecyl-beta-D-maltoside to minimize nonspecific protein adsorption.* Lab on a Chip, 2005. **5**(10): p. 1005-1007.

39. Myers, J.K., C.N. Pace and J.M. Scholtz, *Denaturant m-values and heat-capacity changes - relation to changes in accessible surface-areas of protein unfolding.* Protein Science, 1995. **4**(10): p. 2138-2148.

CHAPTER 8
CONCLUSION AND OUTLOOK

8.1. Summary of achievements

Fluorescence measurements in conjunction with appropriate optical detection arrangements, such as confocal systems, have been widely used in biological and biomedical research. The high sensitivity and detection efficiency offered by confocal microscopy can be further improved by specially configured microfluidic platforms, rendering this combination extremely attractive for a variety of bioanalytical applications. Microfluidic configurations are characterised by low sample consumption, short mixing and reaction times and easy sample manipulation. In addition, in continuous flow applications, positions along a microchannel correspond to time. Therefore, microfluidic devices are perfectly suitable platforms for the study of biomolecular conformational changes and interactions in real time. In this thesis, a novel optical detection and analysis method was used in conjunction with microfluidics to study freely diffusing and flowing molecules with high precision and sensitivity. The superiority of fluorescence lifetime techniques as opposed to fluorescence intensity measurements was clearly demonstrated throughout this work.

Initially, a home-built optical detection system was constructed, consisting of a laser scanning confocal microscope and an integrated custom-built detection path. The use of confocal microscopy combined with APD detectors provided improved signal-to-noise ratio and allowed for single photon counting, enabling high sensitivity measurements. The laser scanning configuration allowed for imaging to be performed with the high sensitivity and resolution of confocal microscopy. The use of pulsed lasers enabled simultaneous fluorescence intensity and fluorescence lifetime measurements. The Fianium supercontinuum source offered a variety of laser lines for sample excitation and the system was flexible, with easy access to filters and dichroics. Thus, a variety of fluorophores could be used and the setup was suitable for potential two colour excitation applications. The incorporation of two APDs allowed for detection in the green and red spectrum regions facilitating FRET measurements.

3-inlet 1-outlet microfluidic devices were designed, fabricated and subsequently tested in conjunction with the custom-built optical setup, in terms of hydrodynamic focusing and mixing performance. More specifically, for both hydrodynamic focusing and mixing

characterisation, FLIM via TCSPC was the detection and analysis method of choice due to its advantages over fluorescence intensity measurements. In addition, a maximum likelihood estimator approach was used for fluorescence lifetime extraction from as little as 10 photons and two-dimensional lifetime maps were constructed visualising the flow within the microchannels. Appropriate algorithms were applied to extract the focused stream width as well as the mixing time under various flow rate conditions and the effect of the side-to-central inlet flow rate ratio on both focusing width and mixing time was investigated. Focusing width values of only a couple of micrometres and mixing times as short as 3 ms were achieved. Considering the sample consumption and the velocity limits required for the stability of the focused stream, it was concluded that the most appropriate chip design and inlet flow rates for an experiment should be selected depending on the specific application requirements.

Subsequently, the sensitivity of the developed optical system was demonstrated by detecting single DNA molecules while flowing down the length of a microfluidic channel. Hydrodynamic focusing was employed as a molecular confinement mechanism to increase the proportion of the sample travelling through the detection volume and, thus, to improve the molecular detection efficiency. Fluorescence burst analysis was performed and useful trends were extracted in terms of burst frequency, height, duration and area. A series of considerations were made with respect to optimum channel geometry and employed flow rates to ensure rapid, high throughput measurements with maximum detection efficiency, combined with low sample consumption and high statistical accuracy.

The custom-built optical detection system was also exploited to perform FRET measurements on freely diffusing and flowing biomolecules. Initially, a fluorescence lifetime-based FRET analysis method was developed, which overcame artefacts arising from the presence of non-fretting donors in the sample and allowed for discrimination, to some extent, between different FRET populations without the need for measurements at the single molecule level. For this purpose, complementary DNA oligos were labelled at known sites with two FRET dye pairs and, following hybridisation, the inter-dye distance was extracted from FRET measurements. By fitting the donor decay to a triple exponential function with the *setup component* and the original donor lifetime τ_D fixed, the estimated donor-acceptor distances were in excellent agreement with the theoretically calculated values.

The developed FRET analysis method was subsequently applied to investigate the biotin-streptavidin binding in equilibrium as well as to monitor the unfolding of bacterioopsin under various SDS concentrations. Fluorescence lifetime FRET measurements indicated that more binding occurred for high biotin-to-streptavidin concentration ratio and it was concluded that

for the conditions used herein ligand excess resulted in three, on average, biotins bound per streptavidin tetramer. Equilibrium measurements performed on bO for a variety of denaturant concentrations yielded intramolecular distances for the folded and unfolded states as well as unfolding characteristics, such as major transition slope, transition midpoint and free energy change upon unfolding at zero SDS concentration, which were in very good agreement with previously reported results. In addition, a microfluidic channel was used as a platform for studying bO unfolding kinetics and hydrodynamic focusing was employed as a mixing enhancement mechanism. The acquired observed rate constant for the major unfolding transition was consistent with results presented by other researchers, confirming that the combination of FRET measurements, time-resolved techniques and microfluidics is a powerful tool for protein folding/unfolding studies.

8.2. Improvements and outlook

It becomes apparent that combining confocal microscopy, time-resolved fluorescence measurements and microfluidics can be a particularly attractive tool for a variety of biological applications. In addition, incorporating FRET techniques completes an ideal method for investigating a variety of biomolecular rearrangements and interactions.

Although the majority of bioanalytical fluorescence and FRET experiments so far employ intensity measurements, fluorescence lifetime methods were proved herein to be extremely advantageous compared to intensity techniques. Not only artefacts associated with sample concentration variations, non-uniform sample illumination, detection efficiency etc. were minimised, but also, in FRET applications, the use of multi-exponential decay fitting enabled discrimination between different populations within the sample, without the need for single molecule measurements. In imaging applications, fluorescence lifetimes were successfully calculated using as little as 10 photons, rendering the MLE method used herein a powerful tool for the study of systems that yield low photon counts. A drawback of the MLE routine in the form that it was used herein was that it provided a single lifetime value. Therefore, if a mixture of lifetime populations were present within the sample, discrimination using the MLE routine could only be achieved by performing measurements at the single molecule level. Otherwise, traditional multi-exponential decay fitting should be used, which however would demand a significant amount of photons to be statistically accurate.

In terms of single molecule detection, fluorescence burst analysis under flow conditions can be extremely useful in high throughput screening applications as well as in performing molecular

separations and sorting. More specifically, burst height, width and area can be related to the size of the molecule, whilst burst frequency can be used for determining sample concentration. In addition, fluorescence lifetime is characteristic for each fluorophore. Therefore, burst height, width, area and lifetime histograms can be used, via appropriate analysis, to distinguish between sample components or between different states/sizes of the same species.

Furthermore, as it was illustrated herein, employing hydrodynamic focusing to confine the sample within a narrow focused stream significantly improves the molecular detection efficiency. In the experiments performed in this work it was observed that at high flow rates or at high sample velocities induced by hydrodynamic focusing, the detection efficiency gradually plateaued due to a fraction of molecules travelling through the probe volume too fast to be detected or resolved. In such occasions, further decreasing the sample concentration would be necessary to partially overcome this problem. Besides, downsizing the channels or applying three-dimensional flow focusing, decreasing at the same time the used flow rates, could offer additional sample confinement, resulting in further improvement of the detection efficiency and sample consumption minimisation.

For the optical arrangement used in this work in conjunction with the DL549-DL633 FRET dye pair, single dye-molecule experiments under FRET could not be performed as both the fluorescence intensity and fluorescence lifetime of FRET-experiencing donor molecules were at levels below the system detection limitations. It should be noted however that the specific dyes possess low quantum yields and the DL549 lifetime is quite short even at non-FRET conditions (~1.16 ns). Performing SMD measurements on molecules labelled with the AF488-AF647 FRET pair could have potentially provided more conclusive single molecule histograms.

Finally, the use of the current system in conjunction with a microfluidic device for monitoring equilibrium protein unfolding and bO unfolding kinetics provided results consistent with previous studies, with very low sample consumption due to both the low concentrations (nM) and low volumes (μl) used. Therefore, this is a perfectly suitable method for studying protein conformational changes as well as a variety of other biomolecular rearrangements/interactions, and especially for investigating early kinetics (μs-ms) and identifying potential intermediate states with minimum sample consumption.

APPENDIX A

MICROFLUIDIC CHIP DESIGNS

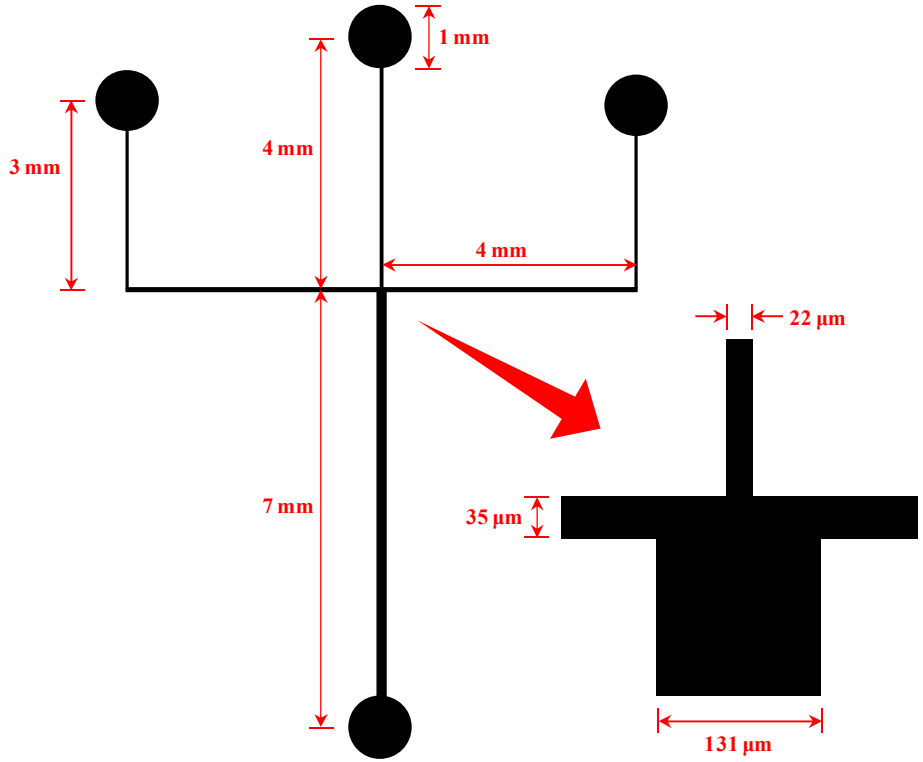

Figure A.1. Microfluidic chip design III. All channels were 50 µm deep. The width of the central inlet, side inlets and outlet channels in chip design I were 11 µm, 17.5 µm and 65.5 µm respectively. In chip design II the respective width values were 15.5 µm, 25 µm and 93 µm. Channel length and depth were the same for designs I, II and III.

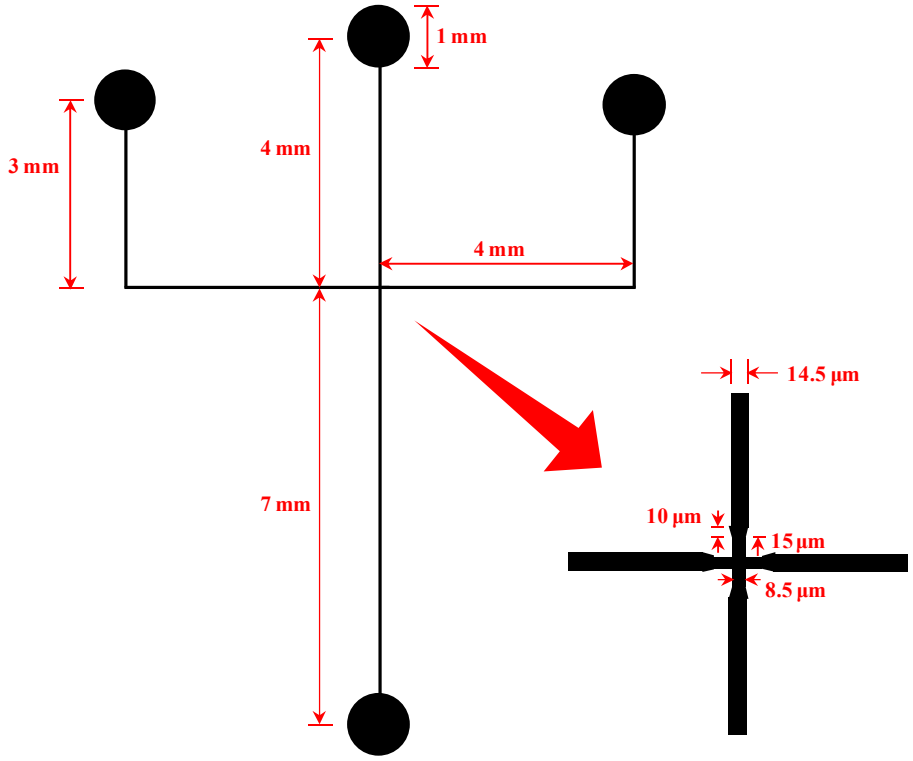

Figure A.2. Improved microfluidic chip design with nozzles, used in hydrodynamic focusing experiments. All channels were 15 µm deep.

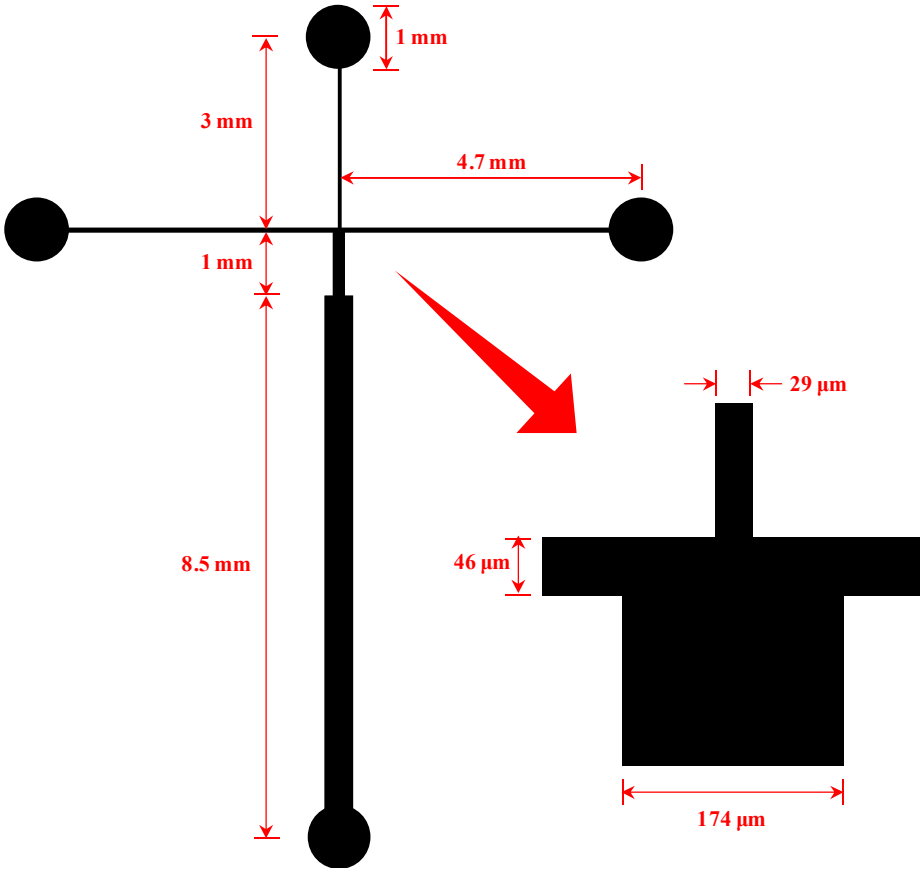

Figure A.3. Chip design a used in mixing under hydrodynamic focusing experiments. All channels were 50 µm deep. This design was also used for performing bO unfolding kinetic analysis measurements.

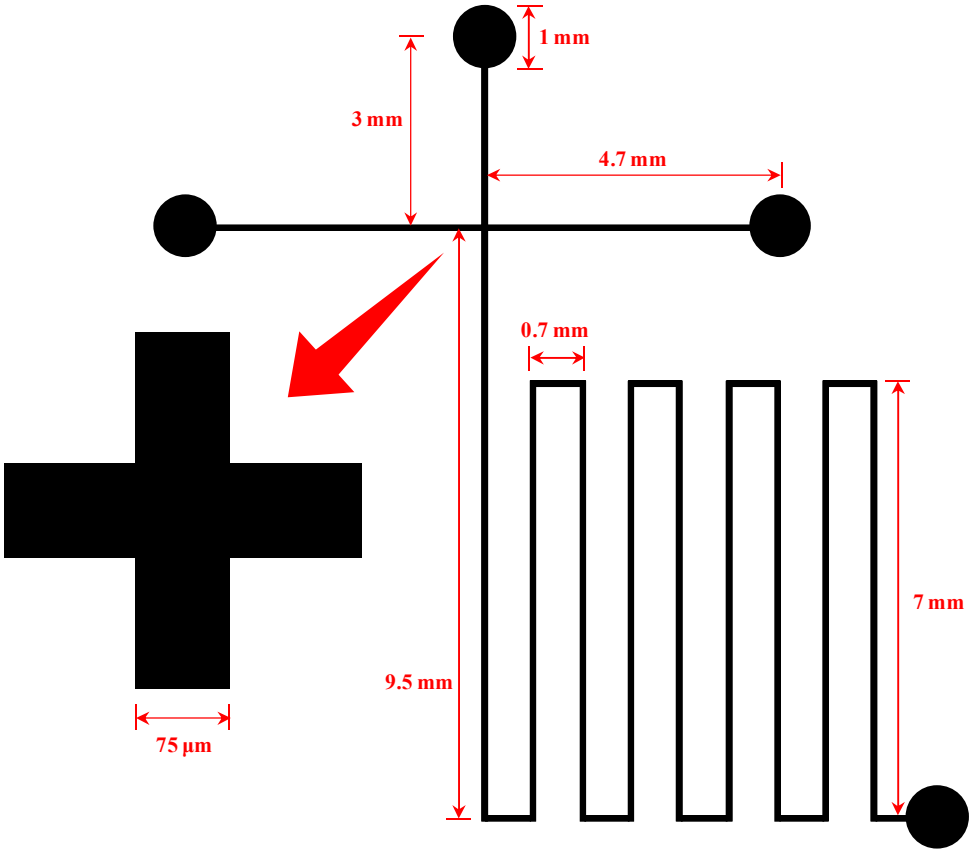

Figure A.4. Chip design b used in mixing under hydrodynamic focusing experiments. All channels were 100 µm deep.

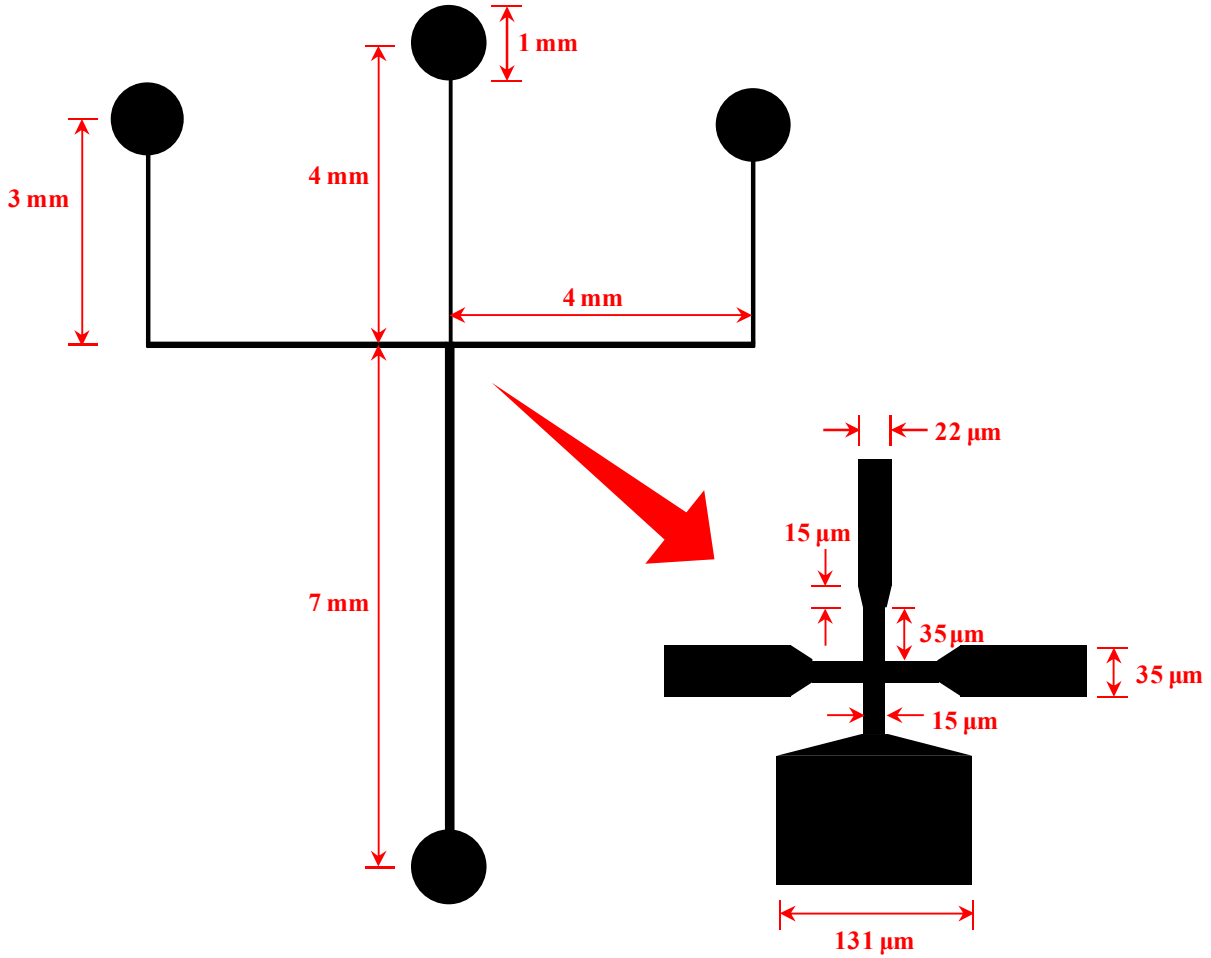

Figure A.5. Chip design used for improving the molecular detection efficiency in single molecule measurements. All channels were 50 µm deep.

APPENDIX B

PERMISSION FOR THIRD PARTY COPYRIGHT WORKS

Table B.1. Summary of permission for third party copyright works

Page number	Type	Source	Copyright holder & year	Permission to re-use	Permission not required
p. 30	Figure	Journal of Physics D-Applied Physics, 2002. 35(9): p. R61-R76	© 2002 IOP Publishing	X	
p. 53	Figure	Analyst, 2000. 125(6): p. 1033-1036 *	© 2000 The Royal Society of Chemistry	X	
p. 55	Figure	Springer Science and Business Media, New York, 2006	© 2006 Springer Science and Business Media	X	
p. 81	Figure	Journal of Micromechanics and Microengineering, 2006. 16(5): p. 1024-1032	© 2006 IOP Publishing	X	
p. 82	Figure	Journal of Micromechanics and Microengineering, 2006. 16(5): p. 1024-1032	© 2006 IOP Publishing	X	
p. 167	Figure	Proceedings of National Academy of Sciences of the USA, 1993. 90(7): p. 2994-2998	© 1993 National Academy of Sciences		X
p. 190	Figure	Immunology Letters, 2006. 103(1): p. 27-32	© 2005 Elsevier	X	
p. 190	Figure	Journal of Molecular Biology, 2010. 403(4): p. 630-642	© 2010 Elsevier	X	

*DOI: http://dx.doi.org/10.1039/B002242J

Proof of permission

Copyright holder IOP Publishing Ltd (pages 30, 81 and 82) – permission acquired via email

From: Permissions <permissions@iop.org>

Date: 24 May 2013 18:48

Subject: Re: Case # 00097090 Copyright permission annual license - Imperial College London

To: margarita.stapountzi06@gmail.com

Dear Margarita,

Thanks for getting back to me with that detail.

We are happy to grant permission for the use you request on the terms set out below. Please note that if your redrawn figure reproduces qualitatively substantial elements of fig 1 of the Lee et al article, then permission would be needed and therefore, this permission and the terms below extend to that use also.

If you have any questions, please feel free to contact our Permissions team at permissions@iop.org. Wishing you the best of luck with the completion of your thesis.

Kind regards,

Laura Sharples
Rights & Permissions Officer
IOP Publishing Ltd
Temple Circus, Temple Way, Bristol BS1 6HG
T: +44 (0)117 930 1001
F: +44 (0)117 920 0997

What do scientific publishers do?

Conditions

Non-exclusive, non-transferrable, revocable, worldwide, permission to use the material in print and electronic form will be granted subject to the following conditions:

· Permission will be cancelled without notice if you fail to fulfil any of the conditions of this letter.

· You will make reasonable efforts to contact the author(s) to seek consent for your intended use. Contacting one author acting expressly as authorised agent for their co-authors is acceptable.

· You will reproduce the following prominently alongside the material:

o the source of the material, including author, article title, title of journal, volume number, issue number (if relevant), page range (or first page if this is the only information available) and date of first publication

o for material being published electronically, a link back to the article (via DOI)

o if practical and IN ALL CASES for works published under any of the Creative Commons licences the words "© IOP Publishing. Reproduced with permission. All rights reserved"

· The material will not, without the express permission of the author(s), be used in any way which, in the opinion of IOP Publishing, could distort or alter the author(s)' original intention(s) and meaning, be prejudicial to the honour or reputation of the author(s) and/or imply endorsement by the author(s) and/or IOP Publishing.

· Payment of £0 is received in full by IOP Publishing prior to use.

Please note: IOP does not usually provide signed permission forms as a separate attachment. Please print this email and provide it to your publisher as proof of permission.

From: Margarita Stapountzis <margarita.stapountzi06@imperial.ac.uk>
To: permissions@iop.org,
Date: 24/05/2013 16:29
Subject: Re: Case # 00097090 Copyright permission annual license - Imperial College London
Sent by: margarita.stapountzi06@gmail.com

Dear Laura,
Thank you very much for your reply. The title of my PhD thesis is 'Development of fluorescence lifetime measurement techniques for use in microfluidic channels', to be submitted in June 2013. I seek your permission to reprint in my thesis extracts from:
1. Cubeddu, R., D. Comelli, C. D'Andrea, P. Taroni and G. Valentini, *Time-resolved fluorescence imaging in biology and medicine.* Journal of Physics D-Applied Physics, 2002. 35(9): p. R61-R76
http://iopscience.iop.org/0022-3727/35/9/201/
The extract to be reproduced is: Figure 4a and Figure 4b
2. Lee, G.B., C.C. Chang, S.B. Huang and R.J. Yang, *The hydrodynamic focusing effect inside rectangular microchannels.* Journal of Micromechanics and Microengineering, 2006. 16(5): p. 1024-1032
http://iopscience.iop.org/0960-1317/16/5/020
The extract to be reproduced is: Figure 2.
I will also be using a similar schematic diagram to Figure 1a from the same paper which is however re-drawn in powerpoint by myself with different notation so I believe I do not need copyright permission for that.
I would like to include the above extracts in the printed examination copy of my thesis and also the electronic version which will be added to Spiral, Imperial's online repository http://spiral.imperial.ac.uk/ and made available to the public under a Creative Commons Attribution-NonCommercial-NoDerivs licence.
If you are happy to grant me all the permissions requested, please return a signed copy of this email (a suggested by Imperial College London format is shown below). If you wish to grant only some of the permissions requested, please list these and then sign.
Yours sincerely,
Margarita Stapountzis

Copyright holder The Royal Society of Chemistry (page 53) – permission acquired via email

From: CONTRACTS-COPYRIGHT (shared) <Contracts-Copyright@rsc.org>
Date: 6 June 2013 16:21
Subject: RE: Website Email: Copyright Permission Request - Imperial College London
To: Margarita Stapountzis <margarita.stapountzi06@gmail.com>

Dear Margarita
The Royal Society of Chemistry hereby grants permission for the use of the material specified below in the work described and in all subsequent editions of the work for distribution throughout the world, in all media including electronic and microfilm. You may use the material in conjunction with computer-based electronic and information retrieval systems, grant permissions for photocopying, reproductions and reprints, translate the material and to publish the translation, and authorize document delivery and abstracting and indexing services. The Royal Society of Chemistry is a signatory to the STM Guidelines on Permissions (available on request). Please note that if the material specified below or any part of it appears with credit or acknowledgement to a third party then you must also secure permission from that third party before reproducing that material.
Please ensure that the published article carries a credit to The Royal Society of Chemistry in the following format:
[Original citation] – Reproduced by permission of The Royal Society of Chemistry
and that any electronic version of the work includes a hyperlink to the article on the Royal Society of Chemistry website. The recommended form for the hyperlink is http://dx.doi.org/10.1039/*DOI suffix*, for example in the link http://dx.doi.org/10.1039/b110420a the DOI suffix is 'b110420a'. To find the relevant DOI suffix for the RSC paper in question, go to the Journals section of the website and locate your paper in the list of papers for the volume and issue of your specific journal. You will find the DOI suffix quoted there.
Regards
Gill Cockhead
Publishing Contracts & Copyright Executive
Gill Cockhead (Mrs), Publishing Contracts & Copyright Executive
Royal Society of Chemistry, Thomas Graham House
Science Park, Milton Road, Cambridge CB4 0WF, UK
Tel +44 (0) 1223 432134, Fax +44 (0) 1223 423623
http://www.rsc.org

From: Margarita Stapountzis [mailto:margarita.stapountzi06@gmail.com]
Sent: 26 May 2013 01:43
To: CONTRACTS-COPYRIGHT (shared)
Subject: Website Email: Copyright Permission Request - Imperial College London

Dear Sir / Madam,
I am completing my PhD thesis at Imperial College London entitled 'Development of fluorescence lifetime measurement techniques for use in microfluidic channels' (to be submitted in June 2013). I seek your permission to reprint, in my thesis an extract from:
Hill, E.K. and A.J. de Mello, Single-molecule detection using confocal fluorescence detection:Assessment of optical probe volumes. Analyst,2000. 125(6): p. 1033-1036
The extract to be reproduced is: figure 2
I would like to include the extract in the printed examination copy of my thesis and also the electronic version which will be added to Spiral, Imperial's online repository http://spiral.imperial.ac.uk/ and made available to the public under a Creative Commons Attribution-NonCommercial-NoDerivs licence.
If you are happy to grant me the permission requested, please return a signed copy of this email (a suggested by Imperial College London format is shown below).
Yours sincerely, Margarita Stapountzis

Copyright holder Springer Science and Business Media (page 55) – permission acquired via email as an attachment

June 21, 2013

Springer reference
Pawley, J.B., Handbook of biological confocal microscopy, 3rd edition.
Springer Science and Business Media, New York, 2006
figure 22.4, page 445

Your project
University: Imperial College London
Title: Dissertation/Thesis - Margarita Stapountzis

With reference to your request to reuse material in which Springer Science+Business Media controls the copyright, our permission is granted free of charge under the following conditions:

Springer material

- represents original material which does not carry references to other sources (if material in question refers with a credit to another source, authorization from that source is required as well);
- requires full credit (book title, year of publication, page, chapter title, name(s) of author(s), original copyright notice) is given to the publication in which the material was originally published by adding: "With kind permission of Springer Science+Business Media";
- may not be altered in any manner. Any other abbreviations, additions, deletions and/or any other alterations shall be made only with prior written authorization of the author and/or Springer Science+Business Media;

This permission

- is non-exclusive;
- is valid for one-time use only for the purpose of defending your thesis, and with a maximum of 100 extra copies in paper.
- includes use in an electronic form, provided it is an author-created version of the thesis on his/her own website and his/her university's repository, including UMI (according to the definition on the Sherpa website: http://www.sherpa.ac.uk/romeo/);
- is subject to courtesy information to the corresponding author;
- is personal to you and may not be sublicensed, assigned, or transferred by you to any other person without Springer's written permission;
- is valid only when the conditions noted above are met.

Permission free of charge does not prejudice any rights we might have to charge for reproduction of our copyrighted material in the future.

Best regards,

Rights and Permissions
Springer-Verlag GmbH
Tiergartenstr. 17
69121 Heidelberg
Germany
E-mail: permissions.heidelberg@springer.com

Copyright holder National Academy of Sciences (page 167) – permission not required

According to the PNAS website (http://www.pnas.org/site/aboutpnas/rightperm.xhtml): 'Anyone may, without requesting permission, use original figures or tables published in PNAS for noncommercial and educational use (i.e., in a review article, in a book that is not for sale) provided that the original source and the applicable copyright notice are cited'.

ELSEVIER LICENSE
TERMS AND CONDITIONS

May 21, 2013

Supplier	Elsevier Limited The Boulevard,Langford Lane Kidlington,Oxford,OX5 1GB,UK
Registered Company Number	1982084
Customer name	Margarita A Stapountzis
Customer address	Imperial College London London, SW7 2AZ
License number	3153710721526
License date	May 21, 2013
Licensed content publisher	Elsevier
Licensed content publication	Immunology Letters
Licensed content title	Essentials of biorecognition: The (strept)avidin–biotin system as a model for protein–protein and protein–ligand interaction
Licensed content author	Meir Wilchek,Edward A. Bayer,Oded Livnah
Licensed content date	28 February 2006
Licensed content volume number	103
Licensed content issue number	1
Number of pages	6
Start Page	27
End Page	32
Type of Use	reuse in a thesis/dissertation
Intended publisher of new work	other
Portion	figures/tables/illustrations
Number of figures/tables/illustrations	1
Format	both print and electronic
Are you the author of this Elsevier article?	No
Will you be translating?	No
Order reference number	
Title of your thesis/dissertation	Development of Fluorescence Lifetime Measurement Techniques for Use in Microfluidic Channels
Expected completion date	Jun 2013
Estimated size (number of pages)	220
Elsevier VAT number	GB 494 6272 12
Permissions price	0.00 USD
VAT/Local Sales Tax	0.0 USD / 0.0 GBP
Total	0.00 USD

ELSEVIER LICENSE
TERMS AND CONDITIONS

May 21, 2013

This is a License Agreement between Margarita A Stapountzis ("You") and Elsevier ("Elsevier") provided by Copyright Clearance Center ("CCC"). The license consists of your order details, the terms and conditions provided by Elsevier, and the payment terms and conditions.

All payments must be made in full to CCC. For payment instructions, please see information listed at the bottom of this form.

Supplier	Elsevier Limited The Boulevard,Langford Lane Kidlington,Oxford,OX5 1GB,UK
Registered Company Number	1982084
Customer name	Margarita A Stapountzis
Customer address	Imperial College London London, SW7 2AZ
License number	3153701247056
License date	May 21, 2013
Licensed content publisher	Elsevier
Licensed content publication	Journal of Molecular Biology
Licensed content title	The Contribution of a Covalently Bound Cofactor to the Folding and Thermodynamic Stability of an Integral Membrane Protein
Licensed content author	Paul Curnow,Paula J. Booth
Licensed content date	5 November 2010
Licensed content volume number	403
Licensed content issue number	4
Number of pages	13
Start Page	630
End Page	642
Type of Use	reuse in a thesis/dissertation
Portion	figures/tables/illustrations
Number of figures/tables/illustrations	1
Format	both print and electronic
Are you the author of this Elsevier article?	No
Will you be translating?	No
Order reference number	
Title of your thesis/dissertation	Development of Fluorescence Lifetime Measurement Techniques for Use in Microfluidic Channels
Expected completion date	Jun 2013
Estimated size (number of pages)	220
Elsevier VAT number	GB 494 6272 12
Permissions price	0.00 USD
VAT/Local Sales Tax	0.0 USD / 0.0 GBP
Total	0.00 USD

TERMS AND CONDITIONS

INTRODUCTION

1. The publisher for this copyrighted material is Elsevier. By clicking "accept" in connection with completing this licensing transaction, you agree that the following terms and conditions apply to this transaction (along with the Billing and Payment terms and conditions established by Copyright Clearance Center, Inc. ("CCC"), at the time that you opened your Rightslink account and that are available at any time at http://myaccount.copyright.com).

GENERAL TERMS

2. Elsevier hereby grants you permission to reproduce the aforementioned material subject to the terms and conditions indicated.

3. Acknowledgement: If any part of the material to be used (for example, figures) has appeared in our publication with credit or acknowledgement to another source, permission must also be sought from that source. If such permission is not obtained then that material may not be included in your publication/copies. Suitable acknowledgement to the source must be made, either as a footnote or in a reference list at the end of your publication, as follows:

"Reprinted from Publication title, Vol /edition number, Author(s), Title of article / title of chapter, Pages No., Copyright (Year), with permission from Elsevier [OR APPLICABLE SOCIETY COPYRIGHT OWNER]." Also Lancet special credit - "Reprinted from The Lancet, Vol. number, Author(s), Title of article, Pages No., Copyright (Year), with permission from Elsevier."

4. Reproduction of this material is confined to the purpose and/or media for which permission is hereby given.

5. Altering/Modifying Material: Not Permitted. However figures and illustrations may be altered/adapted minimally to serve your work. Any other abbreviations, additions, deletions and/or any other alterations shall be made only with prior written authorization of Elsevier Ltd. (Please contact Elsevier at permissions@elsevier.com)

6. If the permission fee for the requested use of our material is waived in this instance, please be advised that your future requests for Elsevier materials may attract a fee.

7. Reservation of Rights: Publisher reserves all rights not specifically granted in the combination of (i) the license details provided by you and accepted in the course of this licensing transaction, (ii) these terms and conditions and (iii) CCC's Billing and Payment terms and conditions.

8. License Contingent Upon Payment: While you may exercise the rights licensed immediately upon issuance of the license at the end of the licensing process for the transaction, provided that you have disclosed complete and accurate details of your proposed use, no license is finally effective unless and until full payment is received from you (either by publisher or by CCC) as provided in CCC's Billing and Payment terms and conditions. If full payment is not received on a timely basis, then any license preliminarily granted shall be deemed automatically revoked and shall be void as if never granted. Further, in the event that you breach any of these terms and conditions or any of CCC's Billing and Payment terms and conditions, the license is automatically revoked and shall be void as if never granted. Use of materials as described in a revoked license, as well as any use of the materials beyond the scope of an unrevoked license, may constitute copyright infringement and publisher reserves the right to take any and all action to protect its copyright in the materials.

9. Warranties: Publisher makes no representations or warranties with respect to the licensed material.
10. Indemnity: You hereby indemnify and agree to hold harmless publisher and CCC, and their respective officers, directors, employees and agents, from and against any and all claims arising out of your use of the licensed material other than as specifically authorized pursuant to this license.
11. No Transfer of License: This license is personal to you and may not be sublicensed, assigned, or transferred by you to any other person without publisher's written permission.
12. No Amendment Except in Writing: This license may not be amended except in a writing signed by both parties (or, in the case of publisher, by CCC on publisher's behalf).
13. Objection to Contrary Terms: Publisher hereby objects to any terms contained in any purchase order, acknowledgment, check endorsement or other writing prepared by you, which terms are inconsistent with these terms and conditions or CCC's Billing and Payment terms and conditions. These terms and conditions, together with CCC's Billing and Payment terms and conditions (which are incorporated herein), comprise the entire agreement between you and publisher (and CCC) concerning this licensing transaction. In the event of any conflict between your obligations established by these terms and conditions and those established by CCC's Billing and Payment terms and conditions, these terms and conditions shall control.
14. Revocation: Elsevier or Copyright Clearance Center may deny the permissions described in this License at their sole discretion, for any reason or no reason, with a full refund payable to you. Notice of such denial will be made using the contact information provided by you. Failure to receive such notice will not alter or invalidate the denial. In no event will Elsevier or Copyright Clearance Center be responsible or liable for any costs, expenses or damage incurred by you as a result of a denial of your permission request, other than a refund of the amount(s) paid by you to Elsevier and/or Copyright Clearance Center for denied permissions.
LIMITED LICENSE
The following terms and conditions apply only to specific license types:
15. Translation: This permission is granted for non-exclusive world English rights only unless your license was granted for translation rights. If you licensed translation rights you may only translate this content into the languages you requested. A professional translator must perform all translations and reproduce the content word for word preserving the integrity of the article. If this license is to re-use 1 or 2 figures then permission is granted for non-exclusive world rights in all languages.
16. Website: The following terms and conditions apply to electronic reserve and author websites:
Electronic reserve: If licensed material is to be posted to website, the web site is to be password-protected and made available only to bona fide students registered on a relevant course if:
This license was made in connection with a course,
This permission is granted for 1 year only. You may obtain a license for future website posting,
All content posted to the web site must maintain the copyright information line on the bottom of each image,
A hyper-text must be included to the Homepage of the journal from which you are licensing at http://www.sciencedirect.com/science/journal/xxxxx or the Elsevier homepage for books at http://www.elsevier.com, and

Central Storage: This license does not include permission for a scanned version of the material to be stored in a central repository such as that provided by Heron/XanEdu.

17. Author website for journals with the following additional clauses:

All content posted to the web site must maintain the copyright information line on the bottom of each image, and the permission granted is limited to the personal version of your paper. You are not allowed to download and post the published electronic version of your article (whether PDF or HTML, proof or final version), nor may you scan the printed edition to create an electronic version. A hyper-text must be included to the Homepage of the journal from which you are licensing at http://www.sciencedirect.com/science/journal/xxxx. As part of our normal production process, you will receive an e-mail notice when your article appears on Elsevier's online service ScienceDirect (www.sciencedirect.com). That e-mail will include the article's Digital Object Identifier (DOI). This number provides the electronic link to the published article and should be included in the posting of your personal version. We ask that you wait until you receive this e-mail and have the DOI to do any posting.

Central Storage: This license does not include permission for a scanned version of the material to be stored in a central repository such as that provided by Heron/XanEdu.

18. Author website for books with the following additional clauses:

Authors are permitted to place a brief summary of their work online only.

A hyper-text must be included to the Elsevier homepage at http://www.elsevier.com. All content posted to the web site must maintain the copyright information line on the bottom of each image. You are not allowed to download and post the published electronic version of your chapter, nor may you scan the printed edition to create an electronic version.

Central Storage: This license does not include permission for a scanned version of the material to be stored in a central repository such as that provided by Heron/XanEdu.

19. Website (regular and for author): A hyper-text must be included to the Homepage of the journal from which you are licensing at http://www.sciencedirect.com/science/journal/xxxxx or for books to the Elsevier homepage at http://www.elsevier.com

20. Thesis/Dissertation: If your license is for use in a thesis/dissertation your thesis may be submitted to your institution in either print or electronic form. Should your thesis be published commercially, please reapply for permission. These requirements include permission for the Library and Archives of Canada to supply single copies, on demand, of the complete thesis and include permission for UMI to supply single copies, on demand, of the complete thesis. Should your thesis be published commercially, please reapply for permission.

21. Other Conditions:

v1.6. If you would like to pay for this license now, please remit this license along with your payment made payable to "COPYRIGHT CLEARANCE CENTER" otherwise you will be invoiced within 48 hours of the license date. Payment should be in the form of a check or money order referencing your account number and this invoice number RLNK501025975.